SPECTRAL, ELECTROCHEMICAL, SINGLE CRYSTAL XRD AND MOLECULAR MODELING STUDIES OF AZOMETHINE AND DIHYDROAZOMETHINE COMPOUNDS OF SUPRAMOLECULAR SIGNIFICANCE

A THESIS

SUBMITTED TO THE

NATIONAL INSTITUTE OF TECHNOLOGY WARANGAL

FOR THE AWARD OF THE DEGREE OF

DOCTOR OF PHILOSOPHY

BY

GUDIPATI SRINIVASARAO

(Roll No. 701087)

DEPARTMENT OF CHEMISTRY

NATIONAL INSTITUTE OF TECHNOLOGY WARANGAL

WARANGAL – 506 004, TELANGANA, INDIA

MARCH, 2016

DECLARATION

I hereby declare that the matter embodied in this thesis entitled, ***"Spectral, Electrochemical, Single Crystal XRD and Molecular Modeling Studies of Azomethine and Dihydroazomethine Compounds of Supramolecular Significance"*** is the results of investigations carried out by me in the Department of Chemistry, National Institute of Technology Warangal, Telangana, India, under the supervision of Prof. A. Ramachandraiah, Department of Chemistry, National Institute of Technology Warangal, Telangana, India and the same has not been submitted either in part or full, elsewhere for any degree or diploma.

Date: (**GUDIPATI SRINIVASARAO)**

Place: **NIT Warangal** Roll Number: **701087**

CERTIFICATE

This is to certify that the work presented in the thesis entitled ***"Spectral, Electrochemical, Single Crystal XRD and Molecular Modeling Studies of Azomethine and Dihydroazomethine Compounds of Supramolecular Significance"*** has been carried out by **Mr. GUDIPATI SRINIVASARAO** under my supervision and the same has not been submitted elsewhere for the award of any degree or diploma.

Dr. A. RAMACHANDRAIAH
Professor of Chemistry
National Institute of Technology, Warangal
(Research Supervisor)

Warangal
March, 2016

ACKNOWLEDGEMENTS

I express my deep sense of gratitude to my research supervisor, **Prof. A. Ramachandraiah**, Professor of Chemistry, National Institute of Technology Warangal, for suggesting an intresting problem and for his invaluable guidance throught my research. I consider myself as very fortunate to work with him. It would have been impossible to achieve this goal without his strong support and care. I remember the research days I have spent with him for ever.

I am very much grateful to **The Director**, National Institute of Technology, Warangal for giving me an opportunity to carry out the research work and allowing me to submit in the form of thesis. I greatly acknowledge **MHRD, Govt. of India** for the financial support in the form of Institute Fellowship.

I express my sincere thanks to the Doctoral Scrutiny Committee members: **Prof. V. Rajeswar Rao**, Chairman and Head, Department of Chemistry, **Prof. K. Laxma Reddy**, Department of Chemistry and **Prof. Y. Pydisetty**, Department of Chemical Engineering, NIT Warangal for their detailed review, constructive suggestions and excellent advice during the progress of my research work.

I place on record my thanks to **Dr. Basavoju Srinivas**, Assistant Professor, Department of Chemistry, NIT Warangal, for his support and help in the recording and solving the single crystal X-Ray data.

I am very much thankful to **Prof. B. V. Appa Rao** (Retd.), Department of Chemistry, NIT Warangal, for his valuable suggestions and help.

I am thankful to all the former Heads of the Department of Chemistry during the period of my research work, for their kindness and affection.

I would like to thank all the faculty members of Chemistry Department namely **Prof. G. V. P. Chandra Mouli**, **Prof. I. Ajit Kumar Reddy**, **Prof. P. Nageswara Rao, Prof. B. Rajitha**, **Dr. K. V. Gobi, Dr. P. V. Srilakshmi**, **Dr. Vishnu Shanker**, **Dr. Venkatathri Narayanan**, **Dr. D. Kasinath, Dr. K. Hari Prasad** and the **other faculty members** for their valuable advice and encouragement throughout the research work.

I convey my heartfelt thanks to **Dr. Chepuri Ramakishan Rao**, Principal Scientist, IICT, Hyderabad, **Prof. D. Narayan Rao** (Physics) and **Dr. Bhargavi** (Chemistry), University of Hyderabad, **Dr. M. Srinivas** (Head Department of Microbiology), Kakatiya University, **Dr. Ramakrishna** (IISER Kolkata) for their support and encouragement.

My Special thanks are due to **Dr. V. Prabhavathi**, Bharathi Nursing Home, **Dr. Thirupathi Reddy** and **Staff** of the Dispensary NIT Wararangal.

I convey my special thanks to my seniors **Dr. Sunil Kumar, Dr. N. Raju, Dr. P. Vijaya Bhaskar, Dr. D. Prabhakara Chary**, and **Dr. V. Krishna** and juniors, **Ashutosh Kumar Yadav, E. Rajesh, K. Rajamouli, Manjula, Divya** and **Ramesh** for their continuous support and encouragement in each and every step of my research work.

I convey my special thanks from the bottom of my heart to my collegues **Dr. K. Chaitanya Kumar, Dr. K. V. V. Satyanarayana, Dr. Ch. Sreenivas, Dr. M. Nooka Raju, Dr. Rajini Dr. K. Koteshwer Reddy, Dr. M Narasimha Reddy, Dr. Kanaka Raju, Dr. B Janarthan, Dr. B. Santosh, Dr. T. Surendar, Dr. T. Ramesh, Dr. P. Kavitha, , Dr. Vijaya Laxmi, Dr. G. Rajitha, K. Vimal Kumar, M. Satyanarayana, K. Yugandar, Ajay, Sunil, Suman, Saikumar, Phani, Harimohan, Vikramsagar, V. Krishnaiah, Raj Kumar, P. Sreenu, Pogaku Vinay, L. Suresh, M. Venkana, Mayuri, Hithavani, Soumya, Ch. Nagaraju, B. Paplal, G. Ramesh, Bharath**, for their continuous support and encouragement in each and every step of my research work.

I would like to convey my heartfelt thanks to **Dr. N. Siva Prasad**, **D. Santosh** (ECE), **Dr. P. Kishore**, **Dr. Vengal Rao**, **Dr. Rajesh**, **Venkat Reddy**, **Ummamahesh** and **Vayunandhana Kishore** (Physics), for their fathomless support in technical discussion.

With all happiness I acknowledge the **Jana Vignana Vedika** members for their friendly encouragement in helping me lend my humble voluntary service to rural science popularization.

I am grateful to the lab assistants **Praveen**, **Srinivas**, **Kishore, Komaraiah** and **other supporting staff** of the Department of Chemistry, **A. Sumanth** and **G. Vimochana** (CAI), NIT Warangal for their cooperation.

My heart goes to my beloved, mother **Mrs. Venkataramana**, Father **Mr. Muthilingam**, wife **Mrs. Saraswathi**, brother **Mr. Nageshwer Rao**, Sister in law **Mrs. Nalini** and nephew **Trilochan** and **Sai thaman** who with all their patience, prayers and faith in the almighty, waited all these long years to see me reaching this stage. Their blessings and care always gave me new fervour and gusto to do something more with dedication.

I always remember and cherish the encouragement and inspiration provided by all my friends and well wishers during the course of my research work.

Date: **GUDIPATI SRINIVASARAO**

CONTENTS

CHAPTER-I
INTRODUCTION

1.1: Schiff Base (>C=N-) Chemistry 3
1.2: Betti Base Chemistry 13
1.3: Objectives of the Present Work 15
References 20

CHAPTER-II
MATERIALS AND METHODS

PART A: MATERIALS 28
2A.1: Biphenyl Bridged Pyridine-2-carboxaldimine Schiff Bases 28
2A.2: The Metalochromes, [M2L2]Cl4 29
2A.3: 2-(((4-Nitrophenyl)imino)methyl)phenol 30
2A.4: Urea Betti Base (UBBH2) and Its Cyclized Oxazinone Derivative (OXAZH) 30
2A.5: The Buffers 31
PART B: METHODS AND MEASUREMENTS 34
2B.1: Sampling Methods and Instrumental Operations 34
2B.1.1: Melting point determination 34
2B.1.2: Elemental analysis 34
2B.1.3: Mass spectra 34
2B.1.4: Infrared spectral studies 34
2B.1.5: NMR spectral studies 35
2B.1.6: ESR spectral studies 35
2B.1.7: Magnetic susceptibility studies 35
2B.1.8: Thermal studies 35
2B.1.9: UV-visible absorption spectral methods 35
2B.1.10: Fluorescence emission spectral methods 36
2B.1.11: Electrochemical methods 36
2B.1.12: X-Ray crystallographic studies 39
2B.1.13: Molecular modeling 40
2B.1.14: Antimicrobial studies 40
2B.2: Functional Principles of Some Important Techniques 40
2B.2.1: Fluorescence spectrophotometric characterization of materials 40
2B.2.2: Cyclic voltammetry as tool for material diagnostics 41
2B.2.3: Thermometry and phase transition of materials 44
2B.2.4: X-ray crystallographic manifestations of material phase transitions 45
2B.2.5: Graphical software for conformational plots 46
2B.2.6: Molecular modeling 46
References 49

CHAPTER-III
BIPHENYL BRIDGED PYRIDINE-2-CARBOXALDIMINE SCHIFF BASES

PART A: SPECTRAL, ELECTROCHEMICAL AND CO-ORDINATION CHEMISTRY STUDIES OF BIPHENYL BRIDGED PYRIDINE-2-CARBOXALDIMINE SCHIFF BASES.....54
3A.1: General Characterization of the Biphenyl Bridged R-Pyral Schiff Base Ligands.....54
3A.2: Infrared Spectral Studies.....54
3A.3: 1H NMR and 13C NMR Spectral Studies.....55
3A.4: Mass Spectral Studies.....60
3A.5: Eletcronic Spectral Studies.....62
3A.6: Thermal Studies.....64
3A.7: Electrochemical Studies.....65
3A.8: Coordination Chemistry Studies.....66
PART B: KINETICS OF HYDROLYSIS OF o-TOLI-PYRAL.....77
3B.1: UV - Visible Absorption Spectral Studies.....77
3B.2: Cyclic Voltammetric Studies.....82
PART C: MOLECULAR MODELING STUDIES OF R-PYRAL AND THEIR METAL COMPLEXES, $[M_2(R\text{-}PYRAL)_2]Cl_4$.....84
References.....100

CHAPTER-IV
2-(((4-NITROPHENYL)IMINO)METHYL)PHENOL

PART A: SPECTRAL AND ELECTROCHEMICAL STUDIES OF PNASH.....103
4A.1: General Characterization of the Non-Linear Schiff Base PNASH.....103
4A.2: Infrared Spectral Studies.....103
4A.3: Electronic Absorption Spectra of PNASH.....106
4A.4: Electronic Fluorescence Emission Spectra of PNASH.....106
4A.5: Electrochemical Studies.....110
4A.6: Linear Sweep Voltammetric Assaying of PNASH.....119
PART B: PHOTOCHROMIC, MECHANOCHROMIC, THERMOCHROMIC AND POLYMORPHIC STUDIES OF PNASH.....123
4B.1: Photochromism/Photo switching of PNASH.....123
4B.2: Mechanochromism and Thermochromism of PNASH.....125
4B.3: Differential Scanning Calorimetric (DSC) Studies.....128
PART C: SINGLE CRYSTAL X-RAY DIFFRACTION STUDIES OF PNASH.....133
4C.1: Powder X-Ray Diffraction Studies.....133
4C.2: Single Crystal X-Ray Diffraction Analysis of PNASH.....136
PART D: MOLECULAR MODELING STUDIES.....140
References.....147

CHAPTER-V
A NOVEL UREA BETTI BASE AND ITS CYCLIZED OXAZINONE DERIVATIVE

PART A: SPECTRAL, THERMAL AND ELECTROCHEMICAL STUDIES OF UBBH2 AND OXAZH 150
5A.1: General Characterization of the UBBH2 and OXAZH 150
5A.2: Optical Rotation Studies 150
5A.3: Infrared Spectral Studies.....151
5A.4: 1H NMR and 13C NMR Spectral Studies 151
5A.5: Mass Spectral Analysis 155
5A.6: Electronic Spectral Studies 156
5A.7: Halochromic Effect of UBBH2 163
5A.8: Differential Scanning Calorimetry (DSC) 163
5A.9: Electrochemical Studies.....166
PART B: SINGLE CRYSTAL X-RAY DIFFRACTION STUDIES OF UBBH2, UBBH2.2DMF AND OXAZH 183
5B.1: Crystal Structure Analysis.....184
PART C: MOLECULAR MODELING STUDIES OF UBBH2, UBBH2.2DMF AND OXAZH 205
References.....220

CHAPTER-VI
BIOLOGICAL ACTIVITY

6.1: Minimum Inhibitory Concentration (MIC).....222
6.2: Antibacterial and Antifungal Activities of o-TOLI-Pyral and Its Metal Complexes ..222
6.3: Antibacterial and Antifungal Activities of UBBH2, R-UBBH2.2DMF, S-UBBH2.2DMF, OXAZH, R-OXAZH and S-OXAZH.....226
References.....230
Summary and Conclusions 231
List of Publications, Conferences and Bio-Data

SYMBOLS AND ABBREVIATIONS

IUPAC	:	International Union for Pure and Applied Chemistry
cm	:	Centimeter
nm	:	Nanometer
i	:	Current
E	:	Potential
ν	:	Scan Rate
µA	:	Microampere
mV	:	Millivolt
µM	:	Micromolar
N	:	Normality
F	:	Faraday Constant
Ω	:	Ohm
DMF	:	Dimethylformamide
MeCN	:	Acetonitrile
EtOAc	:	Ethyl Acetate
MeOH	:	Methanol
SCE	:	Saturated Calomel Electrode
CV	:	Cyclic Voltammetry
SMDE	:	Static Mercury Drop Electrode
GCE	:	Glassy Carbon Electrode
PXRD	:	Powder X-Ray Diffraction
DSC	:	Differential Scanning Calorimetry

CHAPTER - I

INTRODUCTION

The history of Science and Technology has been traversing several epochal stages. The present epoch is said to be Materials Age. Exploration into visualization, generation, characterization and eventually utilization of materials for various kinds of societal need, is mainly the order of the day.

In the 21st century, there is a huge demand for optoelectronic devices aimed to function as organic materials, including LEDs, dye-sensitized solar cells, thin film transistors etc.,. In contrast to general materials, organic materials have many advantages such as increased processability, cost effectiveness and multi-facetedness etc.,. As a result, the development of new organic materials with unusual optoelectronic properties has gained a great deal of interest in recent years. Experimental controls on crystallization result in unusual packing arrangements as desired in rational drug design paradigms[1]. One of the ways of obtaining materials with nonlinear optical (NLO) properties is by crystal engineering of compounds with chiral centre into crystals of non-centrosymmetric (chiral) space groups[2].

Chemistry plays vital role not only in solving the energy crisis, in finding new drugs for life threatening diseases, in understanding the life sciences through proteomics, genomics in overcoming environmental challenges but also in devising and generating smart materials for optoelectronic applications. Optoelectronic chemical sensors, electrochemical sensors, chemodosimeter, chemFETs (chemical field emitting transistors) are some of best examples[3–5]. For instance, metaloporphyrin systems are well-known light harvesting supramolecular systems which help the plants to prepare the food from CO_2, H_2O. From the inspiration of photosynthesis, many artificial photosensitizers are being developed by researchers around the globe to mimic the natural photosynthesis mechanism to bring CO_2 levels into optimum levels[6]. Supramolecular Chemistry which is one of advanced subjects in chemical research intertwined with nano-materials and technology, is fast evolving that would help face these challenges.

Supramolecular host-guest noncovalent interactions render the azomethine (>C=N-) and dihydroazomethine (-HC-NH-) systems some useful credentials such as nonlinear optics (second harmonic generation, SHG activity), ferroelectric and piezoelectric activity. More than any other single class of compounds Schiff bases, as a class of compounds, is being used as the best supramolecular ligand systems. Structurally well-designed Schiff bases and

Betti bases serve as excellent hosts for multiple metal ions in biological fluids and aquatic systems. The resulting multi-metallic supramolecular host-guest complexes frequently exhibit intriguing magnetic, optical, optoelectronic and catalytic properties[7,8]. Many of the specific biological and chemical properties of the Schiff bases, Betti bases stem from the vantage position of the nitrogen, oxygen atoms occupies in the molecular skeleton vis-a-vis the other functional atomic sites[9–11].

J. M. Lehn described the "Supramolecular Chemistry" as "*chemistry beyond the molecule*", the association of molecular or ionic entities held together reversibly by intermolecular forces to yield organised arrays of higher complexity[12,13]. Supramolecular chemistry is one of interdisciplinary sciences, encompassing the traditionally distinct disciplines of organic, inorganic and physical chemistry. The reversibility of supramolecular self-assembly is key to form the thermodynamically most favorable structure. Molecular recognition is one of the features of supramolecular chemistry. It is made possible by usually, guest-host complementarity[14,15]. Supramolecular, non-covalent interactions are understood to involve ion-ion interactions (100-350 kJ mol^{-1}), ion-dipole interactions (50-200 kJ mol^{-1}), dipole-dipole interactions (5-50 kJ mol^{-1}), hydrogen bonding (4-120 kJ mol^{-1}), π-π stacking (0-50 kJ mol^{-1}) and Van der Waals forces (<5 kJ mol^{-1}). The importance of longitudinal distortion in supramolecular systems which can lead to other types of conformational distortions such as rotations. These conformational distortions offer them variety of material properties[16].

Even though, supramolecular chemistry is still in developing stage. Generally supramolecular chemistry focuses mainly in three directions: (a) molecular recognition (b) building specific shapes/architectures and (c) Layer by layer molecular assembly organized from numerous molecules that may even eventually pile up to nanomaterial scale.

In Supramolecular host-guest chemistry, a macrocyclic host involves in Recognition, Transport and Delivery of compatible molecules, ions, solvent molecule or species. The transport of the guest is driven by physico-chemical gradients and chemodynomics before the same is released at the desired or chemically specified target destination. The concept of molecular recognition has been evolved by the observation of enzymatic reactions. Based on these principles, effective supramolecular receptors can be designed.

Deoxyribonucleic acid (DNA), protein α-helices and collagen[17] are well known supramolecuelar helical systems. Helices may retain particular shape through conformational restrictions, hydrogen bonding, or metal ion coordination[18]. Metallofoldamers are the family of oligomers and fold into three-dimensional architectures structures in a well controlled manner upon coordination with metal ions. The shape of the helicates are controlled on the basis of their ability to fold and unfold upon changes in the oxidation state of the coordinated metal ion[19].

1.1: Schiff Base (>C=N-) Chemistry

Condensation of carbonyl compounds with primary amines to form imines was discovered in 1864 by Hugo Schiff and the product is now called a Schiff base compound. Schiff bases (**1**) holding different electron-donating or electron-withdrawing groups (R_1, R_2, R_3 in **1**) on the molecular skeleton exhibit vividity in their chemical, electronic, electrochemical and structural manifestations. They have been continuously attracting research interest due to their involvement in a variety of technologically and biologically significant roles[20,21]. Of late, it is progressively established that some of the Schiff base compounds show amazing supramolecular properties such as solid-state thermochromism, mechanochromism and photochromism[22,23]. Some of the Schiff bases possessing moieties that would offer conformational isomerism to the molecules are found to exhibit polymorphism upon change of solvent and phase[24]. Therefore, the study of crystal packing and the intermolecular interactions in the solid state, of various azomethine can lead to some valuable data for the design and synthesis of new device materials[25–28]. Schiff base molecules having labile protons adjacent to the azomethine moiety such as phenol and naphthol exhibit electronic spectral changes associated with deprotonation. These materials exhibit supramolecular properties such as solvatochromism, halochromism and electrochromism[29–31].

The mechanism of vision is now known to associate with the hydrolysis of azomethine group of the biochemical Schiff bases near the retinal layers[32]. A great deal of chemical research is being carried out all over the world on kinetics of hydrolysis of different kinds of compounds including Schiff bases[33–35].

Phenomena Involving a Stimulated Color Change in Supramolecular systems:

Chromic materials are considerable interest of many researchers for developing efficient artificial receptors for molecular recognition and sensing as they play important functional roles in optochemical sensors[36–40]. There has been growing demand for artificial receptors for sensing, particularly for metal ion sensing over a decade[41–46]. However, design and fabrication of artificial receptors that possess high binding affinity, selectivity and sensitivity to a targeted single molecule, ion, etc., still pose a great challenge to the researchers. There are some compounds arousing interest in scientific community due to their relatively strong binding and directional attractive forces such as hydrogen bonding, ion-dipole, π-π stocking, electrostatic and some other non-covalent interactions. Functional groups such as amides, ureas, amidoureas, etc., are widely used to tag artificial receptors for recognizing neutral molecules and ions via non-covalent interactions[47–56]. Conformational distortions in the supramolecular system which is induced by external stimuli render them variety of properties such as polymorphism, different types of chromic properties,[57–64]etc.,. Some of them are given below with the details of external stimuli.

Thermochromism (Temperature)

Thermochromism denotes the phenomenon of a color change with dependence on temperature. These color change are reversible or irreversible. Thermochromism can be expected from single compounds as well as organic or inorganic composites[65–69]. Thermochrmism is usually occurred due to proton transfer in solid-state. Polymers, liquid crystals, metal complexes, etc., change in the, electronic structure, multilayer interactions affects crystal dimension upon heating render them different colors[70–79], 1,5-bis(hydroxyethylamino)-2,4-dinitrobenzene (BDB)[66] (**1.1**) an organic compound is shown thermochromic behavior due to its polymorphism. BDB exists as a polymorph because of its intra- and intermolecular hydrogen bonds between hydroxy, amino and nitro groups (**Scheme 1**). As a results, BDB changes its color as a function of change in the temperature. The nitro-form is in a benzenoid form (**1.1**) where as the acid form is in its quinoid form (**1.2**). The color change is assigned due to the bathochromic shift from 480 nm to 500 nm while heating (**Figure 1A.1**).

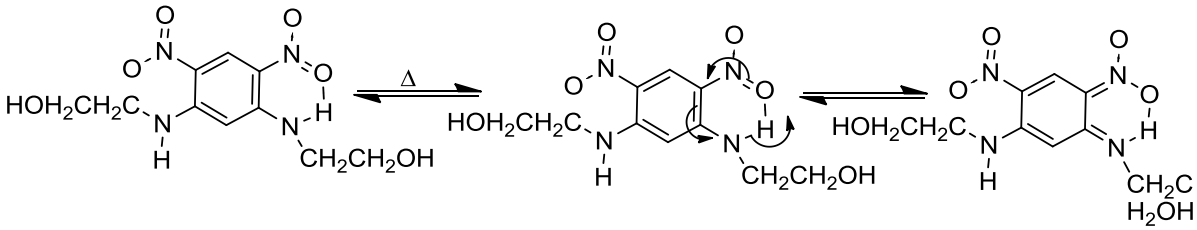

(Nitro-form) (Acid-form)

1.1 **1.2**

Scheme 1

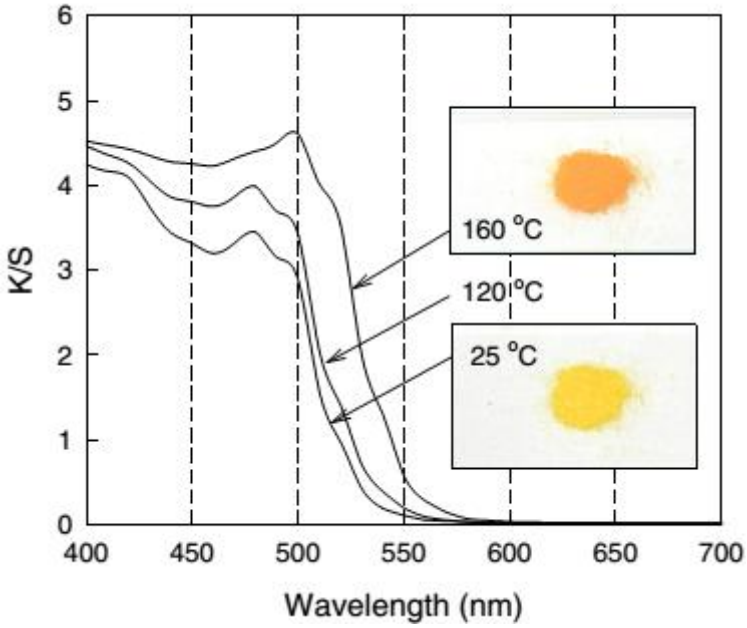

Figure 1A.1: Thermal induced tautomerism in BDB[66]

Solvatochromism (Solvent polarity)

Solvatochromism denotes the change of the color upon solvent change, changing the polarity of the solvent or solvent molecule(s) binding in the crystal structure[80–82]. In the reports, Schiff base iron complex of N,N-Bis(salicylidene)-1,3-propanediamine dimer (**1.3**) exhibits solvatochromism due to a slightly distorted in octahedral geometry. Degree of solvation significantly impacts the arrangements of these dimeric pairs with solvent polarity[83].

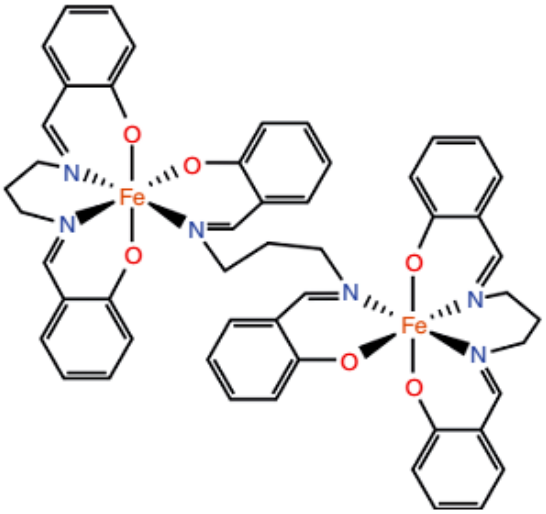

1.3

Mechanochromism (Pressure)

Piroxicam crystals under cryogenic grinding exists as colorless(**1.4**) under mechanical stress, these crystals become yellow amorphous piroxicam (**1.5**) (**Scheme 2**), in which proton transfer accompanies both solid-state disorder and a change in color induced by mechanical stress (**Figure 1A.2**)[84]. Positive solvatochromism is the 4,4'-bis(dimethylamino) fuchsone, which is orange in nonpolar toluene, red in slightly polar acetone and red- violet in more polar methanol. Negative solvatochromism[82] are 4-(4'-hydroxy styryl)- N-methyl pyridinium iodide which is red in 1-propanol , orange in methanol and yellow in water.

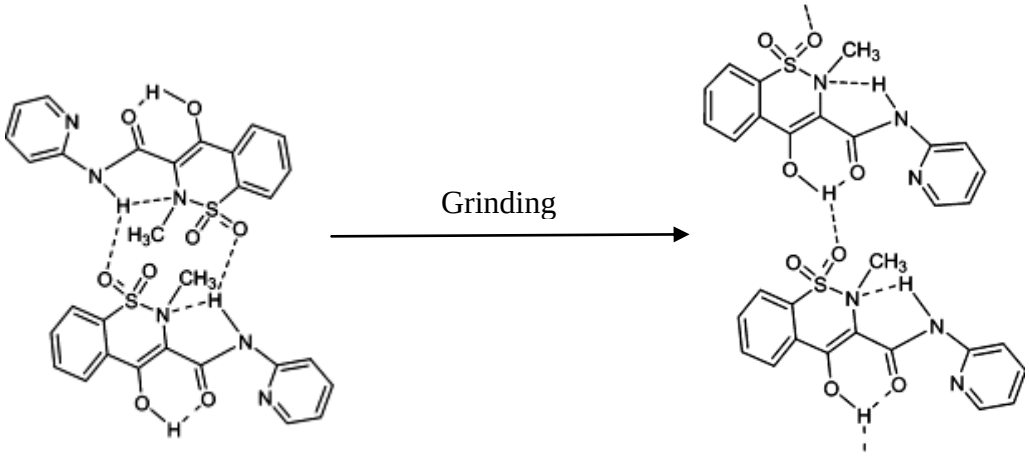

(Colorless – Form I) (Yellow color – Form II)

1.4 **1.5**

Scheme 2

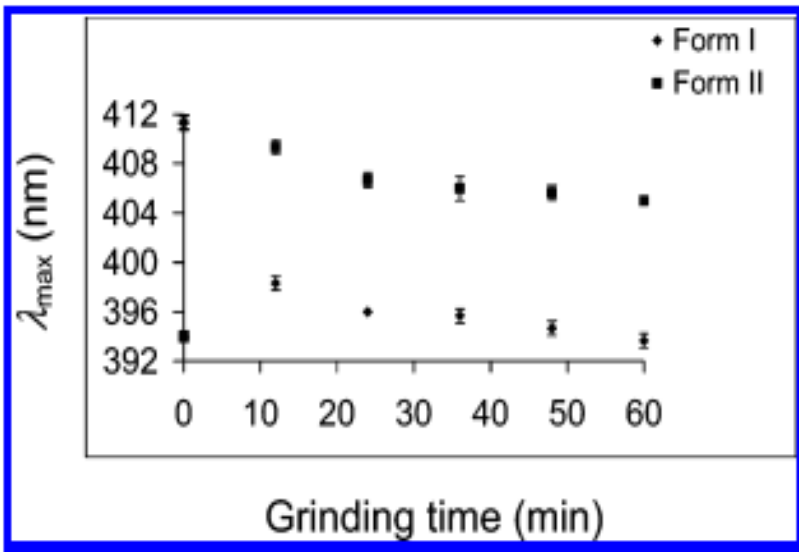

Figure 1A.2: Change in the wavelength maximum absorbance as a function of cryogenic grinding time for piroxicam forms

Photochromism (Photon)

Photo-induced proton transformation is dynamic in nature and is induced by external stimuli[85]. Dynamic proton tautomerism occurs in salicylaldimine (**Scheme 3**)[86], When proton transfer is induced by external stimuli, the tautomeric change is sometimes accompanied by a change in color. 4-Oxopyrimidines are an example of photo-tautomerism, which implies that intramolecular proton transfer is induced by ultraviolet light. Cytosine (**Scheme 4**) is one of such molecules, which exhibits photochromism. Cytosine irradiation with 313 nm laser light results the two imino–oxo forms which are inter convertible as anti (**2.0**) and syn (**2.1**) forms[85]. Water-soluble porphyrin and their conjugates are very rare and they are used in photodynamic therapy[87].

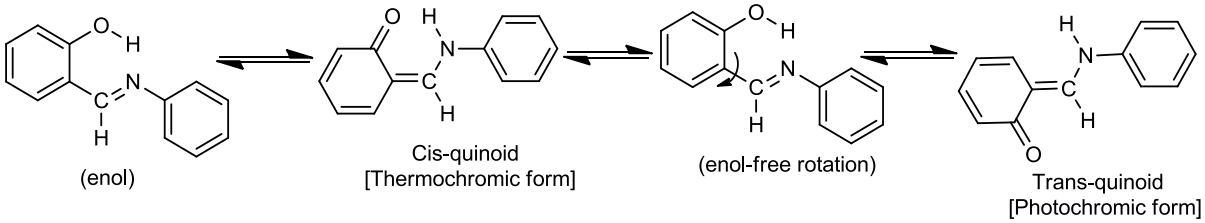

1.6 **1.7** **1.8** **1.9**

Scheme 3

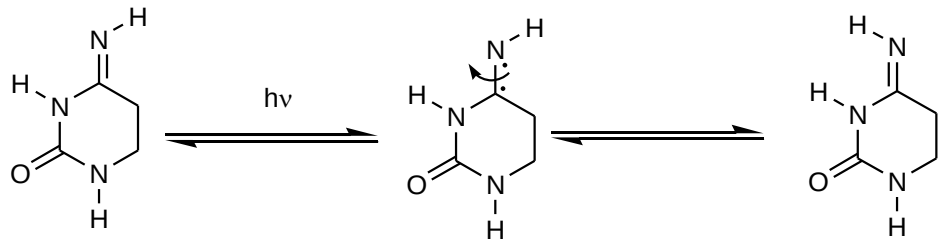

Anti Syn

2.0 **2.1** **2.2**

Scheme 4

S. Giordani et al were reported the photoinduced proton exchange between merocyanine to produce a spiropyran (**Scheme 5**). Photoinduced ring closing of a merocyanine to generate a spiropyran with the simultaneous release of a proton. The liberated proton is further captured by either one of two pyridine derivatives with the formation of their conjugate acids. Relying on this mechanism, an optical input is transduced into a detectable spectroscopic output after the controlled intermolecular exchange of protons. The timescales of the molecular switching steps, however, are limited by the slow reaction kinetics. The photoinduced transformation occurs within minutes, but the thermal reaction reverts the switch state only after several hours[88].

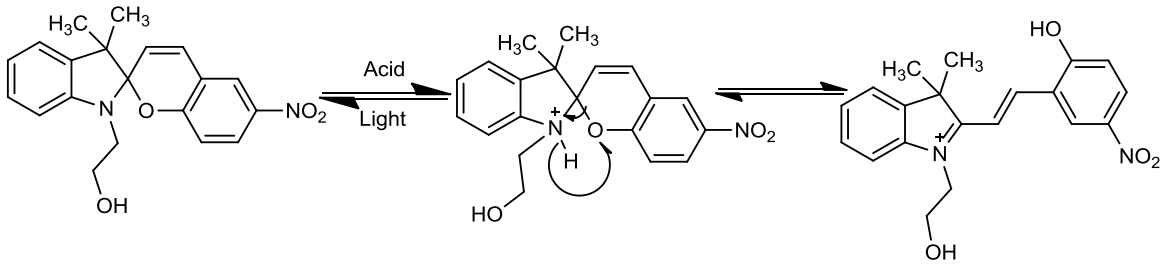

2.3 **2.4** **2.5**

Scheme 5

Electrochromism (Potential)

Thin films which shows change in color upon electric potential is used as external stumli. These thin films are called as electrochromic materials and the phenomena is known as electrochromism. Some of thin films of Schiff base molecules are shown color change when potentials are applied to the films. N^1-(furan-2-ylmethylene)-N^4, N^4-diphenylbenzene-1,4-diamine (**2.6**) is a family of Schiff base and is exhibited reversible electrochromism and acidochromism[89].

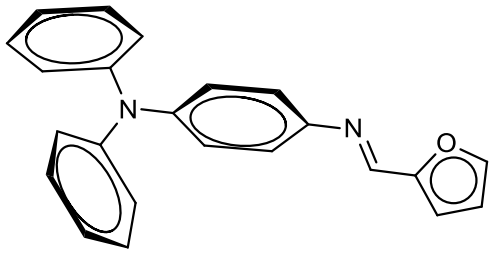

2.6

Conformational polymorphism in Schiff bases

V. Krishna et al[90] have reported a biphenyl naphthaldimine helicate Schiff base ligand 2, 2'-(4, 4'-oxybis(4,1-phenylene)bis(azan-1-yl-1-ylidene))bis(methan-1-yl-1-ylidene) dinaphthalen -1-ol (NDADPE). The Schiff base was synthesised with condensation of 1-hydroxynaphthalene-2-carbaldehyde and 4-(4-aminophenoxy)benzenamine.

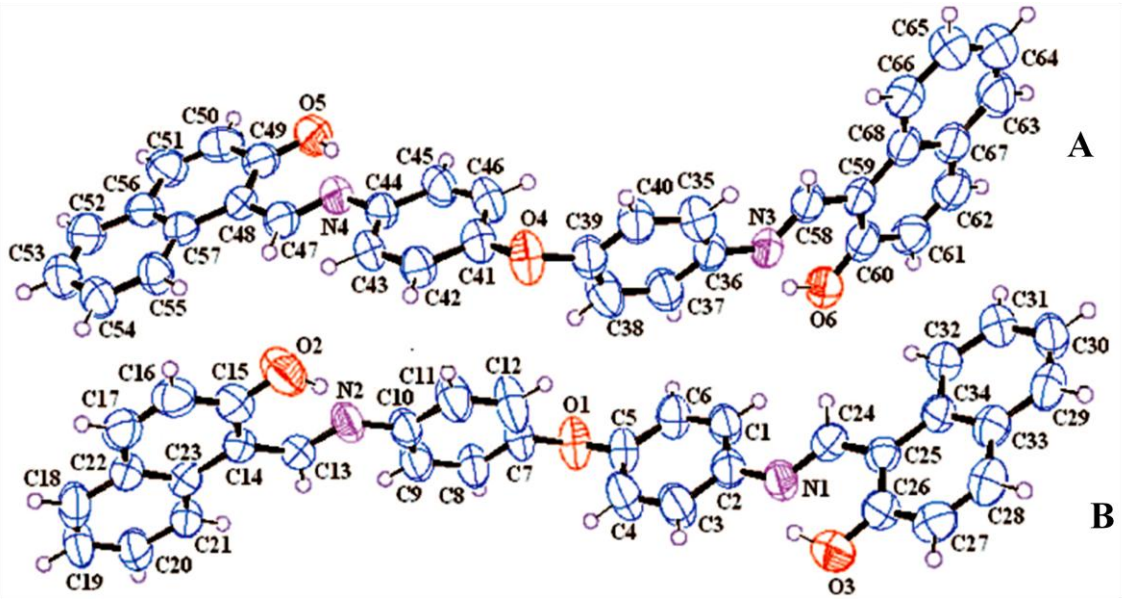

2.7

From the single crystal X-ray diffraction studies, it was confirmed that there were two conformers A and B (**2.7**). Conformer A forms a supramolecular dimer with bifurcated C-H⋯O hydrogen bond synthon, whereas conformer B forms a supramolecular helix due to bifurcated C- H⋯O hydrogen bond synthons. Conformer A and conformer B both are conformational isomers

M. Barboiu et al[91] have reported the controlled self-selection and quantitative parallel amplification of the homonuclear grid architectures derived from the same Schiff base ligand of different conformational geometries in the metal complexes.

Non-linearity in Schiff bases

Four thermotropic liquid crystals, namely N-(3-methoxy-4-hydroxybenzylidine) 4-isopropylaniline (**2.8**), N-(3-methoxy-4-hydroxybenzylidine)-3-isopropoxyaniline (**2.9**), N-(4-trifluoromethylbenzylidine) 4-isopropylaniline (**3.0**), N-(4-trifluoromethylbenzylidine)3-isopropoxyaniline (**3.1**), N(4-Hydroxy)benzylidine 4-isopropylaniline (**3.2**), N(4-Hydroxy)benzylidine 3-isopropoxyaniline (**3.3**) thermotropic liquid crystals nonlinear optical measurements were recorded by D. Mallikharjuna Rao et al[92]. Nonlinear optical properties of these liquid crystals were studied using a Z-scan technique with 7 ns pulse duration at 532 nm. These Schiff base were shown 3-order nonlinear properties[93].

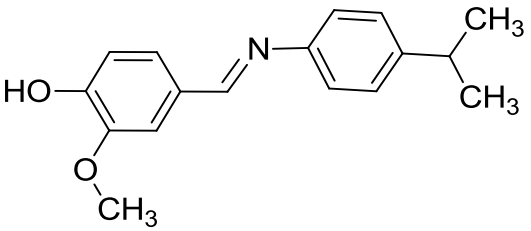

2.8

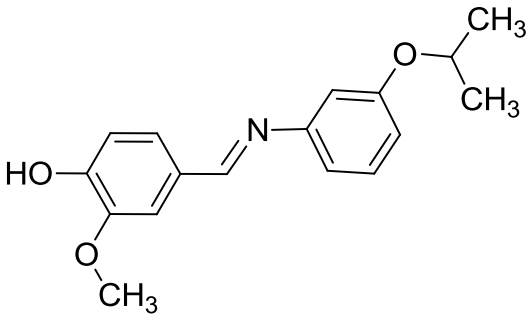

2.9

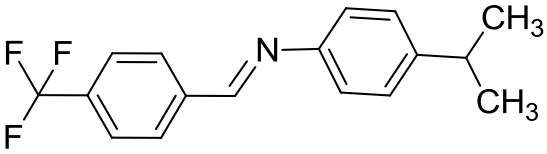

3.0

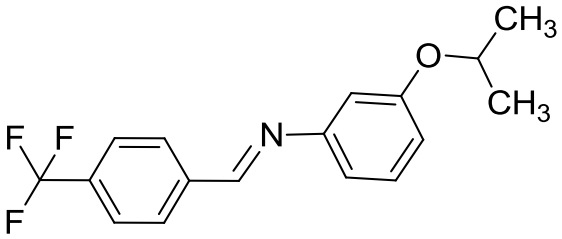

3.1

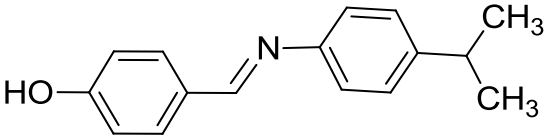

3.2

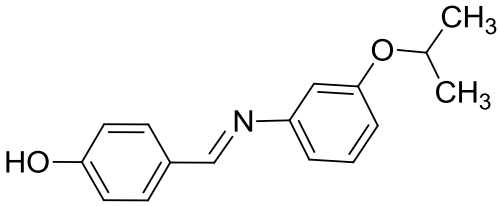

3.3

Ilias Ali et al[94] were synthesized the thermotropic main chain poly(azomethine–urethane)s (**3.9**) by the polyaddition of azadiol (**3.6**), 1,8-octandiol (**3.7**)with methylene bis(phenyl isocyanate) (**3.8**) (**Scheme 6**) and tolylene 2,4-diiso-cyanate (**Scheme 7**). The non linear optical (NLO) activity of the polymers was also investigated.

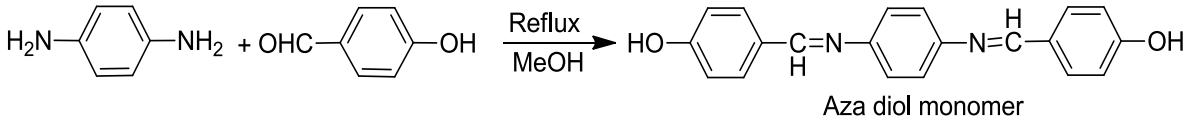

3.4 **3.5** **3.6**

Scheme 6

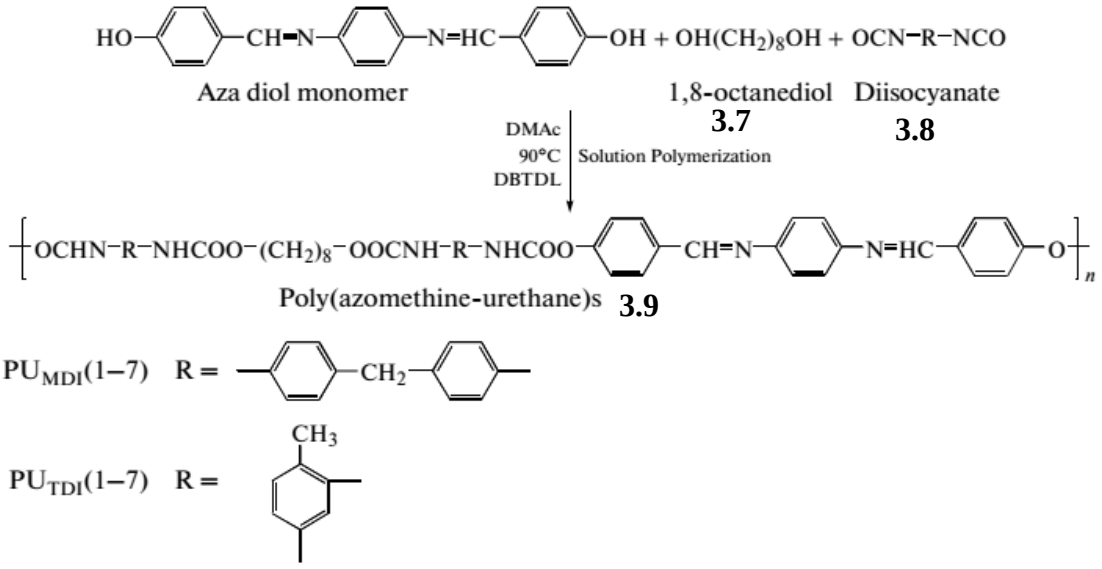

Scheme 7

Michel Sliwa et al[95] were studied the nonlinear optical properties of two new anil molecules N-(4-hydroxy)-salicylideneamino-4-(methylbenzoate) (**4.0**) and N-(3,5-di-tert-butylsalicylidene)-4-aminopyridine (**4.1**) molecules. These anils were shown photochromism in the crystalline state, upon irradiation in the UV, the yellow crystals change color to red, owing to enol-keto intramolecular tautomerism. Nonlinear optical (NLO) properties of these anils were found to be 3-folds more compared to that of urea. The photomodulation efficiency of these compounds were found to be 30%

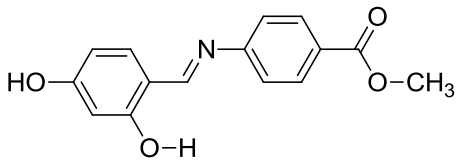

4.0

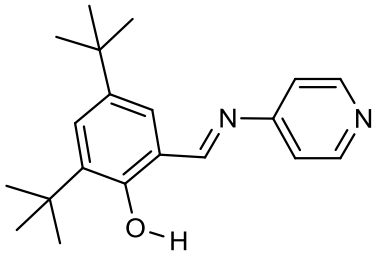

4.1

Schiff base metal complexes

In general, all azomethine systems containing nitrogen, oxygen and sulphur in their molecular skeleton have been found to be a set of potential monodentate, bidentate, tridentate and tetradentate ligands to a variety of metal ions. Hence, these azomethine derivatives are the favourite systems for studies by many investigations of supramoelcular host-guest chemistry. Organic compounds possessing nitrogen atoms at vantage positions render them as a good ligands and offer them biological activity and other functionality of the nitrogen compounds are modified upon complexation with metal ions[96–99]. Nitrogen offers varied chemistry by virtue of its multiple oxidation states, Lewis base character and multiple valences. By and large, these nitrogenous compounds possess electrochemical redox behavior due to nitrogen multiple oxidation states. The feasibility of all routine optical transitions, namely, $\sigma \rightarrow \sigma^*$, $n \rightarrow \sigma^*$, $\pi \rightarrow \pi^*$ and $n \rightarrow \pi^*$ the coplaniarity of the lone-electron-pair-containing-orbital of nitrogen to the -C=N- bond and nuclear spin I=1 of nitrogen give a great scope of electroning, ESR and magnetic studies of the complexes is now voluminous. However, their entry into the supramolecular arena is of recent phenomenon.

Biological importance of Schiff bases

A. C.G. Hotze et al were extensively studied the potential anticancer properties of iron-DADPM metal complex[100]. The complex was shown excellent activity as cis-platin.

U. McDonnell et al were investigated the binuclear ruthenium (II) complexes of diamino biphenylmethane (DADPM)[101]. From the studies, it was found that the metal complex dramatically less active against cancer cell lines.

1.2: Betti Base Chemistry

Azomethine is an intermediate product in the synthesis of Betti base which has been first reported by Marries Betti in the year 1900. Betti bases (**2**) having different electron-donating or electron-withdrawing groups (R_1, R_2, R_3 in **2**) on the molecular skeleton exhibit vividity in their physico-chemical properties. These compounds have been continuously attracting researchers due to their utilities in catalytic applications besides their biologically applications. Some of these Betti bases and co-crystals of Betti bases containing non-centrosymetric space group have shown ferroelectric and piezoelectric properties[88,89]. Non-linear properties of the materials are shown myriad utilities in light modulation, frequency conversion, switching, optical signal storage devices and optical second harmonic generation[90-92]. Co-Crystals of non-linear materials having urea moiety and aminoacids like γ-glycine, L-threonine, L-malic acid, D-tartaric acid and DL-tartaric acid were shown structural, spectral, thermal, dielectric, mechanical properties. Some of Betti base co-crystals exhibit more second harmonic generation efficiency than standard KDP[93]. Self-assembled monolayers of Betti bases could be employed for the optoelectronic applications. Formation of self-assemblies over metal oxide surfaces depends on acid-base equilibrium of molecule and pK_a value (s) of the molecule. The binding nature of sensitizers onto the metal oxides surface requires complete knowledge on the pK_as of the sensitizer. The sensitizer performance effects with protonation and deprotonation[94]. Betti base metal complexes (tetra-dentate ligands) are used as N—arylation agents over imidazoles in the presence of Cu halide salt[95]. Betti bases possess wide range of biological activities like antibacterial, antimicrobial, anti-inflammatory and anthelmintic activities[96]. Urea Betti bases having β-naphthol, usually undergo cyclization and form oxazinone derivatives[97]. From the last few years oxazinone derivatives have been demonstrated to be valuable synthetic intermediates. and also possess important biological activities such as antitubercular, antitumor, antimalarial, antimicrobial and for the treatment of idiopathic pulmonary fibrosis[98].

Zhang Yuan et al[102] were synthesised, 1-((2-hydroxyphenyl)(pyrrolidin-1-yl)methyl)naphthalen-2-ol (**4.2**) and were determined the crystal structure of the compound.

The compound was crystallized in noncentrosymetric space group and the piezoelectric property of the compound was studied by Z-scan method.

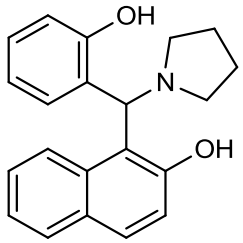

4.2

Biological importance of Betti base and oxazinone

N. Gye´ma´nt et al were reported the in vitro and in vivo multidrug resistance reversal activity by a Betti-base derivative of tylosin[103]. From the results, it is expected that Betti-base derivative of tylosin improves the efficacy of chemotherapy in MDR cancers.

A. Abdul Jameel et al were reported the antimicrobial activities of derivatives of urea Betti base and thiourea Betti base. The synthesized compounds were shown appreciable antibacterial activity against selected organism of gram positive S. aureus, B. substilis, gram negative E. coli, P. aeruginosa when compared with the standard drug ciprofloxacine[104].

So far we have seen that some of the above discussed hosts are chemically azomethine (C=N) and dihydroazomethine (>HC-NH-) systems. At the sites of metal binding, formation of hydrogen bond with adjacent atom(s) and carriage, the azomethine and dihydroazomethine groups play vital role. These kind of binding patterns offer them varieties of chromic properties such as mechanochromism, thermochromism, photochromism, halochromism, metalchromism, solvatochromism, etc.,

Keeping in view the importance, relevance, variance and convenience of azomethines and dihydroazomethines offer, I have considered it suitable to synthesise new classes of azomethine and dihydroazomethine nitrogenous compounds in order to exhibit them as potential supramolecular entities

In the following schemes are described how some of the already reported biphenyl azomethine (C=N) systems and their complexes can be turned into supramolecular entities besides some of novel dihydroazomethine (>HC-NH-) hosts and their solvates.

With the scope, available as suggested above, I have set the following objectives for my investigations

1.3: Objectives of the Present Work

i) To synthesize and characterize a variety of multi-functional azomethine and dihydroazomethine compounds aimed to exhibit mechanochromic, thermochromic, photochromic, halochromic and metal binding properties.

ii) To investigate the spectral, electrochemical, single crystal X- Ray diffractometric and thermal properties of the above compounds.

iii) To study kinetics of hydrolysis of azomethine moiety for the above multi-functional organic ligands and their complexes.

iv) To perform molecular modelling on the synthesized compounds to correlate the modelled properties in juxtaposition to experimental results.

v) To test the pharmacological activity of some selected once among the above ligands and complexes.

The biphenyl bridged pyridine-2-carboxaldimines, nonlinear salicylaldimine, Betti base and its cyclized oxazinone derivative and some of their complexes prepared and investigated in my researches are shown hereunder.

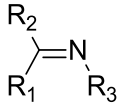 **(1)**	R_1= H, and R_2 = R_3 = ArOH, $ArNO_2$, pyridine, diamino biphenyls, etc.,	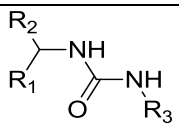 **(2)**	$R_1 \neq R_2$ and R_3 = H, C_2H_5, etc; R_1= R_2 = R_3 =CH_3, ArOH, $ArNO_2$, etc.,

	Z	X	Row combination labeled as
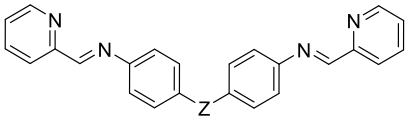 **(3)**	—O—	—	DADPE-Pyral
	—CH_2—	—	DADPM-Pyral
	—	—CH_3	o-TOLI-Pyral
	—	—OCH_3	o-DIANISI-Pyral
	—	—H	BENZ-Pyral

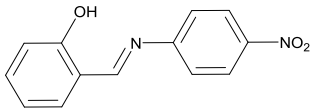 **PNASH (4)**	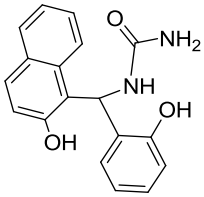 **UBBH2 (5)**	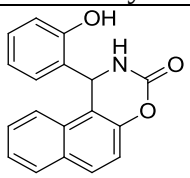 **OXAZH (6)**

	Z	X	Row Combination
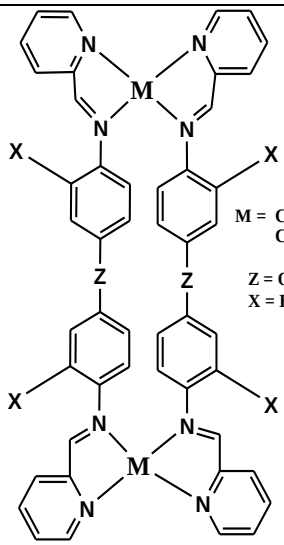 **(7)** M = Co(II), Ni(II), Cu(II) and Zn(II); Z = O, CH_2, Nil; X = H, CH_3, OCH_3	O	H	**$[M_2(DADPE\text{-}Pyral)_2]Cl_4$**
	CH_2	H	**$[M_2(DADPM\text{-}Pyral)_2]Cl_4$**
	-	OCH_3	**$[M_2(o\text{-}DIANISI\text{-}Pyral)_2]Cl_4$**
	-	CH_3	**$[M_2(o\text{-}TOLI\text{-}Pyral)_2]Cl_4$**
	-	H	**$[M_2(BENZ\text{-}Pyral)_2]Cl_4$**

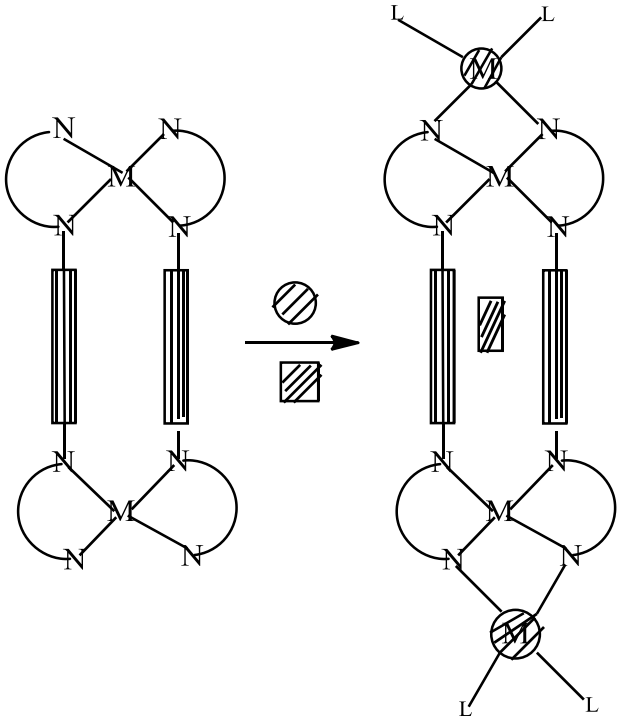
L
L
M
N
N
M
N
N
N
N
M
N
N
N
N
M
N
N
M
L
L

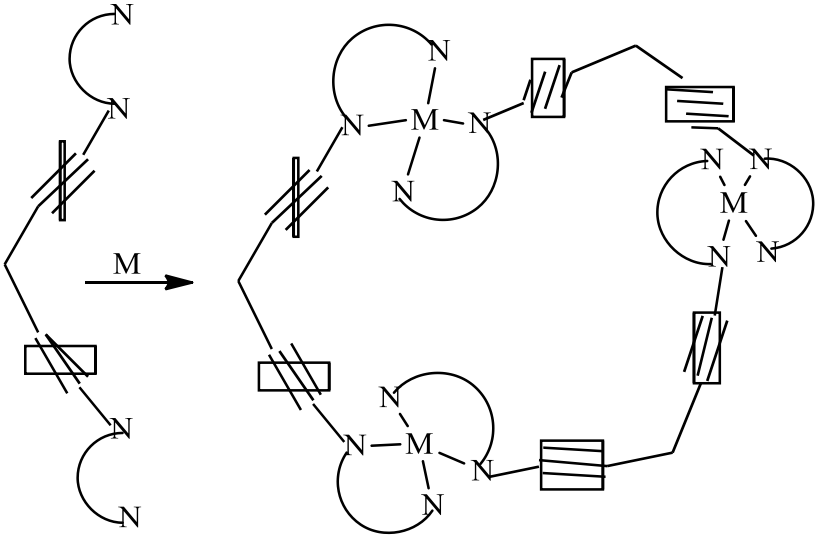
N
N
M
N
N
M
N
N
N
N
M
N
N
N
N
M
N
N
N
N

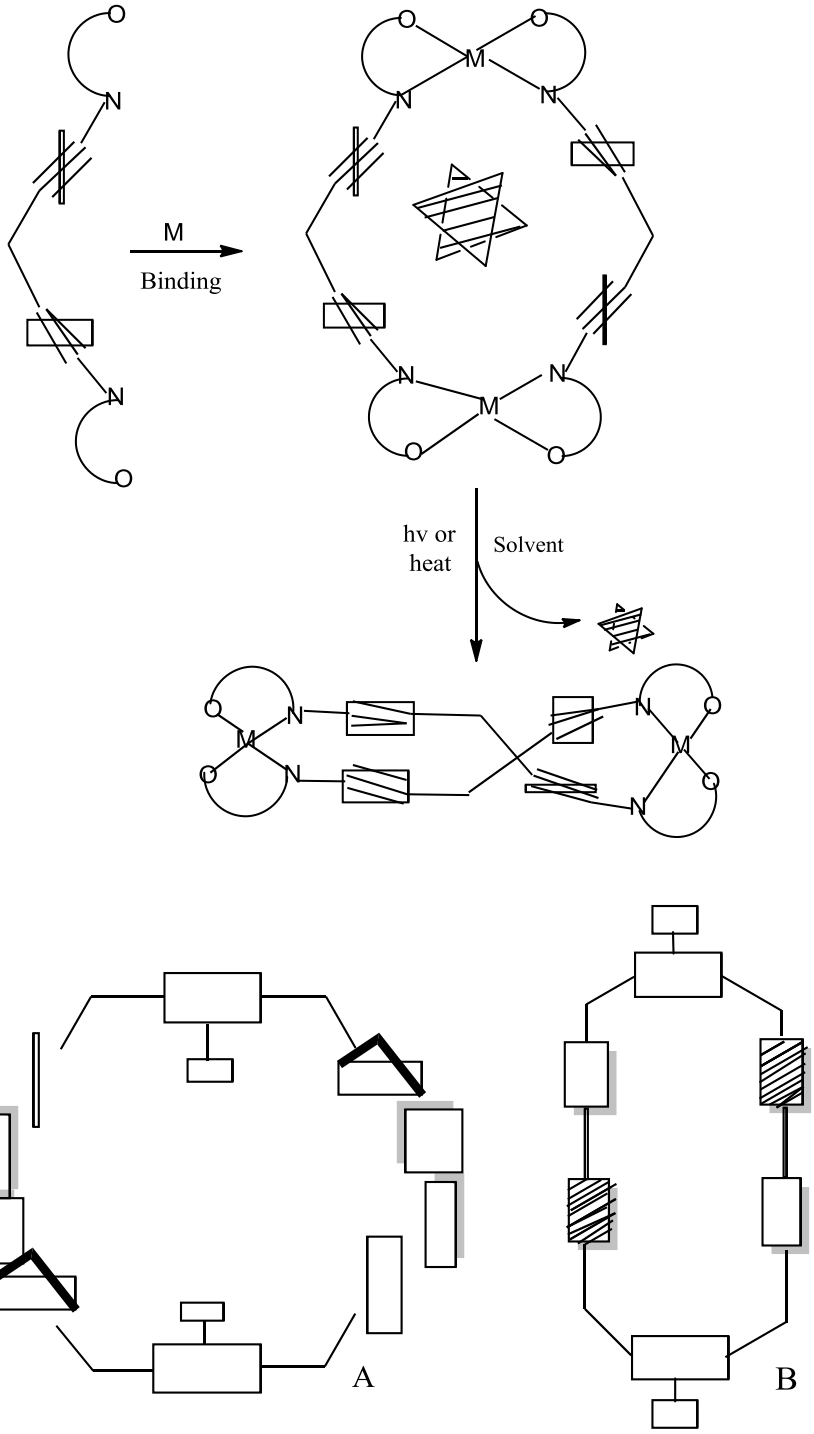

The studies made on these systems are embodied in this thesis entitled, **"Spectral, Electrochemical, Single Crystal XRD and Molecular Modeling Studies of Azomethine and Dihydroazomethine Compounds of Supramolecular Significance".** It presents the physico-chemical, analytical, electronic spectral, fluorescence, electrochemical, molecular

modeling, single crystal X-ray diffraction, ESR spectral, *etc*., of the ligands besides similar and thermal and bioassying studies of the Betti base, its cyclized oxazinone derivative and some of metal complexes of biphenyl bridged pyridine-2-carboxaldimines.

The thesis is divided into 6 chapters including this 'Introduction' Chapter.

In **Chapter II**, the details of synthesis of new compounds, preparation reported compounds, regents, buffers, etc., are provided.

The experimental conditions set for investigations, advanced instrumental techniques used, brief introductions to supramolecular mechanics, X-Ray diffractometry of helical molecular stacking, low temperature ESR and susceptibility, fast scan voltammetry, ICPOES, a newly designed PTFE based HMDE electrode, molecular modeling, conformational analysis by Surfer and Grapher, antibacterial assaying, etc., are provided for the benefit of general readership of this thesis. The names and brands of major instruments used during our investigations are given.

In **Chapter III**, the spectral and electrochemical characterization, kinetic of hydrolysis of one of biphenyl bridged pyridine-2-carboxaldimines besides metal complexes (Co^{2+}, Ni^{2+}, Cu^{2+} and Zn^{2+}) characterization and molecular modeling studies of biphenyl bridged pyridine-2-carboxaldimine Schiff bases are presented and discussed.

Chapter IV, contains a non-linear salicylaldimine Schiff base spectral, crystal structure determination electrochemical and molecular modeling studies besides its mechanochromic, thermochromic, photochromic and polymorphic behavior are presented and discussed.

In **Chapter V**, the synthesis, spectral, optical activity, electrochemical, single XRD, thermal and molecular modeling studies of Betti base and its cyclized oxazinone derivative are presented and discussed.

In the last chapter, i.e., **Chapter VI,** the biological activity of binucleating and tetranucleating ligands and their metal complexes besides Betti base and its cyclized derivative are briefly described.

Wherever and whenever reports of other scientists and investigations were taken for support of synthesis, interpretation and lead, due acknowledgements have been made by citing their works in the list of literature at the end of each chapter.

References

1. J. J. Novoa, D. Braga and L. Addadi, *Engineering of Crystalline Materials Properties*, Springer Netherlands, Dordrecht, 2008.
2. K. M. Priyadarshini, A. Chandramohan, G. A. Babu and P. Ramasamy, *Solid State Sci.*, 2014, **28**, 95–102.
3. S. O. Krabbenborg, C. Nicosia, P. Chen and J. Huskens, *Nat. Commun.*, 2013, **4**, 1667.
4. A. K. Gupta, A. Dhir and C. P. Pradeep, *Dalton Trans.*, 2013, **42**, 12819–23.
5. H. Qazi, a Mohammad and M. Akram, *Sensors*, 2012, **12**, 16522–16556.
6. P. G. Hoertz, T. E. Mallouk, U. V Park and V. Pennsyl, 2005, **44**, 6828–6840.
7. Shardul Bhatt and Bhavna Trivedi, *Polyhedron*, 2012, **35**, 15–22.
8. Bojie Weng and Jing-Hua Li, *Appl. Organomet. Chem.*, 2009, **23**, 375–378.
9. X. Wang, Y. Dong, J. Sun, X. Xu, R. Li and Y. Hu, *J. Org. Chem.*, 2005, **70**, 1897–1900.
10. G. Cheng, X. Wang, R. Zhu, C. Shao, J. Xu and Y. Hu, 2011, 2694–2700.
11. E. Rajanarendar, D. Nagaraju, S. Ramakrishna and B. Kishore, 2014, **53**, 412–418.
12. J. M. Lehn, *Proc. Natl. Acad. Sci.*, 2002, **99**, 4763–4768.
13. P. Ceroni, A. Credi and M. Venturi, *Chem. Soc. Rev.*, 2014, **43**, 4068.
14. P. A. Gale, *Philos. Trans. R. Soc. A Math. Phys. Eng. Sci.*, 2000, **358**, 431–453.
15. J. W. Steed and J. L. Atwood, *Supramolecular Chemistry*, John Wiley & Sons, Ltd, Chichester, UK, 2009.
16. J. E. Laaser, Y. Jiang, S. R. Petersen, T. M. Reineke and T. P. Lodge, *J. Phys. Chem. B*, 2015, **119**, 15919–15928.
17. J. Malina, M. J. Hannon and V. Brabec, *Chem. A Eur. J.*, 2015, **21**, 11189–11195.
18. A. Lavalette, J. Hamblin, A. Marsh, D. M. Haddleton and M. J. Hannon, *Chem. Commun.*, 2002, 3040–3041.
19. C. Schalley, *Angew. Chemie Int. Ed.*, 2013, **52**, 12777–12777.
20. D. Thassu, M. Deleers and Y. Pathak, *Nanoparticulate Drug Delivery Systems*, CRC Press, Taylor & Francis Group, 2007.
21. V. Ambike, S. Adsule, F. Ahmed, Z. Wang, Z. Afrasiabi, E. Sinn, F. Sarkar and S.

Padhye, *J. Inorg. Biochem.*, 2007, **101**, 1517–1524.

22. E. Hadjoudis, M. Vittorakis and I. Moustakali-Mavridis, *Tetrahedron*, 1987, **43**, 1345–1360.
23. H. Bouas-Laurent and H. Dürr, *Photochromism : Molecules and systems*, 2003.
24. H. Ünver, *Spectrosc. Lett.*, 2001, **34**, 783–791.
25. K. T. Holman, *Science.*, 2001, **294**, 1907–1911.
26. T. Kudernac, N. Sändig, T. F. Landaluce, B. J. Van Wees, P. Rudolf, N. Katsonis, F. Zerbetto and B. L. Feringa, *J. Am. Chem. Soc.*, 2009, **131**, 15655–15659.
27. J. M. Fernández-G, F. Del Rio-Portilla, B. Quiroz-García, R. A. Toscano and R. Salcedo, *J. Mol. Struct.*, 2001, **561**, 197–207.
28. M. Muthuraman, Y. Le Fur, M. Bagieu-Beucher, R. Masse, J. F. Nicoud, S. George, A. Nangia and G. R. Desiraju, *J. Solid State Chem.*, 2000, **152**, 221–228.
29. S. Hisaindee, J. Graham, M. A. Rauf and M. Nawaz, *J. Mol. Liq.*, 2012, **169**, 48–53.
30. C. Reichardt, *Chem. Soc. Rev.*, 1992, **21**, 147.
31. W. T. Wong, W.Y. Wong, *J. Organomet. Chem.*, 1999, **584**, 48–57.
32. M. I. Page, *The Chemistry of Enzyme Action*, 1984, vol. 6.
33. H. Zhong, Y. Zhang, Z. Wen and L. Li, *Nat. Biotechnol.*, 2004, **22**, 1291–6.
34. A. Krogdahl, G. I. Hemre and T. P. Mommsen, *Aquac. Nutr.*, 2005, **11**, 103–122.
35. R. W. Torget, J. S. Kim and Y. Y. Lee, *Ind. Eng. Chem. Res.*, 2000, **39**, 2817–2825.
36. J. H. Hartley, T. D. James and C. J. Ward, *J. Chem. Soc. Perkin Trans. 1*, 2000, **14**, 3155–3184.
37. P. D. Beer and P. A. Gale, *Angew. Chem. Int. Ed. Engl.*, 2001, **40**, 486–516.
38. R. Martínez-Máñez and F. Sancenón, *Chem. Rev.*, 2003, **103**, 4419–4476.
39. I. Stibor, *Anion sensing*, Springer-Verlag, Berlin, 2005.
40. R. P. Haugland, *The handbook: A Guide to Fluorescent Probes and Labeling Technologies*, 2005, vol. 10.
41. P. D. Beer and S. R. Bayly, *Top. Curr. Chem.*, 2005, **255**, 125–162.
42. P. D. Beer and J. Cadman, *Coord. Chem. Rev.*, 2000, **205**, 131–155.
43. K. J. Waldron, J. C. Rutherford, D. Ford and N. J. Robinson, *Nature*, 2009, **460**, 823–30.

44. B. Kuswandi, Nuriman, W. Verboon and D. N. Reinhoudt, *Sensors*, 2006, **6**, 978–1017.

45. A. Punning, M. Kruusmaa and A. Aabloo, *Sensors Actuators, A Phys.*, 2007, **136**, 656–664.

46. L. Basabe-Desmonts, F. van der Baan, R. S. Zimmerman, D. N. Reinhoudt and M. Crego-Calama, *Sensors*, 2007, **7**, 1731–1746.

47. B. Tomapatanaget, T. Tuntulani and O. Chailapakul, *Org. Lett.*, 2003, **5**, 1539–1542.

48. N. Kerdpaiboon, B. Tomapatanaget, O. Chailapakul and T. Tuntulani, *J. Org. Chem.*, 2005, **70**, 4797–4804.

49. K. K. Sung, H. B. Ju, R. A. Bartsch, Y. L. Jin and S. K. Jong, *Org. Lett.*, 2005, **7**, 4839–4842.

50. S. O. Kang, R. A. Begum and K. Bowman-James, *Angew. Chemie - Int. Ed.*, 2006, 45, 7882–7894.

51. Q. Y. Cao, T. Pradhan, M. H. Lee, K. No and J. S. Kim, *Analyst*, 2012, **137**, 4454.

52. O. Sénèque, M. N. Rager, M. Giorgi and O. Reinaud, *J. Am. Chem. Soc.*, 2000, **122**, 6183–6189.

53. A. E. Hargrove, S. Nieto, T. Zhang, J. L. Sessler and E. V. Anslyn, *Chem. Rev.*, 2011, 111, 6603–6782.

54. S. Aoki and E. Kimura, *Rev. Mol. Biotechnol.*, 2002, **90**, 129–155.

55. D. Coquière, S. Le Gac, U. Darbost, O. Sénèque, I. Jabin and O. Reinaud, *Org. Biomol. Chem.*, 2009, **7**, 2485–2500.

56. C. Di Natale, R. Paolesse and A. D'Amico, *Sensors Actuators, B Chem.*, 2007, **121**, 238–246.

57. M. Avadanei, N. Kuş, V. Cozan and R. Fausto, *J. Phys. Chem. A*, 2015, **119**, 9121–9132.

58. E. Hadjoudis and I. M. Mavridis, *Chem. Soc. Rev.*, 2004, **33**, 579–588.

59. E. Hadjoudis, K. Yannakopoulou, S. D. Chatziefthimiou, A. Paulidou and I. M. Mavridis, *J. Photochem. Photobiol. A Chem.*, 2011, **217**, 293–298.

60. E. Hadjoudis, A. Rontoyianni, K. Ambroziak, T. Dziembowska and I. M. Mavridis, *J. Photochem. Photobiol. A Chem.*, 2004, **162**, 521–530.

61. V. I. Minkin, A. V. Tsukanov, A. D. Dubonosov and V. A. Bren, *J. Mol. Struct.*, 2011, **998**, 179–191.

62. E. Hadjoudis and J. Argyroglou, *J. Mol. Struct.*, 1984, **114**, 41–44.

63. S. H. Kim, H. J. Suh, J. Z. Cui, Y. S. Gal, S. H. Jin and K. Koh, *Dye. Pigment.*, 2002, **53**, 251–256.

64. M. Kojima, *Monogr. Ser. Int. Conf. Coord. Chem. held Period. Smolenice Slovakia*, 2003, **6**, 207–212.

65. Y. Morita, S. Suzuki, K. Fukui, S. Nakazawa, H. Kitagawa, H. Kishida, H. Okamoto, A. Naito, A. Sekine, Y. Ohashi, M. Shiro, K. Sasaki, D. Shiomi, K. Sato, T. Takui and K. Nakasuji, *Nat. Mater.*, 2008, **7**, 48–51.

66. S. C. Lee, Y. Gyu, W. Ho, H. Kim, J. Jang, K. Park and I. Hee, 2006, **825**, 70–78.

67. Q. L. Zhu and Q. Xu, *Chem. Soc. Rev.*, 2014, **43**, 5648–5512.

68. J. H. Day, *Chem. Rev.*, 1970, **227**, 419–419.

69. A. Patlolla, J. Zunino, A. I. Frenkel and Z. Iqbal, *J. Mater. Chem.*, 2012, **22**, 7028.

70. I. Sage, *Liq. Cryst.*, 2011, **38**, 1551–1561.

71. T. H. Kim, Y. W. Shin, J. H. Jung, J. S. Kim and J. Kim, *Angew. Chemie - Int. Ed.*, 2008, **47**, 685–688.

72. C. Yang, F. P. Orfino and S. Holdcroft, *Macromolecules*, 1996, **29**, 6510–6517.

73. Z. Yuan, C. W. Lee and S. H. Lee, *Polymer (Guildf).*, 2006, **47**, 2970–2975.

74. T. Polymers, *Polymer (Guildf).*, 2002, **12**, 143–165.

75. Z. Yuan, C. W. Lee and S. H. Lee, *Polymer (Guildf).*, 2006, **47**, 2970–2975.

76. U. El-Ayaan, F. Murata and Y. Fukuda, *Monatshefte fur Chemie*, 2001, 132, 1279–1294.

77. M. A. White and M. Leblanc, *J. Chem. Educ.*, 1999, **76**, 1201–1205.

78. C. Tanioku, K. Matsukawa and A. Matsumoto, *ACS Appl. Mater. Interfaces*, 2013, **5**, 940–948.

79. S. H. Park, J. Y. Kim, H. Kim and K. Lee, *J. Korean Phys. Soc.*, 2005, **46**, 1049–1052.

80. M. Li, J. Huang, X. Zhou and H. Luo, *Spectrochim. Acta - Part A Mol. Biomol. Spectrosc.*, 2010, **75**, 753–759.

81. A. Filarowski, M. Lopatkova, P. Lipkowski, M. Van Der Auweraer, V. Leen and W. Dehaen, *J. Phys. Chem. B*, 2015, **119**, 2576–2584.

82. T. Akitsu and Y. Einaga, *Polyhedron*, 2005, **24**, 1869–1877.

83. J. Sirirak, D. J. Harding, P. Harding, L. Liu and S. G. Telfer, *Aust. J. Chem.*, 2015, **68**, 766.

84. A. R. Sheth, J. W. Lubach, E. J. Munson, F. X. Muller and D. J. W. Grant, *J. Am. Chem. Soc.*, 2005, **127**, 6641–6651.

85. M. A. Chowdhury, M. Joshi and B. S. Butola, *J. Eng. Fiber. Fabr.*, 2014, **9**.

86. P. J. Coelho, C. J. R. Silva, C. Sousa and S. D. F. C. Moreira, *J. Mater. Chem. C*, 2013, **1**, 5387.

87. R. C. Evans, H. D. Burrows and P. Douglas, *Applied Photochemistry*, Springer Netherlands, Dordrecht, 2013.

88. A. Seeboth, D. Lötzsch, R. Ruhmann and O. Muehling, *Chem. Rev.*, 2014, **114**, 3037–3068.

89. H. Wen, H. Niu, B. Li, X. Ma, X. Bai, Y. Zhang and W. Wang, *Synth. Met.*, 2015, **202**, 89–97.

90. V. Krishna, S. Basavoju and A. Ramachandraiah, *Mol. Cryst. Liq. Cryst.*, 2012, **562**, 265–290.

91. M. Barboiu, E. Petit, A. Van Der Lee, G. Vaughan, F. M. Cedex, E. Synchrotron and R. Facility, 2006, **45**, 2005–2007.

92. M. R. Darla and S. Varghese, *Liq. Cryst.*, 2012, **39**, 63–70.

93. D. M. Rao, K. N. Sharafudeen, K. Chandrasekharan and S. Varghese, *Opt. Commun.*, 2013, **287**, 224–227.

94. I. Ali, S. M. Al Zahrani and S. K. Dolui, 2012, **54**, 342–348.

95. M. Sliwa, S. Le, I. Malfant, M. Nierlich, P. G. Lacroix, C. Cedex, L. De Chimie, I. Lci, C. Umr and R. V May, 2005, 4727–4735.

96. K. Singh, *J. Enzyme Inhib. Med. Chem.*, 2006, **21**, 557–562.

97. Z. H. Chohan, M. F. Jaffery and C. T. Supuran, *Met. drugs*, 2001, **8**, 95–101.

98. K. Singh, M. S. Barwa and P. Tyagi, *Eur. J. Med. Chem.*, 2006, **41**, 147–153.

99. Z. H. Chohan, S. H. Sumrra, M. H. Youssoufi and T. B. Hadda, *Eur. J. Med. Chem.*, 2010, **45**, 2739–2747.

100. A. C. G. Hotze, N. J. Hodges, R. E. Hayden, C. Sanchez-Cano, C. Paines, N. Male, M. K. Tse, C. M. Bunce, J. K. Chipman and M. J. Hannon, *Chem. Biol.*, 2008, **15**,

1258–67.

101. U. McDonnell, M. R. Hicks, M. J. Hannon and A. Rodger, *J. Inorg. Biochem.*, 2008, **102**, 2052–2059.

102. R. Zhang Yuan, Han, Mengting, Ye, Qiong and Xiong, *Chin. J. Chem*, 2010, **28**, 1533–1537.

103. N. Gyémánt, H. Engi, Z. Schelz, I. Szatmári, D. Tóth, F. Fülöp, J. Molnár and P. A. M. de Witte, *Br. J. Cancer*, 2010, **103**, 178–85.

104. A. Abdul Jameel and M. Syed Ali Padusha, *Asian J. Chemsirty*, 2010, **22**, 3422–3428.

CHAPTER - II

MATERIALS AND METHODS

It is highlighted in **CHAPTER I** that our objectives are to generate new classes of azomethine and dihydroazomethine ligands and their ensuing coordination compounds as possible supramolecular hosts and for possible model applications. The ligands and metal complexes which were prepared by me have been tested for their supramolecular ion-dipole (metal to ligand), inter- and intra-molecular H-bonding (helical geometry), dipole-dipole interactions (solvated crystal systems) etc.,. These compounds fall into different classes on the basis of their structural features. The compounds were characterized by various physiochemical techniques employing modern analytical instruments. Some of these compounds exhibit Metalochromic, Mechanochromic (Tribochromic**)**, Thermochromic, Halochromic and Solvatochromic effects. Thus, these smart materials promise some of useful applications. This Chapter compiles all the experimental procedures adopted in the synthesis of the azomethine and dihydroazomethine ligands and their complexes besides details of characterization of all of them by various instrumental techniques.

This Chapter is divided into two parts. **Part A** entitled 'Materials' describes the synthesis and sampling of the investigated compounds while **Part B**, 'Methods', the details of characterization by modern instruments.

PART A: MATERIALS

2A.1: Biphenyl Bridged Pyridine-2-carboxaldimine Schiff Bases

The general structure of the Schiff base is presented in **2A.1**. By independent and coupled variation through Z and X, biphenyl bridged polynucleating ligands have been synthesized. The general synthetic procedure is same for the compounds as given below.

Biphenyl bridged bis-bidentate Schiff base ligands (L) were prepared[1,2] by mixing hot methanol solution of any biphenyl bridged primary diamine (10 mmole), like (4-aminophenoxy)benzenamine, (4-aminobenzyl)phenylamine, o-diansidine, o-tolidine and benzidine, with that of pyridine-2-carboxaldehyde (20 mmole). The ligands precipitated were filtered through suction and washed repeatedly with cold methanol followed by acetone and dried in vacuo at 90 $^{\circ}$C overnight.

The procedure for the preparation of a Schiff base ligand, o-TOLI-Pyral is given here. 2.12 g (10 mmoles) of o-tolidine and 2.40 g (20 mmoles) of pyridine-2-carboxaldehyde were dissolved in 50 ml methanol separately in 100 ml beakers. When the aldehyde was mixed with vigorous stirring to the amine while heating at ~50 $^{\circ}$C, a bright yellow colored substance was obtained which on standing overnight, gave yellow crystalline solid. The mass was recrystallized from methanol and dried in vacuo. The other ligands, viz., BENZ-Pyral, DADPM-Pyral, etc., were prepared by employing the same procedure[3].

The physicochemical characterizations of these ligands are described in **PART A** of **CHAPTER III**.

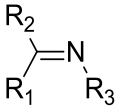 **(2A.1)**	R_1= H, and R_2 = R_3 = ArOH, $ArNO_2$, pyridine, Diamino biphenyls, etc.,
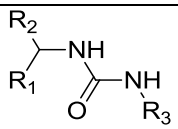 **(2A.2)**	$R_1 \neq R_2$ and R_3 = H, C_2H_5, etc; R_1= R_2 = R_3 = CH_3, ArOH, $ArNO_2$, etc.,

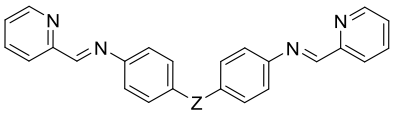

(2A.3)

Z	X	Row combination labeled as [L]
—O—	—	DADPE-Pyral
—CH_2—	—	DADPM-Pyral
—	—CH_3	o-TOLI-Pyral
—	—OCH_3	o-DIANISI-Pyral
—	—H	BENZ-Pyral

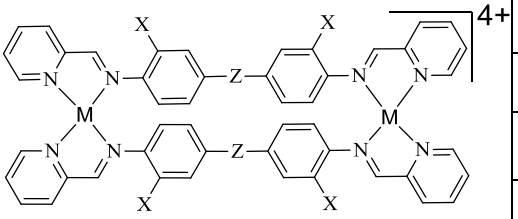

Z= O, -CH_2- and NIL, X = H, CH_3 and OCH_3

M = Co (II), Ni (II), Cu (II) and Zn (II)

(2A.4)

Z	X	Row combination labeled as $[M_2L_2]^{4+}$
—O—	—	$[M_2(DADPE\text{-}Pyral)_2]^{4+}$
—CH_2—	—	$[M_2(DADPM\text{-}Pyral)_2]^{4+}$
—	—CH_3	$[M_2(o\text{-}TOLI\text{-}Pyral)_2]^{4+}$
—	—OCH_3	$[M_2(o\text{-}DIANISI\text{-}Pyral)_2]^{4+}$
—	—H	$[M_2(BENZ\text{-}Pyral)_2]^{4+}$

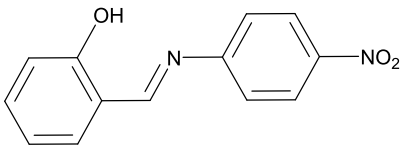

PNASH
(2A.5)

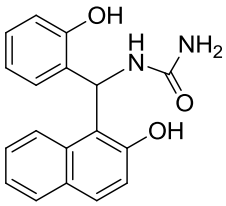

UBBH2
(2A.6)

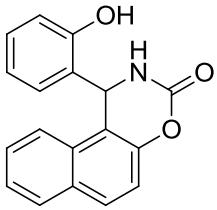

OXAZH
(2A.7)

2A.2: The Metalochromes, $[M_2L_2]Cl_4$

The biphenyl bridged pyridine-2-carboxaldimine ligand systems are potential bis-binucleating ligands. If the ligands are generalized as 'L', the anticipated binuclear structure is given in structure **2A.3** for the complexes, $[M_2L_2]^{2n+}$(**2A.4**) where M is a metal ion of charge +n. The general synthetic procedure of generating the metal complexes, $[M_2L_2]^{2n+}$, is nearly the same for any M and 'L' combination. Representative synthetic method for the preparation of a few complexes, are provided here.

Cobalt(II) Complexes

A warm solution, containing 2 mmoles (1.0138 g) of cobalt chloride in methanol was added, while stirring, to a solution containing 2 mmoles (1.017 g) of o-TOLI-Pyral in

acetone. The mixture turned deep red and the contents were kept standing overnight to yield a bright crystalline red coloured binuclear cobalt(II) cationic complex.

Nickel(II) Complexes

A warm solution, containing 2 mmoles (0.3996 g) of nickel chloride in methanol was added to a solution containing 2 mmoles (1.013 g) of o-TOLI-Pyral in acetone while stirring. The mixture turned green and the contents were kept standing overnight to yield a bright crystalline yellow coloured binuclear nickel(II) cationic complex.

Copper(II) Complexes

A warm solution, containing 2 mmoles (0.439 g) of copper chloride in methanol was added, while stirring, to a acetone solution of 2 mmoles (1.1057 g) of o-TOLI-Pyral. The deep brown colored solution gave a crystalline binuclear copper(II) cationic complex when kept standing overnight.

Zinc(II) Complexes

A moderately hot solution, of 2 mmoles (0.439 g) of zinc chloride in methanol was added, to a solution of 2mmole (1.041 g) of o-TOLI-Pyral in acetone. The light yellow contents gave a crystalline light yellow colored binuclear zinc(II) cationic complex upon standing overnight.

2A.3: 2-(((4-Nitrophenyl)imino)methyl)phenol

A non-linear Schiff base (**2A.5**) which is having an electron donating and an electron accepting groups which are separated by conjugated π-electron system have been prepared in one-pot synthesis.

2-(((4-nitrophenyl)imino)methyl)phenol (**PNASH**) was prepared by the reported procedure[4,5]. An amount of 1.38 g (10 mmoles) of 4-nitroaniline and 1.40 g (10 mmoles) of salicylaldehyde were dissolved in methanol and refluxed at ~ 60 $^{\circ}$C for about 2 h. An orange red colored substance was precipitated. The mass was recrystallized from methanol and dried in vacuo.

The physical and chemical characteristics of **PNASH** ligand, mentioned in structure **2A.5** are given in **PART A** of **CHAPTER IV**.

2A.4: Urea Betti Base (UBBH2) and Its Cyclized Oxazinone Derivative (OXAZH)

The general structure of the urea Betti base is given in **2A.2** whereas its equivalent (UBBH2) synthesized by me is in **2A.6**. Its cyclized oxazinone derivative (OXAZH) is shown in **2A.7**.The UBBH2 and OXAZH are synthesized following a procedure reported

elsewhere[6,7]. 10 mmoles of each of salicylaldehyde, 2–naphthol and urea were mixed in 15 mL of absolute ethanol in a 100 mL round bottom flask and refluxed at ~ 80 °C for 10 h. A crude pale yellow precipitate was obtained which was recrystallised from ethanol. The reaction is highly sensitive to temperature. Overheating of the reaction mixture (~ 85-95 °C) leads to cyclization and results cyclized oxazinone derivative (**2A.7**). Refluxion of the reaction mixture beyond 85 °C does not result in UBBH2 (**2A.6)**, but takes the reaction forward till OXAZH (**2A.7**) is produced. On the other hand, OXAZH is produced by cyclization of UBBH2 (**2A.6)** through refluxion of its ethanolic solution at 90 °C for about 10 h. OXAZH and UBBH2 compounds were further recrystallized from ethanol.

The physical and chemical characteristics of UBBH2 (**2A.6**) and OXAZH (**2A.7**) ligands, are given in **PART A** of **CHAPTER V**.

2A.5: The Buffers

Since the spectral and electrochemical studies of the compounds have been carried out mostly in aqueous buffers, a series of aqueous buffer solutions of constant ionic strength of 0.1 M covering a wide pH range (1.0-13.0) was prepared. The stock solutions mentioned in **Table 2A.1** were first prepared and used in different combinations according to the reported procedure to get the solution of the desired pH[8].

Table 2A.1: *Stock solutions for preparing the buffers*

Index No.	Solute	Concentration
I	Hydrochloric Acid (HCl)	0.10 M
II	Potassium Chloride (KCl)	0.10 M
III	Sodium Chloride (NaCl)	0.10 M
IV	Sodium citrate ($Na_3C_6H_5O_7$)	0.02 M
V	Sodium Acetate ($NaOOCCH_3$)	0.10 M
VI	Acetic Acid (CH_3COOH)	0.10 M
VII	Sodium Tetra Borate ($Na_2B_4O_7$)	0.04 M
VIII	Glycine (H_2NCH_2COOH)	0.10 M
IX	Sodium Hydroxide (NaOH)	0.10 M

The pH values expected by Henderson's equation and measured by pH metry are collected in **Table 2A.2**.

Table 2A.2: *Preparation of buffer solutions with the stock solutions*

(a) ***pH Range 1.10 - 4.50***

S.No.	$Na_3C_6H_5O_7$	HCl	Capacity (ml)	pH Calculated	pH Measured
1	4.70	95.30	100	1.14	1.12
2	10.50	89.50	100	1.52	1.50
3	30.45	69.55	100	2.12	2.04
4	49.37	50.63	100	2.52	2.59
5	68.34	31.66	100	3.02	3.09
6	78.00	22.00	100	3.53	3.55
7	81.70	18.30	100	4.06	4.01
8	82.75	17.25	100	4.51	4.57

(b) ***pH Range 5.00 - 6.50***

S.No.	CH_3COONa	CH_3COOH	Capacity (ml)	pH Calculated	pH Measured
1	77.67	22.33	100	5.08	5.14
2	81.19	18.81	100	5.52	5.61
3	82.75	17.25	100	6.09	6.13
4	83.12	16.88	100	6.53	6.61

(c) ***Neutral pH Range***

The stock KCl solution was pH-metrically tuned by KOH / HCl

(d) ***pH Range 7.75 - 9.00***

S.No.	$Na_2B_4O_7$	HCl	Capacity (ml)	pH Calculated	pH Measured
1	12.07	87.93	100	7.76	7.82
2	18.90	81.10	100	8.01	8.08
3	38.63	61.37	100	8.53	8.55
4	55.85	44.15	100	9.01	8.98

(e) ***pH Range 9.50 - 11.00***

S.No.	$Na_2B_4O_7$	NaOH	Capacity (ml)	pH Calculated	pH Measured

1	66.25	33.75	100	9.56	9.51
2	69.83	30.17	100	10.10	10.14
3	70.84	29.16	100	10.54	10.59
4	71.23	28.77	100	11.01	11.07

(f) ***pH Range 11.50 - 12.90***

S.No.	Glycine	NaOH	Capacity (ml)	pH Calculated	pH Measured
1	0.95	99.05	100	11.61	11.54
2	0.35	99.65	100	12.05	12.10
3	0.12	99.88	100	12.52	12.61
4	0.05	99.95	100	12.90	12.97

PART B: METHODS AND MEASUREMENTS

The methods of sampling for various instrumental analysis along with the types of instrumental techniques are broadly presented in this Part. For the benefit of readers of the thesis who would take leads from our investigations and studies, a brief introduction is portrayed at the end of this Chapter about the principles of some of the modern methods of investigation that we have utilized.

2B.1: Sampling Methods and Instrumental Operations

2B.1.1: *Melting point determination*

Conventional Stuart SPM 30 Digital Melting Point Apparatus[9] was used to measure the melting points and the data are uncorrected. The melting points along with the heat of fusion of all the compounds were obtained on TA Instruments Model Q10 Differential Scanning Calorimeter[10].

2B.1.2: *Elemental analysis*

The C, H, N and S elemental analysis of the ligands and complexes were done on a Carlo Erba Model EA 1108 CHNS-O Elemental Analyser[11] equipped with DP 200 Data Processor and a microgram sensitive Mettler MC5 Microbalance[12]. The metal analysis of copper, cobalt, nickel and zinc present in the complexes were analysed adapting standard chemical and spectrophotometric procedures. The analyses of a few metal ions were found by Agilent Technologies Model 720 ICP-OES Spectrometer[13].

2B.1.3: *Mass spectra*

Electrospray ionisation Mass Spectra (ESI-MS) were determined on a Perkin Elmer Model (SCIEX API- 2000, ESI-MS) Spectrometer.

2B.1.4: *Infrared spectral studies*

The IR spectra were recorded in KBr pellets on Perkin Elmer Model Spectrum 100 S spectrophotometer[14] at a 2 cm^{-1} resolution. Additionally, Shimadzu Model 8201 PC FT-IR were also used.

2B.1.5: *NMR spectral studies*

The ligands and some of the soluble diamagnetic complexes were characterised by ^{1}H and ^{13}C NMR spectra, recorded on a Bruker Avance 400 MHz NMR spectrometer, using TMS as an internal reference at room temperature operating at 400 MHz. Deuteriated solvents were used to prepare the solutions of ~10-12 mg/ml. During the ^{13}C NMR studies, Deuteriated solvent, itself, several as the locking isotope.

2B.1.6: *ESR spectral studies*

EPR spectra were measured using a JEOL FA 100 X-Band Spectrometer[15] on the powder, solution and frozen glass.

2B.1.7: *Magnetic susceptibility studies*

The solid-state magnetic susceptibility of crystalline samples was measured at a field of 0.1 mT using a Batington MS2 Magnetometer. and MS2G single frequency sample sensor[16]. Diamagnetic corrections were made using Pascal's constants.

2B.1.8: *Thermal studies*

Differential Scanning Calorimetric thermal analyses of the samples were performed on a Thermal Advantage DSC Q10 V9.8 Build 296 (TA Instrument, USA)[10] module which was calibrated for temperature and cell constants using indium and sapphire. The instrument was equipped with refrigerator cooling system (RCS). The crystals (3-5 mg) were crimped in aluminum pans (non-hermetic) (30 μL) scanned at a heating rate of 10 $^{\circ}$C/min in the range 30–300 $^{\circ}$C under a dry nitrogen atmosphere (flow rate 50 mL/min).

2B.1.9: *UV-visible absorption spectral methods*

The UV-Visible electronic spectra of all compounds were recorded on either a Thermo Scientific Evolution 600[17] or a Perkin Elmer Lambda 25 Spectrophotometers[18] in the wavelength range 900-200 nm. The Peltier accessory was used for variable temperature studies. Thus pH-metric and spectrophotometric titration for studying the protonation, deprotonation equilibria and chemical kinetics were monitored by viewing the spectral variation.

2B.1.10: *Fluorescence emission spectral methods*

The UV-Visible fluorescence emission spectra of all compounds were recorded on Analytika F96pro Fluorescence Spectrophotometer[19] in the wavelength range 900-200 nm. The excitation light was mostly that of 365 nm. The pH-metric and spectrophotometric titration for studying the protonation and deprotonation equilibria were monitored by viewing the spectral variation.

2B.1.11: *Electrochemical methods*

The work presented in this thesis is considerably electrochemical and spectroelctrochemical in nature. Hence, a number of electroanalytical methods were used during the studies of the compounds. Since electrochemical techniques usually need ultra pure materials and methods of reproducibility, the purification of the materials and setting up experiments were done with utmost care.

The pH of the buffers, stock solutions and reaction mixtures were measured by an Orion Model EA 940 Expandable Ion Meter[20] equipped with Ag|AgCl combined glass electrode. Preliminary electrochemical measurements were taken on a EG & G Princeton Applied Research Corporation (PARC) Model 264 A3 Polarographic Analyzer/Stripping Voltammeter and on a Bio Analytical System Model CV-27 Voltamograph[21] equipped with an EG & G PARC Model 303 A SMDE. Metrohm 663 VA[22] and CHI 619D Electrochemical Analyzers[23] were used for final studies. We set the mercury electrode surface area as 0.26 mm^2 for our studies. A low-cost novel PTFE (polytetraflouroethylene) based static mercury dropping electrode (SMDE) was fabricated by us. Its configuration is shown in **Figure 2B.1**. It is a kind of portable electrode used for the analysis of organic, inorganic salts, heavy metal ions pollutants in electronics, electroplating industrial applications.

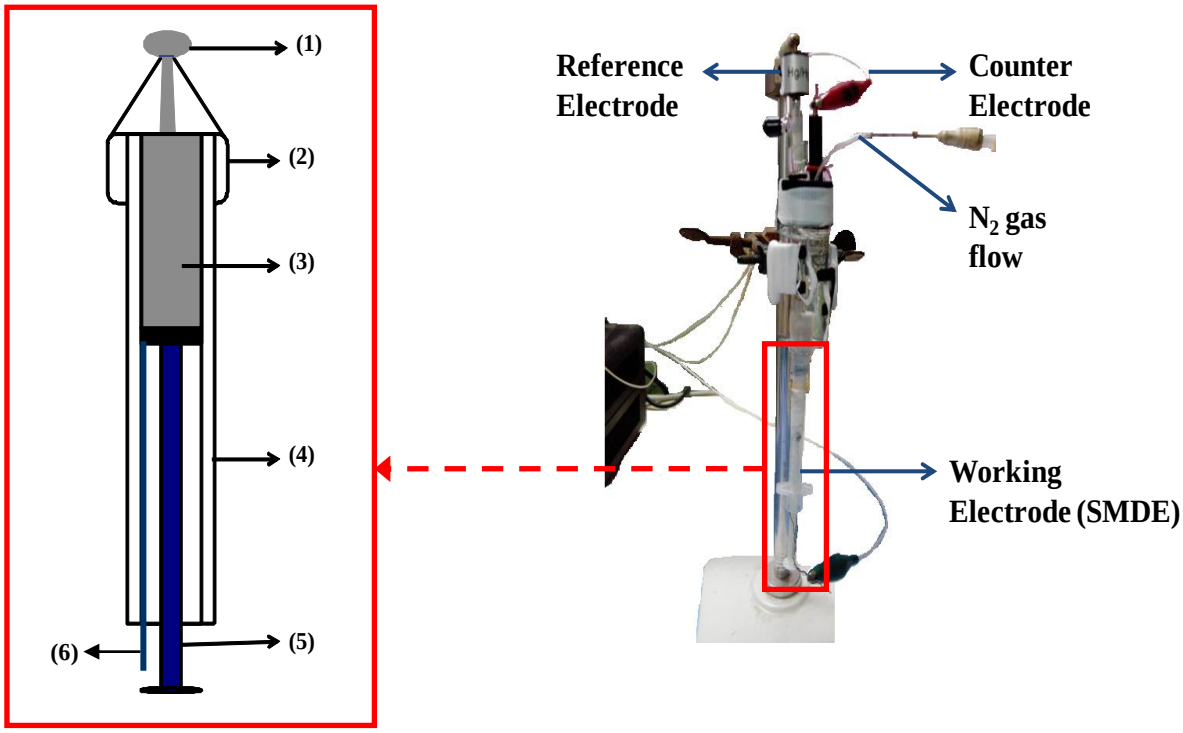

Figure 2B.1: A novel PTFE based SMDE electrode (1) Mercury drop (2) Teflon cap (3) Mercury pool (4) PTFE barrel (5) Plunger (6) Pt-wire

Pre-run preparatory methods

Purification of mercury

AR grade mercury was purchased from S.D Fine Chemicals Ltd. 1 Kg of mercury was filtered through chemoise leather. Then it was treated with saturated solution of mercuric chloride for separation of other metals from mercury. This operation was repeated thrice. The mercury, thus obtained, was again dried with pieces of Whitman filter paper several times. Finally, it was purified by double distillation under reduced pressure and was stored in dark polythene bottles.

Treatment of platinum wire and auxiliary electrode

Platinum wire which was used as auxiliary electrode in our studies was activated by heating in blue flame of Bunsen burner. Ignition was done after the electrode was dipped in ethyl alcohol and retrieved. During the electrochemical measurements the above procedure was carried out quite often.

Cleaning of Ag|AgCl reference electrode

The Ag|AgCl was used as reference electrode. It contains a saturated solution of AgCl and KCl filled in glass tube. The Ag|AgCl electrode was always kept in saturated KCl solution. Whenever it was needed, AgCl and KCl solution of reference electrode were changed.

Electrochemical measurement

The electrochemical measurements were done in a thermostatted three-electrode system cell, comprising of the working electrode (SMDE) or solid Pt or graphite reference electrode [Ag|AgCl|Cl (sat) or SCE] and auxiliary electrode (Pt foil or wire). The three electrode assembly is shown in **Figure 2B.2**.

Stock solutions of 10^{-3}M concentration of the compounds were prepared in 50 ml standard flasks. 20 ml of the buffer was taken in the electrochemical cell and 2 ml of the pure solvent of the stock solution of compound was added to it. This mixture was the blank. The contents of the cell were purged with AR grade nitrogen gas for 8 minutes to remove the dissolved oxygen. Then under the bed of the same nitrogen gas the electrochemical measurements were carried out as per the set experimental conditions. Mixing of 2 ml the relevant solution instead of the solvent alone to 20 ml of the buffer gave the solution for which the baseline correction was done under similar experimental conditions.

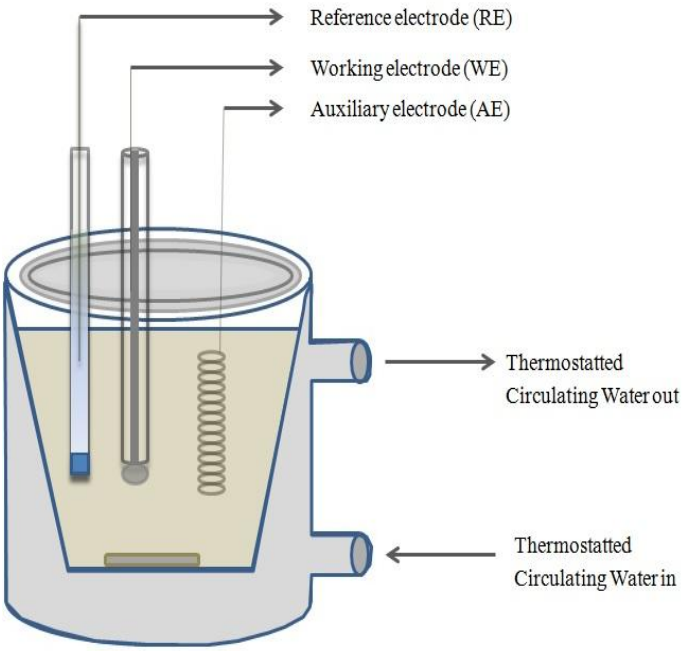

Figure 2B.2: Thermostatted three-electrode electrochemical cell

2B.1.12: *X-Ray crystallographic studies*

Growing Crystals

Whenever XRD measurement were undertaken, the respective recrystallized pure azomethine and dihydroazomethine compounds were dissolved in dichloromethane or dimethyl formamide or acetonitrile or ethyl acetate (10 mg per 2 ml). To this solution were added a few drops of methanol and the test tubes were closed with aluminum foils with one or two perforations. The test tubes were then kept buried in a stout sheet of thermocoal to avoid sudden temperature fluctuations; the whole setup was secluded into a wooden chest for 3-7 days. The tubes were then removed after a couple of weeks to see single crystals of varied sizes. These crystals were sorted by looking through a compound microscope. The best crystal, suitable for the single crystal XRD studies, was carefully picked, washed with pure ether to remove solvent residues and then air dried before, it was taken for mounting on the single crystal XRD machine.

Crystallographic data collection

After obtaining a suitable crystal for an X-ray experiment, the single crystal X-ray data was collected on Bruker-Nonius SMART APEX CCD diffractometer[24] at 293(2) K using graphite-monochromated Cu Kα radiation (λ = 1.54184 Å). This instrument is designed to aim X-ray beams through a crystal and record where the beams diffract and to measure the intensity of the reflection. A schematic of the setup is shown in **Figure 2B.3**.

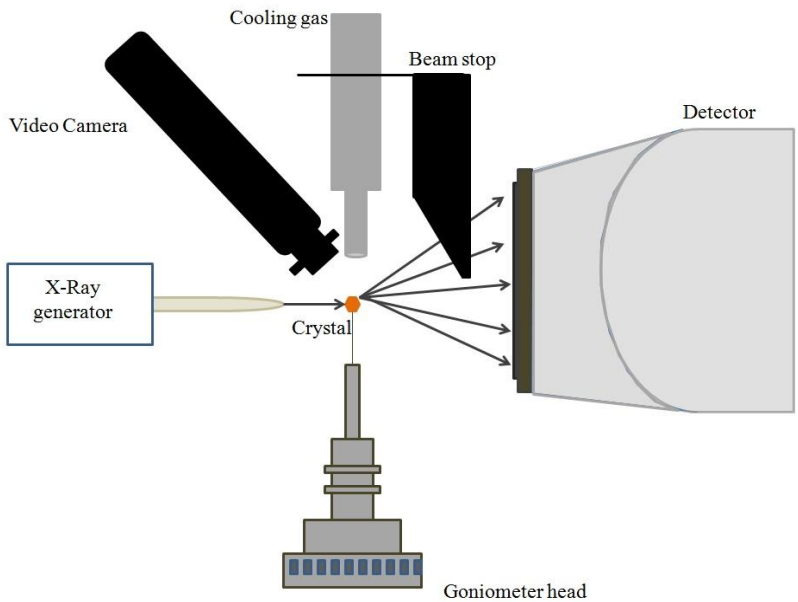

Figure 2B.3: Schematic of an X-ray diffractometer

2B.1.13: *Molecular modeling*

ChemOffice Ultra was used for molecular modeling of the compounds. Thermodynamic parameters such as heat of formation, dipole movement and HOMO-LUMO energies were obtained using this molecular modeling software. HOMO-LUMO energy values were used to verify the observed λ_{max} values for different species. The energy minimized structures were put to single and double dihedral conformational analysis. Golden software's Surfer 10 was used for 3-D counter plots of double-dihedral conformational analysis charts.

2B.1.14: *Antimicrobial studies*

The antimicrobial and antifungal activities of the compounds were determined by paper disc method and the minimum inhibitory concentration by liquid dilution method at microbiology department Kakatiya University. Details are given in **Chapter VI**.

2B.2: Functional Principles of Some Important Techniques

A brief sketch of some of the modern methods of characterisation of ligands and complexes that I have investigated is presented here. Though excellent books, review articles and resource material are available on these methods, a brief introduction may be a ready-reckoner. Only those methods, which gave deeper insight into the thermodynamic, chemical kinetics, electronic, structural, redox, magnetic, mechanochromic, thermochromic, photochromic, halochromic and spectral character of the compounds are covered hereunder.

2B.2.1: *Fluorescence spectrophotometric characterization of materials*

Electromagnetic radiation interacts with matter when they exposed to it. Depending up on material nature a number of processes can occur such as reflection, scattering, absorbance, fluorescence/ phosphorescence and photochemical reaction[25,26]. In general, one can understand the way of fluorescence emission by Jablonski diagram (**Figure 2B.4**). In **Figure 2B.4**, the absorption of selected excitation wavelength by molecule is promoting the ground state electron into excited state ($S_0 \rightarrow S_1$). The excited electron, usually undergo different process as follows[27,28]

(i) It may come to ground state ($S_1 \rightarrow S_0$) without any losses; this process is known as 'Resonance Fluorescence'. Here both the excited and emission wavelength are having same energy.

(ii) It may come to ground state ($S_1 \rightarrow S_0$) with losses of energy (vibrational relaxation in excited state), this process is known as 'Fluorescence'

(iii) It may come to ground state initially from $S_1 \rightarrow T_1$ (intersystem crossing) later $T_1 \rightarrow S_0$. This process known as 'Phosphorescence'

(iv) It may come to ground state after the electron in the excited singlet state cascades down to lower sub-energy levels of the singlet state before actually emitting a photon. This is not a radiative process. It is a thermal process. This process is known as 'Time Delayed Fluorescence'.

These fluorescence techniques obey the Beer-Lambert's law. Fluorescence emission spectrum is effected by pH, temperature, viscosity, polarity, etc., of the medium.

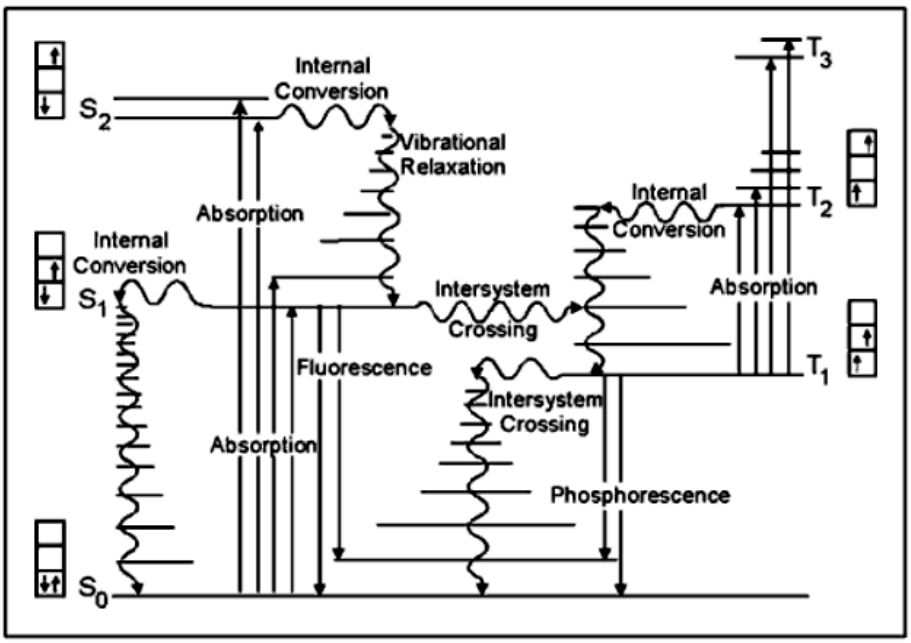

Figure 2B.4: Basic concepts of Jablonski diagram

2B.2.2: ***Cyclic voltammetry as tool for material diagnostics***

Cyclic voltammetry (CV) has become an important and widely used voltammetric technique in many areas such as chemical engineering, material science and chemical sciences. CV involves sweeping an electrode potential linearly as a function of time and measuring the corresponding current signal at each potential which is typically a 3-

electrode electrochemicalcell. In this technique the potential at working electrode changes in both forward and reverse direction while monitoring the current. A typical wave form applied at working electrode is shown in **Figure 2B.5** and resultant cyclic voltammogram is presented in **Figure 2B.6**. However, repetitive cyclic voltammograms can be used for a variety of applications, including the determination of Nernstian (reversible) and nonNernstian (irreversible) behavior of a redox couple, stability of reaction products, number of electrons transferred in an electrochemical event, reaction kinetic, etc.,

Randles-Sevcik equation[29,30] explains the effect of scan rate, area of the electrode material and concentration of the analyte on electrochemical run. However, the ratio of peak currents can be significantly influenced by chemical event coupled to the electrochemical event. **Figure 2B.7** describes the variations in i_{pa}/i_{pc} as a function of scan rate for a variety of electrochemical mechanisms[31].

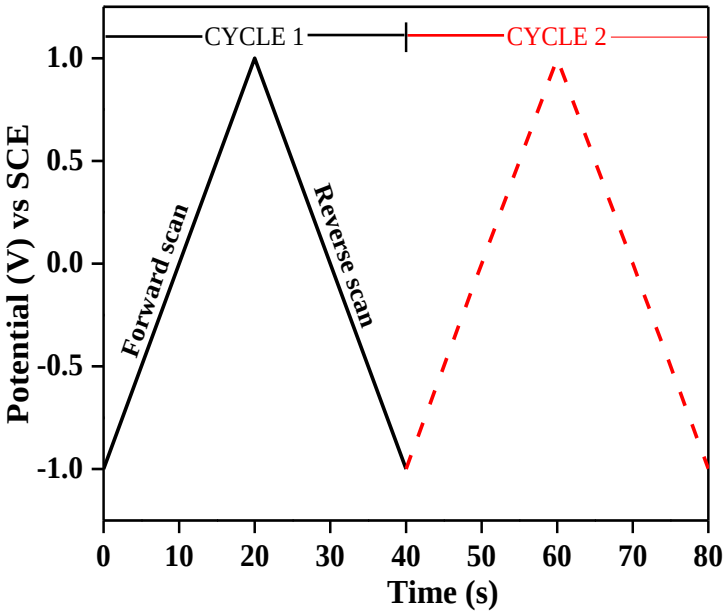

Figure2B.5: Typical triangular potential wave form of cyclic voltammetry technique (e.g., between -1.0 to +1.0 vs SCE)

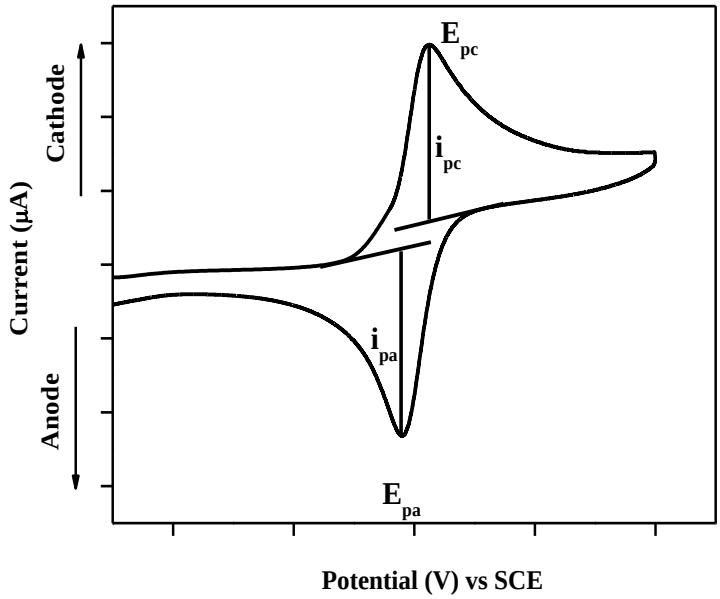

Figure 2B.6: Typical reversible cyclic voltammogram

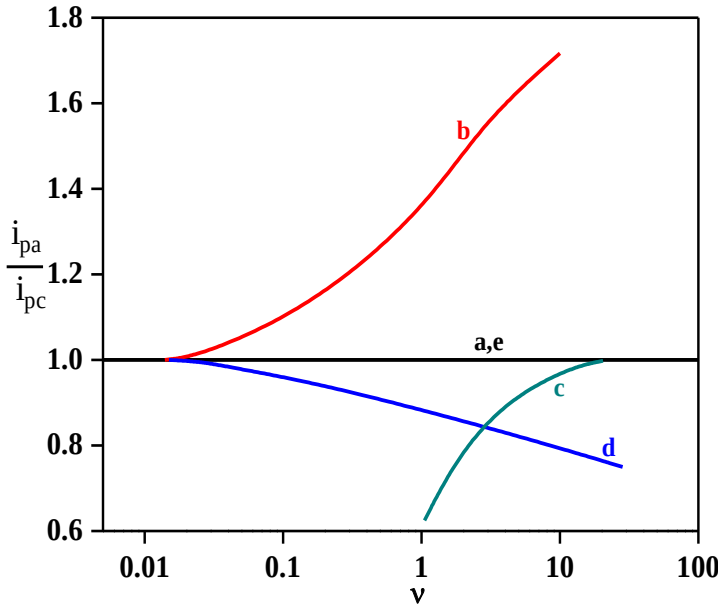

Figure 2B.7: Variations in the ratio of anodic and cathodic peak current as a function of scan rate for several electrode processes with reversible electron transfer[31].

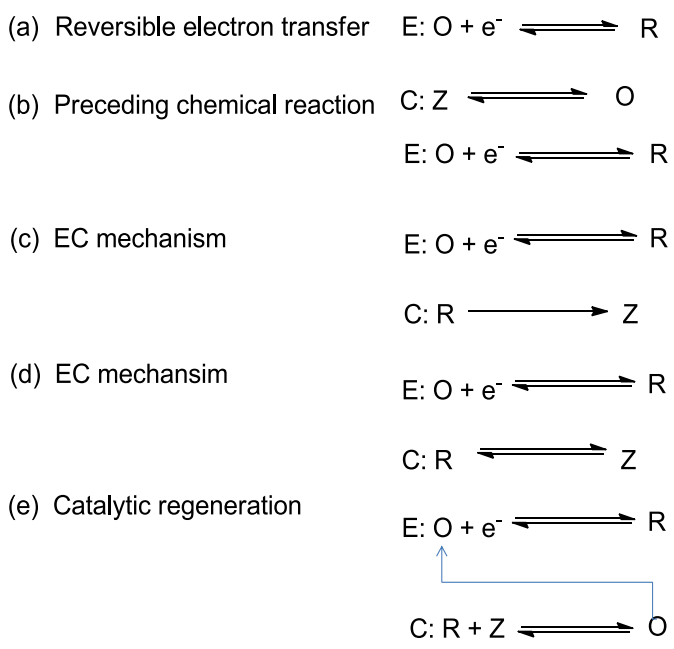

2B.2.3: *Thermometry and phase transition of materials*

Thermometric analysis plays vital role in sciences and enginnering. In thermometric analysis Differential Scanning Calorimetry (**DSC**) is one of widely used techniques to characterize the *thermophysical* properties of materials. Typically, DSC sample pans are made of aluminum. However, gold, platinum and stainless steel pans are used for specific applications requiring higher temperatures or pressures[32]. The DSC experiment consists of a curve with heat flux on y-axis and temperature or time on x-axis. This curve can be used to calculate the glass transition, phase transition, desolvation temperatures, percentage of crystallinity, polymer blending, meting and other thermometric events besides heat of enthalpy for every thermometric events[33]. This is done by integrating the peak corresponding to a given transition. The enthalpy of transition can be expressed by using the following equation: $\Delta H = KA$

here ΔH is the enthalpy of transition, K is the calorimetric constant and A is the area under the curve. K value usually changes from instrument to instrument and can be determined by analyzing a well-characterized sample with known parameters. In present case, DSC used to find the phase transition and the desolvation temperatures of crystal systems besides to find the fusion temperature of the crystals and to find the heat of enthalpy of corresponding thermometric event. In general, phase transition is very common phenomenon in polymorphs. They are further divided into two types i.e., enantiotropic polymorphs and

monotropic polymorphs. From the DSC thermogram, one can find out the type of polymorphic behavior. In **Figure 2B.8**, one can observe the energy versus temperature plots of enantiotropic polymorphism and monotropic polymorphism.

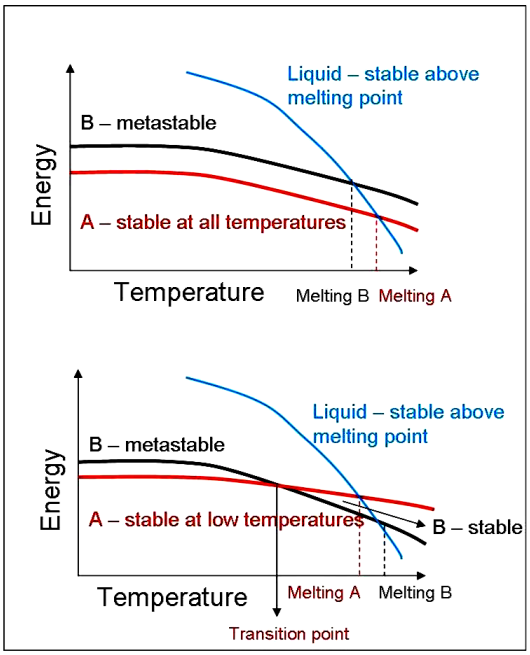

Figure 2B.8: Energy versus temperature plot shows the two types of polymorphic behavior of solid and liquid phases of a single compound (a) enantiotropic polymorphism and (b) monotropic polymorphism[33]

2B.2.4: *X-ray crystallographic manifestations of material phase transitions*

Crystallography is the experimental science of determining the arrangement of atoms in the crystalline solids. These techniques are being used by materials science, biological science, astronomy etc., scientist to know the structure and other geometrical parameters of the crystalline materials. Crystallographic methods now depend on analysis of the diffraction patterns of a sample targeted by a beam of X-rays generated from a anodic material such as Cu, Mo, etc.,. In this technique, X-rays interact with the spatial distribution of electrons in the sample. Because of their highly ordered and repetitive structure, crystals give diffraction patterns of sharp Bragg reflection spots and are ideal for analyzing the structure of solids. In present investigation, we mentioned some of Schiff base and Betti base derivatives crystal structures in Chapters IV and V besides correlation between geometrical parameters obtained from X-ray diffraction analysis data with molecular modeling data.

2B.2.5: *Graphical software for conformational plots*

Surfer® is a powerful statistical data treatment software[34]. It has more gridding methods and has more controls over gridding parameters. It displays grid as counter 3D surface, 3D wireframe, watershed, vector, image, shaded relief, ect.,. In this thesis, 3D wireframe is used for the plot of experimental data by using surfer® software.

The data is plotted as for the given mathematical function i.e., z = f(x,y) where x, y are variables.

Example: z = (pow(x,2) + pow(y,2)) * (sin(8*atan2(x,y))) with the boundary conditions of -50 < x < 50 and -50 < y < 50 the 3D wireframe (**Figure 2B.8**) is obtained.

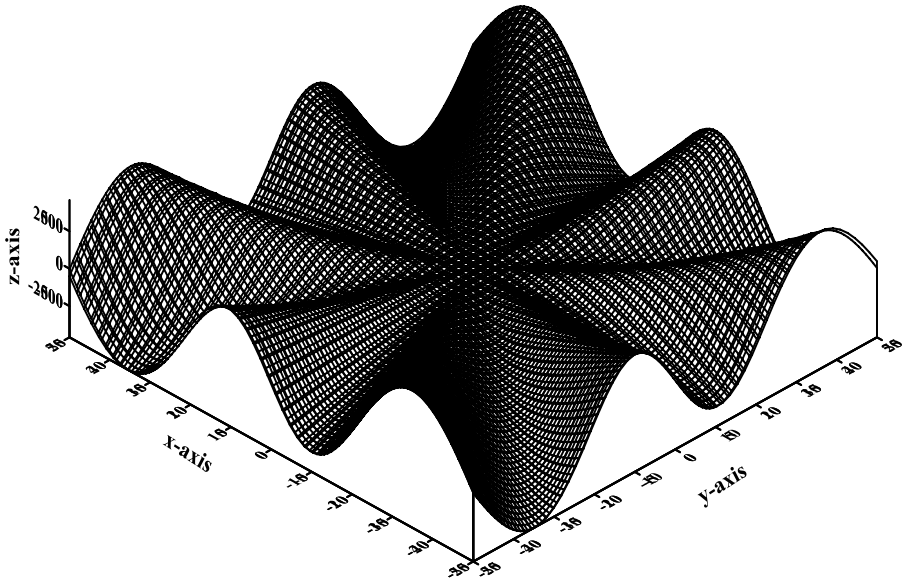

Figure 2A.5: 3D wireframe image of the function z = (pow(x,2) + pow(y,2)) * (sin(8*atan2(x,y))) with boundary conditions -50 < x < 50 and -50 < y < 50

2B.2.6: *Molecular modeling*

Computational chemistry is the science of representing molecular structures numerically and simulating their behavior with the equations of quantum and classical physics. Computational chemistry is also known as molecular modeling and is the application of computer-based models to simulation the chemical processes and the computation of chemical properties. Some of molecular modeling software such as ChemOffice Ultra, HyperChem, Gaussian, Spartan, Sybyl, etc., are being used for the calculation of single point energy, geometrical optimization and property (prediction of the certain physical and chemical properties like heat of formation, HOMO-LUMO, dipole moment).

Molecular modeling is result of two mathematical methods. Those are Molecular Mechanics (MM) and Quantum Mechanics (QM). All type of calculations are not possible for all methods and no one method is best for all purposes.
The following is a brief introduction to four major methods of computational chemistry[35–39]

a) Ab Initio:

These methods are based on quantum mechanics (i.e. solving of Schrödinger equation). Hartree-Fock (HF) and Quantum Monte Carlo (QMC) are two common wave-functions-used in ab initio calculations. Density Functional Theory is another type of ab initio calculation which is based on total electron density rather than wave functions. It is most promising approach to accurate quantum chemical calculations for large systems. Ab initio calculations give excellent quantitative results for small molecules.

b) Semi-empirical:

Semi-empirical calculations are much faster than ab initio methods. These calculations involve a series of approximations, restrictions and incorporation of experimental data. Depending upon requirement different semi-empirical methods are optimized. The MNDO, AM1 and PM3 methods are some of methods which are designed to reproduce heats of formation and structures of a huge organic molecules. Some of methods like ZINDO/S is one of specifically designed methods to predict the electronic transitions in the UV/VIS spectral region.

c) Molecular Mechanics (MM):

In this MM calculation, Newtonian mechanics (classical physics) is employed to predict the structures and properties of molecules. In this method nuclei is treated as spheres and connected bonds are treated as springs. These MM methods can be used to model huge molecules such as DNA or proteins.

d) Molecular Dynamics (MD):

Molecular dynamics calculations are employed to simulate the time-dependent behavior of molecules. MD method is used to study the diffusion of a solute molecule through a liquid. These calculation can be used for calculations involving large bio-molecules in solution.

In this thesis, we used ChemOffice Ultra as a molecular modeling tool for the calculations of heat of enthalpy, geometrical parameters like bond lengths, bond angles, torsional angles along with torsional energies, protonation and deprotonation energies of acid-base equilibrium. Further, we constructed conformational single dihedral and double dihedral plots. The objective of conformational search is to find all the possible values of dihedral angles that could be assigned to each rotatable bond in a molecular structure. On the basis of Boltzmann statistics, the number of possible conformers are contructed in following Chapters III, IV and V. A typical potential energy versus variable is shown in **Figure 2B.9** for the interest of the reader.

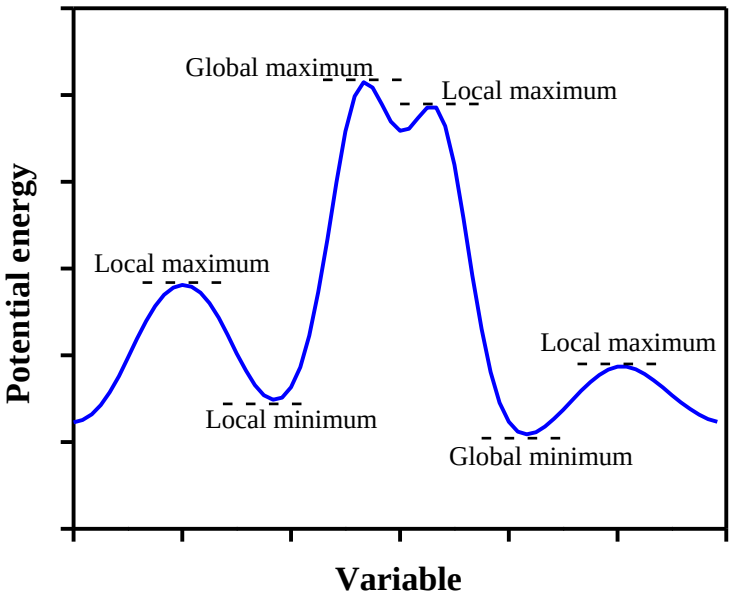

Figure 2B.9: A typical potential energy versus variable plot

Some of advanced versions of software packages were used to the calculations, statistical treatment and plotting of experimental data. Some of them are Origin Pro 8.0, Surfur 12.0, Mercury-2.3, X-seed, Diamond-10.0 for single crystal X-ray data refinement. ChemOffice Ultra software package were used for the molecular modeling and structures drawing purpose. MSOffice 2007, Mendeley Desktop, etc., were used to typeset the documents, graphics embedding , sorting and inserting the citations.

References

1. S. Dehghanpour, J. Lipkowski, A. Mahmoudi and M. Khalaj, *Polyhedron*, 2010, **29**, 2802–2806.
2. H. B. Tanh Jeazet, J. Mizera, T. Doert, K. Gloe, A. Heine, G. Bernhard and K. Gloe, *J. Incl. Phenom. Macrocycl. Chem.*, 2011, **71**, 343–352.
3. V. Krishna, S. Basavoju and A. Ramachandraiah, *Mol. Cryst. Liq. Cryst.*, 2012, **562**, 265–290.
4. B. Koşar, C. Albayrak, M. Odabaşoglu and O. Büyükgüngör, *Crystallogr. Reports*, 2010, **55**, 1207–1210.
5. X. X. Gong and H. J. Xu, *Acta Crystallogr. Sect. E Struct. Reports Online*, 2008, **64**, o1188–o1188.
6. A. Abdul Jameel and M. Syed Ali Padusha, *Asian J. Chemsirty*, 2010, **22**, 3422–3428.
7. C. Cardellicchio, M. Annunziata, M. A. M. Capozzi and F. Naso, *Tetrahedron: Asymmetry*, 2010, **21**, 507–517.
8. V. Krishna, *Synthesis and Characterization of Some New Series of Biphenyl Bridged Polynucleating Ligands and Their Bivalent Metal Complexes as Possible Supramolecular Hosts*, 2012.
9. http://www.keison.co.uk/products/stuart/SMP30Manual.pdf, 2016.
10. http://nmtprg.weebly.com/uploads/3/1/1/0/31101989/ta_mdsc_manual.pdf, 2007.
11. http://www.labtech.eu/files/ckeditor/pdf/Katalog_CHNOS_anal%C3%BDzy.pdf, 1998.
12. http://www.dnsmp.com/Manuals/METTLER%20TOLEDO/micobalanceSPEC.pdf, 2005.
13. http://www.agilent.com/cs/library/usermanuals/public/2337.pdf, 2011.
14. http://www.perkinelmer.com/CMSResources/Images/46-74472BRO_Spectrum 100FTIR.pdf, 2005.
15. https://www.liag-hannover.de/en/s/s3/research-fields/sediment-dating/electron-spin-resonance-laboratory.html, 2013.
16. http://www.bartington.com/Literaturepdf/Operation%20Manuals/om0408% 20MS2.pdf, .
17. http://thermo.com.cn/Resources/200802/productPDF_1844.pdf, 2006.
18. http://people.bath.ac.uk/gp304/uv/PerkinElmer_Lambda35_manual_EN.pdf, 2000.

19. http://www.mrclab.com/data/products/Spectro-96_OPR.pdf, .

20. http://www.expotechusa.com/Catalog_Thermo_Electron/Orion%20EA940%20 and Advanced%20Ion%20Selective%20Meter%2002-05.pdf, .

21. https://www.basinc.com/mans/cv27.pdf, 1984.

22. http://www.ecochemie.nl/download/NovaTutorials/VA_tutorial.pdf, .

23. http://www.vtpup.cz/common/manual/PrF_labsystruktan_ and CHInstruments _600C_manual_EN.pdf, .

24. http://xraysweb.lbl.gov/BL1131/1131website/doc/BrukerAPEX2%20 and User%20Manual.pdf, 2004.

25. PerkinElmer, *An Introduction to Fluorescence Spectroscopy*, 2000, vol. 65.

26. T. Owen, *Principles and Applications of UV-Visible Spectroscopy*, 1996.

27. A. Hayer, H. Bässler, B. Falk and S. Schrader, *J. Phys. Chem. A*, 2002, **106**, 11045–11053.

28. Thermo Spectronic, *ThermoSpectronic*, 2013, 1–28.

29. R. Gulaboski and C. M. Pereira, *Electroanalytical Techniques and Instrumentation in Food Analysis*, 2008.

30. A. J. Bard, L. R. Faulkner, E. Swain and C. Robey, *Fundamentals and Applications*, John Wiley & Sons, Inc, 2001.

31. P. T. Kissinger and W. R. Heineman, *Laboratory Techniques in Electroanalytical Chemistry*, Marcel Dekker, Inc., New York and Basel, 1984.

32. D. D. MacNeil, S. Trussler, H. Fortier and J. R. Dahn, *Thermochim. Acta*, 2002, **386**, 153–160.

33. D. Giron, *J. Therm. Anal. Calorim.*, 2001, **64**, 37–60.

34. http://downloads.goldensoftware.com/guides/Surfer12_Users_Guide_Preview.pdf, 1111.

35. J. B. Ealy, *J. Sci. Educ. Technol.*, 1999, **8**.

36. T. Gardner, *Molecular Modeling in Undergraduate Chemical Education*, 2005.

37. W. J. H. J. Schnitker, *Molecular Modeling in Teaching Undergraduate Chemistry Molecular Modeling in Teaching Undergraduate Chemistry*, .

38. L. L. Jones, K. D. Jordan and N. A. Stillings, *Chem. Educ. Res. Pract.*, 2005, **6**, 136–149.

39. www.wellesley.edu/Chemistry/Chem105manual/Chem105manual and Summer 07/Lab08/lab08.html,.

CHAPTER - III

BIPHENYL BRIDGED PYRIDINE-2-CARBOXALDIMINE SCHIFF BASES

In this Chapter, the studies of the biphenyl bridged pyridine-2-carboxaldimine Schiff base ligands is presented. These ligands were characterized by spectral (NMR, mass, IR and electronic), elemental analysis, electrochemical and thermal studies besides kinetics of hydrolysis of some of these ligands. These molecules are rich of nitrogen binding sites to bind to the metal ions and to form metaloporphyrin-like complexes. Some of their metal complexes such as cobalt(II), nickel(II), copper(II) and zinc(II) complexes have been prepared and characterized by physical, analytical, spectral and thermal studies and those details are also presented in this Chapter.

The general structures of these Schiff bases and their metal complexes are depicted in **3.1** and **3.2** respectively. Based on the structural vividity, this Chapter is documented separately as **PART A**, **PART B** and **PART C**.

In **PART A**, the physical, analytical data besides the spectral, electrochemical and co-ordination chemistry studies of some of the biphenyl bridged Schiff bases ligands **3.1** are presented and discussed.

In **PART B**, studies of kinetics of hydrolysis of the azomethine group of o-TOLI-Pyral as a function of temperature in aqueous methanol media are described.

In **PART C**, molecular modeling studies of these biphenyl bridged Schiff bases and their metal complexes are presented.

PART A: SPECTRAL, ELECTROCHEMICAL AND CO-ORDINATION CHEMISTRY STUDIES OF BIPHENYL BRIDGED PYRIDINE-2-CARBOXALDIMINE SCHIFF BASES

The chemical structures of the class of biphenyl bridged pyridine-2-carboxaldimine Schiff base ligands **R-Pyral** are presented in **3.1**.

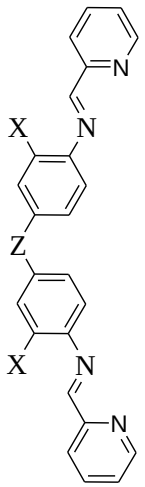

Z = -O-, $-CH_2-$ and NIL
X = H, CH_3 and OCH_3

3.1

Z	X	Row Combination (R-Pyral) Labeled
-O-	-H	**DADPE-Pyral**
$-CH_2-$	-H	**DADPM-Pyral**
-	$-OCH_3$	**o-DIANISI-Pyral**
-	$-CH_3$	**o-TOLI-Pyral**
-	-H	**BENZ-Pyral**

3A.1: General Characterization of the Biphenyl Bridged R-Pyral Schiff Base Ligands

The physical and analytical data of the biphenyl bridged pyridine-2-carboxaldimine Schiff base ligands are presented in **Table 3A.1**. The elemental analysis data are in good agreement with the chemical structure shown in **3.1**. The spectral studies of these ligands are briefly presented here.

3A.2: Infrared Spectral Studies

The FT-IR spectra of the ligands **3.1** in KBr disc were recorded in mid infrared region (400-4000 cm^{-1}). The FT-IR spectra of BENZ-Pyral and DADPM-Pyral are shown in **Figures 3A.1-3A.2**. Some of the relevant frequencies are presented in **Table 3A.2**. The lowering of carbonyl frequency upon condensation is a strong indication of the Schiff base formation[1,2]. The bands present at 1630-1615 cm^{-1} attributable to $\nu_{C=N}$ stretch of the Schiff base arising from the carbonyl group of –HC=O of pyridine-2-carboxaldehyde with frequencies 1730-1710 cm^{-1}. In the ligands BENZ-Pyral, o-TOLI-Pyral and DADPM-

Pyral a medium intensity bands are present around 3000 cm^{-1} which correspond to the stretching frequencies of the aromatic and azomethine protons. Aromatic ring frequencies are observed for all the ligands in the range of 1500-1375 cm^{-1} for $\nu_{C=C}$ and wagging frequencies are observed in the range of 3058-3020 cm^{-1} for ν_{C-H}.

3A.3: ^{1}H NMR and ^{13}C NMR Spectral Studies

The ^{1}H NMR and ^{13}C NMR spectra of BENZ-Pyral, o-TOLI-Pyral and DADPM-Pyral are recorded in $CDCl_3$ and are presented in **Figures 3A.3-3A.6**, respectively. The NMR signals of the compounds are compatible with the respective spectra (**Table 3A.4**).

Table 3A.1: *Physical and analytical data of R-Pyral Schiff base ligands*

Compound (R-Pyral)	Appearance	M. P. (°C)	Molecular Formula	Molecular Weight#	Elemental Analysis* %C	% H	% N
DADPE-Pyral	Yellow	130-132	$C_{24}H_{18}N_4O$	378	76.02 (76.80)	4.81 (4.15)	14.83 (15.17)
DADPM-Pyral	Pale yellow	146-148	$C_{25}H_{20}N_4$	376	79.82 (79.21)	5.33 (5.73)	14.85 (15.06)
o-TOLI-Pyral	Yellow	171-173	$C_{26}H_{22}N_4$	390	79.89 (79.26)	5.72 (5.38)	14.39 (15.36)
BENZ-Pyral	Greenish Yellow	177-179	$C_{24}H_{18}N_4$	362	79.55 (80.19)	5.02 (4.32)	15.43 (15.49)

*, data in parenthesis are calculated ones

#, data in parenthesis are obtained from ESI(+ve) mass spectra

Table 3A.2: *Infrared spectral data of R-Pyral Schiff base ligands*

S. No.	Compound (R-Pyral)	IR spectral data (cm^{-1})# $\nu_{C=N}$	ν_{C-N}	Aromatic (ν_{C-H})
1	**BENZ-Pyral**	1626	1262	3048w, 1493, 1319
2	**o-TOLI-Pyral**	1623	1257	3051w, 1497, 1321
3	**DADPM-Pyral**	1628	1264	3062w, 1499, 1344

#, in KBr pellet, w; weak

Table 3A.3: *UV-Visible and fluorescence spectra of R-Pyral Schiff base ligands*

S.No.	Compound	Electronic data λ_{max} ($\bar{\upsilon}$)(ϵ)[a]	Fluorescence data excited (nm)	Fluorescence data emission (nm)	Stokes shift (nm)
1	**BENZ-Pyral**	362 (27624, 82000)	365	462, 540	97, 175
2	**O-TOLI-Pyral**	365 (27397, 88666)	365	464, 541	99, 176
3	**DADPM-Pyral**	336 (29762, 92666)	365	461, 539	96, 174

a, λ_{max} (in nm), $\bar{\upsilon}$ (in cm^{-1}), ϵ(lit. mol^{-1}. cm^{-1})

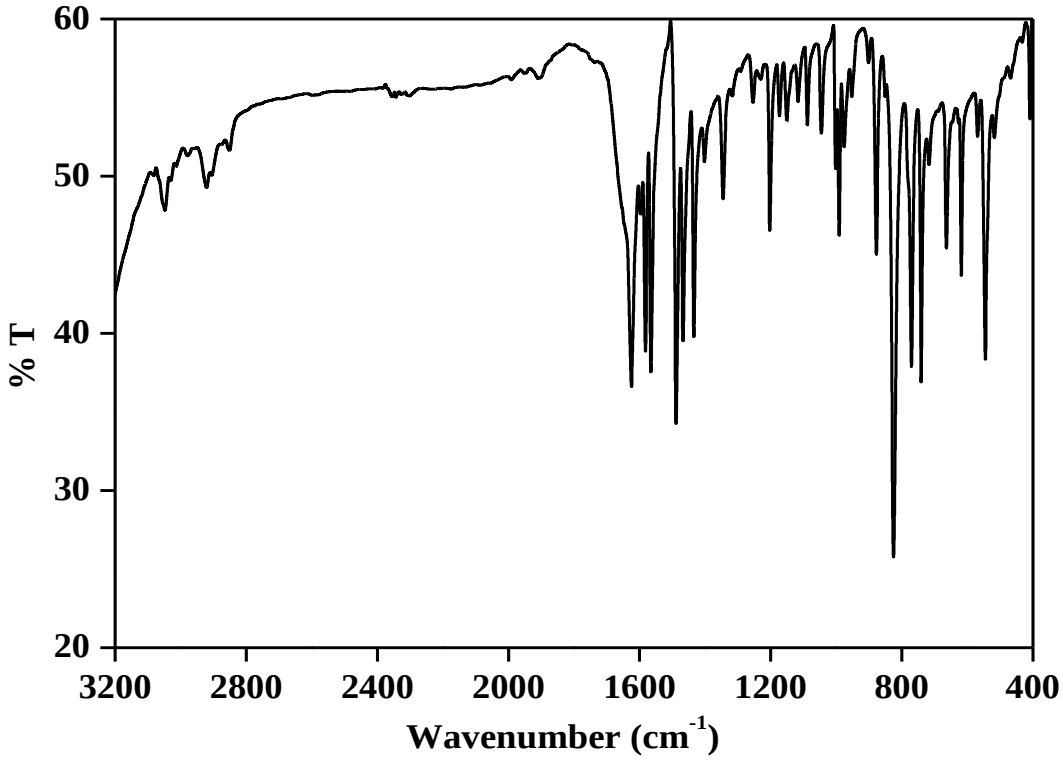

Figure 3A.1: FTIR spectrum of BENZ-Pyral

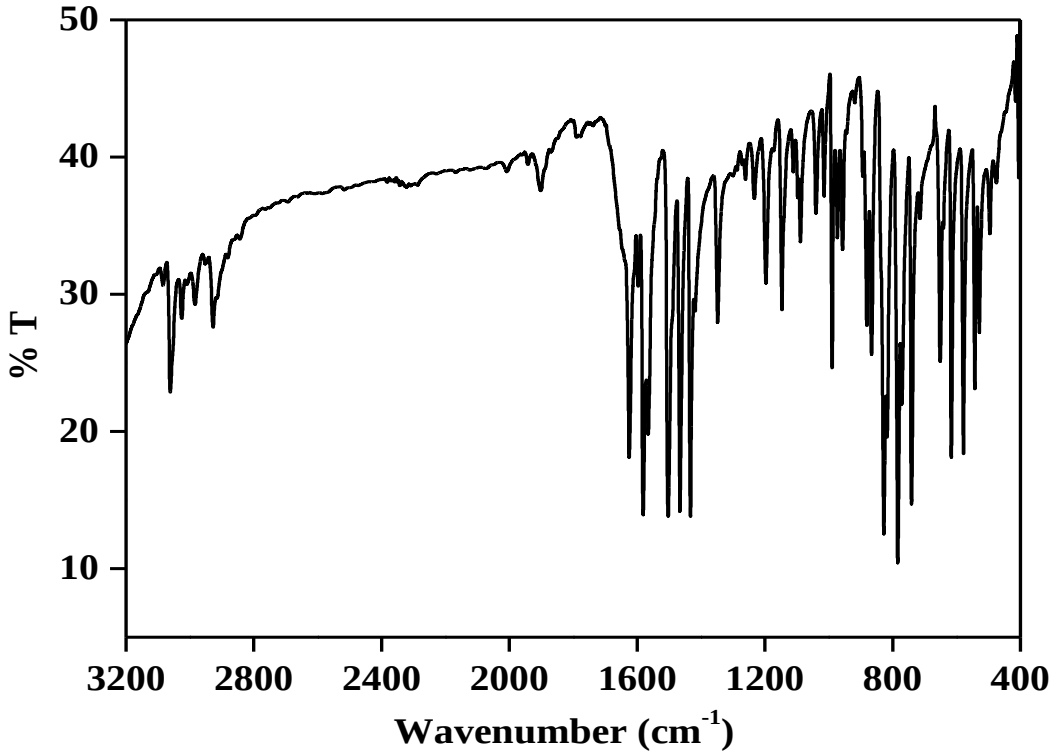

Figure 3A.2: FTIR spectrum of DADPM-Pyral

Table 3A.4: *^{1}H NMR and ^{13}C NMR spectral data of R-Pyral Schiff base ligands*

S. No.	Compound	δ ^{1}H NMR (ppm)	δ ^{13}C NMR (ppm)
1	**BENZ-Pyral**	8.77-8.59 (m, 4H), 8.34-8.17 (d, 2H), 7.91-7.77 (m, 2H), 7.75-7.62 (m, 4H), 7.51-7.36 (m, 6H).	121.6, 121.8, 125.0, 127.6, 136.5, 138.8, 149.6, 149.9, 154.4, 160.2 (HC=N).
2	**o-TOLI-Pyral**	8.73 (d, 2H), 8.59 (d, 2H), 8.29 (d, 2H), 7.92-7.78 (m, 2H), 7.55-7.47 (m, 3H), 7.42-7.32 (m, 3H), 7.16-7.06 (m, 2H), 2.47 (d, 6H).	17.9 (CH_3), 117.8, 121.5, 125.1, 128.8, 132.8, 136.4, 138.7, 149. 4, 154.7, 159.4 (HC=N).
3	**DADPM-Pyral**	8.71 (d, 3H), 8.62 (s, 3H), 8.20 (d, 3H), 7.80 (t, 4H), 7.36 (t, 4H), 4.04 (s, 3H).	40.9 (CH2), 121.2, 121.6, 124.8, 129.6, 136.4, 139.6, 148.8, 149.5, 154.5, 159.8 (HC=N)

s = singlet, d = doublet, t = triplet, m = multiplet

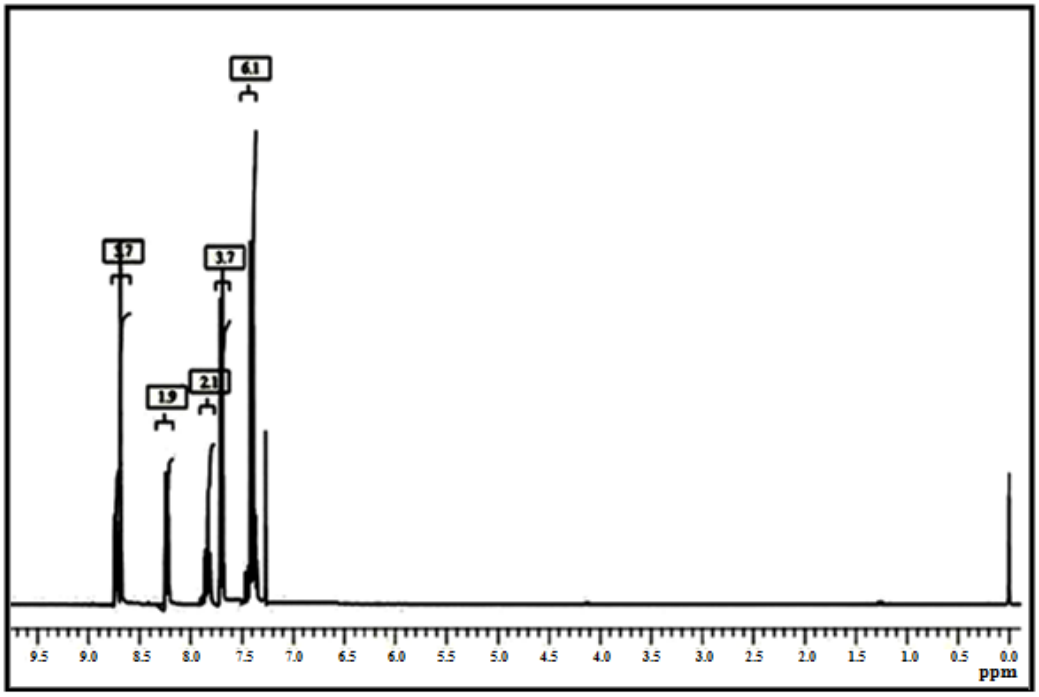

Figure 3A.3: ^{1}H NMR spectrum of BENZ-Pyral in $CDCl_3$

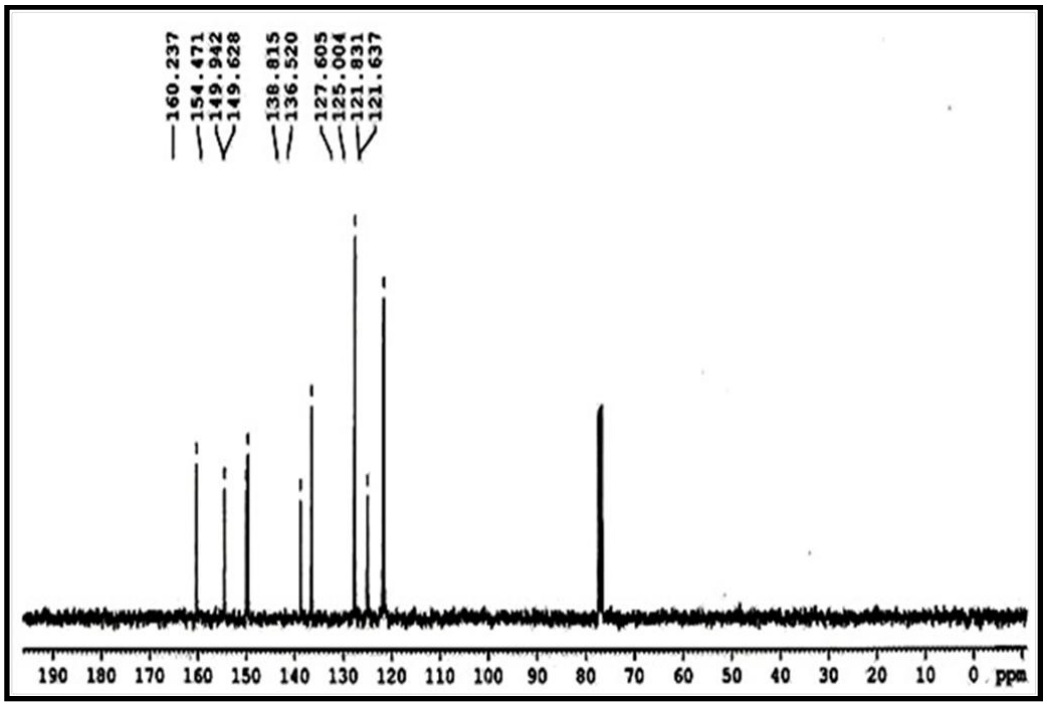

Figure 3A.4: ^{13}C NMR spectrum of BENZ-Pyral in $CDCl_3$

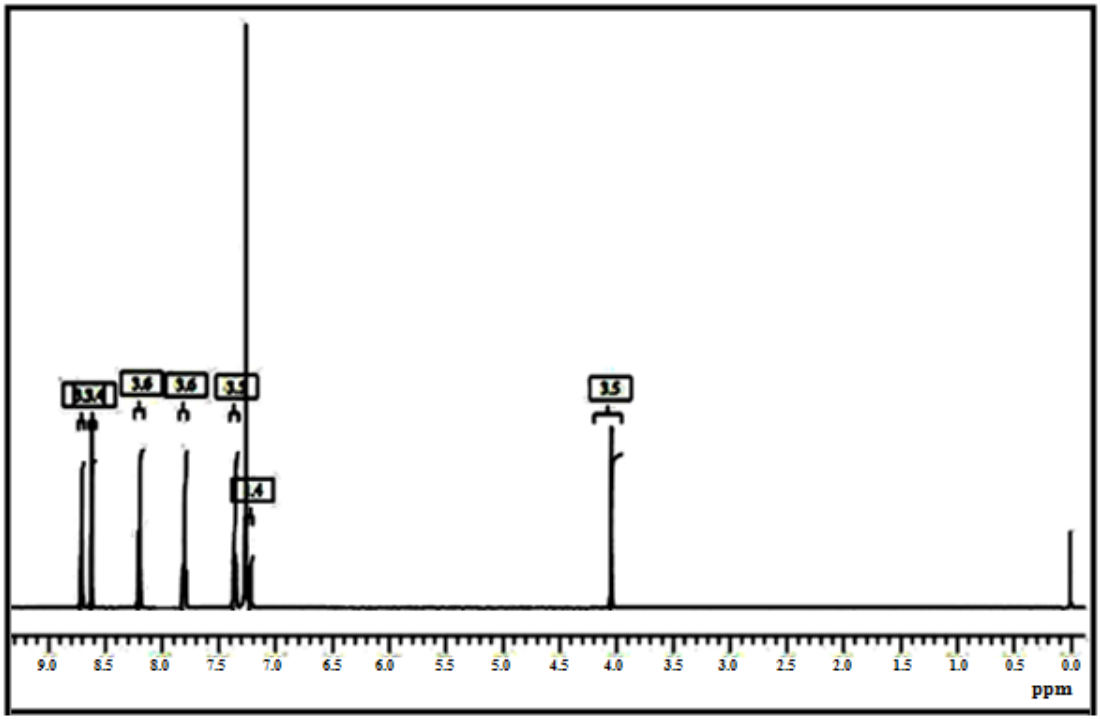

Figure 3A.5: ^{1}H NMR spectrum of DADPM-Pyral in $CDCl_3$

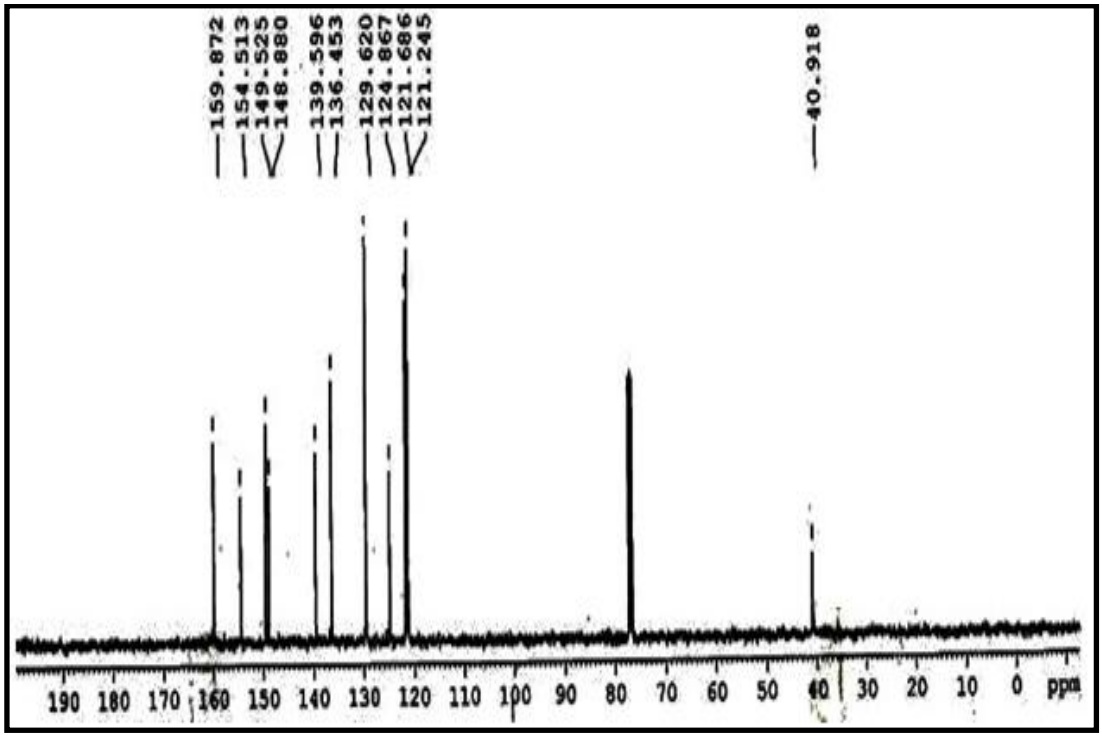

Figure 3A.6: ^{13}C NMR spectrum of DADPM-Pyral in $CDCl_3$

3A.4: Mass Spectral Studies

The electrospray ionization mass spectra (MS-ESI$^+$) of BENZ-Pyral, o-TOLI-Pyral and DADPM-Pyral have been investigated. Representative such spectra are presented in **Figures 3A.7-3A.9**. The molecular ion peaks were obtained for BENZ-Pyral, o-TOLI-Pyral and DADPM-Pyral are at [M+1], i.e. 363.1 (50.1 %), 391.1 (14.2 %) and 377.1 (7.3 %) respectively. However, from the mass spectra one can see BENZ-Pyral, o-TOLI-Pyral and DADPM-Pyral base peaks are at [M+Na], i.e. 385.1 (100 %), 413.1 (100 %) and 399.1 (100 %) respectively.

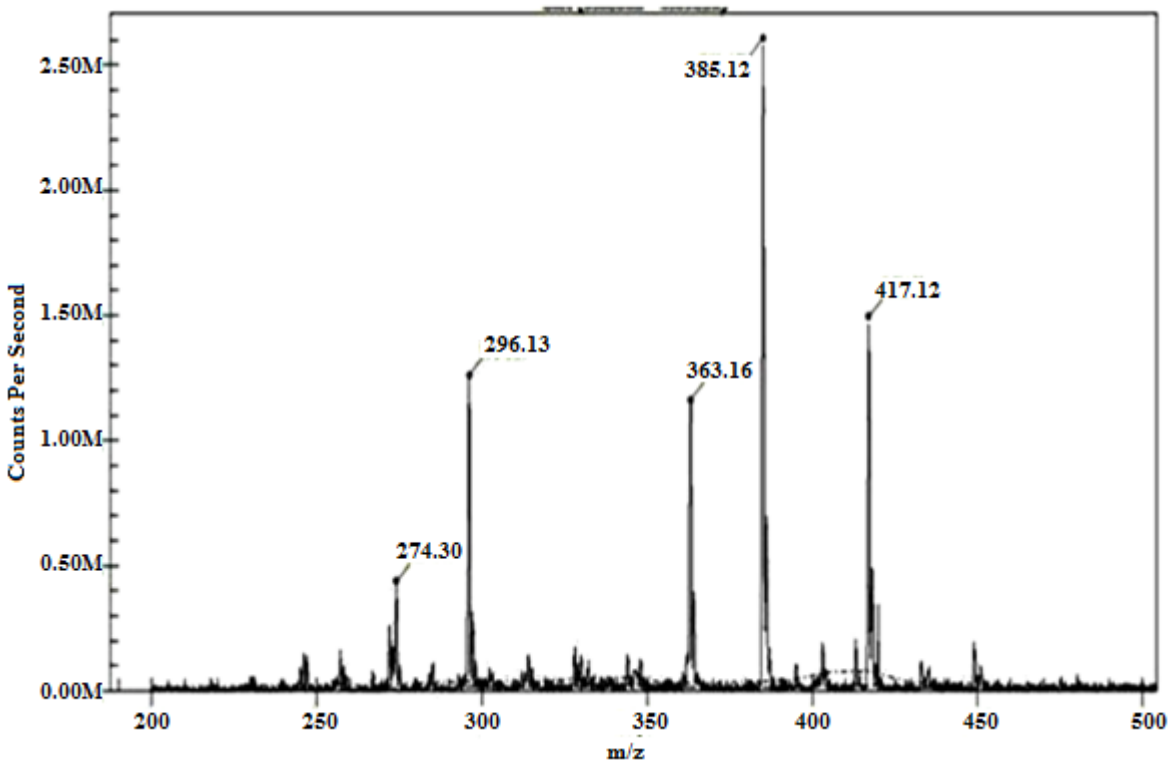

Figure 3A.7: Mass spectrum of BENZ-Pyral

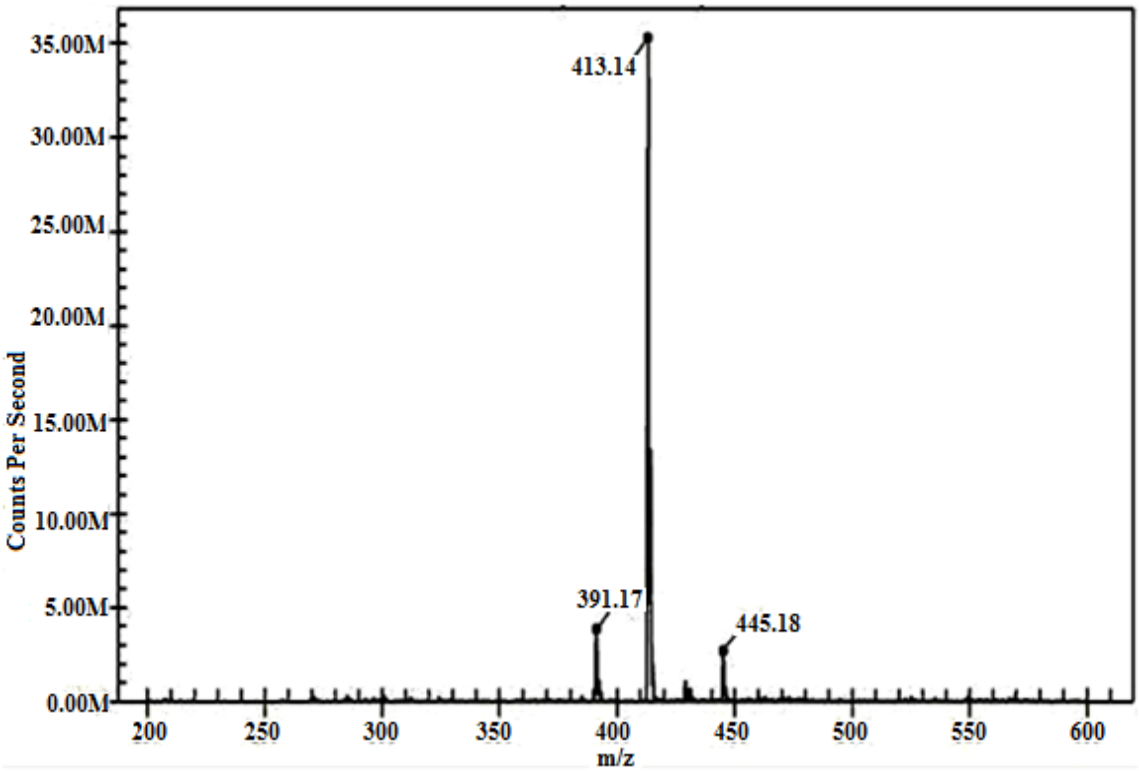

Figure 3A.8: Mass spectrum of o-TOLI-Pyral

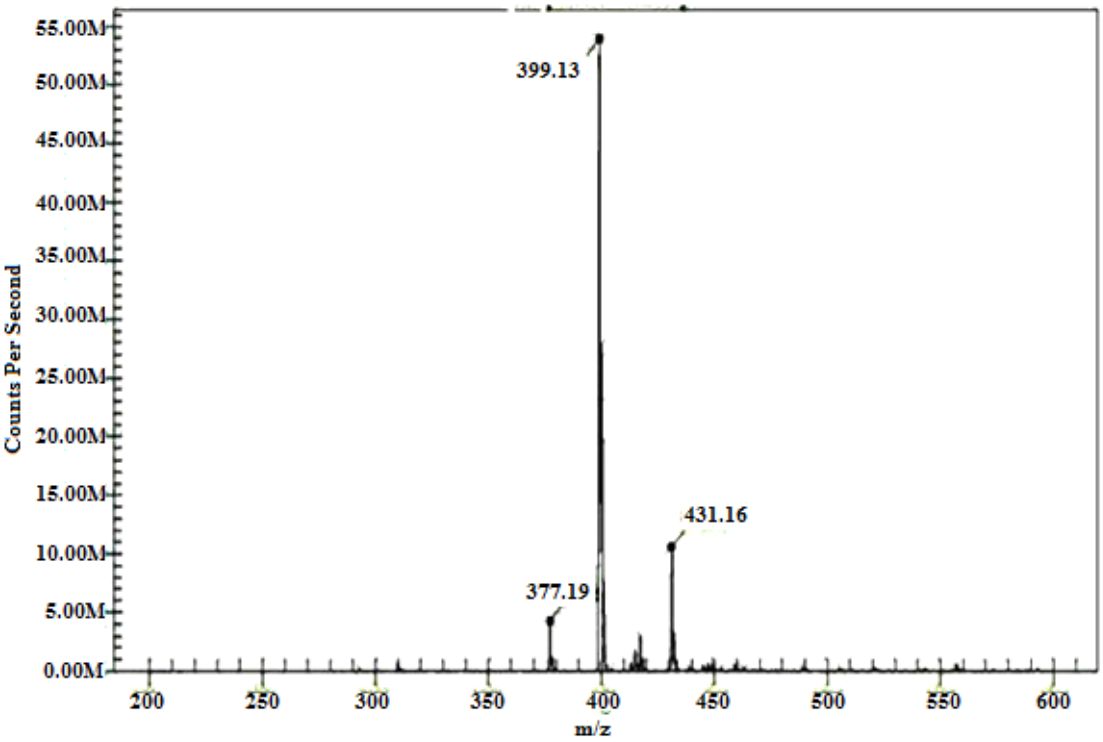

Figure 3A.9: Mass spectrum of DADPM-Pyral

3A.5: Eletcronic Spectral Studies

3A.5.1: *UV-Vis absorption spectra of R-Pyral Schiff base ligands*

The UV-Visible electronic absorption spectra of BENZ-Pyral, o-TOLI-Pyral and DADPM-Pyral are depicted in **Figures 3A.10** through **3A.12** respectively. These compound show absorption bands at 362 nm, 365 nm and 336 nm respectively (**Table 3A.3**), which are assigned to their imine (-HC=N-) $n \rightarrow \pi^*$ electronic transitions.

3A.5.2: *Fluorescence emission spectra of R-Pyral Schiff base ligands*

Pyridine-2-carboxaldimines connected to conjugated biphenyl rings are famous for fluorescence emission[34]. The R-Pyrals have been investigated by spectrofluorimetry. The fluorescence emission and electronic spectra of these compounds are shown in **Figures 3A.10-3A.12**. Some of the relevant data are collected in **Table 3A.3**. The compounds show two fluorescence emission lines, which correspond to their $n \rightarrow \pi^*$ electronic transitions at 462, 464 and 461. Further the Stokes shift values of these ligands have been calculated and given in the **Table 3A.3**. From the data, the Stokes shift energy is dissipated in the non-radiative vibrational relaxation in their excited states.

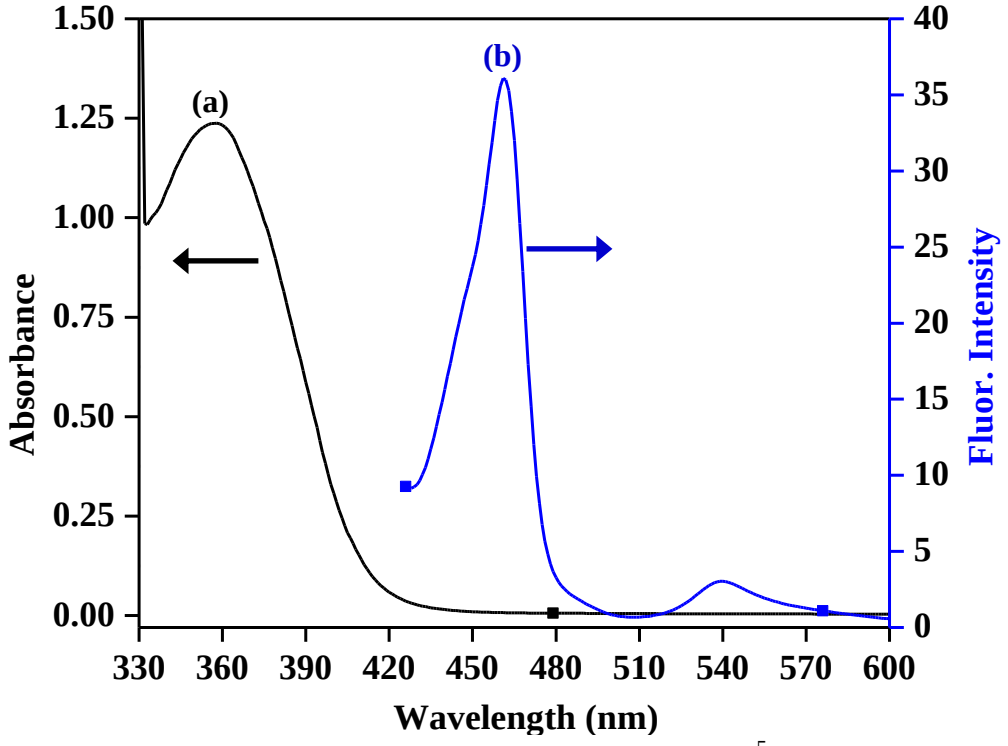

Figure 3A.10: Electronic spectra of BENZ-Pyral (1.5 x 10^{-5} M) (a) UV-Visble absorption and (b) Fluorescence emission spectra in MeOH at 365 nm excitation wavelength

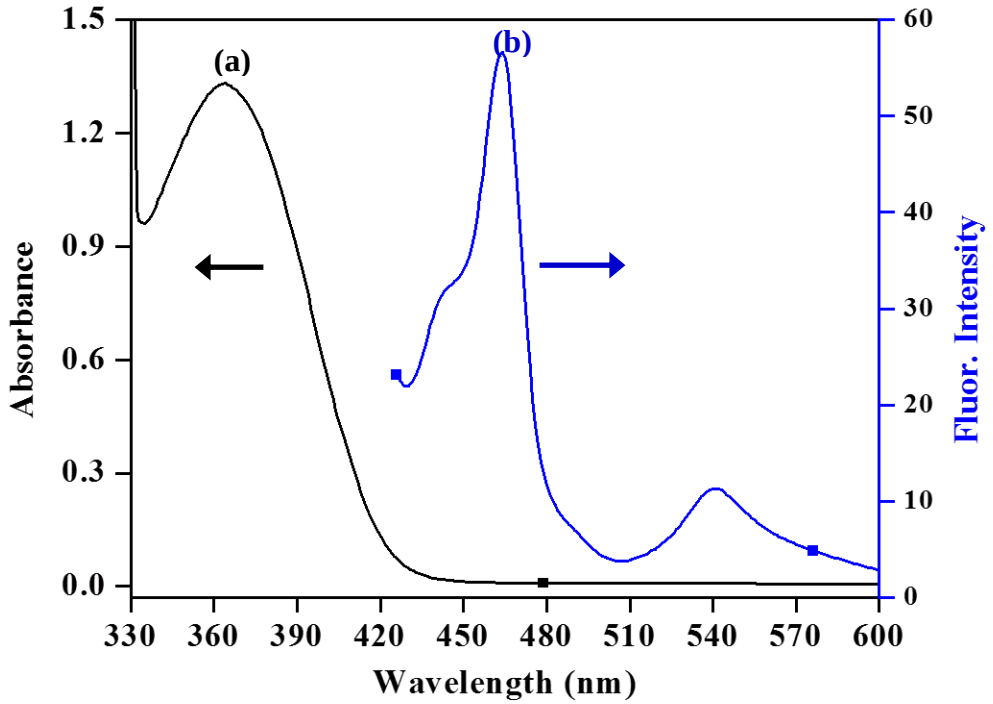

Figure 3A.11: Electronic spectra of O-TOLI-Pyral (1.5 x 10^{-5} M) (a) UV-Visble absorption and (b) Fluorescence emission spectra in MeOH at 365 nm excitation wavelength

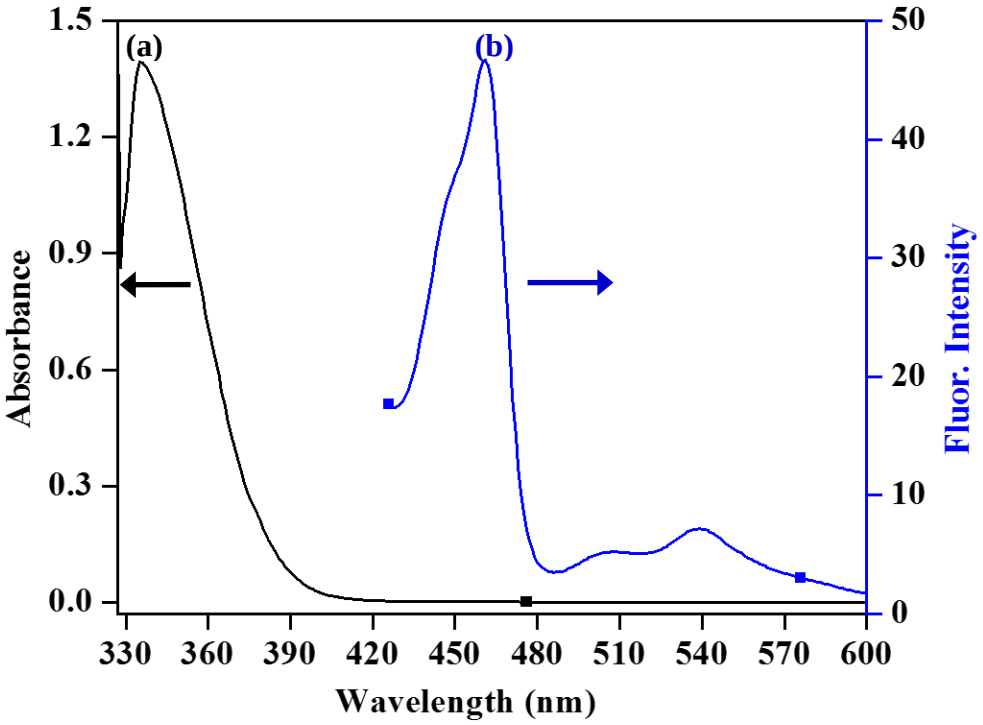

Figure 3A.12: Electronic spectra of DADPM-Pyral (1.5 x 10^{-5} M) (a) UV-Visble absorption and (b) Fluorescence emission spectra in MeOH at 365 nm excitation wavelength

3A.6: Thermal Studies

The thermal investigations of BENZ-Pyral, o-TOLI-Pyral and DADPM-Pyral have been carried out by differential scanning calorimetry (DSC). The thermograms are shown in **Figure 3A.13**. All the compounds show endothermic peaks. There is only a single endothermic peak for BENZ-Pyral, o-TOLI-Pyral and DADPM-Pyral at 178, 172 and 149 ˚C respectively in the thermal window 25-200 ˚C. These endothermic peaks are assigned to the melting events of these ligands. The thermal data such as melting point and heat of enthalpy of these compounds are presented in **Table 3A.5**.

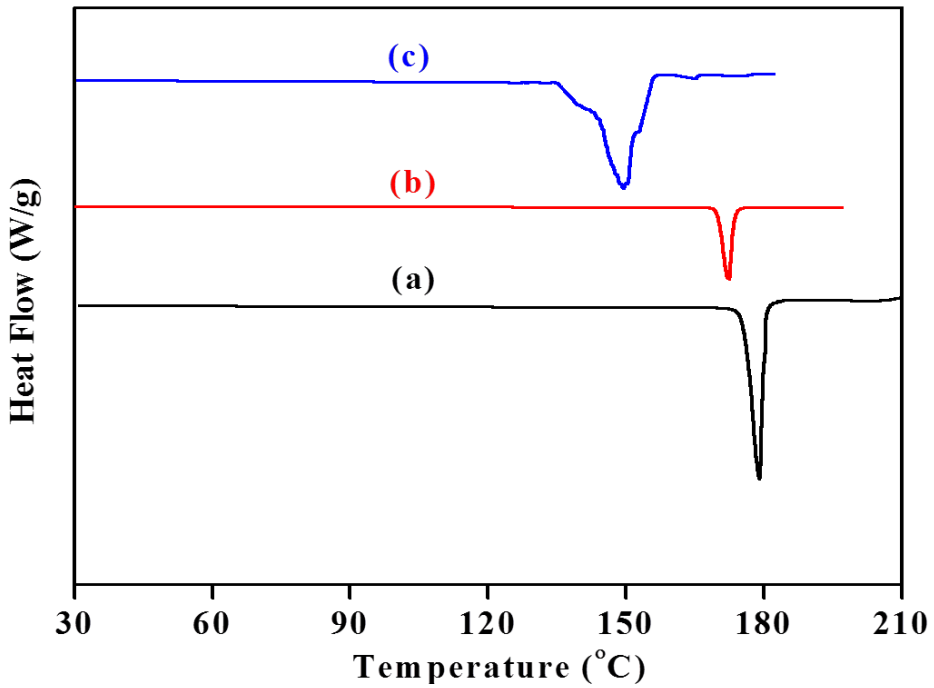

Figure 3A.13: Differential scanning calorigrams (a) BENZ-Pyral (b) o-TOLI-Pyral and (c) DADPM-Pyral

Table 3A.5: *Differential scanning calorimetry data of R-Pyral Schiff base ligands*

S.No.	Compound	Melting point (°C)	ΔH (kJ mol^{-1})
1	**BENZ-Pyral**	178	15.00
2	**o-TOLI-Pyral**	172	9.15
3	**DADPM-Pyral**	149	14.32

3A.7: Electrochemical Studies

The electron transfer properties of the ligands were studied in DMF with tetraethyl ammonium perchlorate (TEAP) as the supporting electrolyte. A typical cyclic voltammogram of o-TOLI-Pyral, obtained in the anodic region on GCE, is presented in **Figure 3A.14**. An irreversible peak at -0.30 V (SCE) is noticed in the anodic region. Futher, the corresponding data of the compounds are collected and presented in **Table 3A.6** and appropriate electron transfer mechanism is given in **Scheme 3.1**[4].

Anodic

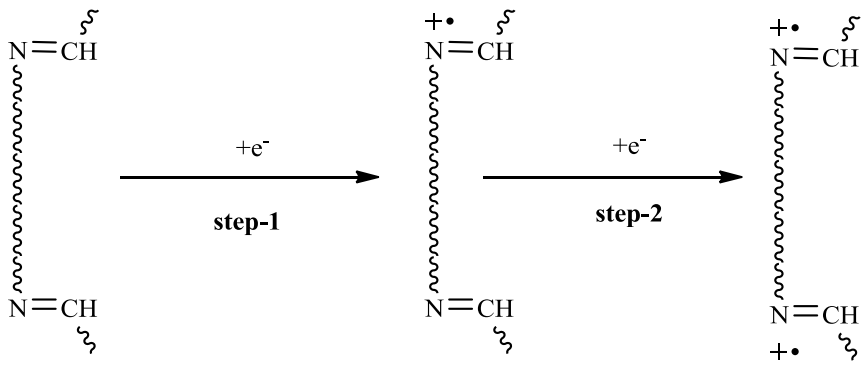

Scheme 3.1

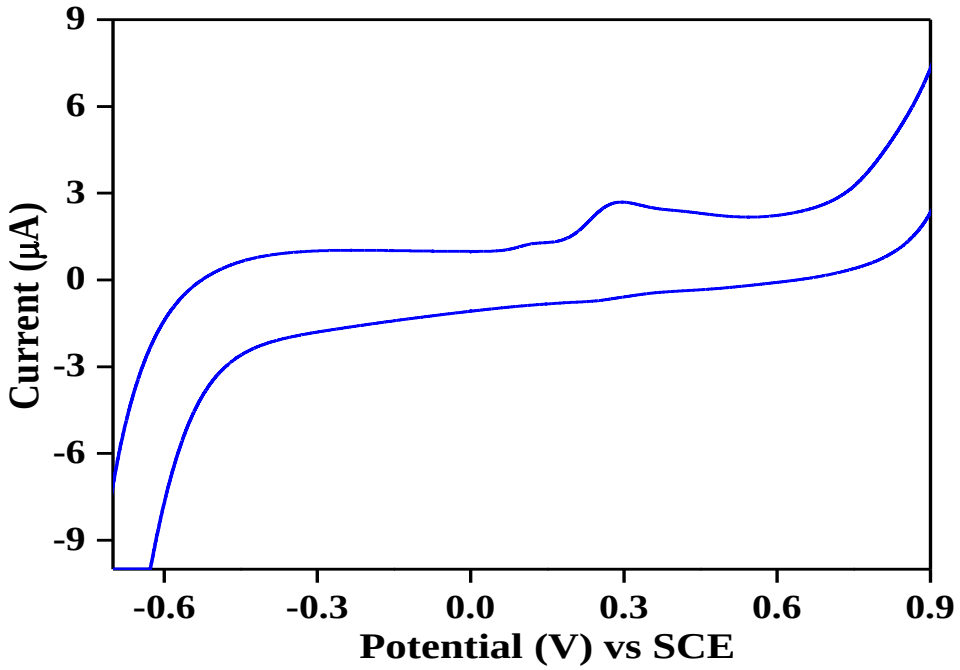

Figure 3A.14: Cyclic voltammogram of o-TOLI-Pyral in DMF on GCE at scan rate, 100 mVs^{-1}, with TEAP (0.1 M)

Table 3A.6: *Voltammetric data of R-Pyral Schiff base ligands*

S.No.	Compound	E_{pa} (V)	i_{pa}(μA)
1	**BENZ-Pyral**	0.28	2
2	**o-TOLI-Pyral**	0.34	3
3	**DADPM-Pyral**	0.31	3

3A.8: Coordination Chemistry Studies

Holding 2 donor –nitrogen atoms in a vantage position at each side of the biphenyl skeleton, the R-Pyrals would serve as binucleating (bidentate each site) and tetra dentate ligands[5,6]. Due to lack of labile protons on them, their complexes with metal ions would have to be also cationic complexes[7–9]. The physical and analytical data of the complexes of R-Pyral are given in **Table 3A.7**. Analytical data obtained are consistent with the proposed tetra dentate binuclear structure shown in **3.2**.

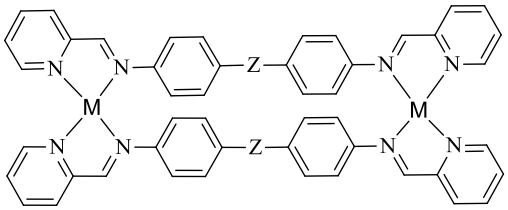

Z= O, $-CH_2-$ and NIL, X = H, CH_3 and OCH_3
M = Co (II), Ni (II), Cu (II) and Zn (II)

3.2 (M_2(R-Pyral)$_2$)

Z	X	Row combination labeled as M_2(R-Pyral)$_2$
$-CH_2-$	-H	M_2(DADPM-Pyral)$_2$
-	$-CH_3$	M_2(o-TOLI-Pyral)$_2$
-	-H	M_2(BENZ-Pyral)$_2$

Table 3A.7: *Physical characterization, analytical, molar conductance and magnetic susceptibility data of complexes*

S. No.	*Compound*	Content (Found/Cal.)*				$^{\#}\Lambda_M$ x 10^{-3}	Magneti moment μ_{eff} (BM)
		% M[a]	% C	% H	% N		
1	$[Co_2(BENZ\text{-}Pyral)_2]Cl_4$	12.8701 (12.8709)	59.10 (59.21)	3.56 (3.27)	11.28 (11.39)	17	4.34
2	$[Ni_2(BENZ\text{-}Pyral)_2]Cl_4$	11.9703 (11.9712)	60.20 (60.11)	3.65 (3.81)	11.60 (11.25)	22	2.79

3	$[Cu_2(BENZ\text{-}Pyral)_2]Cl_4$	12.1127 (12.1121)	59.52 (59.41)	3.92 (4.03)	12.01 (11.79)	38	1.72
4	$[Zn_2(BENZ\text{-}Pyral)_2]Cl_4$	12.6746 (12.6741)	58.89 (58.77)	3.77 (3.55)	12.51 (12.29)	31	-
5	$[Co_2(O\text{-}TOLI\text{-}Pyral)_2]Cl_4$	12.2708 (12.2712)	59.02 (58.89)	3.58 (3.37)	11.33 (11.71)	12	4.61
6	$[Ni_2(O\text{-}TOLI\text{-}Pyral)_2]Cl_4$	12.0393 (12.0398)	60.11 (60.29)	3.61 (3.83)	11.57 (11.27)	19	2.88
7	$[Cu_2(O\text{-}TOLI\text{-}Pyral)_2]Cl_4$	12.1323 (12.1317)	59.42 (59.67)	3.90 (4.07)	12.31 (12.15)	31	1.71
8	$[Zn_2(O\text{-}TOLI\text{-}Pyral)_2]Cl_4$	12.7661 (12.7659)	58.81 (58.64)	3.71 (3.91)	12.41 (12.64)	27	-
9	$[Co_2(DADPM\text{-}Pyral)_2]Cl_4$	12.7557 (12.7550)	59.61 (59.73)	3.51 (3.76)	11.17 (11.35)	14	4.53
10	$[Ni_2(DADPM\text{-}Pyral)_2]Cl_4$	11.9917 (11.9907)	60.15 (60.31)	3.73 (3.47)	11.47 (11.17)	17	2.84
11	$[Cu_2(DADPM\text{-}Pyral)_2]Cl_4$	12.2715 (12.2721)	59.25 (59.04)	3.81 (3.65)	12.11 (11.91)	34	1.70
12	$[Zn_2(DADPM\text{-}Pyral)_2]Cl_4$	12.8597 (12.8593)	58.47 (58.71)	3.63 (3.82)	11.62 (11.87)	32	-

*, data in parenthesis are calculated ones

a, metal percentage calculated from ICPOES

#, mho cm^2 mol^{-1}

3A.8.1: *Infrared spectral studies*

The FTIR spectra of these metal complexes have been recorded and corresponding data are given in **Table 3A.8**. The spectra of the ligands display sharp peaks characteristics of the C=N bond at 1630-1620 cm^{-1}. The complexes show a shift to lower frequency (1601-1615 cm^{-1}) in comparison to the corresponding R-Pyrals. This is due to the coordination of the imino nitrogen to the metal ion. The band for the complexes in the region 430-485 cm^{-1} is ascribed to the M-N bonds. All the IR data suggest that metal is bonded to the azomethine (>C=N-) group through pyridine and imine nitrogen.

Table 3A.8: *Important IR spectral frequencies of Co(II), Ni(II), Cu(II) and Zn(II) complexes*

S.No.	Compound	IR frequencies[a] (cm^{-1})			
		$\nu_{(C-H)}$	$\nu_{(C=N)}$	$\nu_{(C-N)}$	$\nu_{(M-N)}$
1	$[Co_2(BENZ\text{-}Pyral)_2]Cl_4$	3026	1607	1651	431
2	$[Ni_2(BENZ\text{-}Pyral)_2]Cl_4$	3028	1603	1645	436
3	$[Cu_2(BENZ\text{-}Pyral)_2]Cl_4$	3031	1604	1647	435
4	$[Zn_2(BENZ\text{-}Pyral)_2]Cl_4$	3029	1606	1652	433
5	$[Co_2(O\text{-}TOLI\text{-}Pyral)_2]Cl_4$	3024	1616	1642	467
6	$[Ni_2(O\text{-}TOLI\text{-}Pyral)_2]Cl_4$	3025	1613	1635	471
7	$[Cu_2(O\text{-}TOLI\text{-}Pyral)_2]Cl_4$	3027	1614	1638	476
8	$[Zn_2(O\text{-}TOLI\text{-}Pyral)_2]Cl_4$	3029	1617	1634	473
9	$[Co_2(DADPM\text{-}Pyral)_2]Cl_4$	3030	1605	1645	457
10	$[Ni_2(DADPM\text{-}Pyral)_2]Cl_4$	3028	1611	1648	453
11	$[Cu_2(DADPM\text{-}Pyral)_2]Cl_4$	3026	1615	1650	459
12	$[Zn_2(DADPM\text{-}Pyral)_2]Cl_4$	3031	1612	1649	451

a, collected in KBr disc

3A.8.2: *UV-Visible absorption spectral studies*

Electronic absorption spectra of pyridine-2-carboxaldimines metal complexes are recorded in aqueous medium. A typical electronic spectra of $[Cu_2(BENZ\text{-}Pyral)_2]Cl_4$ is shown in **Figure 3A.15**. The Cu(II) complexes exhibit a intensity bands around 700 in the visible region, which is attributed to the d-d transition. Based on the electronic spectra of Cu(II) complexes, it is found these complexes exhibit three spin allowed transitions, viz., $2B_{1g}\rightarrow 2A_{1g}$ ($d_{x^2-y^2}\rightarrow d_{z^2}$), $2B_{1g}\rightarrow 2B_{2g}$ ($d_{x^2-y^2}\rightarrow d_{xy}$), $2B_{1g}\rightarrow 2E_g$($d_{x^2-y^2}\rightarrow d_{xz}$), expected for square-planar complexes. The complexes of Co(II) have shown three bands due to $4T_{1g}(F)\rightarrow 4T_{2g}(F)$, $4T_{1g}(F)\rightarrow 4T_{2g}(P)$ and $4T_{1g}(F)\rightarrow 4A_{2g}(F)$. The complexes of Ni(II) also

show three bands due to $1A_{1g}(F) \rightarrow 1A_{2g}(F)$, $4T_{1g}(F) \rightarrow 4T_{2g}(P)$, $4T_{1g}(F) \rightarrow 4A_{2g}(F)$. Further, the moderately intense broad band of Zn(II) complexes is assigned to the N→Zn(II) ligand to metal charge transfer. Relevant electronic spectral data of these complexes are collected into **Table 3A.9**.

Table 3A.9: *Electronic spectral data of Co(II), Ni(II), Cu(II) and Zn(II) complexes*

S.No.	Complex	Electronic data in H_2O λ_{max} ($\bar{\nu}$)(∈)[a]
1	$[Co_2(BENZ\text{-}Pyral)_2]Cl_4$	692 (14450), (44,650)
2	$[Ni_2(BENZ\text{-}Pyral)_2]Cl_4$	694 (14,409) (47,750)
3	$[Cu_2(BENZ\text{-}Pyral)_2]Cl_4$	697 (14, 347)(60,601)
4	$[Co_2(O\text{-}TOLI\text{-}Pyral)_2]Cl_4$	701(14, 265)(39,968)
5	$[Ni_2(O\text{-}TOLI\text{-}Pyral)_2]Cl_4$	703(14,224)(43,670)
6	$[Cu_2(O\text{-}TOLI\text{-}Pyral)_2]Cl_4$	705(14,184)(53,421)
7	$[Co_2(DADPM\text{-}Pyral)_2]Cl_4$	681(14,684)(51,201)
8	$[Ni_2(DADPM\text{-}Pyral)_2]Cl_4$	685(14,598)(53,207)
9	$[Cu_2(DADPM\text{-}Pyral)_2]Cl_4$	688(14,534)(67,314)

a, λ_{max} (in nm), $\bar{\nu}$ (in cm^{-1}), ∈ (lit. mol^{-1}. cm^{-1})

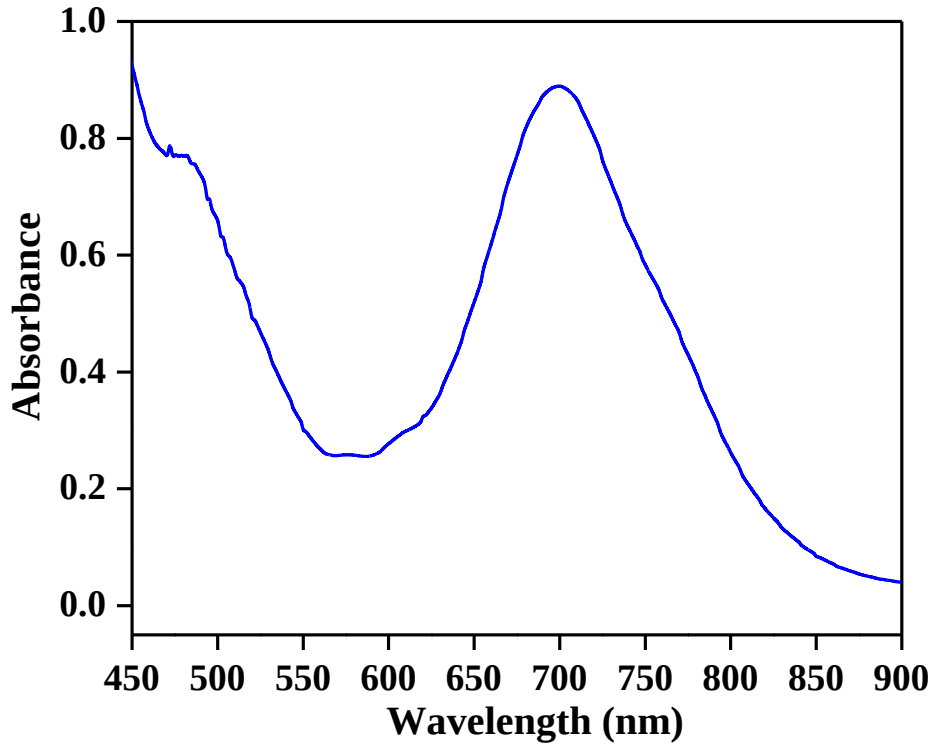

Figure 3A.15: Electronic spectra of $[Cu_2(BENZ\text{-}Pyral)_2]Cl_4$ (1.5 x 10^{-4}M) in water

3A.8.3: ***Jobs monovariation studies***

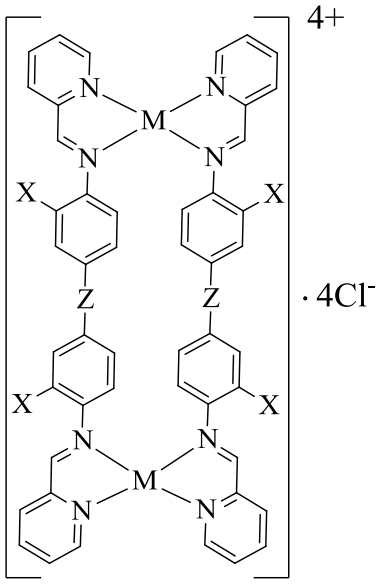

Scheme 3.2

Z = NIL, -O-, CH_2,
X = H, CH_3 and OCH_3,
M = Co(II), Ni(II),
Cu(II) and Zn(II)

In order to ascertain the metal to ligand stoichiometry Jobs plots were taken for the complexation[10,11]. The overlay UV-Visible electronic absorption spectra of Cu(II) metal ion solution, o-TOLI-Pyral and mixture of equimolar concentration of Cu(II) and o-TOLI-Pyral solutions are presented in **Figure 3A.16**. From the spectra one can see the Cu_2(o-TOLI-Pyral)$_2$ complex exhibits a clear high intensity band in visible region at 705 nm. Appearance of this band is ascribed to the n→π^* transition associated with the azomethine ion-dipole supramolecular interaction and L→M charge transfer. The Co(II), Ni(II), Cu(II) and Zn (II) complex may be subjected to the geometry is square planar similar to the porphyrins MN_4 structure.

However, the stoichiometric ratio of metal to ligand is calculated from the Jobs monovariation plot, which is shown in **Figure 3A.17**. The metal precursor used for the complexation is bivalent metal chloride salts of cobalt, nickel, copper and zinc. The presence of Cl^- ions outside the coordination sphere confirmed by the $AgNO_3$ test where Cl^- ions are precipitated as AgCl. From these observation, appropriate metal complex structure for these biphenyl bridged Schiff base metal complexes are given in **Scheme 3.2**. Hence, the stoichiometric ratio of metal to ligand suggested as 1:1 and the metal complexes are cationic nature where the biphenyl bridged Schiff base ligands in ligation with metal ions through tetra dentate nitrogen atoms. The four Cl^- ions are laying outside the ionic sphere as counter ions.

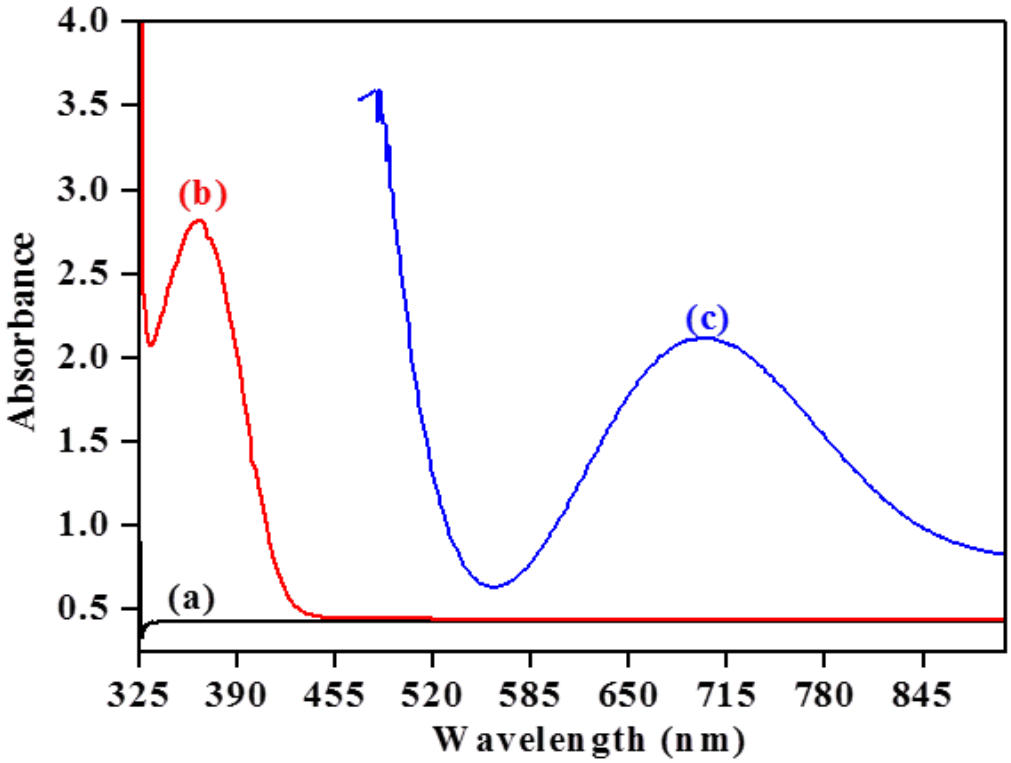

Figure 3A.16: Electronic spectra of (a) Cu(II) (b) o-TOLI-Pyral (c) complex of $[Cu_2(o\text{-}TOLI\text{-}Pyral)_2]Cl_4$

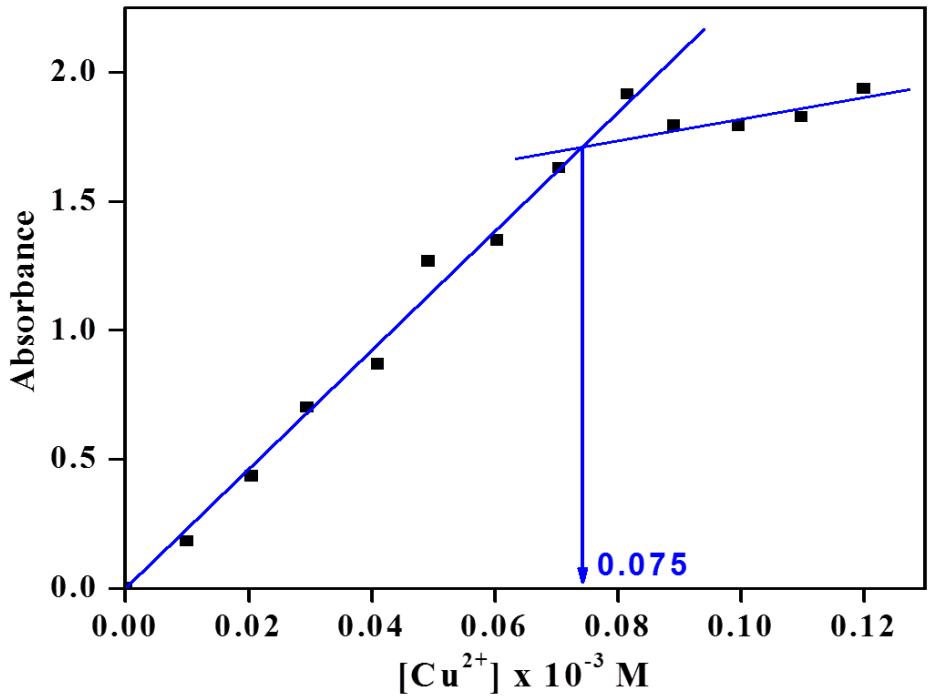

Figure 3A.17: Job's plot at 705 nm for the complexation of Cu^{2+} with DADPM-Pyral.

3A.8.4: ***Conductometric and magnetic susceptibility studies***

Based on the Job's monovariation plot and $AgNO_3$ test, it is clear that the metal complexes are ionic complexes. Further, conductometric analysis has been undertaken on these metal complexes. A typical conductometric titration of Cu(II) versus o-TOLI-Pyral is depicted in **Figure 3A.18**. The conductometric titration studies also confirm that metal to ligand stoichiometric ratio is 1:1 which is in good agreement with Job's monovariation method. The molar conductance values of these metal complexes are presented in **Table 3A.7**.

The magnetic dipole moments of the metal complexes of Co(II), Ni(II) and Cu(II) measured at room temperature are listed in **Table 3A.7**. The Co(II) and Ni(II) complexes show magnetic moment values around 4.6 and 2.8 BM, which are lower than the corresponding spin only values. This indicates a weak antiferromagnetic coupling interaction between the metal ions, which further support the dinuclear nature of metal complexes. The Cu(II) complexes have shown a magnetic moment around 1.70 BM, which is slightly lower than the spin only value.

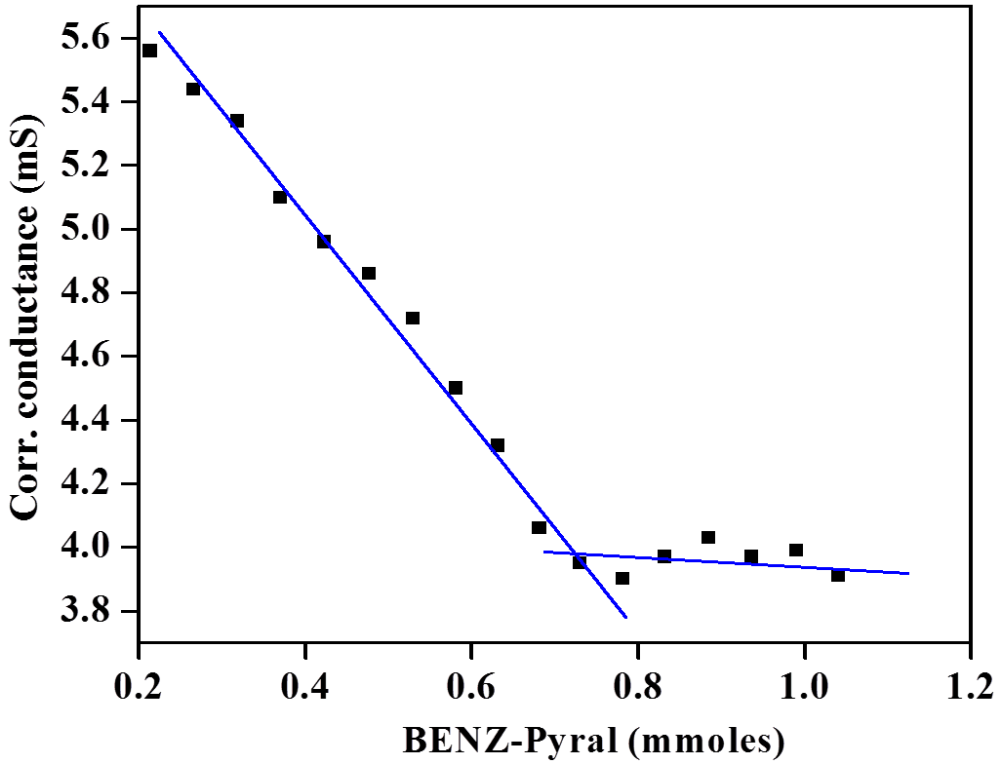

Figure 3A.18: Conductometric titration of Cu(II) versus BENZ-Pyral

3A.8.5: ***ICP-OES analysis R-Pyral Schiff base metal complexes***

In order to ascertain the metal percentage of R-Pyral Schiff base metal complexes, ICP-OES analysis has been carried out. A series of stock solutions of Co(II), Ni(II), Cu(II) and Zn (II) are prepared from the Agilent ICP-OES multi-standard solution in 5% HNO_3 aqueous medium. The calibration plots are shown in **Figure 3A.19** and corresponding data of Co (II), Ni(II), Cu(II) and Zn(II) are given in **Table 3A.10**.

Table 3A.10: *ICP-OES analysis of Co(II), Ni(II), Cu(II) and Zn(II) complexes*

S.No.	Concentration (ppm)	Cobalt (CPS) 238.893[a]	Nickel (CPS) 231.604[a]	Copper (CPS) 324.754[a]	Zinc (CPS) 213.856[a]
1	0	630	596	652	456
2	4	2.67×10^5	3.31×10^5	2.95×10^5	2.79×10^5
3	8	4.87×10^5	6.12×10^5	5.76×10^5	5.14×10^5
4	12	6.57×10^5	8.43×10^5	7.91×10^5	8.01×10^5
5	16	8.73×10^5	11.70×10^5	10.07×10^5	9.78×10^5

a, data collected at the wavelength in nm

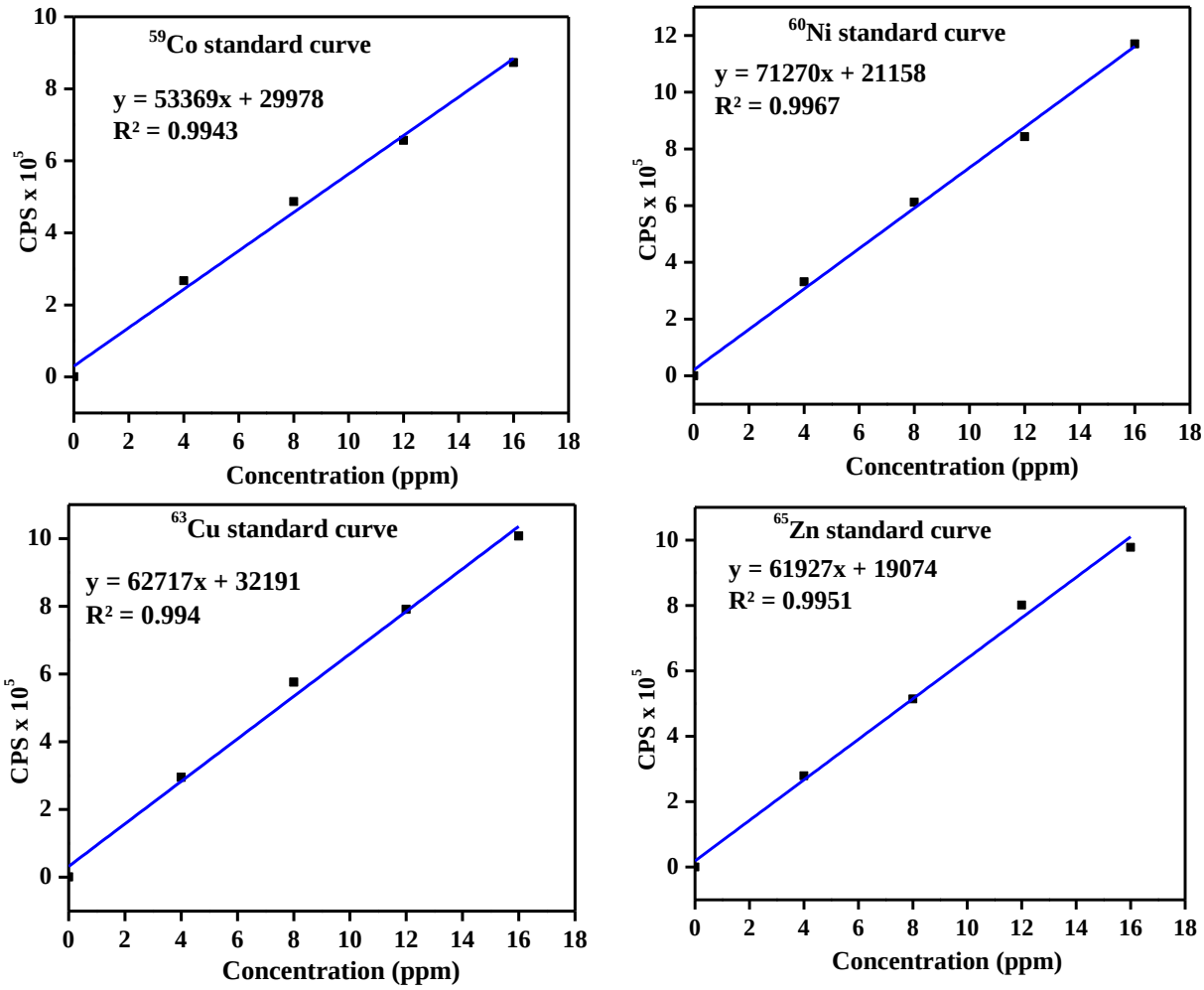

Figure 3A.19: ICP-OES calibration curves of Co(II), Ni(II), Cu(II) and Zn(II)

3A.8.6: *ESR spectral studies*

The X-band powder ESR spectra of Cu(II) metal complexes show a strong absorption signal at g ~2.12. The complexes even after considerable freezing didn't give any changes in hyperfine splitting pattern. The frozen glass esr spectra of the complexes are presented in **Figures 3A.20 - 3A.22**. Relevant esr data of the complexes are presented in **Table 3A.11**. Further, the $A_{\parallel}$ and $A_{\perp}$ values are determined by taking one third of the line widths at half maximum while A_o values are calculated from the relation $A_o = 1/3\ (A_{\parallel} + 2A_{\perp})$. In general, the deviation from the square planar geometry towards tetrahedral the A_o values will be lowered by nearly three times from those of perfect square planar copper (II)

complexes. A_o value for tetrahedral geometry is of the order of 45 G (40 x 10^{-4} cm^{-1}). The observed A_o values, in the present series of Cu(II) complexes are ~ 35 G. There are a series of pseudo tetrahedral complexes which do not exhibit any hyperfine esr splitting pattern in solution[12]. The absence of the splitting in solution even at liquid nitrogen (frozen glass) temperature is due to dipolar line broadening[13]. Due to the same effect the A_o value is further reduced in the present Schiff base complexes. The above observation supports that the geometry around copper can best be described as slightly distorted square planer as predicted from the electronic spectral data.

Table 3A.11: *ESR spectra data of Cu (II) complexes*

S. No.	Complex	$g_{\parallel}$	$g_{\perp}$	g_o	$A_{\parallel}$	$A_{\perp}$	A_o
1	$[Cu_2(BENZ\text{-}Pyral)_2]Cl_4$	2.10	2.12	2.13	5.7	3.4	4.2
2	$[Cu_2(O\text{-}TOLI\text{-}Pyral)_2]Cl_4$	2.09	2.15	2.16	5.8	3.6	4.3
3	$[Cu_2(DADPM\text{-}Pyral)_2]Cl_4$	2.12	2.13	2.13	5.8	3.3	4.1

a, $g_o = 1/3\ (g_{\parallel} + 2g_{\perp})$ and $A_o = 1/3\ (A_{\parallel} + 2A_{\perp})$

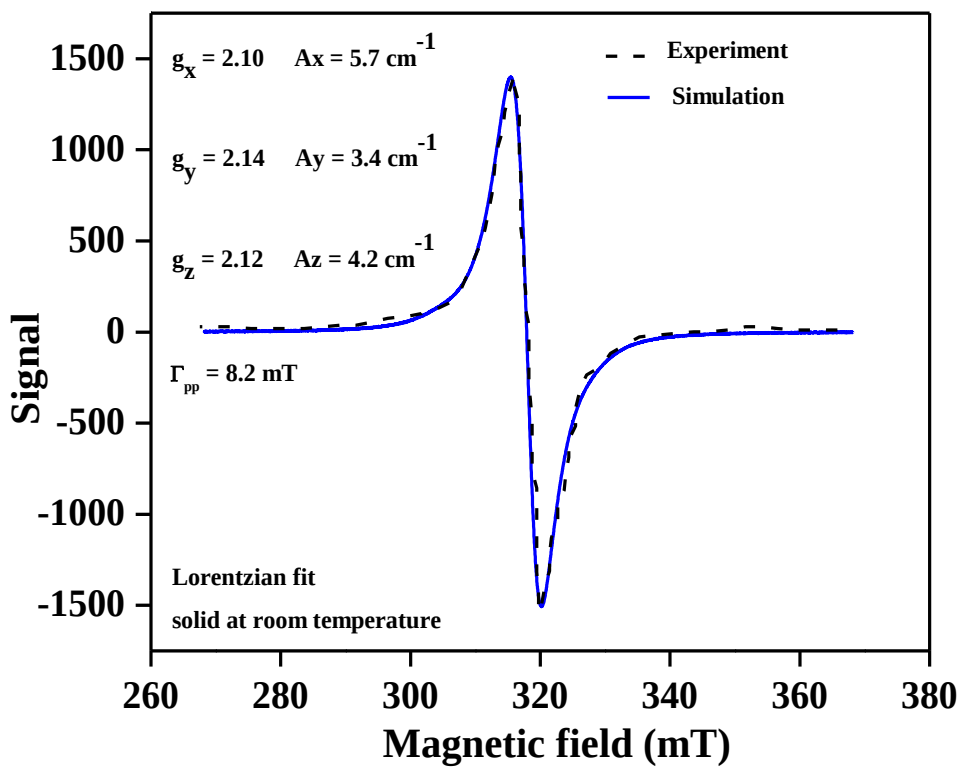

Figure 3A.20: Frozen glass EPR spectrum of $[Cu_2(BENZ\text{-}Pyral)_2]Cl_4$

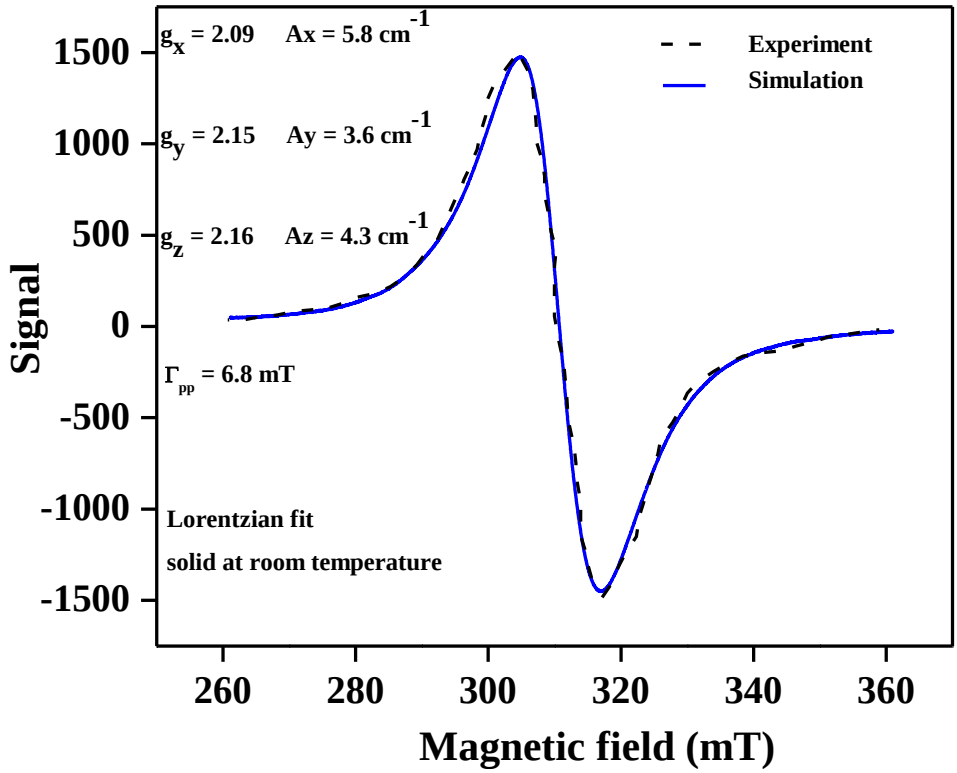

Figure 3A.21: Frozen glass EPR spectrum of $[Cu_2(O\text{-}TOLI\text{-}Pyral)_2]Cl_4$

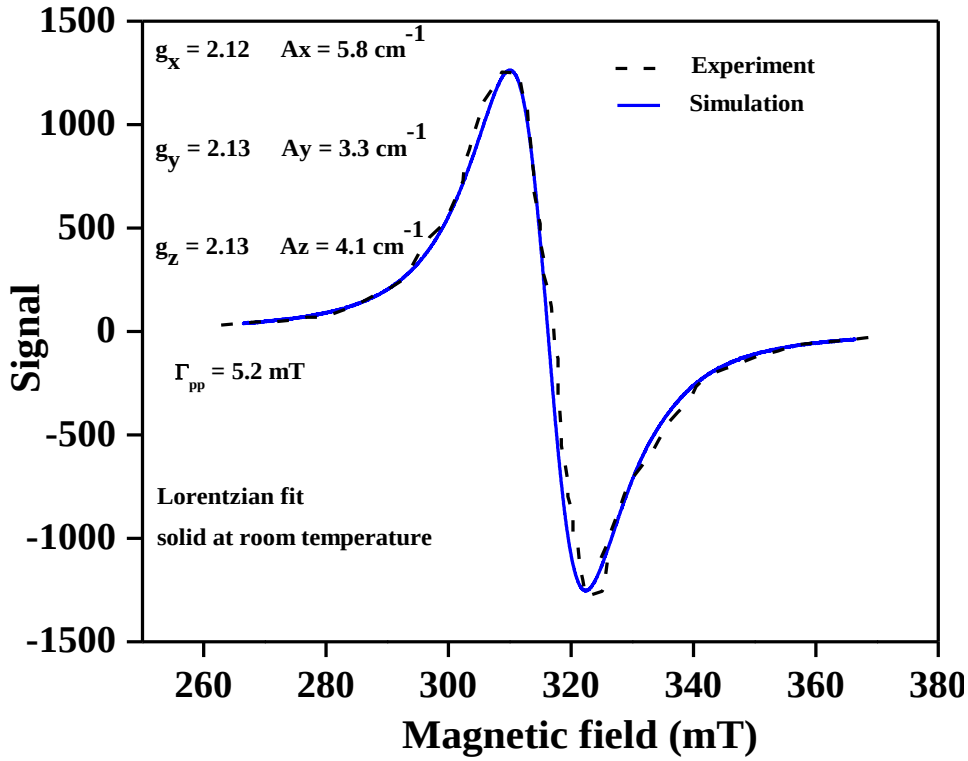

Figure 3A.22: Frozen glass EPR spectrum of $[Cu_2(DADPM\text{-}Pyral)_2]Cl_4$

PART B: KINETICS OF HYDROLYSIS OF o-TOLI-PYRAL

The imine site, >C=N-, is well known for its hydrolytic cleavage as >C=N- + H_2O → -CHO + H_2N- under suitable conditions. The mechanism of vision is now known to associate with the hydrolysis of azomethine group of the biochemical Schiff bases in the retinal layers. A great deal of chemical research is being carried out all over the world on the kinetics of hydrolysis of different kinds of compounds including Schiff bases. This Part is describes the studies of kinetics of hydrolysis of one of biphenyl Schiff base o-TOLI-Pyral as a function of temperature in aqueous methanol media. The kinetics were monitored by both spectral and voltammetric means.

3B.1: UV - Visible Absorption Spectral Studies

The studies of kinetics of hydrolysis of two azomethine sites in o-TOLI-Pyral have been investigated in aqueous methanol/water 1:9 (v/v) mixture by electronic absorption spectral studies. Time-shifted repetitive spectra of the o-TOLI-Pyral at two temperatures, separated by about 10 K are shown in **Figures 3B.1 – 3B.2**. It is observed that the last spectrum (infinite) resembles the mathematical sum of the spectra of the o-Tolidine and 2-pyridine carboxaldehyde recorded separately for equivalent stoichiometric concentrations. **Figure 3B.3** shows the photometric response of o-TOLI-Pyral with time at 365 nm for four selected temperatures. The plots of ln $([A_t - A_{inf}]/[A_0 - A_{inf}])$ versus time are depicted in **Figure 3B.4** for some selected temperatures from where the rate constants have been evaluated under pseudo first order conditions. The rate constant at each temperature are collected in **Table 3B.1**. The Arrhenious plots are presented in **Figure 3B.5**. The activation energy of the reaction along with relevant thermodynamic parameters have been calculated from Eyring equation[14] are also listed in **Table 3B.1**. Based on the literature, a plausible mechanism as shown in **Scheme 3B.1** is proposed for the hydrolysis of o-TOLI-Pyral.

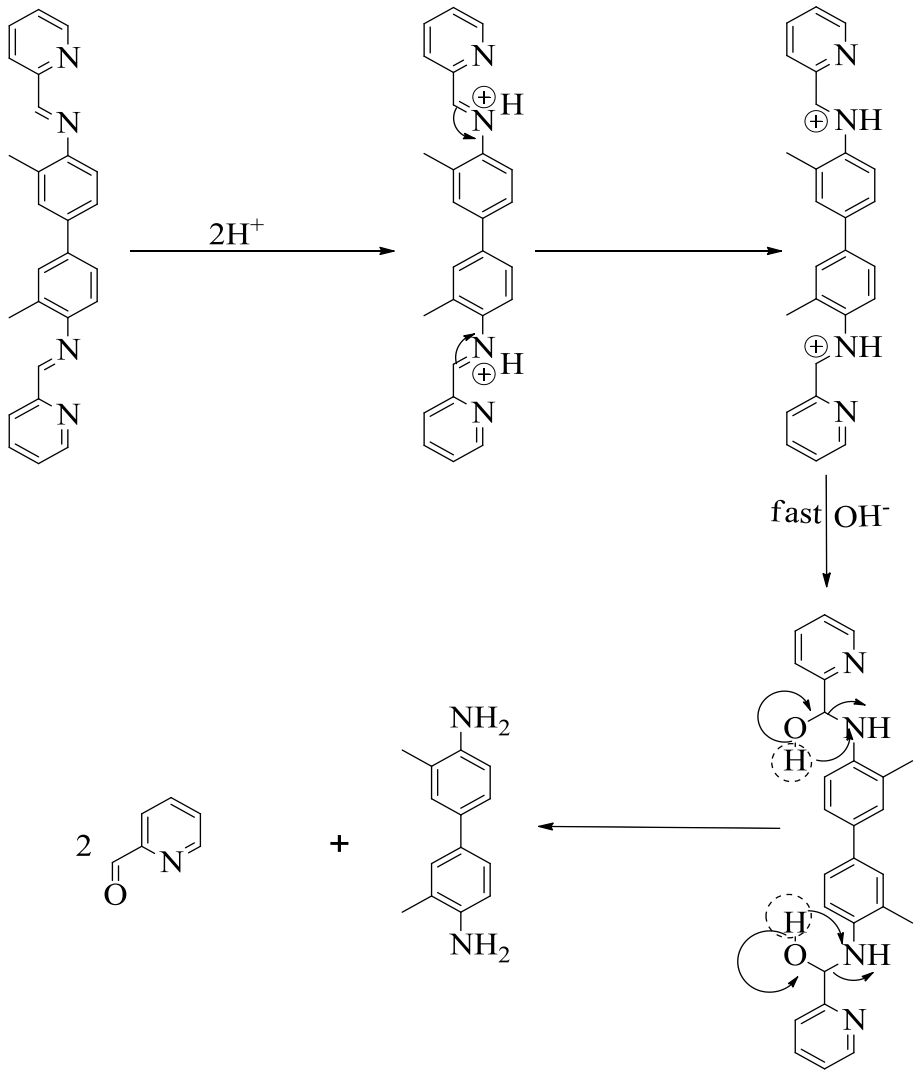

Scheme 3B.1

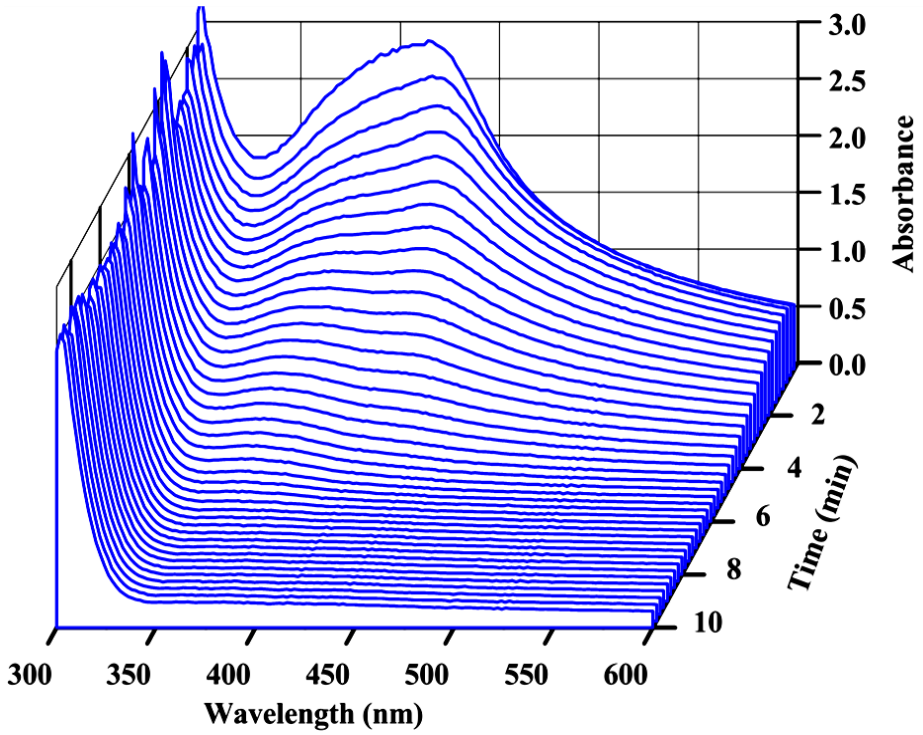

Figure 3B.1: Time-shifted repetitive uv-vis electronic absorption spectra of o-TOLI-Pyral (1.5×10^{-5} M) at 283 K in MeOH: H_2O 1:9 (v/v)

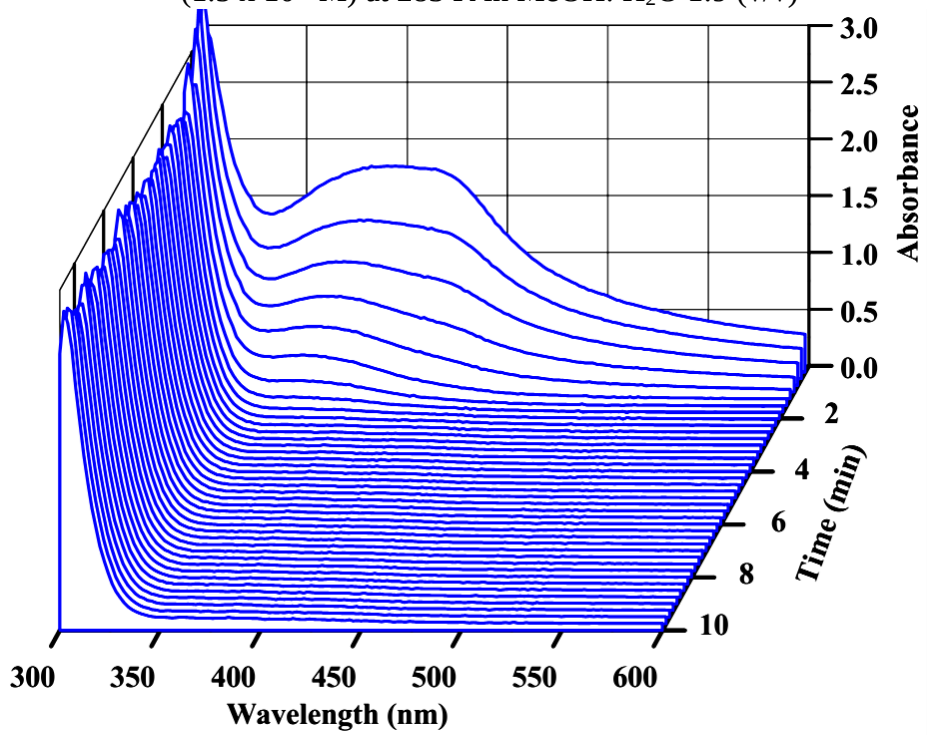

Figure 3B.2: Time-shifted repetitive uv-vis electronic absorption spectra of o-TOLI-Pyral (1.5×10^{-5} M) at 292 K in MeOH: H_2O 1:9 (v/v)

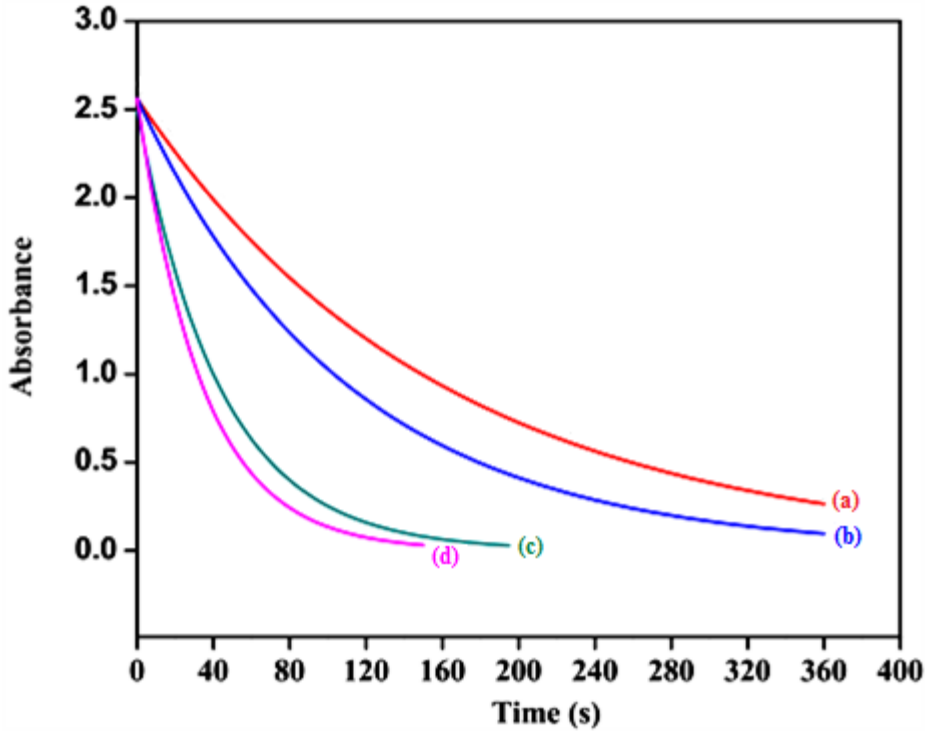

Figure 3B.3: Time scan mode of kinetics of hydrolysis of o-TOLI-Pyral at variable temperatures (a) 283.0 K (b) 287.5 K (c) 294.2 K (d) 296 K at 365 nm

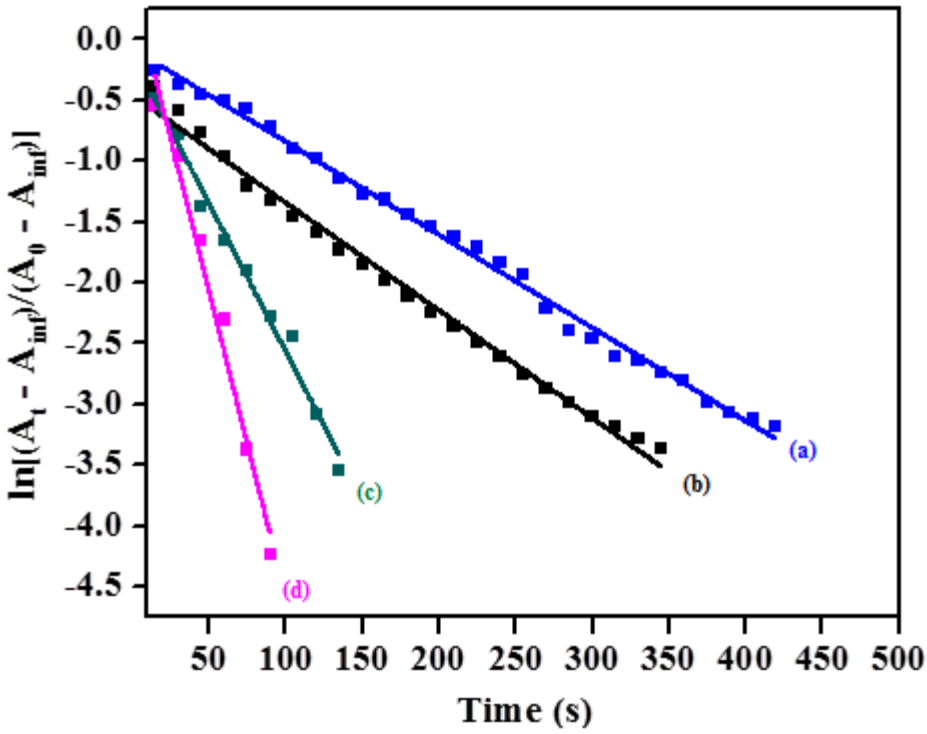

Figure 3B.4: Plot of $\ln[(A_t\text{-}_{Ainf})/A_0\text{-}A_{inf})]$ versus time of o-TOLI-Pyral at variable temperatures (a) 283 K (b) 287.5 K (c) 294.2 K (d) 296 K

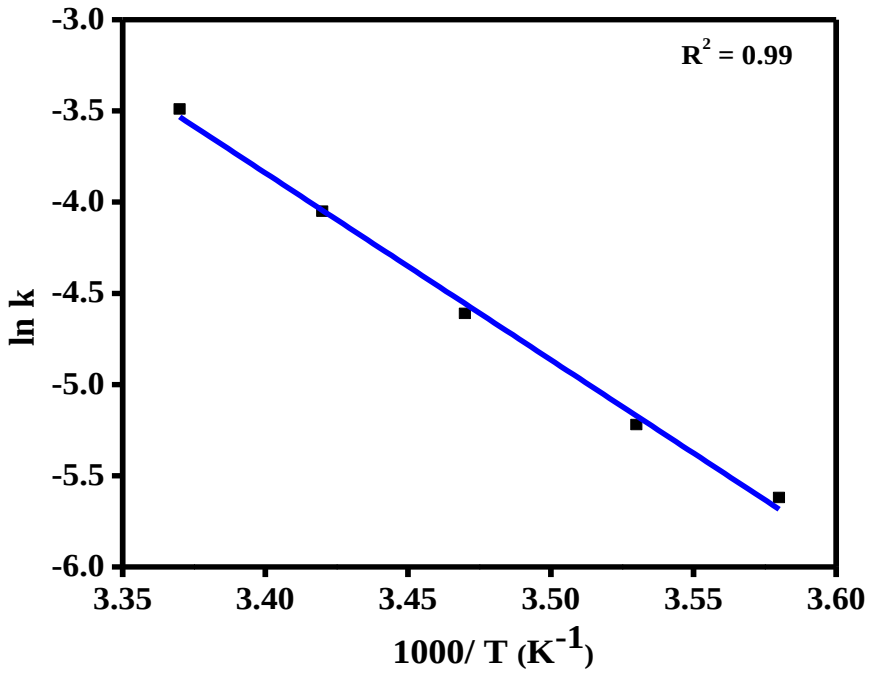

Figure 3B.5: Arrhenius plot of temperature dependence of rate constants ln k versus 1000/T

Table 3B.1: *Thermodynamic and kinetics data of hydrolysis of o-TOLI-Pyral*

$\frac{1000}{T}$ (K^{-1})	k x 10^{-3}	ln k	$\Delta G^{\#}$	E_a	$\Delta H^{\#}$	$\Delta S^{\#}$
			(kJ mol^{-1})			(kJ mol^{-1} K^{-1})
3.58	4.55	-5.39101	12.505	7.04	60.26	0.17
3.53	6.31	-5.06562	11.918			
3.47	9.13	-4.69619	11.225			
3.42	13.51	-4.30400	10.463			
3.37	20.16	-3.90370	96.06			

3B.2: Cyclic Voltammetric Studies

The kinetics of hydrolysis of imine (>C=N-) moieties of o-TOLI-Pyral have been investigated over SMDE and GCE as working electrodes in the potential window from -0.1 V to -1.6 V versus Ag|AgCl. A few of such voltammograms are shown in **Figure 3B.6**. From these figures, one can notice a cathodic peak at -0.65 V and an anodic peak at -0.5 V assigned to a quasi-reversible electron transfer across the C=N moiety. A few of the time-shifted cyclic voltammograms of o-TOLI-Pyral are presented in **Figure 3B.6**. It can further be observed that the peak currents gradually increase, reach a maximum and then start falling. The oxidative peak current versus time plot is shown in **Figure 3B.7**. These kinds of trends are indicative of the involvement of an intermediate. This plot supports the Scheme presented in **3B.1**. The voltammograms of two o-Tolidine and 2-pyridine carboxaldehyde have been recorded under similar experimental conditions. Interestingly, their voltammograms match well with that of the o-TOLI-Pyral at infinite time.

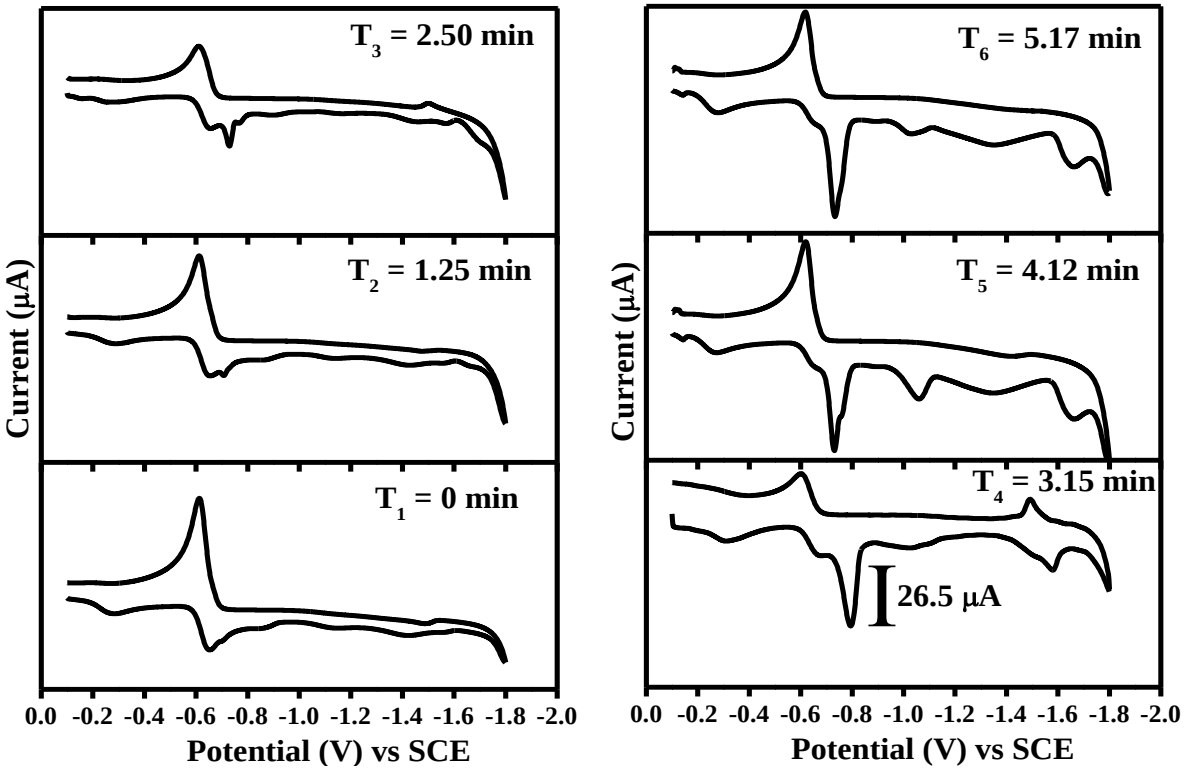

Figure 3B.6: Panel view of cyclic voltammograms of O-TOLI-Pyral (5 x 10^{-5} M) in aqueous medium at varied time interval

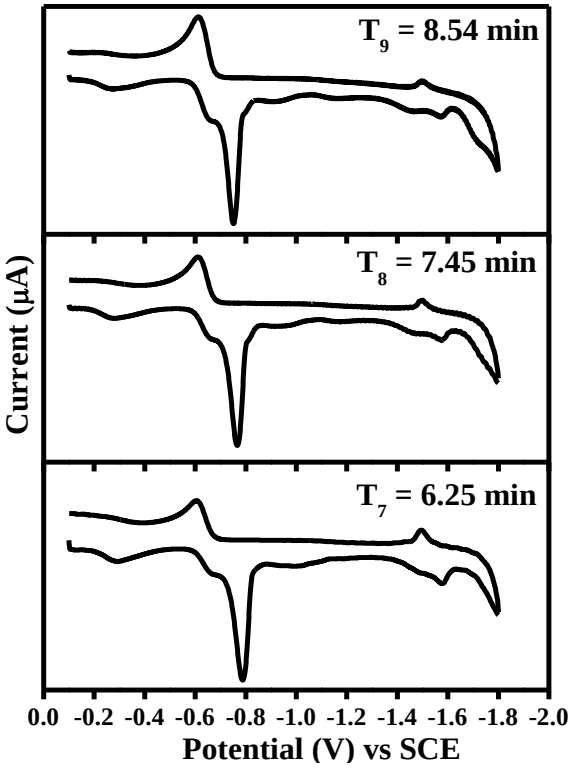

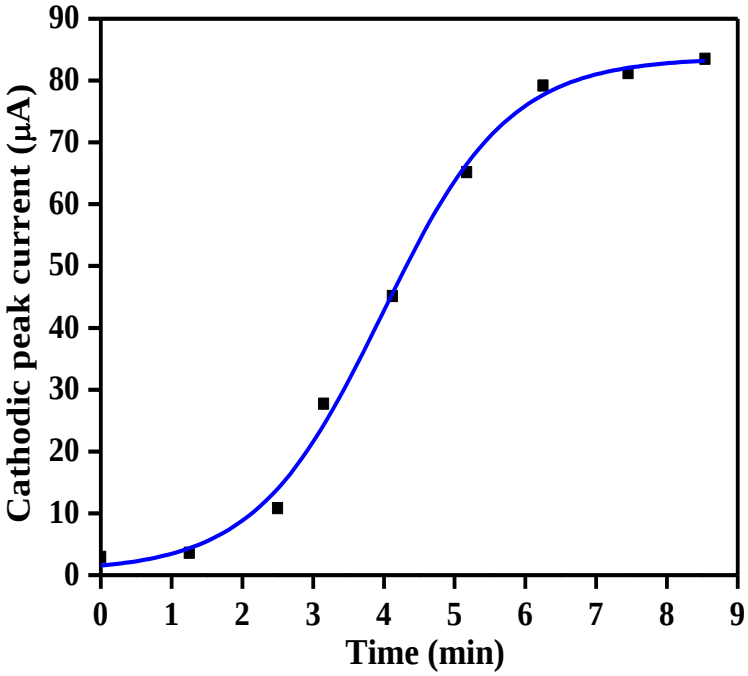

Figure 3B.7: Plot of cathodic peak current versus time of o-TOLI-Pyral

PART C: MOLECULAR MODELING STUDIES OF R-PYRAL AND THEIR METAL COMPLEXES, $[M_2(R\text{-}PYRAL)_2]Cl_4$

Molecular modeling studies have been employed for addressing the stability aspects of the Schiff bases and for finding, the conformational visualizations of the molecules in different formats. The global energy minimized structures are obtained through MM2 force field calculations method at RMS gradient 0.01. Further, the double dihedral torsional and conformational analysis have been performed over C-N=C bonds to visualize the relative and stable dihedral angles of the pyridine and biphenyl molecular planes. The numbering patterns of these ligands are presented in **Figure 3C.1**. In **Table 3C.1-3C.3** some of important structural parameters such as bond length, bond angles and torsional angle of BENZ-Pyral, o-TOLI-Pyral and DADPM-Pyral ligands are presented. There is an excellent agreement among the respective experimental and modelled data. The global minimized structures of these ligands in stereographic projection are portrayed in **Figure 3C. 2**.

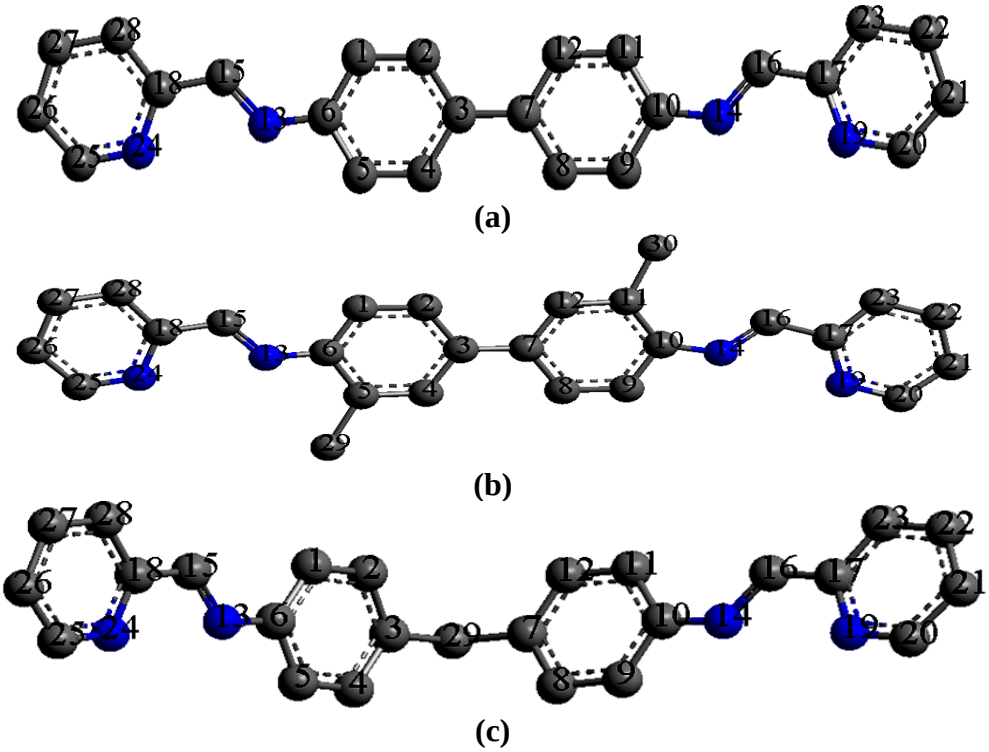

Figure 3C.1: Ball-Stick model of (a) BENZ-Pyral (b) o-TOLI-Pyral and (c) DADPM-Pyral with number tags

In **Figures 3C.3-3C.6** are presented the torsional energy conformational 3D plots of these ligands.

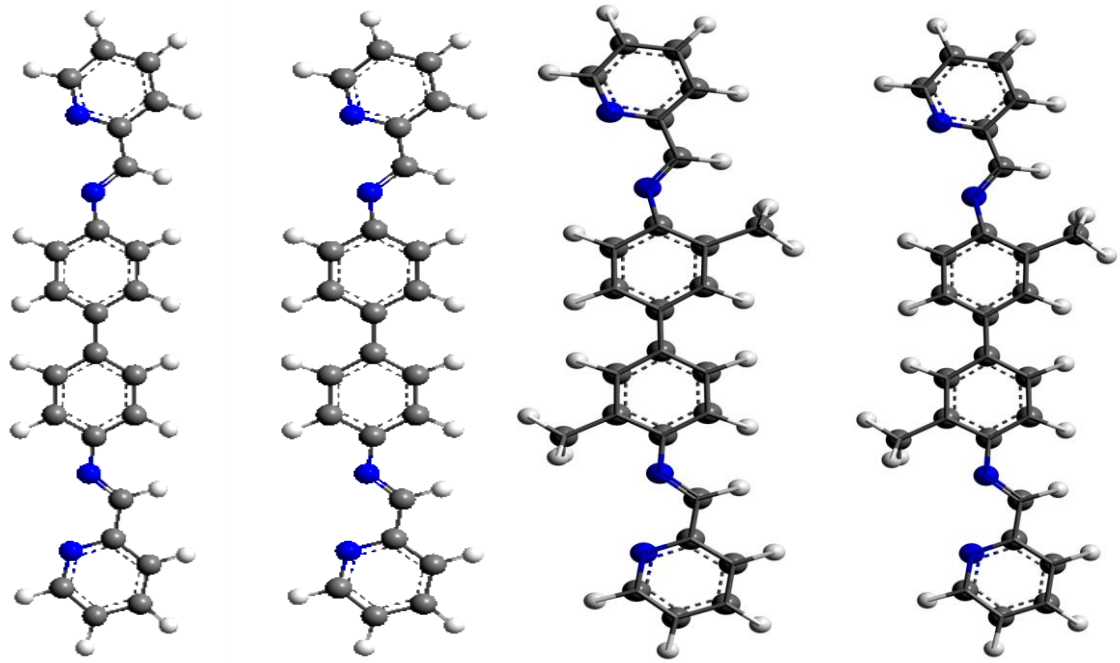

(a) **(b)**

The quantum mechanical HOMO-LUMO orbitals energy calculations have been used for computing the expected gas-phase electronic transitions. Some of the important HOMO-LUMO molecular orbitals are displayed in **Figure 3C.7-3C.9**. Useful modeled data are collected into **Table 3C.4** along with some experimental spectral data. The theoretical and experimental absorption maxima are in good agreement. The conformation energy plots of these ligands have been obtained and the same are presented in **Figure 3C.10-3C.12**. The solvent accessible zonal

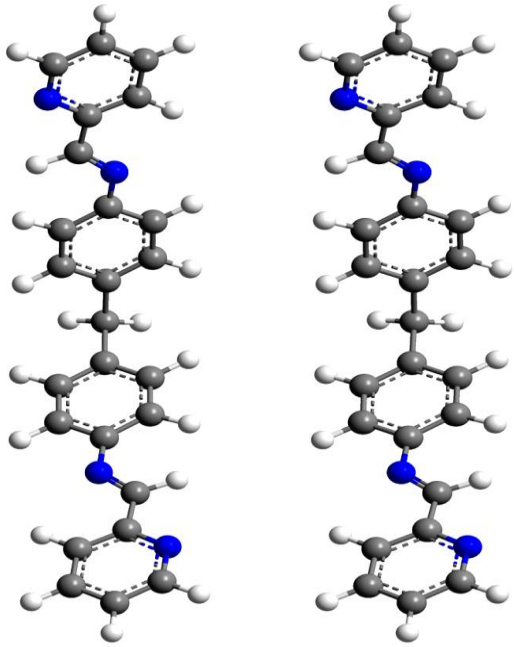

(c)

Figure 3C.2: Stereographic view of (a) BENZ-Pyral (b) o-TOLI-Pyral and (c) DADPM-Pyral after global minimization along with the scheme of the atoms

clouds of these ligands are shown in **Figure 3C.13-3C.15**. The HOMO-LUMO of their metal complexes are generated and depicted in **Figures 3C.16-3C.18**. The solvent accessible zonal clouds in wire mesh format of these metal complexes are presented in **Figures 3C.19-3C.21**. Relevant modeled data are collected in **Table 3C.5**.

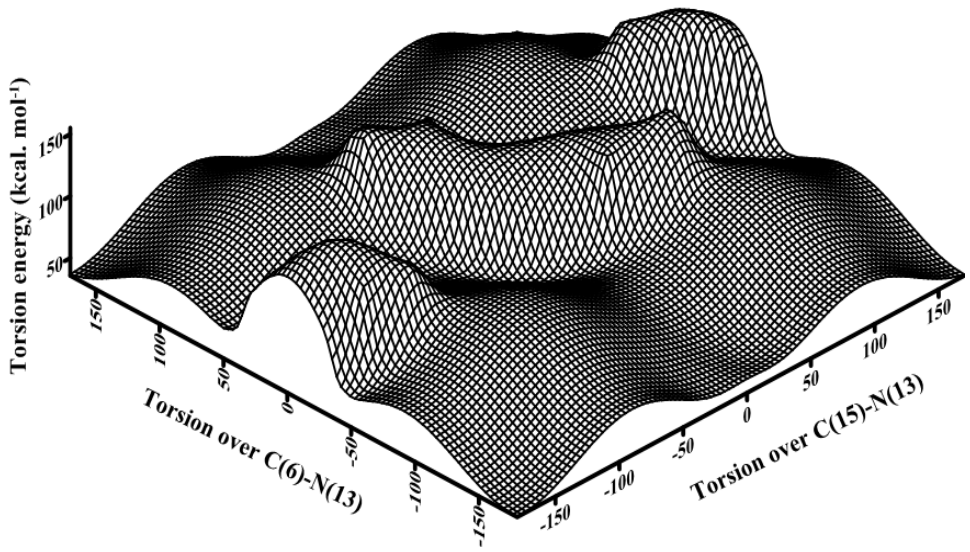

Figure 3C.3: Double dihedral torsional energy plot of BENZ-Pyral over (left) C(6)-N(13) and (right) C(15)-N(13) bonds from -180 to +180° (Refer **Figure 3C.1(a)** for numbering scheme for the atoms). Energy beyond 150 kcal. mol^{-1} is intentionally chopped to gain greater clarity at low energy barriers

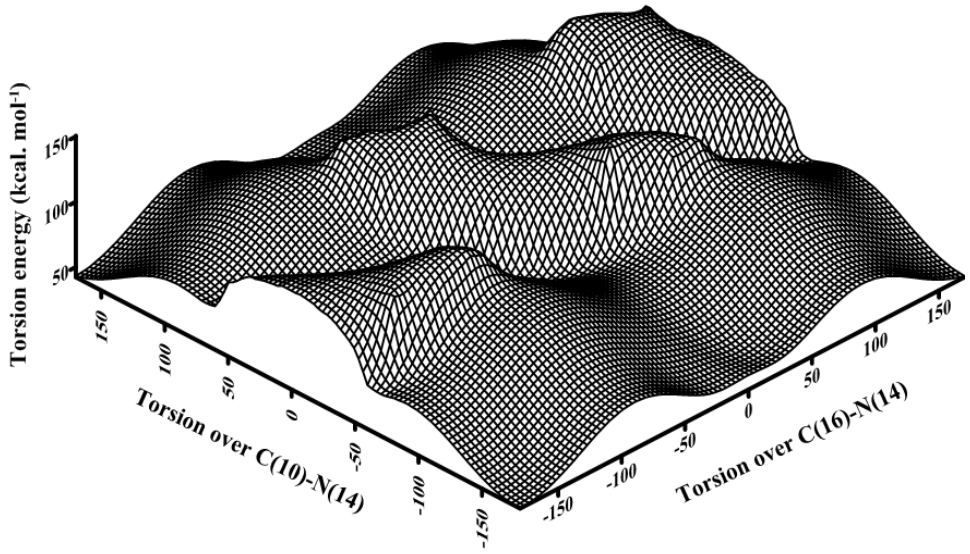

Figure 3C.4: Double dihedral torsional energy plot of o-TOLI-Pyral over (left) C(10)-N(14) and (right) C(16)-N(14) bonds from -180 to +180° (Refer **Figure**

3C.1(b) for numbering scheme for the atoms). Energy beyond 150 kcal. mol^{-1} is intentionally chopped to gain greater clarity at low energy barriers

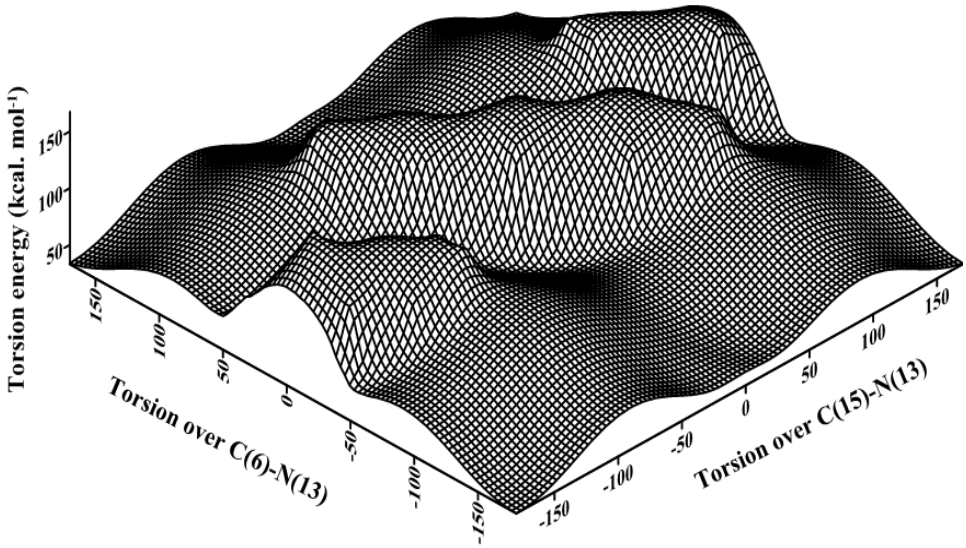

Figure 3C.5: Double dihedral torsional energy plot of DADPM-Pyral over (left) C(6)-N(13) and (right) C(15)-N(13) bonds from -180 to +180° (Refer **Figure 3C.1(c)** for numbering scheme for the atoms). Energy beyond 150 kcal. mol^{-1} is intentionally chopped to gain greater clarity at low energy barriers

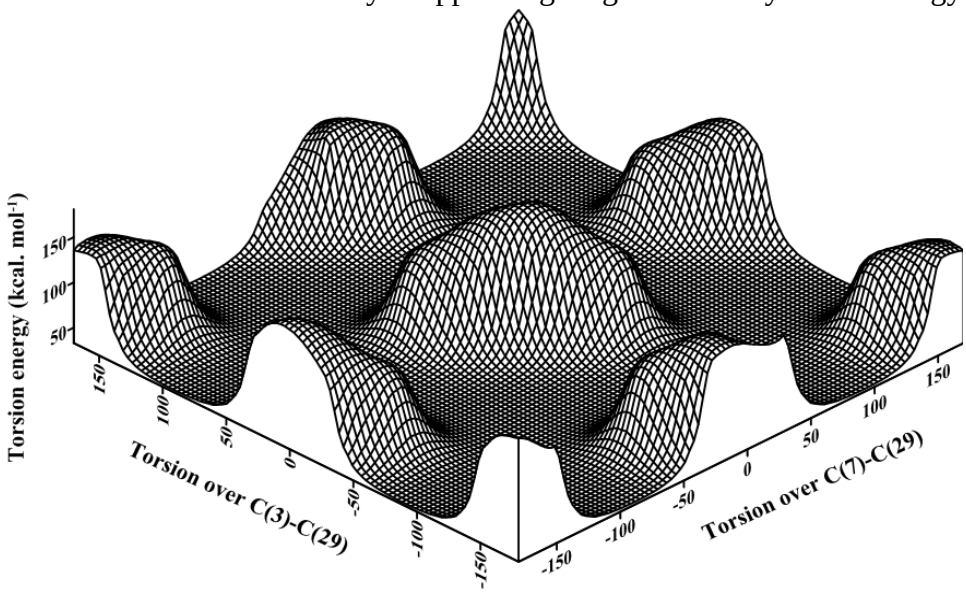

Figure 3C.6: Double dihedral torsional energy plot of DADPM-Pyral over (left) C(3)-C(29) and (right) C(7)-C(29) bonds from -180 to +180° (Refer **Figure 3C.1(c)** for numbering scheme for the atoms). Energy beyond 150 kcal. mol^{-1} is intentionally chopped to gain greater clarity at low energy barriers

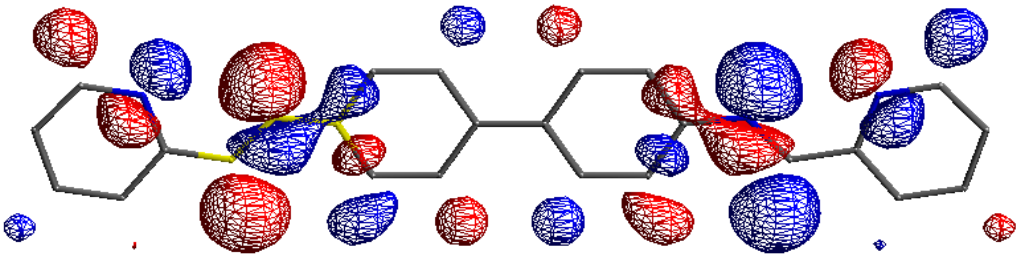

HOMO (-7.860 eV)

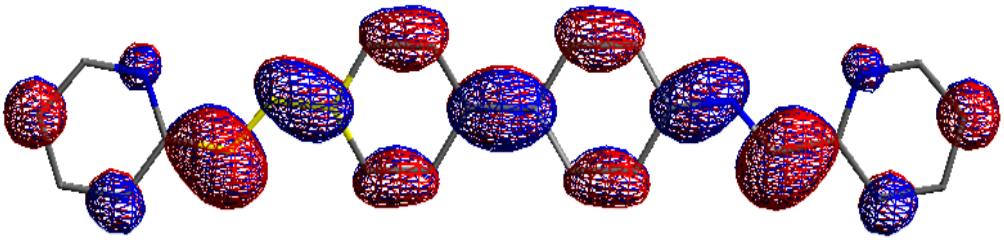

LUMO (-4.034 eV)

Figure 3C.7: HOMO and LUMO molecular orbitals of BENZ-Pyral in wire mesh format (All the H-atoms are excluded for clarity)

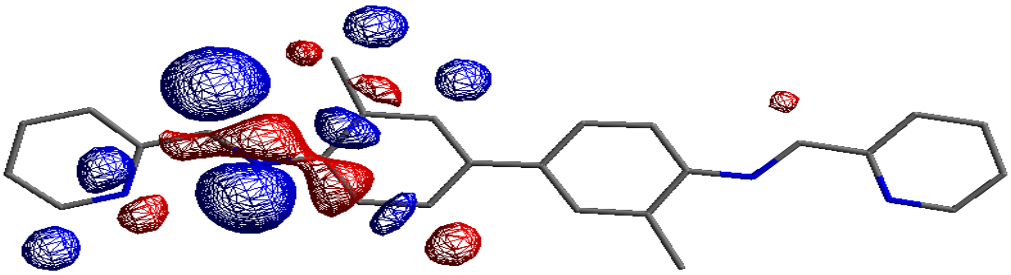

HOMO (-7.431 eV)

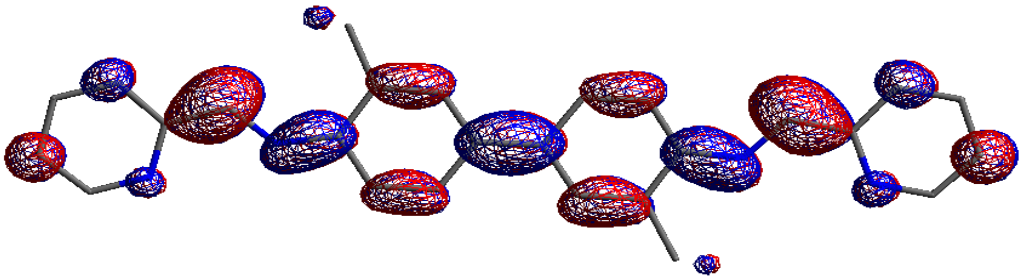

LUMO (-3.720 eV)

Figure 3C.8: HOMO and LUMO molecular orbitals of o-TOLI-Pyral in wire mesh format (All the H-atoms are excluded for clarity)

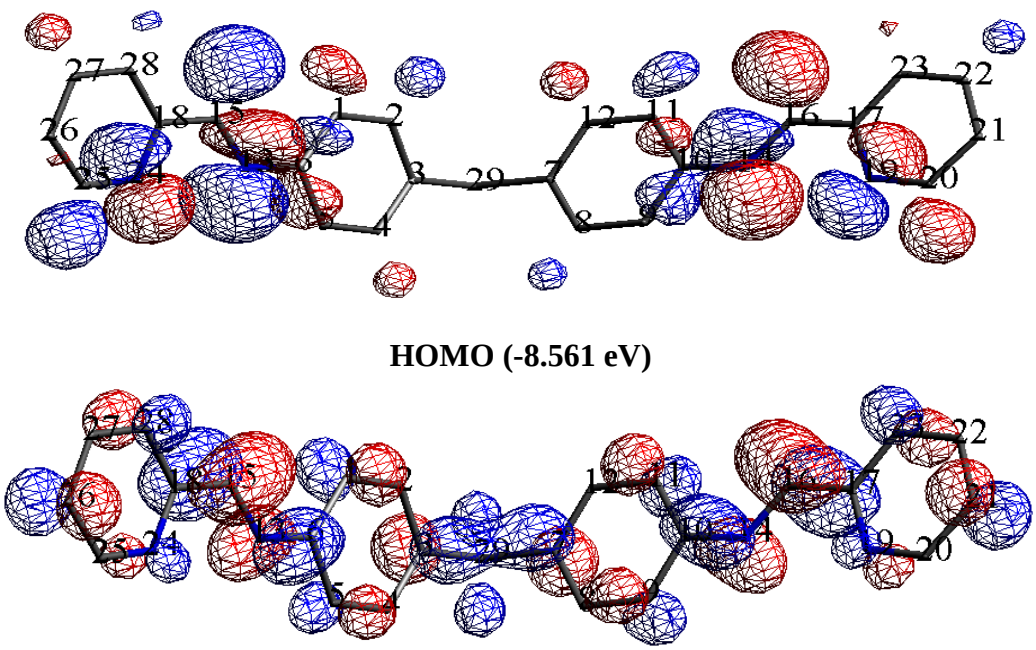

HOMO (-8.561 eV)

LUMO (-3.493 eV)

Figure 3C.9: HOMO and LUMO molecular orbitals of DADPM-Pyral in wire mesh format (All the H-atoms are excluded for clarity)

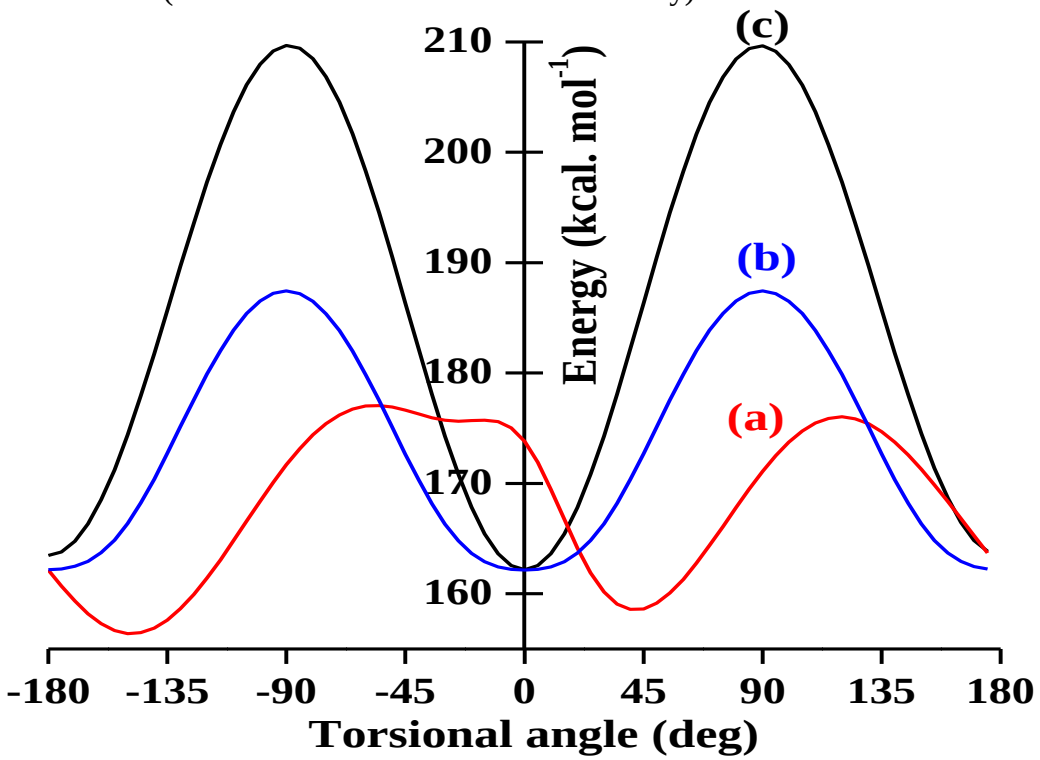

Figure 3C.10: Conformation single dihedral energy plot of BENZ-Pyral over (a) C(6)-N(13) (b) C(3)-C(7) and (c) C(15)-C(18)

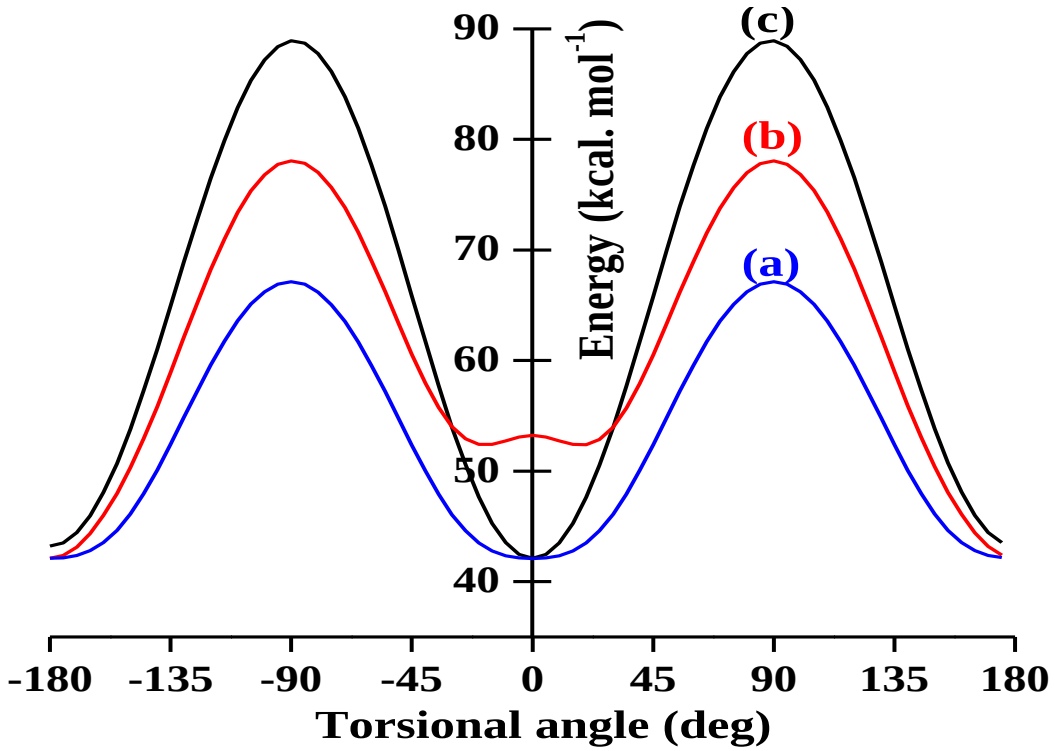

Figure 3C.11: Conformation single dihedral energy plot of o-TOLI-Pyral over (a) C(6)-N(13) (b) C(3)-C(7) and (c) C(15)-C(18)

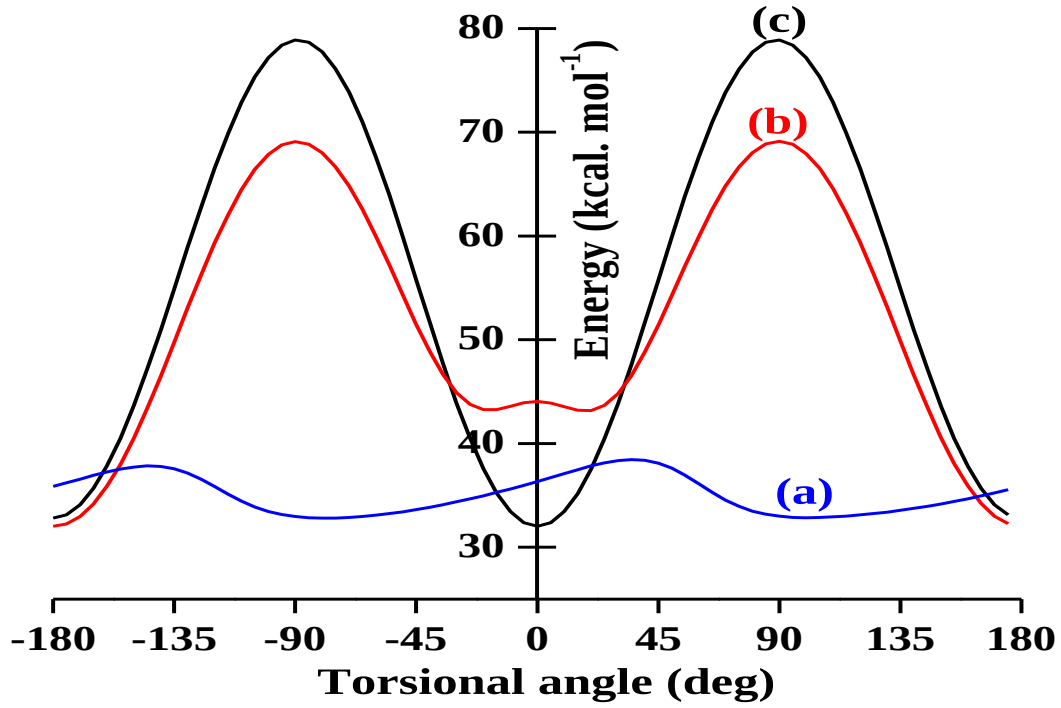

Figure 3C.12: Conformation single dihedral energy plot of DADPM-Pyral over (a) C(3)-C(29) (b) C(6)-N(13) and (c) C(15)-C(18)

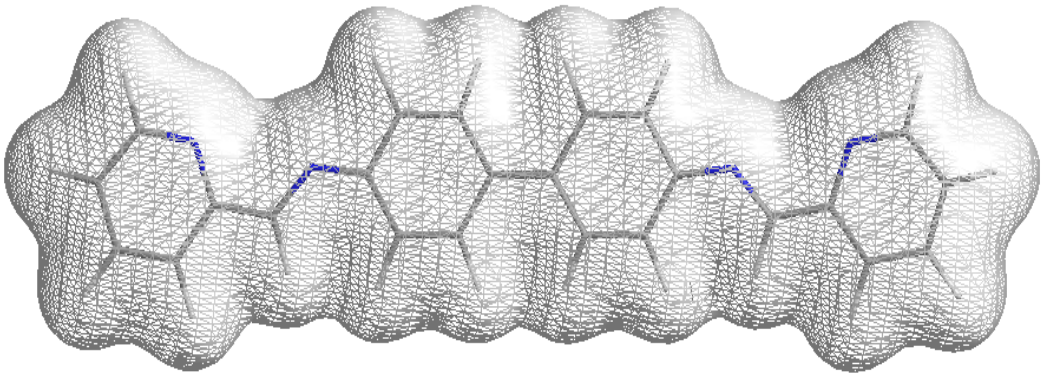

Figure 3C.13: Solvent accessible zonal cloud of BENZ-Pyral in wire mesh found

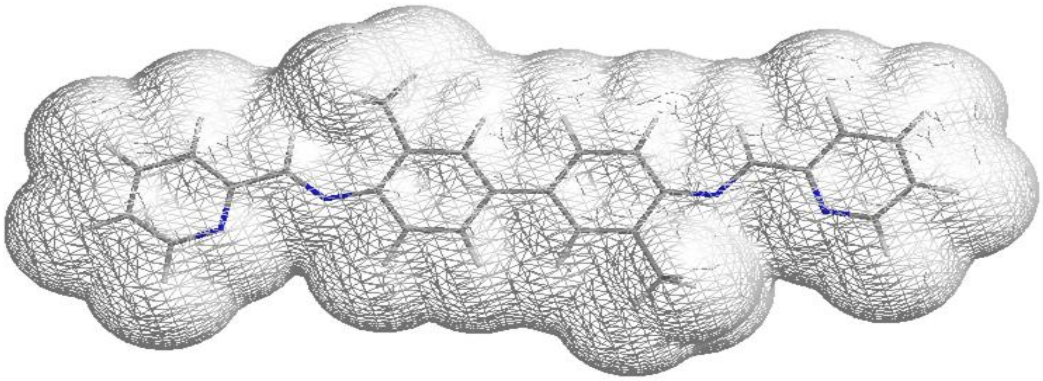

Figure 3C.14: Solvent accessible zonal cloud of o-TOLI-Pyral in wire mesh found

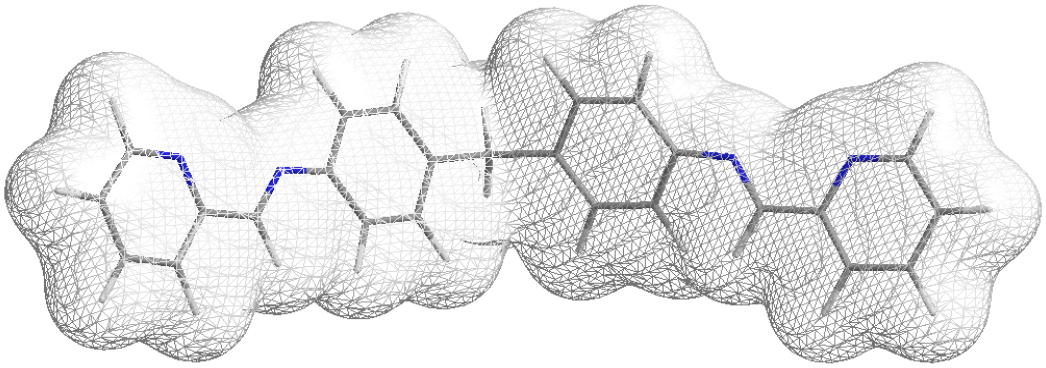

Figure 3C.15: Solvent accessible zonal cloud of DADPM-Pyral in wire mesh found

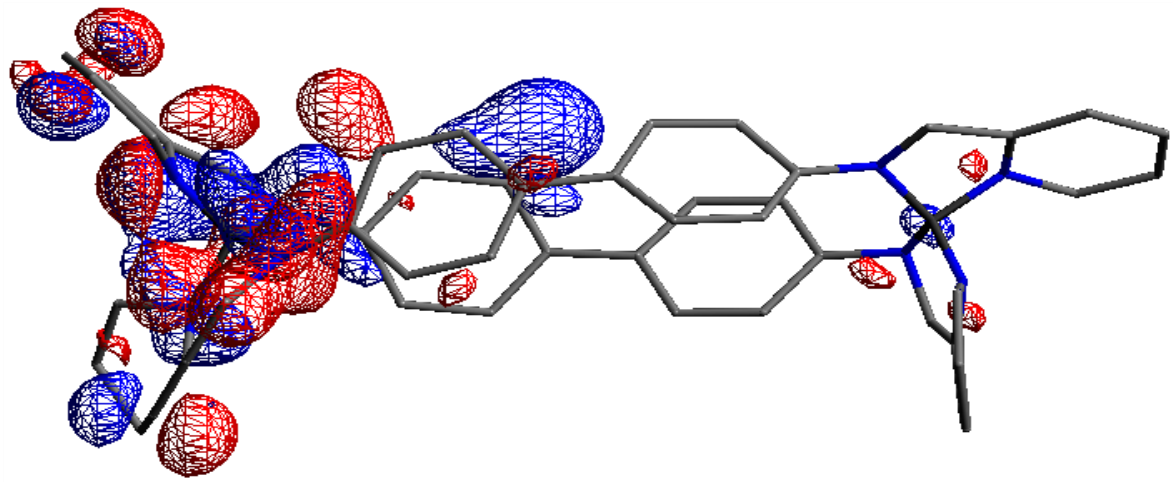

HOMO (-2.371 eV)

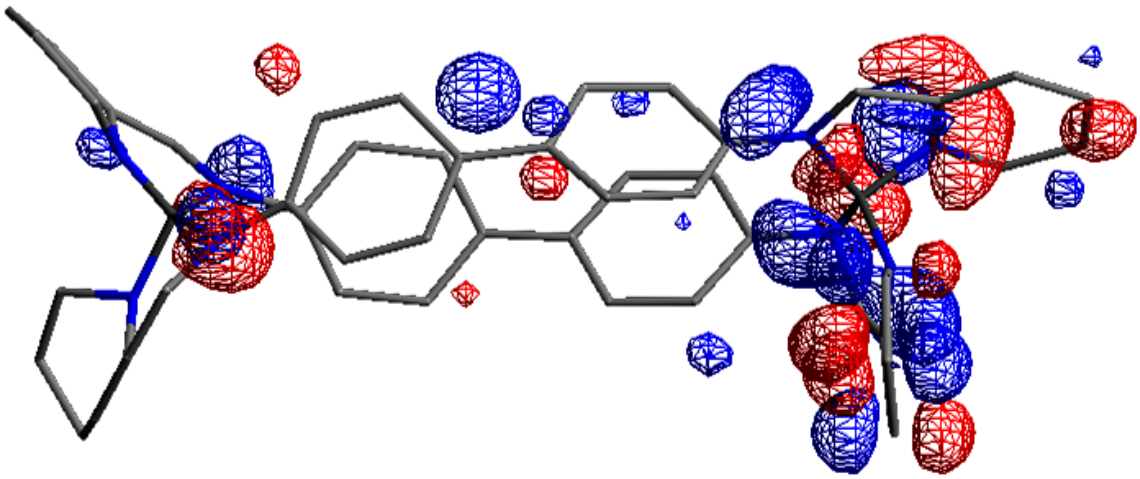

LUMO (-1.412 eV)

Figure 3C.16: HOMO and LUMO molecular orbitals of $[Cu_2(BENZPyral)_2]$ in wire mesh format (All the H-atoms are excluded for clarity)

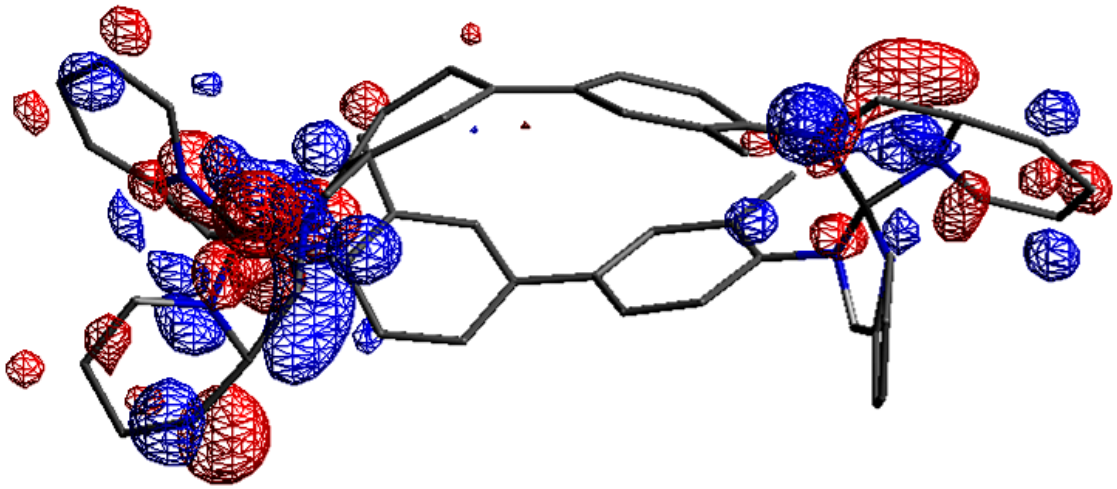

HOMO (-2.612 eV)

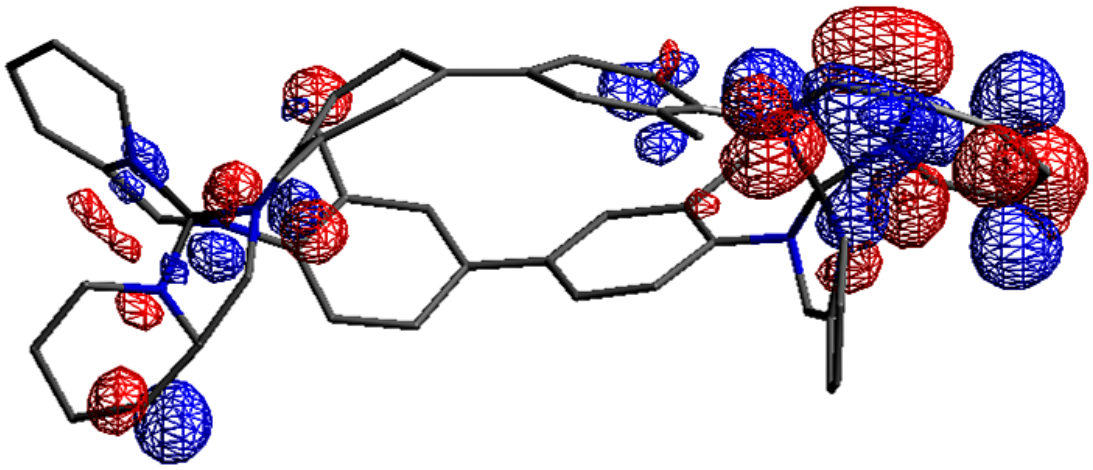

LUMO (-1.703 eV)

Figure 3C.17: HOMO and LUMO molecular orbitals of [Cu_2(o-TOLI-Pyral)$_2$] in wire mesh format (All the H-atoms are excluded for clarity)

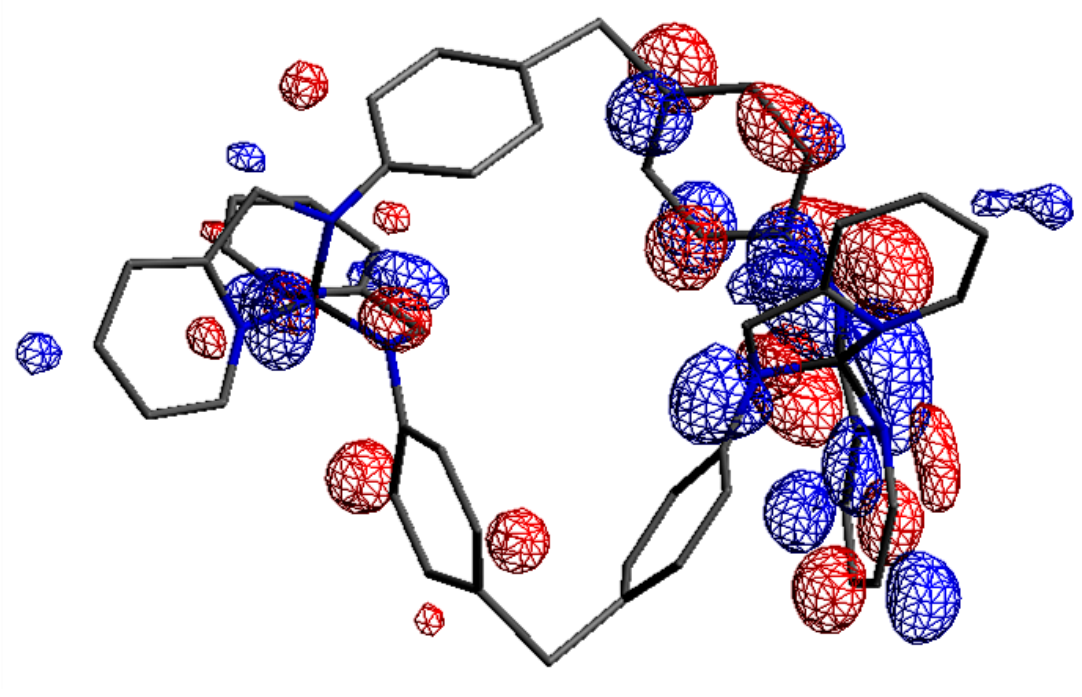

HOMO (-2.112 eV)

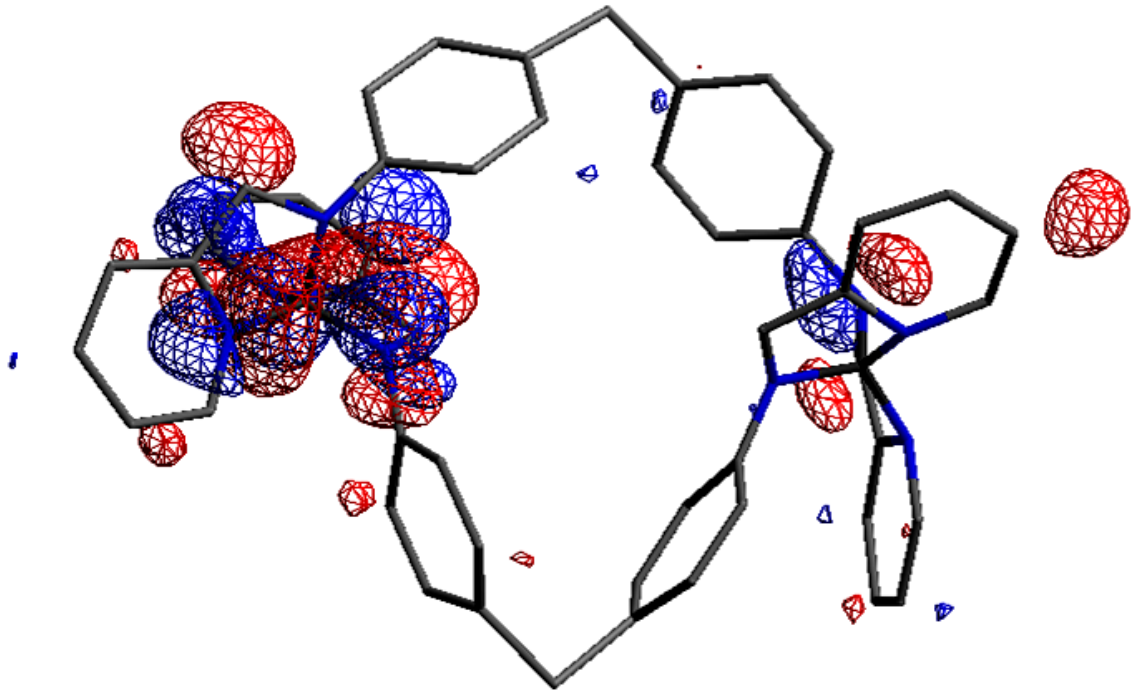

LUMO (-1.002 eV)

Figure 3C.18: HOMO and LUMO molecular orbitals of $[Cu_2(DADPM\text{-}Pyral)_2]$ in wire mesh format (All the H-atoms are excluded for clarity)

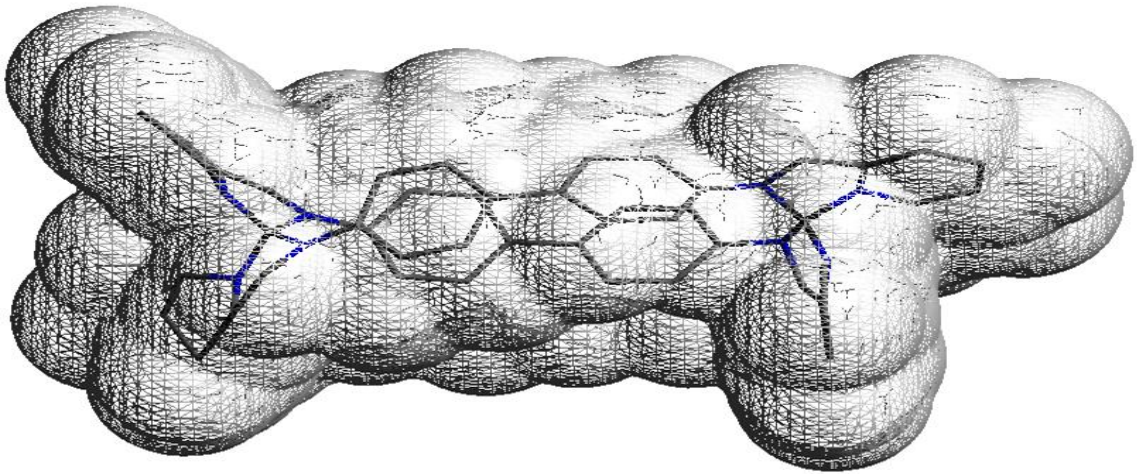

Figure 3C.19: Solvent accessible zonal cloud of [Cu_2(BENZ-Pyral)$_2$] in wire mesh found

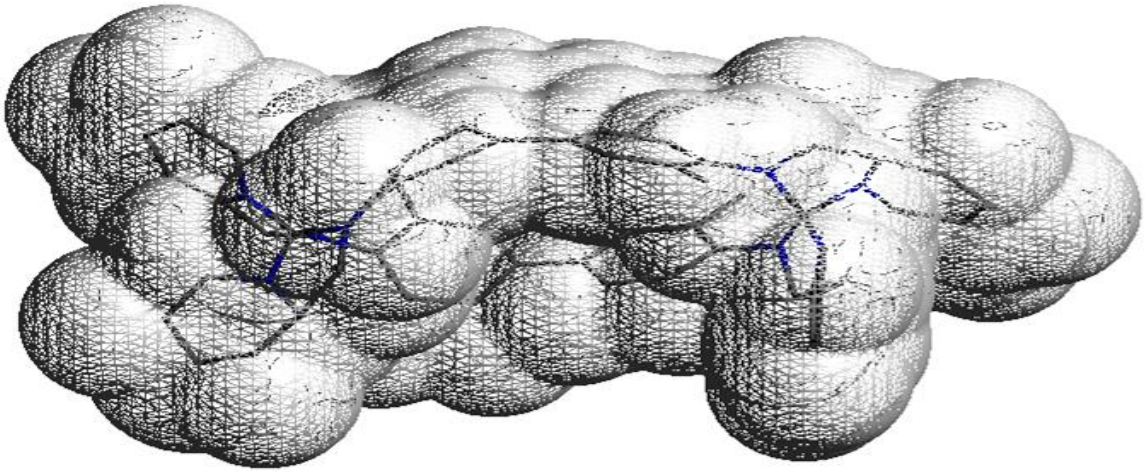

Figure 3C.20: Solvent accessible zonal cloud of [Cu_2(o-TOLI-Pyral)$_2$] in wire mesh found

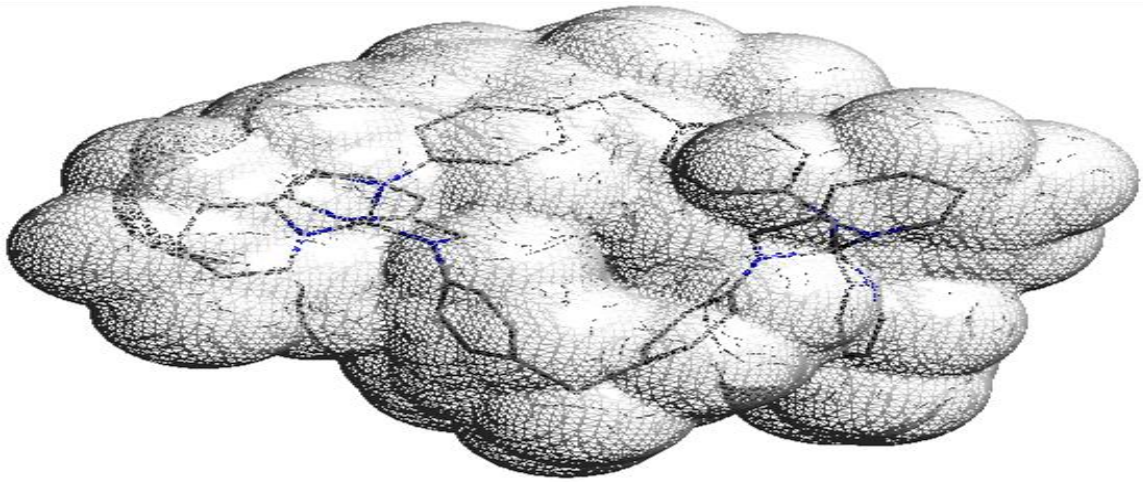

Figure 3C.21: Solvent accessible zonal cloud of [Cu_2(DADPM-Pyral)$_2$] in wire mesh found

Table 3C.1: *Some of the important geometric parameters of BENZ-Pyral*

Bond	Bond length (Å)	Bond	Bond angle (deg)	Bond	Dihedral angle (deg)
C(28)-C(18)	1.3488	C(28)-C(18)-C(15)	120.230	C(27)-C(28)-C(18)-C(15)	0.028
N(24)-C(18)	1.2704	N(24)-C(18)-C(15)	119.540	C(2)-C(1)-C(6)-N(13)	0.052
C(7)-C(3)	1.3623	C(18)-C(15)-N(13)	124.199	C(4)-C(5)-C(6)-N(13)	0.062
C(15)-C(18)	1.3505	C(15)-N(13)-C(6)	127.209	C(1)-C(2)-C(3)-C(7)	0.101
N(13)-C(15)	1.2674	C(1)-C(6)-N(13)	128.251	C(8)-C(7)-C(3)-C(2)	0.211
C(6)-N(13)	1.2703	C(5)-C(6)-N(13)	116.408	C(8)-C(7)-C(3)-C(4)	0.160
		C(2)-C(3)-C(7)	123.447	C(12)-C(7)-C(3)-C(2)	0.175
				N(13)-C(15)-C(18)-N(24)	0.027
				N(13)-C(15)-C(18)-C(28)	0.049
				C(6)-N(13)-C(15)-C(18)	0.093
				C(5)-C(6)-N(13)-C(15)	0.080

Table 3C.2: *Some of the important geometric parameters of o-TOLI-Pyral*

Bond	Bond length (Å)	Bond	Bond angle (deg)	Bond	Dihedral angle (deg)
C(28)-C(18)	1.3487	C(15)-C(18)-C(28)	120.257	C(27)-C(28)-C(18)-C(15)	0.021
N(24)-C(18)	1.2705	C(15)-C(18)-N(24)	119.500	C(25)-N(24)-C(18)-C(15)	0.067
C(1)-C(6)	1.3441	N(13)-C(15)-C(18)	123.880	C(2)-C(1)-C(6)-N(13)	0.085
C(5)-C(6)	1.3501	C(6)-N(13)-C(15)	127.961	C(4)-C(5)-C(6)-N(13)	0.089
C(7)-C(3)	1.3631	C(3)-C(7)-C(12)	123.962	C(29)-C(5)-C(6)-C(1)	0.039
C(15)-C(18)	1.3506	C(3)-C(7)-C(8)	123.382	C(3)-C(4)-C(5)-C(29)	0.040
N(13)-C(15)	1.2673	N(13)-C(6)-C(1)	126.760	C(1)-C(2)-C(3)-C(7)	0.168
C(6)-N(13)	1.2706	N(13)-C(6)-C(5)	116.921	C(12)-C(7)-C(3)-C(4)	0.118
		C(29)-C(5)-C(6)	120.465	N(13)-C(15)-C(18)-N(24)	0.010
		C(29)-C(5)-C(4)	119.413	N(13)-C(15)-C(18)-C(28)	0.011
		C(7)-C(3)-C(4)	123.457	C(6)-N(13)-C(15)-C(18)	0.129
		C(7)-C(3)-C(2)	123.530	C(5)-C(6)-N(13)-C(15)	0.134
				C(1)-C(6)-N(13)-C(15)	0.013

Table 3C.3: *Some of the important geometric parameters of DADPM-Pyral*

Bond	Bond length (Å)	Bond	Bond angle (deg)	Bond	Dihedral angle (deg)
(28)-C(18)	1.3488	C(3)-C(29)-C(7)	109.650	C(27)-C(28)-C(18)-C(15)	0.006
N(24)-C(18)	1.2704	C(15)-C(18)-C(28)	120.235	C(25)-N(24)-C(18)-C(15)	0.087
C(5)-C(6)	1.3487	C(15)-C(18)-N(24)	119.535	C(29)-C(7)-C(12)-C(11)	0.371
C(7)-C(29)	1.5122	C(28)-C(18)-N(24)	120.229	C(29)-C(7)-C(8)-C(9)	0.542
C(3)-C(29)	1.5122	N(13)-C(15)-C(18)	124.163	C(2)-C(1)-C(6)-N(13)	0.027
C(15)-C(18)	1.3505	C(6)-N(13)-C(15)	127.321	C(4)-C(5)-C(6)-N(13)	0.036

N(13)-C(15)	1.2674	C(29)-C(7)-C(12)	121.506	C(29)-C(3)-C(4)-C(5)	0.558
C(6)-N(13)	1.2707	N(13)-C(6)-C(1)	127.602	C(1)-C(2)-C(3)-C(29)	0.361
		N(13)-C(6)-C(5)	115.646	C(8)-C(7)-C(29)-C(3)	79.804
		C(1)-C(6)-C(5)	116.751	C(12)-C(7)-C(29)-C(3)	81.441
		C(29)-C(3)-C(4)	121.447	C(2)-C(3)-C(29)-C(7)	79.506
		C(29)-C(3)-C(2)	120.876	C(4)-C(3)-C(29)-C(7)	79.221
		C(4)-C(3)-C(2)	117.673	N(13)-C(15)-C(18)-N(24)	0.056
				N(13)-C(15)-C(18)-C(28)	0.052
				C(6)-N(13)-C(15)-C(18)	0.012
				C(5)-C(6)-N(13)-C(15)	0.134
				C(1)-C(6)-N(13)-C(15)	0.047

Table 3C.4: *HOMO-LUMO energies of the ligands*

S.No.	Species	$\Delta H°_f$ (kcal. mol^{-1})	HOMO (eV)	LUMO (eV)	Calculated λ_{max} (nm)	Observed λ_{max} (nm)
1	BENZ-Pyraal	35.524	-7.860	-4.034	324	362
2	o-TOLI-Pyral	42.105	-7.431	-3.720	334	365
3	DADPM-Pyral	30.977	-8.561	-4.493	305	336

Table 3C.5: *important geometric parameters of R-Pyral Schiff base metal complexes*

S.No.	Compound	$\Delta H°_f$ (kcal mol^{-1})	M-N (Å)	M-M (Å)
1	$[Co_2(BENZ\text{-}Pyral)_2]$	547.612	1.82	10.31
2	$[Ni_2(BENZ\text{-}Pyral)_2]$	611.732	1.80	10.57
3	$[Cu_2(BENZ\text{-}Pyral)_2]$	713.951	1.33	10.49

4	$[Zn_2(BENZ\text{-}Pyral)_2]$	765.443	1.93	10.90
5	$[Co_2(O\text{-}TOLI\text{-}Pyral)_2]$	1239.349	1.77	10.67
6	$[Ni_2(O\text{-}TOLI\text{-}Pyral)_2]$	560.827	1.81	10.70
7	$[Cu_2(O\text{-}TOLI\text{-}Pyral)_2]$	839.335	1.34	10.16
8	$[Zn_2(O\text{-}TOLI\text{-}Pyral)_2]$	797.243	1.93	10.53
9	$[Co_2(DADPM\text{-}Pyral)_2]$	496.851	1.82	8.21
10	$[Ni_2(DADPM\text{-}Pyral)_2]$	487.533	1.81	8.17
11	$[Cu_2(DADPM\text{-}Pyral)_2]$	512.601	1.36	8.12
12	$[Zn_2(DADPM\text{-}Pyral)_2]$	501.824	1.93	8.20

References

1. R. M. Ahmed, E. I. Yousif and M. J. Al-Jeboori, *Sci. World J.*, 2013, **2013**, 2–7.
2. A. M. A. Alaghaz and H. A. Bayoumi, *Int. J. Electrochem. Sci.*, 2013, **8**, 11860–11876.
3. N. Yoshida, K. Ichikawa and M. Shiro, *J. Chem. Soc. Perkin Trans. 2*, 2000, 17–26.
4. V. Krishna, *Synthesis and Characterization of Some New Series of Biphenyl Bridged Polynucleating Ligands and Their BIivalent Metal Complexes as Possible Supramolecular Hosts*, 2012.
5. H. B. Tanh Jeazet, J. Mizera, T. Doert, K. Gloe, A. Heine, G. Bernhard and K. Gloe, *J. Incl. Phenom. Macrocycl. Chem.*, 2011, **71**, 343–352.
6. H. B. Tanh Jeazet, K. Gloe, T. Doert, O. N. Kataeva, A. Jäger, G. Geipel, G. Bernhard, B. Büchner and K. Gloe, *Chem. Commun. (Camb).*, 2010, **46**, 2373–5.
7. Y. Parajó, J. Malina, I. Meistermann, G. J. Clarkson, M. Pascu, A. Rodger, M. J. Hannon and P. Lincoln, *Dalt. Trans.*, 2009, 4868–4874.
8. L. C. Matsinha, S. F. Mapolie and G. S. Smith, *Polyhedron*, 2013, **53**, 56–61.
9. N. Chanda, B. Mondal, G. Puranik and G. Kumar, 2002, **21**, 2033–2043.
10. E. J. Olson and P. Bühlmann, *J. Org. Chem.*, 2011, **76**, 8406–8412.
11. D. Maity and T. Govindaraju, *Inorg. Chem.*, 2010, **49**, 7229–7231.
12. J. Telser, *J. Braz. Chem. Soc.*, 2010, **21**, 1139–1157.
13. D. T. Edwards, T. Huber, S. Hussain, K. M. Stone, M. Kinnebrew, I. Kaminker, E. Matalon, M. S. Sherwin, D. Goldfarb and S. Han, *Structure*, 2014, **22**, 1677–1686.
14. Z. Zhan, D. Gupta and A. A. Khan, *Int. J. Chem. Kinet.*, 1992, **24**, 481–487.

CHAPTER - IV

2-(((4-NITROPHENYL)IMINO) METHYL)PHENOL

In this Chapter, the characterization of a non-linear Schiff base molecule 2-(((4-nitrophenyl)imino)methyl)phenol (**PNASH**) is discussed. Spectral (IR, uv-visible absorption and fluorescence emission), thermal, electrochemical properties, single crystal X-ray diffraction and molecular modeling studies have been carried out extensively because of their interesting photophysical, physico-chemical and redox properties of azomethine (>C=N-) functional group.

2-hydroxy benzaldehyde condensed with p-nitroaniline to get binucleating non-linear Schiff base. The synthesis procedure of PNASH has been described in **Chapter II**.

This Chapter is presented in four parts. In **PART A**, the spectral and electrochemical studies of PNASH are presented and discussed.

In **PART B**, the mechanochromic, thermochromic and polymorphic studies of PNASH are described.

PART C covers the single crystal X-ray and powder X-ray diffraction studies of PNASH besides its supramolecular right handed and left handed helical structures.

PART D focuses on the conformational analysis and molecular modeling calculation of geometrical parameters of PNASH such as bond length, bond angles, torsional angles along with HOMO-LUMO orbital energies, solvent accessible zonal clouds, single and double dihedral analysis, etc.,.

PART A: SPECTRAL AND ELECTROCHEMICAL STUDIES OF PNASH

Structure of the compound

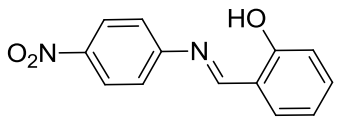

4.1.

2-(((4-nitrophenyl)imino)methyl)phenol

(**PNASH**)

4A.1: General Characterization of the Non-Linear Schiff Base PNASH

The spectral (IR, uv-visible absorption and fluorescence emission) studies of PNASH in aqueous, nonaqueous buffer media and solid state have been carried out besides electrochemical studies. Further, the results are concisely elaborated here.

4A.2: Infrared Spectral Studies

PNASH having electron donating and accepting groups in the molecular skeleton is expected to exhibit polymorphic behavior[1–3]. The ground and unground PNASH powders have been recrystallized in different organic solvents. The crystals obtained from ethyl acetate (**EtOAc**), acetone and dimethyl formamide (DMF) are in similar in shapes whereas some of crystals which are obtained in dichloromethane (DCM) and acetonitrile are in different shapes. On the basis of these observation, FT-IR spectra of PNASH crystals obtained from **EtOAc** and in **MeCN** have been separately recorded. They are presented in **Figure 4A.1**. One can see significant change as noticeable in magnified zones shown in **Figure 4A.2** as deconvolution spectra. Hereafter, **PNASH-EtOAc** crystals are denoted as **Form – I** whereas **PNASH-MeCN** crystals as **Form – II**. From the FT-IR spectra of **Forms – I** and **II** crystals, the stretching and bending frequencies of functional groups like —OH, >C=N— and —NO_2 are found to be slightly different. FT-IR spectral data of these functional groups are given in **Table 4A.1**. In case of azomethine functional group, the stretching frequency ($\bar{\nu}_{(C=N)}$) of **Form – I** is observed at 1623.0 cm^{-1} and that of **Form – II** at

1638.1 cm^{-1}.Similar changes have been noticed in nitro group frequencies of **Forms – I** and **II** to be 1330.4 cm^{-1} and 1338.1 cm^{-1} respectively. The asymmetric stretch of nitro group of **Forms I** and **II** appear in range of 1560 – 1475 cm^{-1}(s)[4]. The molecular stacking during crystal growth seems to be influenced by the kind of salvation in solution state that is taken further in the respective crystal shapes. Subtle changes in the rocking modes of NO_2 out of bending modes of phenolic –OH for **Forms I** and **II** are observed.

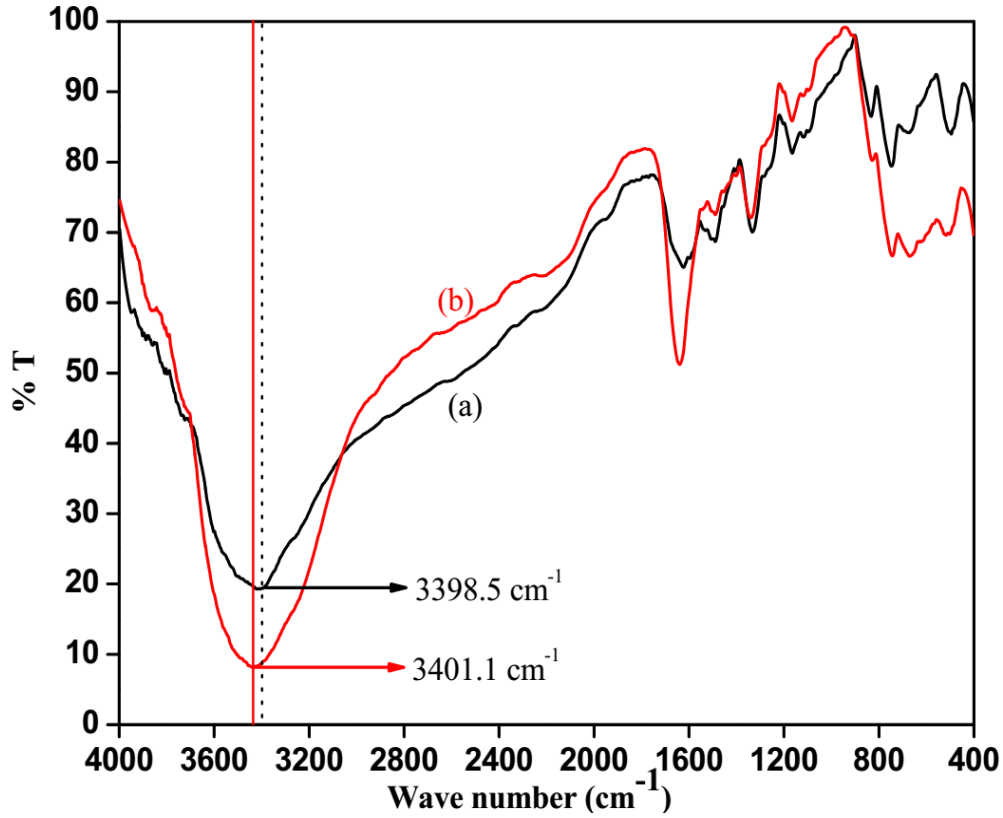

Figure 4A.1: FT-IR spectrum of PNASH in KBr disc (a) **Form – I** and (b) **Form –II** (shift of –O-H stretching frequencies have shown)

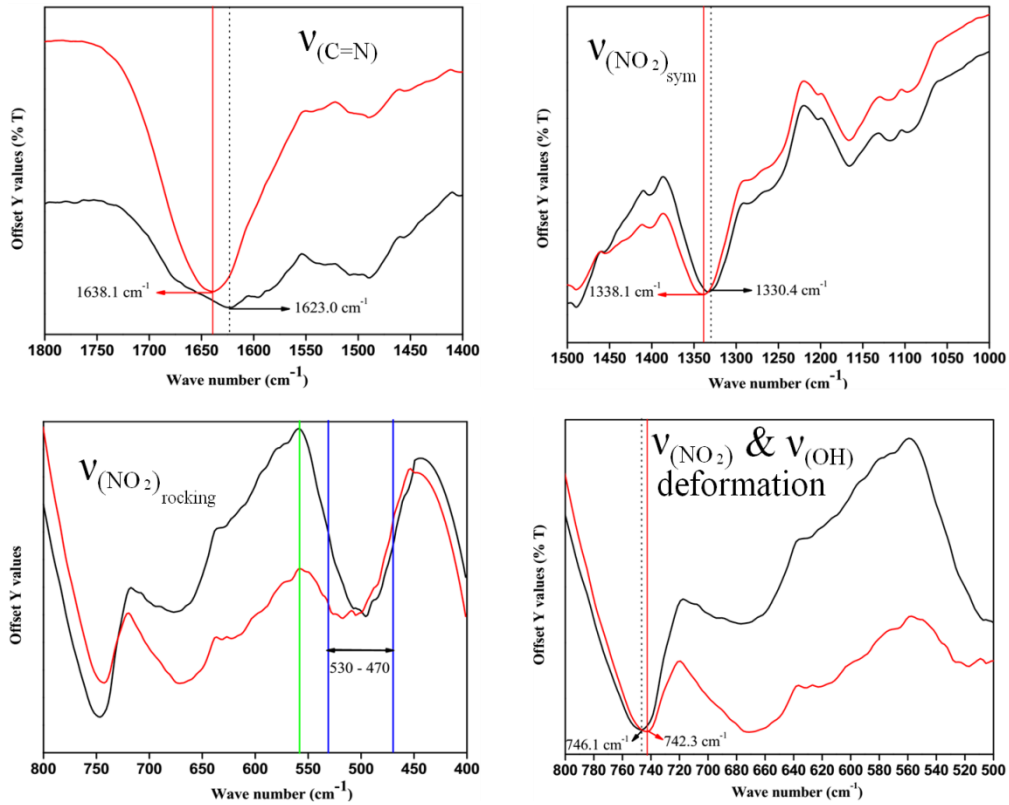

Figure 4A.2: Deconvolution FTIR spectra of **Forms-I** and **II**

Table 4A.1: *Characteristic IR absorption frequencies of **Forms-I** and **II***

Functional Group	Type of Vibration	Characteristic Absorptions (cm^{-1})		Intensity#
		Form-I	Form-II	
$\bar{\nu}_{(O—H)}$	Stretch, H-bond in Ar—OH	3398.5	3401.1	s
	Ar—OH (out of plane deformation)	746.1	742.3	s, br
$\bar{\nu}_{(C=N)}$	Stretch	1623.0	1638.1	s
$\bar{\nu}_{(NO2)}$	Ar—NO_2, symmetric stretch	1330.4	1338.1	vs
	Ar—NO_2, deformation	580 – 520	580 – 520	m
	Ar—NO_2, rocking	530 – 470	530 – 470	m-s

#, Data from Joseph B. Lambert, et al., Introduction to organic spectroscopy, Macmillan, New York publication, 1987.

†, s – strong, m – medium, w – weak, v – very, br – broad

4A.3: Electronic Absorption Spectra of PNASH

Electronic absorption spectra of PNASH recorded in several buffers are depicted in stacked view in **Figure 4A.3**. A bathochromic shift with increase of pH is observed. In the electronic absorption spectra of PNASH, there are two distinct peaks at ~250 nm (assigned to $\pi \rightarrow \pi^*$ transition) and at 375 nm (attributed to $n \rightarrow \pi^*$) which suffer red-shift with increased pH. An isosbestic point at about ~ 346 nm is recognised. The red shift and the presence of is isosbestic point strongly suggest an electronic isomerisation of PNASH from benzenoid form into a quinoid form upon deprotonation. The deprotonation equilibrium, **PNASH** $\rightleftharpoons$ **PNAS**$^-$ + H^+, is shown in the **Scheme 4A.1**. Curve-fitting of plots of absorbance versus pH at the λ_{max} gives the pK_a of PNASH as 5.9 and corresponding absorbance versus pH plot are shown in **Figure 4A.4**.

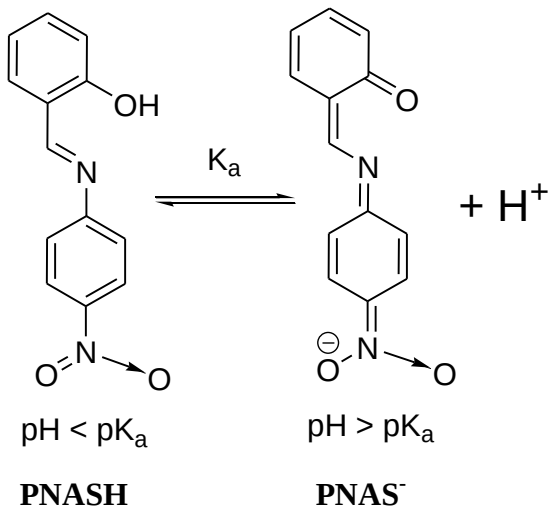

Scheme 4A.1

4A.4: Electronic Fluorescence Emission Spectra of PNASH

The fluorescence spectrum of PNASH in DMF solvent is presented in **Figure 4A.5** along with its closest higher energy electronic absorption spectrum. The effect of pH on the fluorescence spectrum has also been studies. Electronic fluorescence emission spectra of PNASH in DMF/Aq. buffers (1:9 v/v) have been recorded at 365 nm excitation wavelength. They are portrayed in 3D-stacking in **Figure 4A.6**. One can see a bathochromic shift with increase of pH. Fluorescence emissivity of PNASH in acid media is found to increase with

pH in the range 2-6 due to the dipole (non-linearity) character of the molecule. However, in basic pH range (8-12) the fluorescence emission intensities suffers a decrease with increase of the pH. These changes are assigned to the difference in π-cloud of quinoid benzenoid forms of PNASH. A typical uv-vis absorption and fluorescence emission spectra of PNASH at pH = 12 are shown in **Figure 4A.7** and corresponding data has been given in **Table 4A.2**. From stoke shift data one can see with increase of pHs of the solution there is decrease in the quantity of non-radiative decay energies.

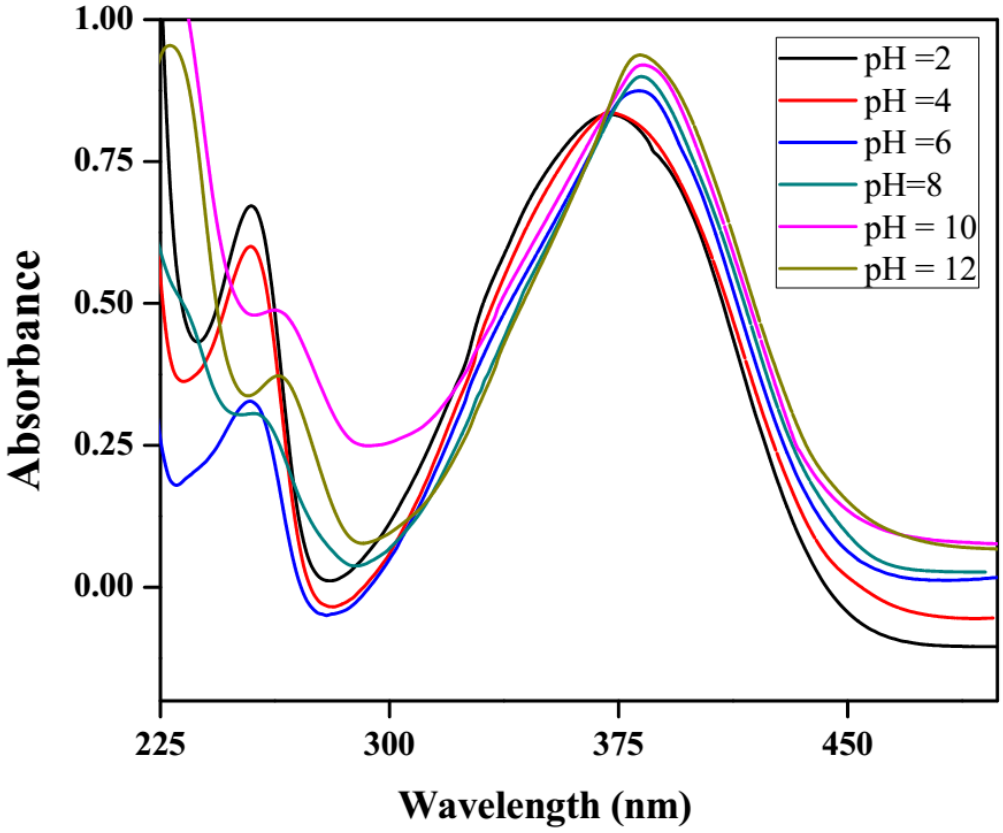

Figure 4A.3: Overlay Uv-visible absorption spectra of PNASH (1 x 10^{-5} M) in aqueous buffers

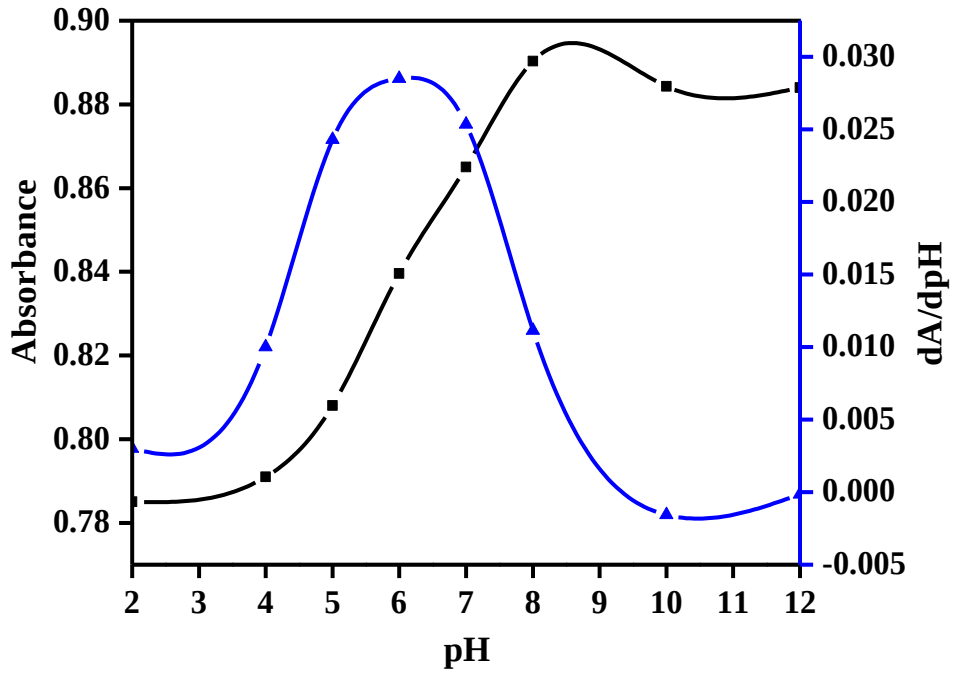

Figure 4A.4: Plot of absorbance versus pH of PNASH

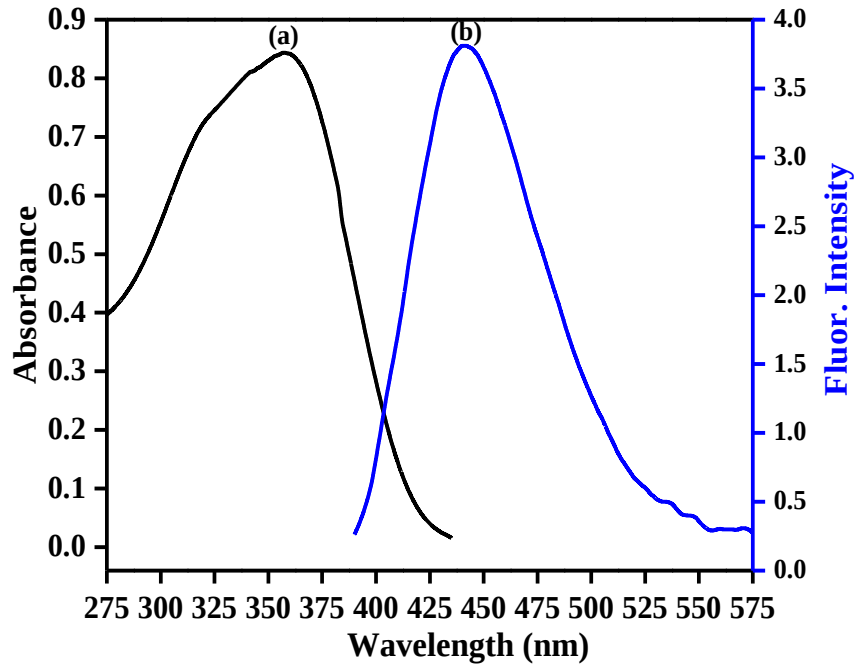

Figure 4A.5: Electronic absorption and fluorescence emission spectra of PNASH (1 x 10^{-5} M) in DMF (a) electronic absorption spectrum (b) fluorescence emission spectrum at 365 nm excitation wavelength

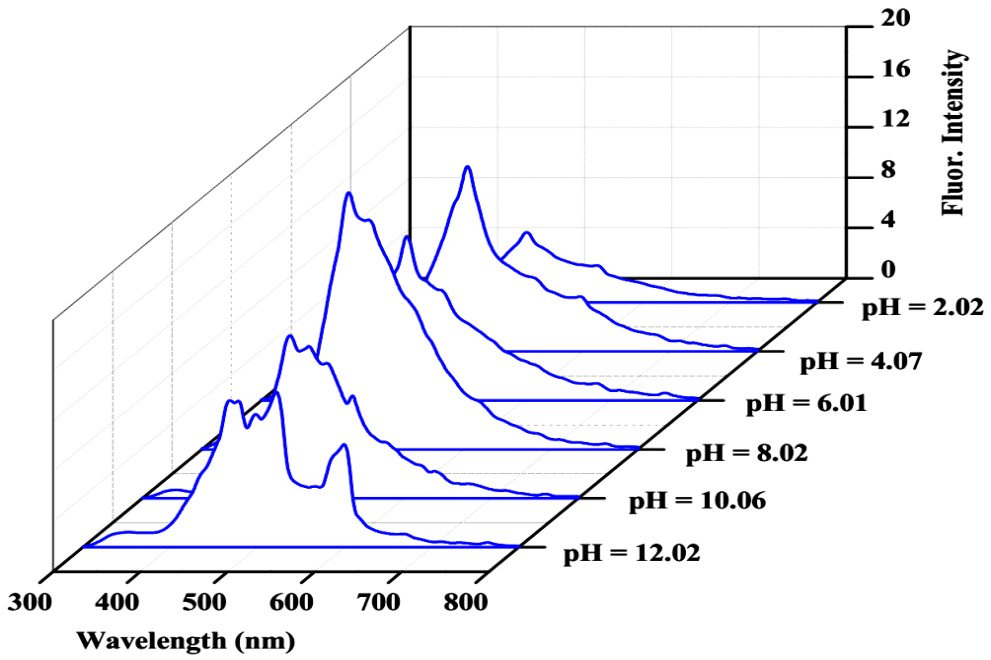

Figure 4A.6: Stacked electronic fluorescence emission spectra of PNASH ($1x10^{-5}$ M) in aqueous buffers (pH = 2 – 12) at 365 nm excitation wavelength

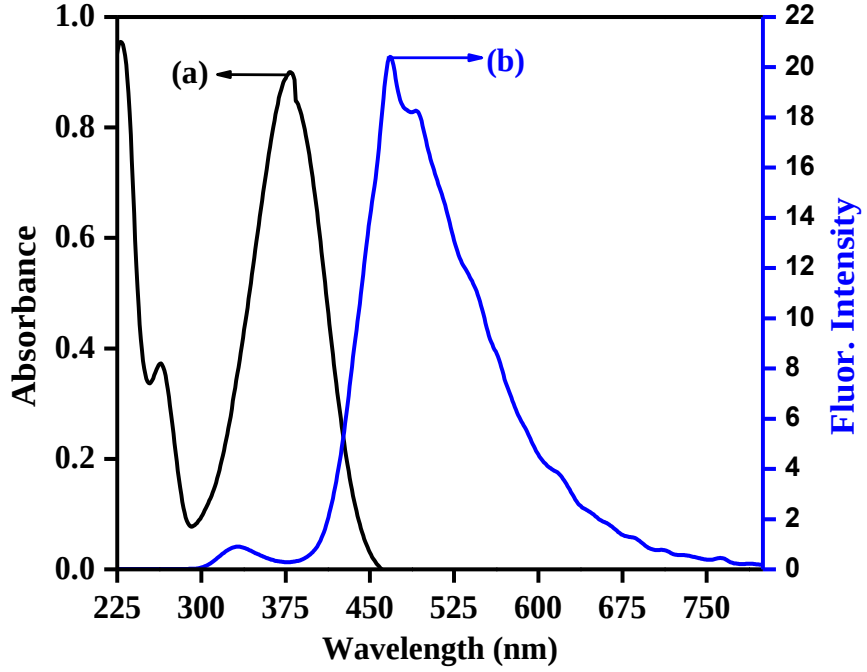

Figure 4A.7: Overlay of electronic absorption and emission spectra of PNASH (1×10^{-5} M) in 1:9 v/v DMF: pH = 12 buffer (a) absorption (b) fluorescence emission spectrum (excitation wavelength = 365 nm)

Table 4A.2: *Electronic absorption and fluorescence emission spectral data of PNASH*

pH	$\lambda_{absorption}$ (nm)	$\lambda_{emission}$ (nm)	Stokes Shift # (nm)
2.02	377.6	467.3	102.3
4.07	377.7	467.6	102.6
6.01	377.9	467.9	102.9
8.02	379.1	467.9	102.9
10.06	379.5	468.9	103.9
12.02	379.9	469.1	104.1
Non-aqueous	365.0	441.0	76.0

#, Data collected at excitation wavelength 365 nm

4A.5: Electrochemical Studies

PNASH is chemically weak acid. Due to the presence of phenolic group at the same time PNASH is also a base by being a Schiff base. The acid-base equilibrium of PNASH is already discussed in **section 4A.3**. In the pH range $2 \leq pH \leq pK_a$ the PNASH exits in benzenoid form only. Whereas $pK_a \leq pH \leq 12$ considerable quantity of $PNAS^-$ forms which in turn takes quinoid structure. Hence, a pH-dependent electrochemistry is expected for PNASH in pH range 2-12. In **Figures 4A.8-4A.9**, the cyclic voltammetric response in pH range 2-12 is shown. Irrespective of benzenoid and quinoid forms PNASH has electrochemically active nitro group. In low pH the azomethine group is the only electroreducible moiety besides nitro group. Whereas in alkaline pH quinone moieties are the electrochemical active zones. Usually, electrochemical reduction potentials of nitro and azomethine groups are very close[5,6]. Hence, a broad and single cyclic voltammetric profile is expected. The cyclic voltammograms show in (a), (b) and (c) of **Figure 4A.8** is concur with this expectations.

As mentioned above, in the alkaline media three reduction peaks due to ortho-quinoid, para-azomethine moieties and nitrozo moieties of $PNAS^-$ are expected. The cyclic voltammograms of (d), (e) and (f) of **Figure 4A.8** are in line with this argument.

Using Randles–Sevcik equation for irreversible electron transfer process[7,8], various electrochemical parameters have been evaluated and the same are presented in **Table 4A.3**. In **Figure 4A.10** through **4A.12** are shown the cyclic voltammograms exhibiting the effect of scan rate on the cyclic voltammetric profile at the pHs 2, 8 and 12 respectively. In this figures the details of electron transfer are more resolved for various electrochemical sites than at low scan rate. In **Figure 4A.13** through **4A.15** the effect of scan rate on the peak current (i_p) is presented for both i_p versus ν and i_p versus $\nu^{1/2}$. The regression coefficients of plots of i_p versus ν are not only higher than those of i_p versus $\nu^{1/2}$ but also closer to 1. This suggests that the electron transfer process at PNASH and $PNAS^-$ are mostly adsorption-controlled on SMDE electrode.

Similarly, the oxidative behavior of PNASH and $PNAS^-$ are studied on glassy carbon electrode in the anodic scan in the potential range -1.5V to +1.5V versus SCE. Some of the cyclic voltammograms are shown in **Figures 4A.16** through **4A.19** recorded at selected buffers. The effect of scan rate on the peak currents are shown in the **Figures 4A.20** through **4A.23**. The plots of peak current versus scan rate indicates diffusion controlled electron transfer for PNASH and $PNAS^-$ The electron transfer mechanism of PNASH in aqueous media is presented in **Scheme 4A.2**.

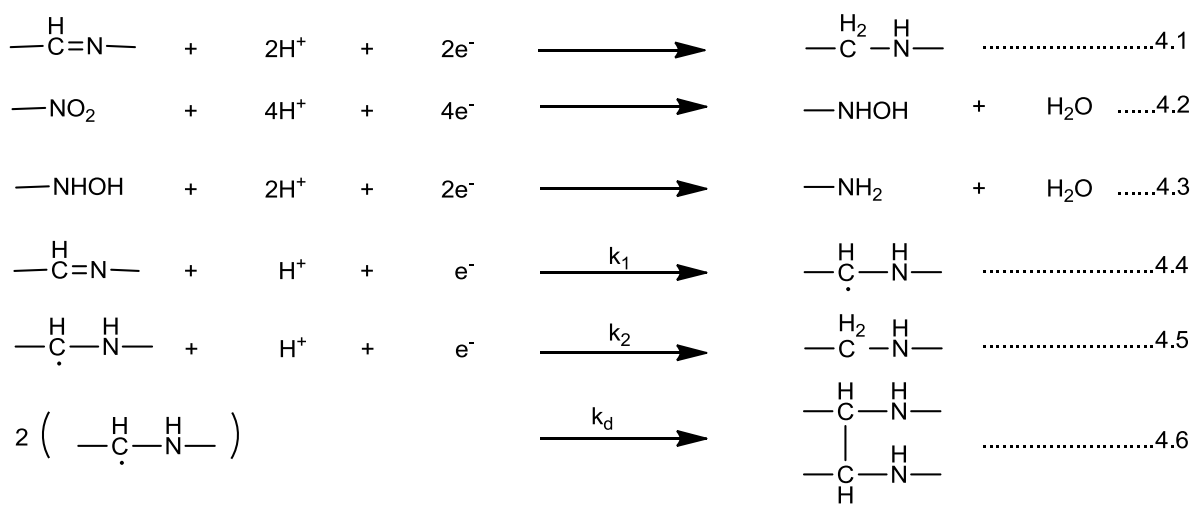

Scheme 4A.2

where k_1 and k_2 are the intrinsic heterogeneous rate constants.

When $k_1 >>> k_2$, the first reaction triggers a parallel dimerisation process (**4.6**)

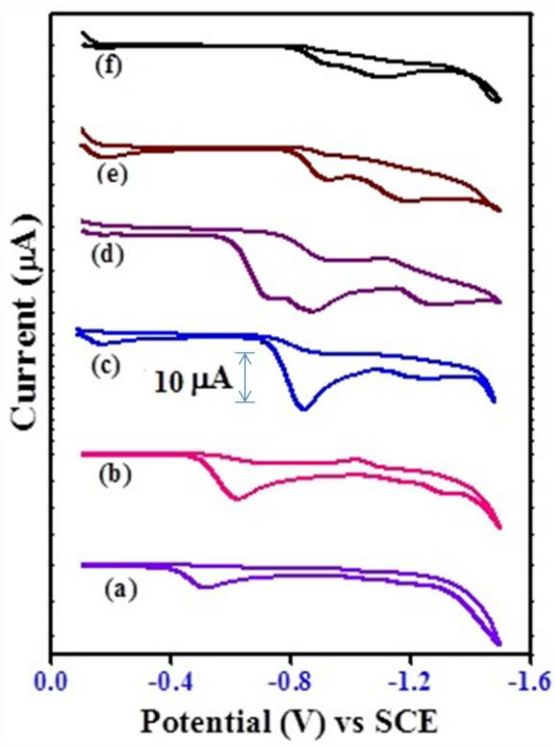

Figure 4A.8: Stacked cathodic sweep cyclic voltammograms of PNASH (1 x 10^{-5} M) on SMDE in aqueous buffers of pH (a) 2.02 (b) 4.07 (c) 6.01 (d) 8.02 (e) 10.06 (f) 12.02

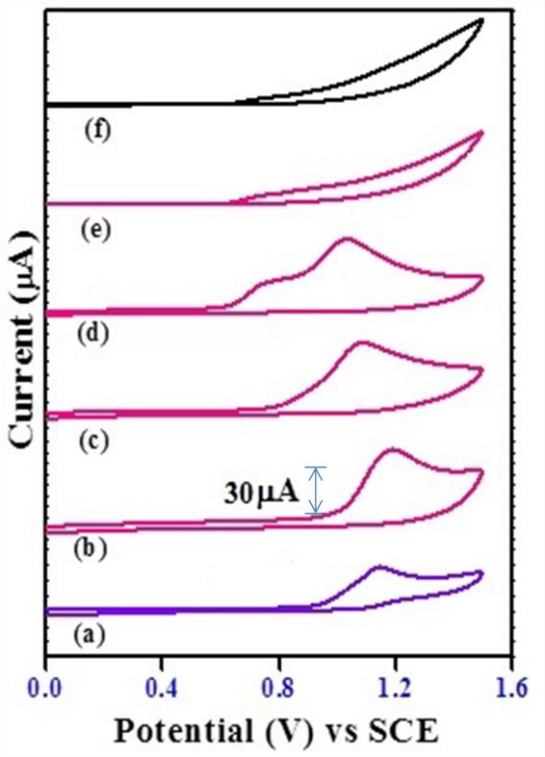

Figure 4A.9: Stacked anodic sweep cyclic voltammograms of PNASH (1 x 10^{-5} M) on SMDE in aqueous buffers of pH (a) 2.02 (b) 4.07 (c) 6.01 (d) 8.02 (e) 10.06 (f) 12.02

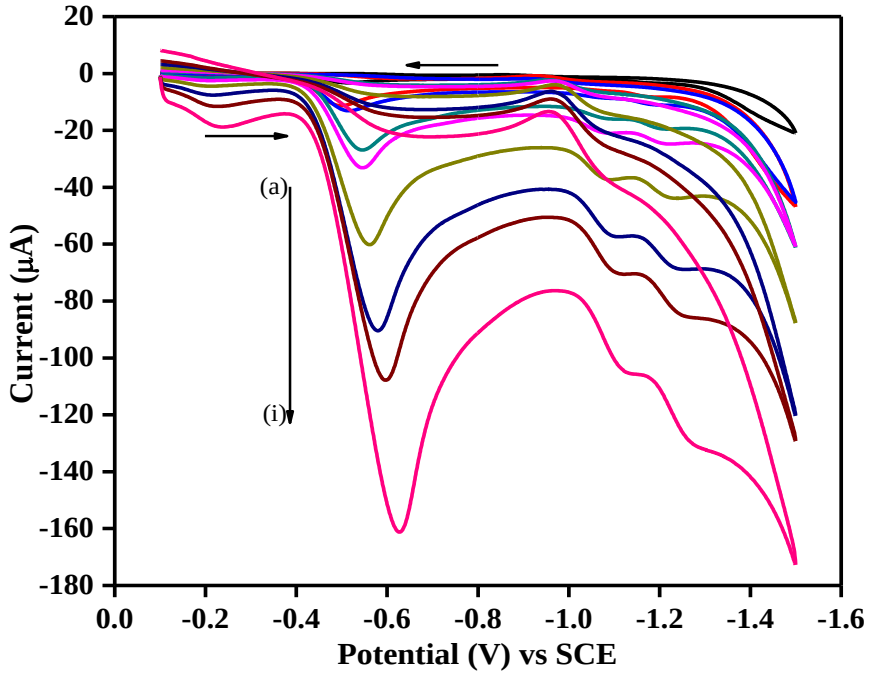

Figure 4A.10: Cyclic voltammograms of PNASH (1 x 10^{-5} M) in 1:9 v/v DMF/aq. Buffer media of pH = 2.02, on SMDE at various scan rate (a) 20 mVs^{-1} (b) 50 mVs^{-1} (c) 100 mVs^{-1} (d) 600 mVs^{-1} (e) 1000 mVs^{-1} (f) 1500 mVs^{-1} (g) 2000 mVs^{-1} (h) 3000 mVs^{-1} (i) 5000 mVs^{-1}

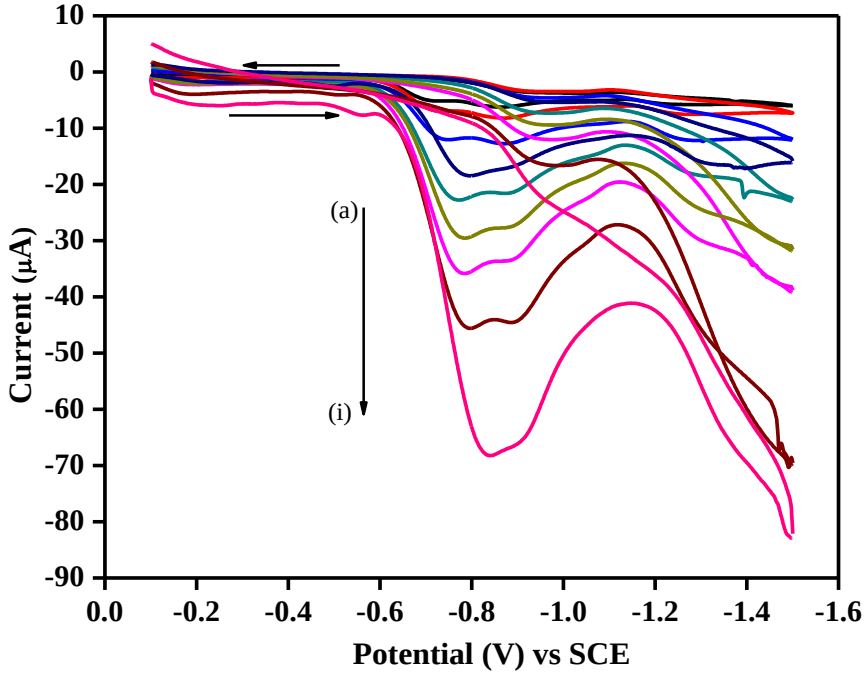

Figure 4A.11: Cyclic voltammograms of PNASH (1 x 10^{-5} M) in 1:9 v/v DMF/aq. Buffer media of pH = 8.02, on SMDE at various scan rate (a) 20 mVs^{-1} (b) 50 mVs^{-1} (c) 100 mVs^{-1} (d) 600 mVs^{-1} (e) 1000 mVs^{-1} (f) 1500 mVs^{-1} (g) 2000 mVs^{-1} (h) 3000 mVs^{-1} (i) 5000 mVs^{-1}

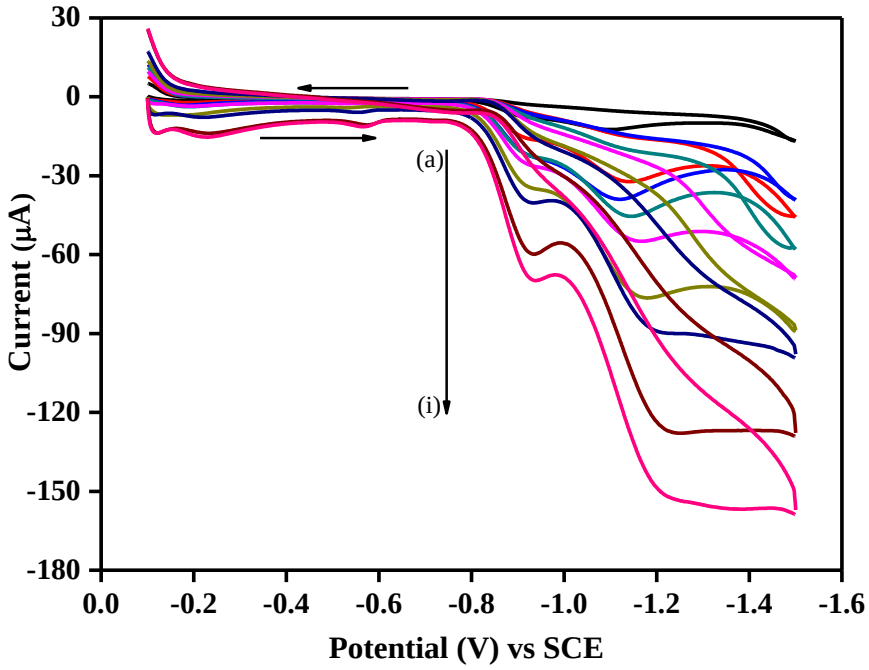

Figure 4A.12: Cyclic voltammograms of PNASH (1 x 10^{-5} M) in 1:9 v/v DMF/aq. Buffer media of pH = 12.02, on SMDE at various scan rate (a) 20 mVs^{-1} (b) 50 mVs^{-1} (c) 100 mVs^{-1} (d) 600 mVs^{-1} (e) 1000 mVs^{-1} (f) 1500 mVs^{-1} (g) 2000 mVs^{-1} (h) 3000 mVs^{-1} (i) 5000 mVs^{-1}

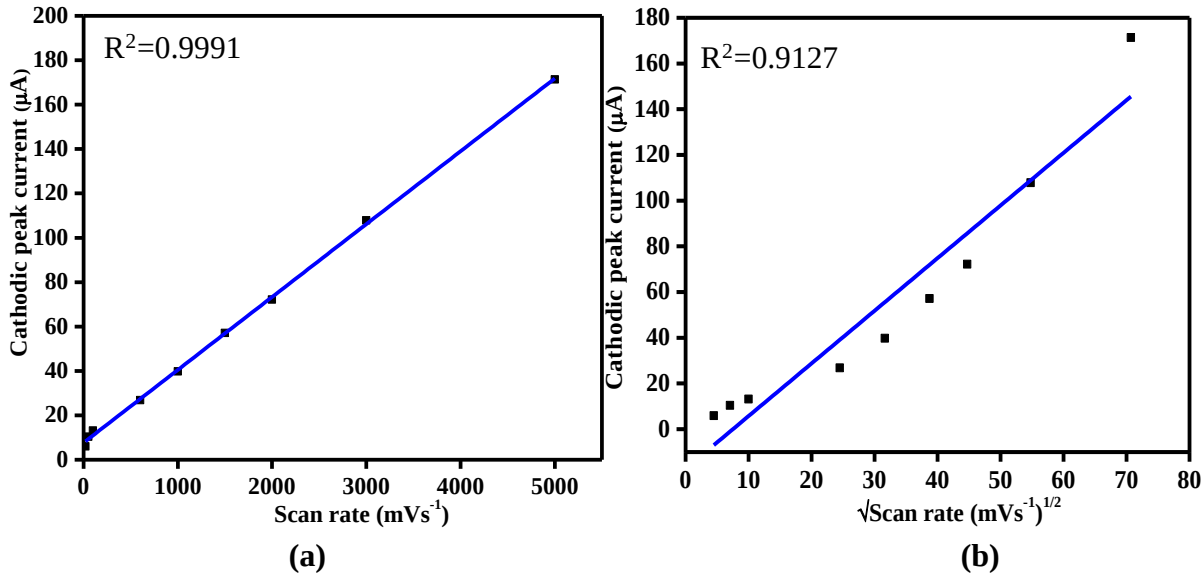

Figure 4A.13: Effect of scan rate on cathodic peak current in 1:9 v/v DMF/aq. Buffer media of pH = 2.02 (a) ν versus i_{pc} (b) $\nu^{1/2}$ versus i_{pc}

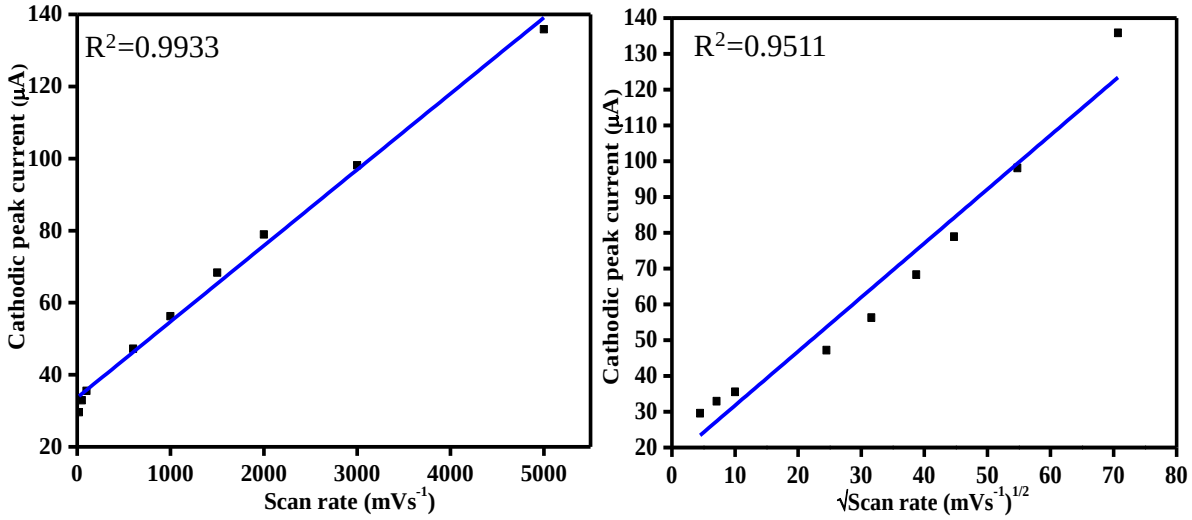

(a) **(b)**

Figure 4A.14: Effect of scan rate on cathodic peak current in 1:9 v/v DMF/aq. Buffer media of pH = 8.02 (a) ν versus i_{pc} (b) $\nu^{1/2}$ versus i_{pc}

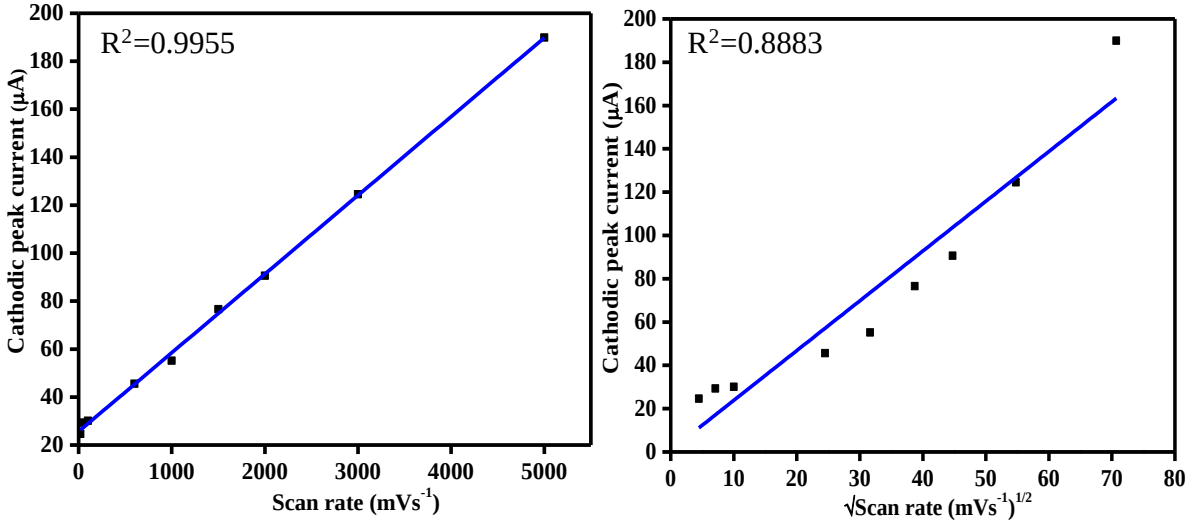

(a) **(b)**

Figure 4A.15: Effect of scan rate on cathodic peak current in 1:9 v/v DMF/aq. Buffer medium of pH = 12.02 (a) ν versus i_{pc} (b) $\nu^{1/2}$ versus i_{pc}

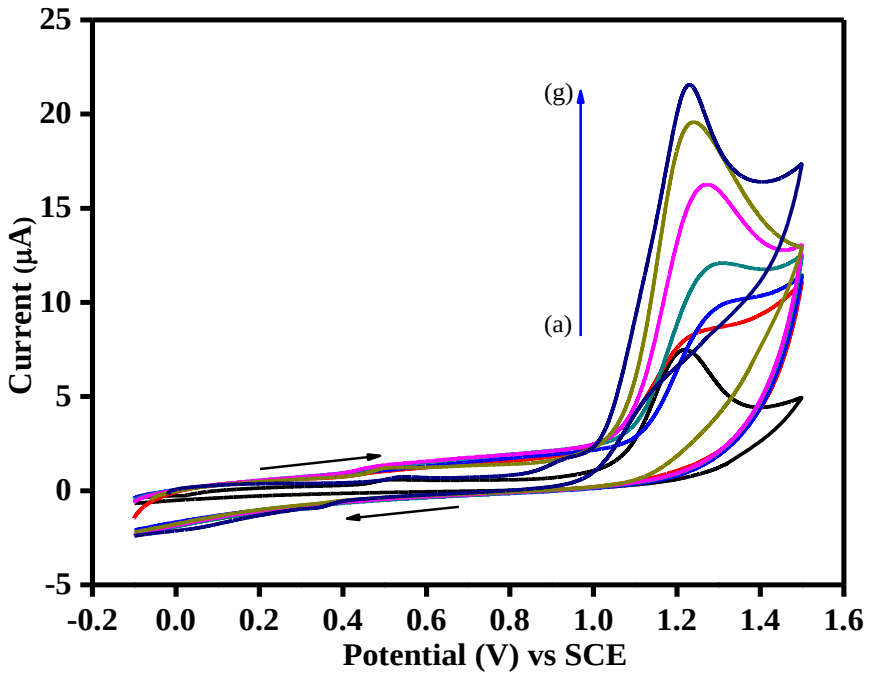

Figure 4A.16: Cyclic voltammograms of PNASH (1 x 10^{-5} M) in 1:9 v/v DMF/aq. Buffer media of pH = 2.02, on GCE at various scan rate (a) 20 mVs^{-1} (b) 50 mVs^{-1} (c) 100 mVs^{-1} (d) 200 mVs^{-1} (e) 300 mVs^{-1} (f) 400 mVs^{-1} (g) 500 mVs^{-1}

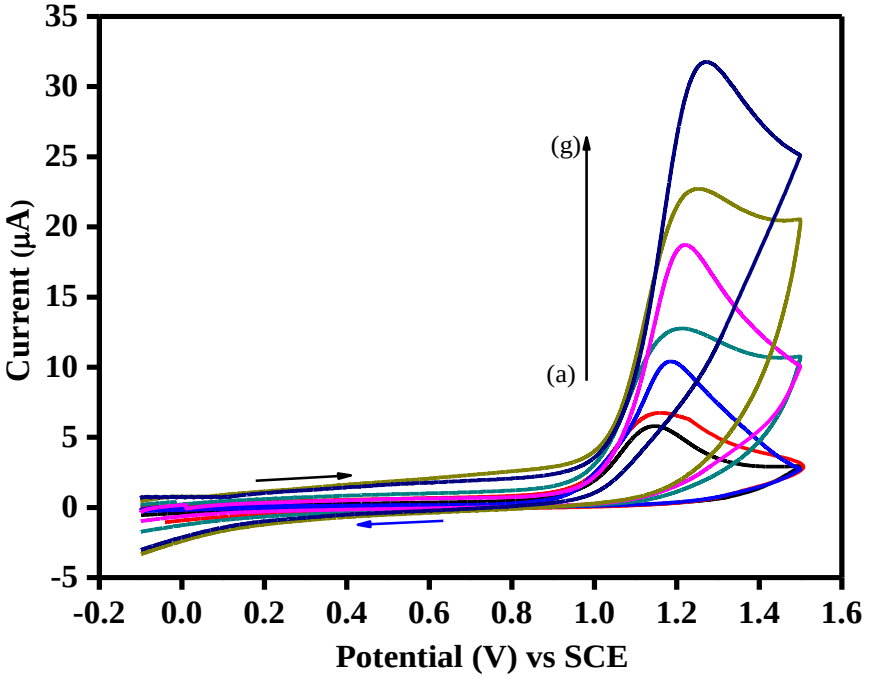

Figure 4A.17: Cyclic voltammograms of PNASH (1 x 10^{-5} M) in 1:9 v/v DMF/aq. Buffer media of pH = 4.07, on GCE at various scan rate (a) 20 mVs^{-1} (b) 50 mVs^{-1} (c) 100 mVs^{-1} (d) 200 mVs^{-1} (e) 300 mVs^{-1} (f) 400 mVs^{-1} (g) 500 mVs^{-1}

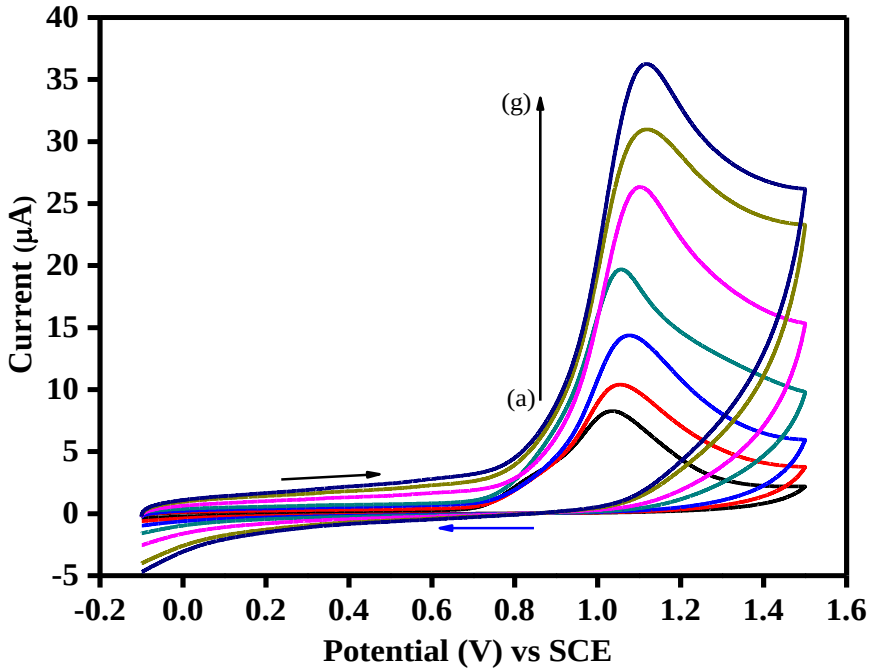

Figure 4A.18: Cyclic voltammograms of PNASH (1 x 10^{-5} M) in 1:9 v/v DMF/aq. Buffer media of pH = 6.01, on GCE at various scan rate (a) 20 mVs^{-1} (b) 50 mVs^{-1} (c) 100 mVs^{-1} (d) 200 mVs^{-1} (e) 300 mVs^{-1} (f) 400 mVs^{-1} (g) 500 mVs^{-1}

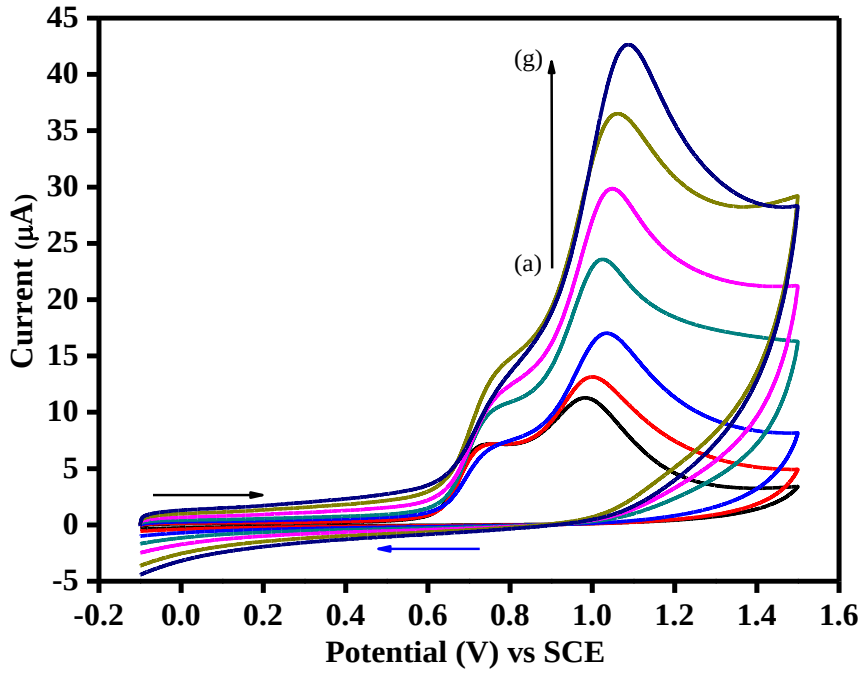

Figure 4A.19: Cyclic voltammograms of PNASH (1 x 10^{-5} M) in 1:9 v/v DMF/aq. Buffer media of pH = 8.02, on GCE at various scan rate (a) 20 mVs^{-1} (b) 50 mVs^{-1} (c) 100 mVs^{-1} (d) 200 mVs^{-1} (e) 300 mVs^{-1} (f) 400 mVs^{-1} (g) 500 mVs^{-1}

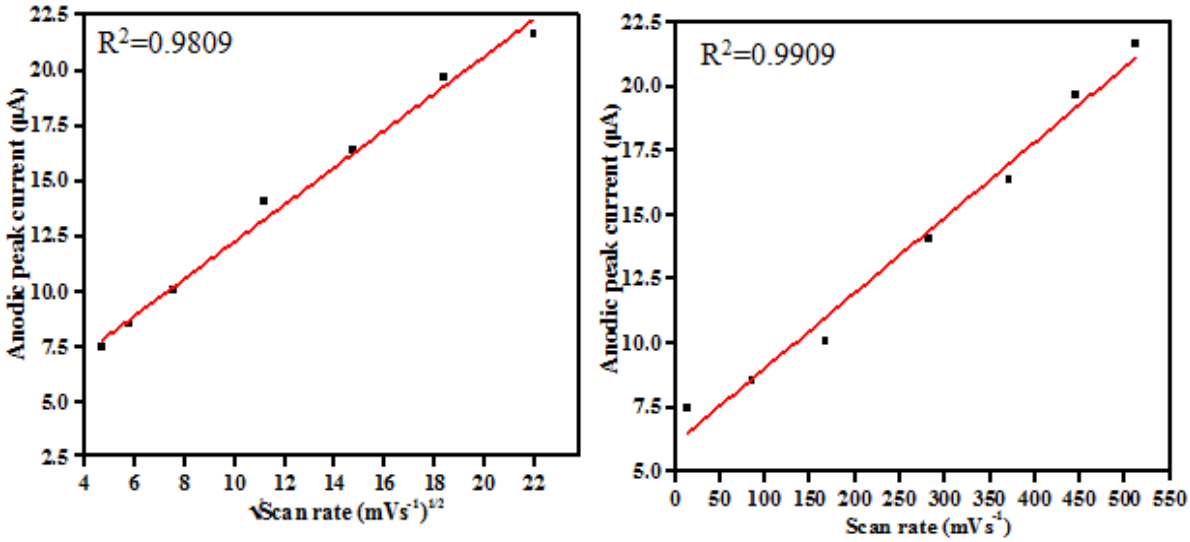

(a) **(b)**

Figure 4A.20: Effect of scan rate on anodic peak current in 1:9 v/v DMF/aq. Buffer medium of pH = 2.02 (a) $\nu^{1/2}$ versus i_{pc} (b) ν versus i_{pc}

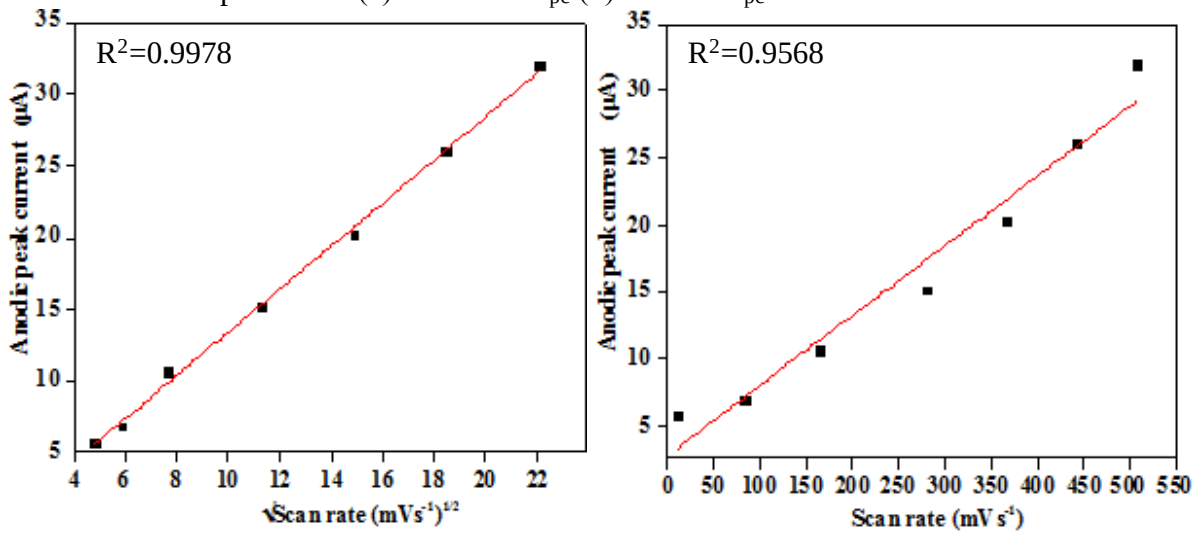

(a) **(b)**

Figure 4A.21: Effect of scan rate on anodic peak current in 1:9 v/v DMF/aq. Buffer medium of pH = 4.07 (a) $\nu^{1/2}$ versus i_{pc} (b) ν versus i_{pc}

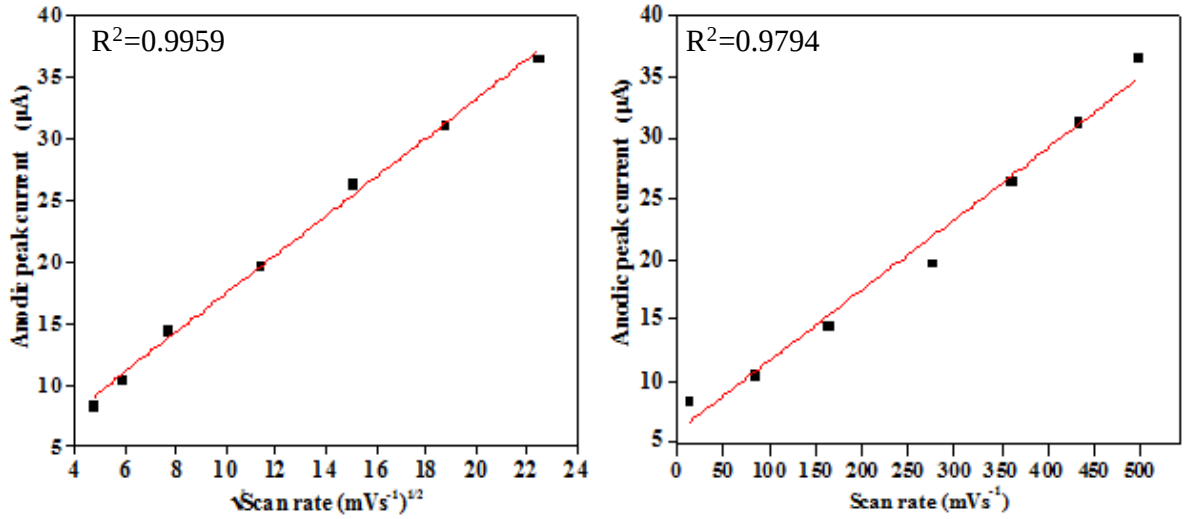

(a) **(b)**

Figure 4A.22: Effect of scan rate on anodic peak current in 1:9 v/v DMF/aq. Buffer medium of pH = 6.01 (a) $v^{1/2}$ versus i_{pc} (b) ν versus i_{pc}

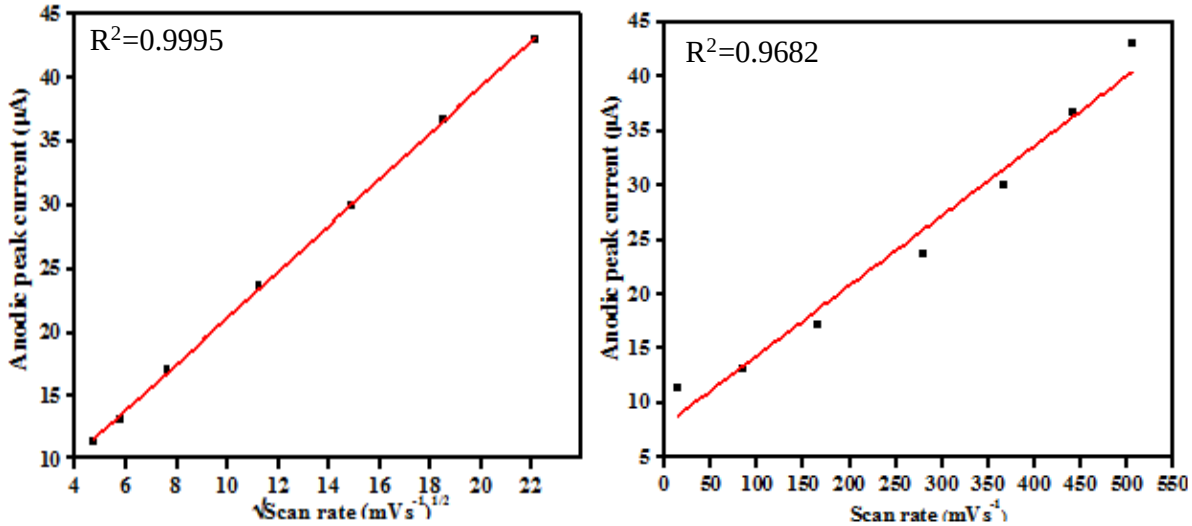

(a) **(b)**

Figure 4A.23: Effect of scan rate on anodic peak current in 1:9 v/v DMF/aq. Buffer medium of pH = 8.02 (a) $v^{1/2}$ versus i_{pc} (b) ν versus i_{pc}

4A.6: Linear Sweep Voltammetric Assaying of PNASH

As PNASH exhibits simple and highly defined irreversible cyclic voltammetric profile in the buffers pH = 6 at scan rate of 100 mVs^{-1}, a quantitative analysis of PNASH using linear sweep voltammetric technique has been attempted.

In **Figure 4A.24** is shown a calibration plot for PNASH. The reductive electrochemistry of PNASH is mostly hydrogenation. In order to understand aprotic electron transfer behavior of

PNASH, its non-aqueous electrochemistry by cyclic voltammetry has been undertaken in dimethyl formamide with tetraethyl ammonium perchlorate as the supporting electrolyte.

In **Figure 4A.25** the cyclic voltammogram of PNASH in wide potential range on the glassy carbon electrode an irreversible cathodic response observed at 0.25 V whereas another anodic irreversible response observed at -0.23 V.

Based on the information available in the literature non-aqueous electrochemistry of azomethine group a plausible reduction mechanism[9] is proposed in **Scheme 4A.3** for PNASH.

Anodic reaction

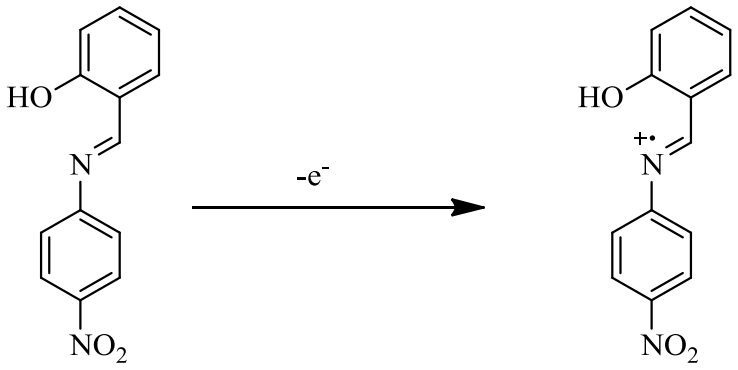

Cathodic reaction

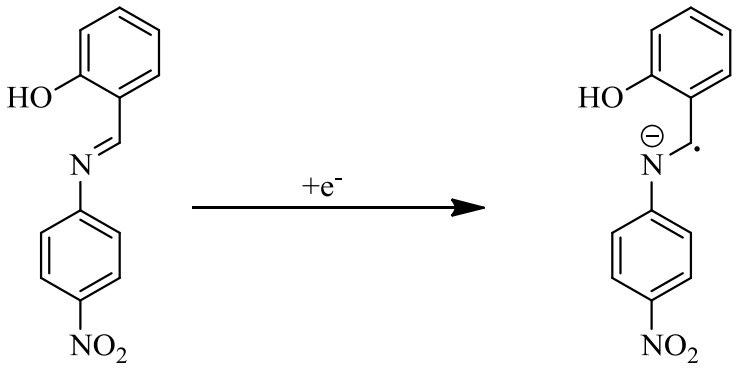

Sheme 4A.3

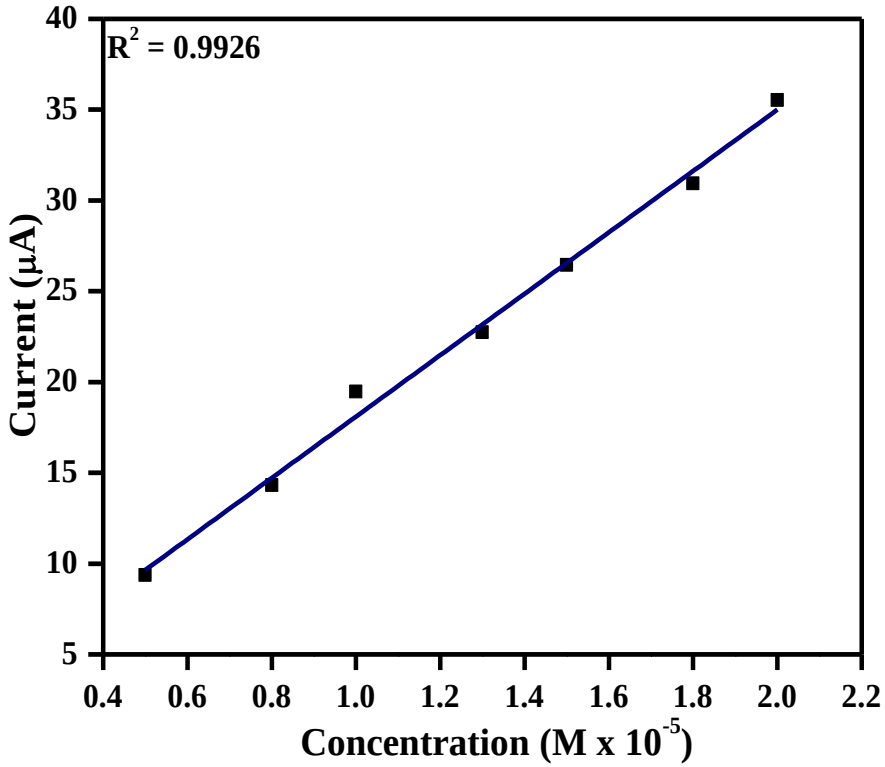

Figure 4A.24: Calibration plot of PNASH

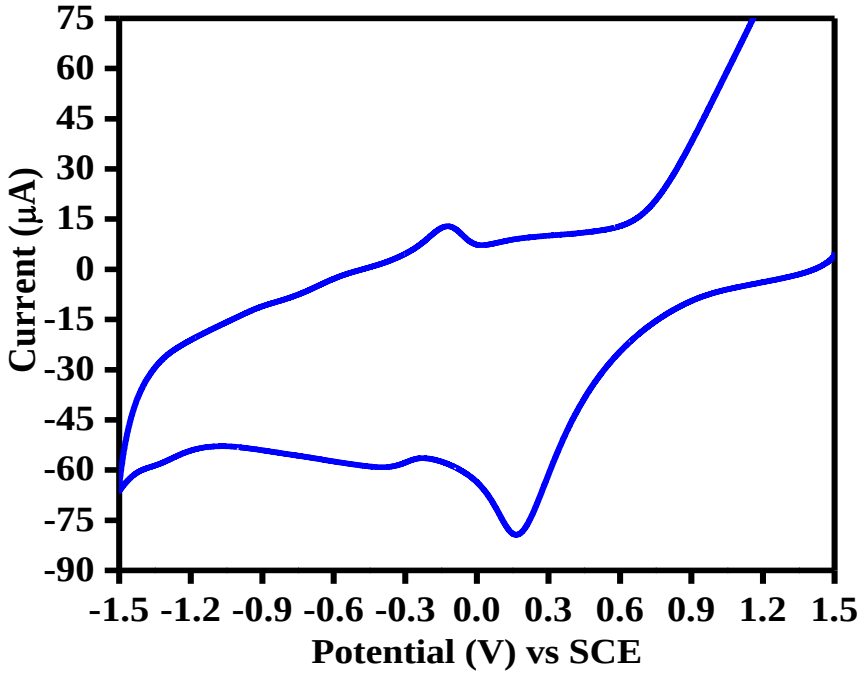

Figure 4A.25: Cyclic voltammogram of PNASH (1×10^{-5} M) in DMF on GCE at Scan rate, 3000 mVs^{-1}, with TEAP (0.1M)

Table 4A.3: *Cyclic voltammetric data of PNASH*

pH	$-E_p$ (V)	α_{na} (mV)	k^o_h x10^9 (cm^2 s^{-1})	D_o x 10^6 (cm^2 s^{-1})
2.02	0.516	0.21	4.11	6.18
4.07	0.619	0.36	3.51	6.32
6.01	0.857	0.39	3.14	6.45
8.02	0.874	0.41	2.67	7.12
10.06	1.122	0.49	2.13	7.71
12.02	1.132	0.55	1.76	8.19

PART B: PHOTOCHROMIC, MECHANOCHROMIC, THERMOCHROMIC AND POLYMORPHIC STUDIES OF PNASH

4B.1: Photochromism/Photo switching of PNASH

Electronic fluorescence emission spectra of PNASH in non-aqueous medium and that after a time interval of 10 minutes (recorded at 365 nm excitation wavelength) are presented in **Figure 4B.1**. The peak at 450 nm, as already mentioned is due to the $n \rightarrow \pi^*$ electronic transition in both immediate and after 10 minutes irradiation. One can see a new peak emerged at about 550 nm after irradiation. This new peak is tentatively assigned to the photo-induced tautomerism of PNASH as shown in **Scheme 2**. At the same time the intensity of the fluorescence emission band at ~450 nm has corresponding upon irradiation. Mathematical combination of areas before and after irradiation under the curve(s) is found near constant. However, PNASH solid state fluorescence spectra (**Figure 4A.2**) have been recorded in both immediate and after 10 minutes irradiation. This indicates that the area submerged by the photo-induced proton transformation phenomenon of PNASH is reversible. From this, one can say PNASH is *photo-switching* in between the **Form - (a)** and **Form - (b)** as shown in **Scheme 2**. The electronic fluorescence emission spectrum of PNASH in solid state at 365 nm excited radiation is presented in **Figure 4B.3**. From the figure, one can see two distinct peaks noticed at ~ 460 nm (weak) and ~ 600 nm (intense) whereas in solution state, thus are noticed at ~ 450 nm and ~ 540 nm. One can see a correlation between solution and solid state spectra such that solution state emission line at ~450 nm is related to the solid state emission at ~460 nm and that at ~540 nm to that at ~600 nm. These bathochromic shift are attributed to the population of **Form – (a)** and **Form – (b)** in solution (free molecule) and solid (lattice-locked) states. In other words, PNASH is understood to be crystallized predominantly in **Form – (b)** which is relatively under strain.

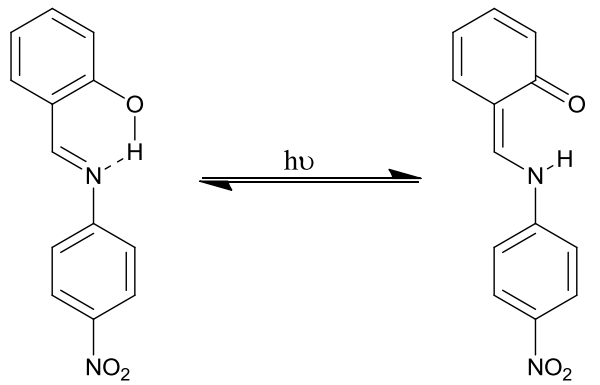

Form-(a) **Form-(b)**

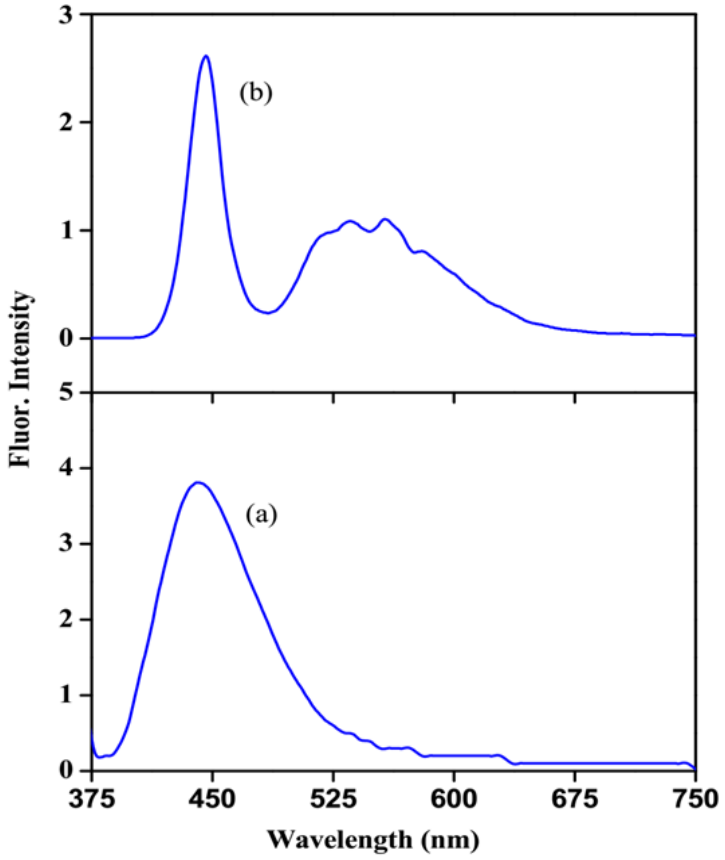

Figure 4B.1: Fluorescence spectra of PNASH (a) in solution ($1x10^{-5}$ M) (b) after 10 min irradiation with excitation at 365 nm

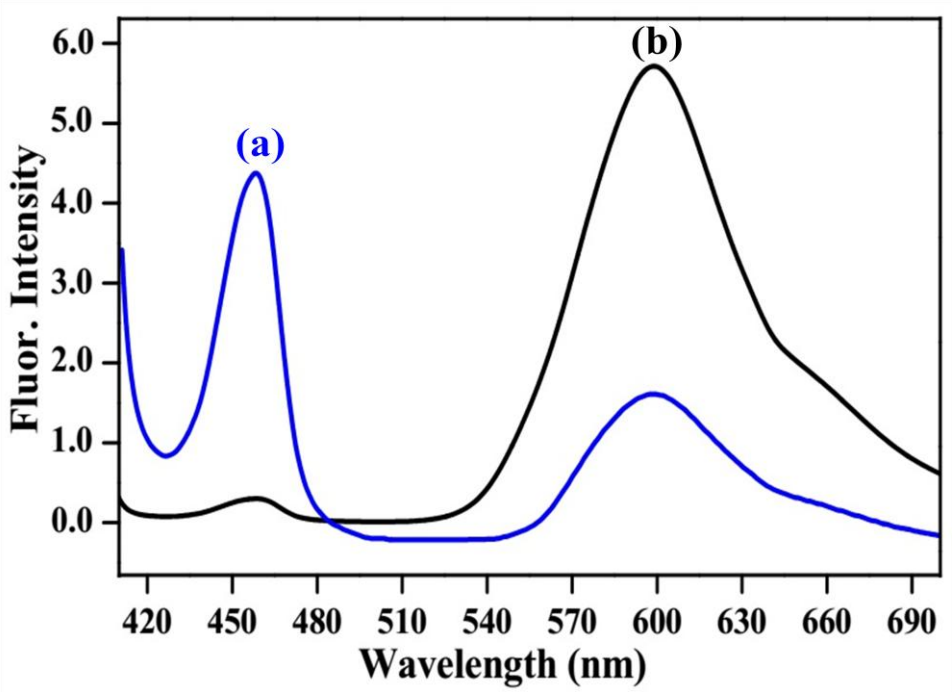

Figure 4B.2: Fluorescence spectra of PNASH (a) instantly (b) after 10 min irradiation with excitation at 365 nm

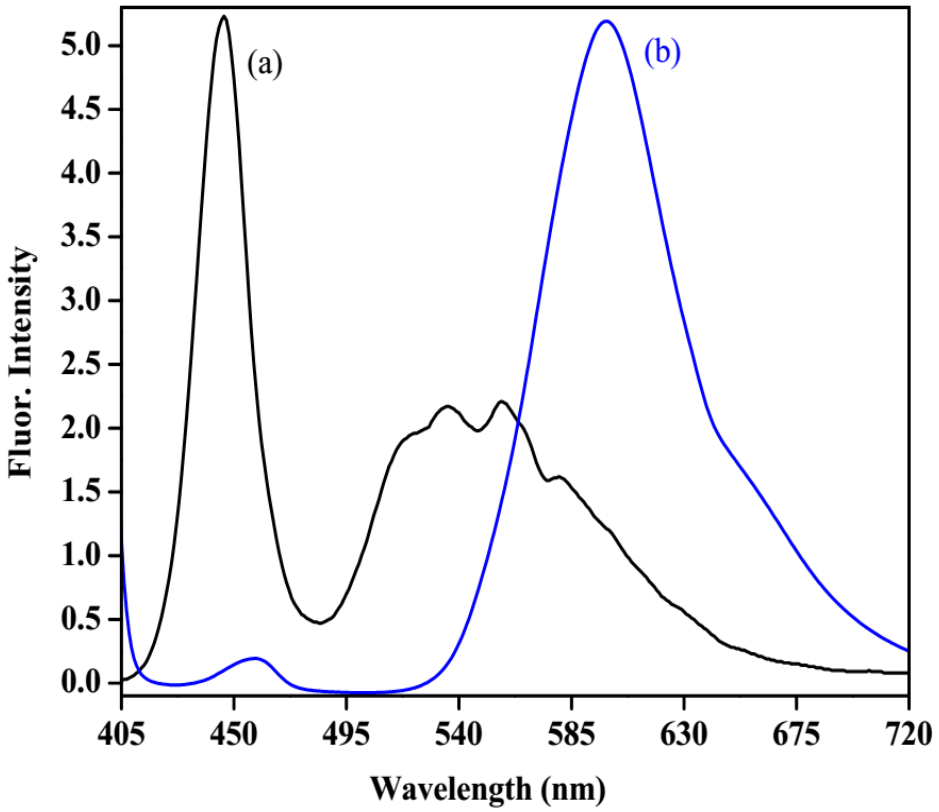

Figure 4B.3: Fluorescence spectra of PNASH under irradiation with 365 nm in (a) solution ($1x10^{-5}$ M) and (b) polycrystalline states

4B.2: Mechanochromism and Thermochromism of PNASH

When PNASH was ground, the otherwise orange colored material turns yellow. Those orange and yellow color powders of PNASH are shown in **Figure 4B.4**. These two chromo-forms were crystallized from different solvents. Form of crystals obtained from ethyl acetate (**EtOAc**) is denoted as **Form – I**, while that from acetonitrile (**MeCN**) as **Form – II**. The ground powder is labeled as **Form – III**. **Form – I** and **Form – II** though obtained without grinding from different solvents, are different in their morphology as shown in **Figure 4B.5**. The DSC calorigrams of **Forms – I, II** and **III** are presented in **Figure 4B.6**. This kind of phenomenon is known as reversible thermochromism. During heat-cool cyclic process **Form – I** turns from orange to deep red while **Form – II** crystals turned from pale yellow to red as shown in **Figure 4B.7**. This thermochromism suggests possible crystallographic reorganization during the thermal episodes. The crystallographic stabilization of these forms are discussed in part C of this Chapter.

(a) (b)

Figure 4B.4: Photographs show that the colors of the powders of PNASH (a) orange color unground; (b) pale yellow color ground (**Form – III**) shows the mechanochromism.

(a) **(b)**

Figure 4B.5: Micrographs show the morphologies of crystals of PNASH (a) **Form – I** (prismatic shape) and (b) **Form – II** (rectangular blocks).

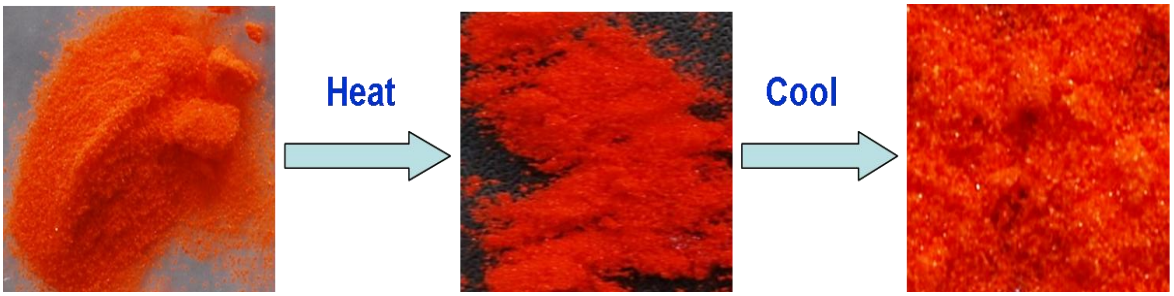

(a)

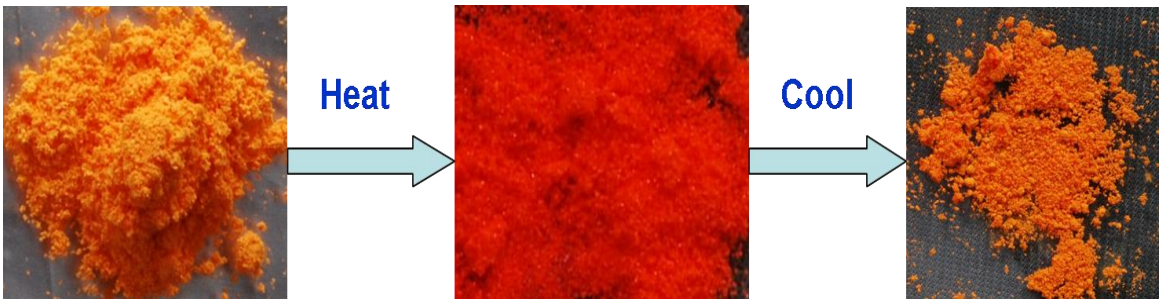

(b)

Figure 4B.6: Photographs show the reversible thermochromism of PNASH (a) unground polycrystalline powder (orange colour) (b) ground polycrystalline powder (**Form – III** yellow color)

(a)

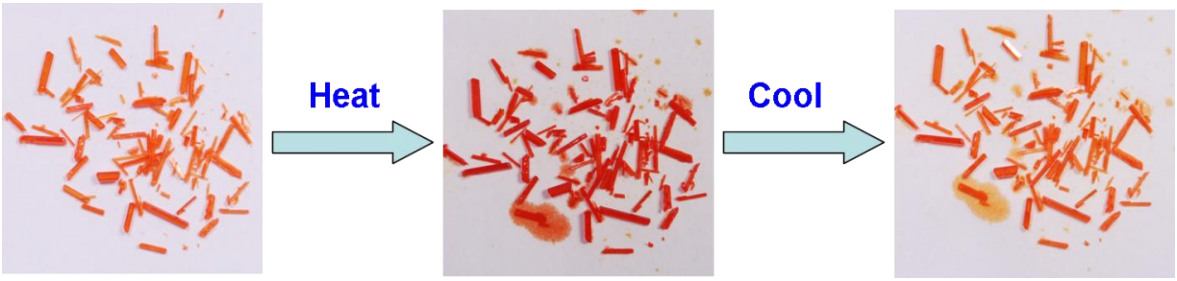

(b)

Figure 4B.7: Reversible thermochromism in crystals of **Forms – I** and **II**, (a) **Form – I** (orange to thick red) (b) **Form – II** (pale yellow to thick red)

4B.3: Differential Scanning Calorimetric (DSC) Studies

In order to critically investigate the thermochromic behavior of PNASH Differential Scanning Calorimetric (DSC) studies have been undertaken on its various forms viz., **Form – I**, **Form – II** and **Form – III**. The DSC thermogram of **Form – I** crystals is shown in **Figure 4B.8**. One can see a major endotherm at 161.44 $^{\circ}$C (enthalpy of fusion: 77.96 kJ mol^{-}

[1]), attributed to its melting event. The thermograms of **Form – II** crystals is depicted in **Figure 4B.9**. One can see here two endotherms at 119.67 °C (enthalpy of transition: 3.396 kJ mol^{-1}) that could be interpreted to a solid–solid phase transition and a major endotherm at 156.88 °C (25.33 kJ mol^{-1}) corresponding to a melting event. A cyclic *heat – cool – heat* studies have been carried out over **Form – I**, **Form – II** and **Form – III** to understand the reversibility nature of the phase transition. From the studies, it is noticed that the thermograms of these forms are not similar. **Form – I** has a clear single endothermic peak at ~166 °C whereas **Form – II** yields two broad (diffuse) peaks, one at ~ 120 °C and another at ~159 °C. The pale yellow ground powder (**Form – III**) shows a major endotherm at ~120 °C and a melting event at ~159 °C (since the thermogram of **Form – III** has partial features of both **Form – I** and **Form – II** the calorimetry of **Form – II** is revisited). In **Figure 4B.10** is shown the calorimetric studies of **Form – II** under various controls. Curve (a) in that figure is the used wide – temperature range (60 – 180 °C) thermograms. This feature repeated after cooling and reheating. Curve (b) is calorigram of **Form – II** in short range of temperature (60 – 120 °C) well before the fusion point. This calorigram shows the early thermal event at ~119 °C. However, this does not repeat after cooling and reheating. Instead, it traces similar to the calorigram as shown in curve (c). This feature indicates a distinct morphological difference between **Form – I** and **II**. A magnified image of **Form – III** in **Figure 4B.11** between the temperature range 115 – 140 °C indicates the presence of **Form – II** also in a slight quantity alone with **Form – I** in larger amounts. The crystallography of **Form – I** and **II** is discussed in part C of this Chapter. The corresponding thermograms of **Froms – I**, **II** and **III** are presented in **Figure 4B.11**. The data obtained from the thermal analysis is given in **Table 4B.1**. In **Figure 4B.12**, thermogram of *heat – cool – heat* of **Form – II** shows an endotherm peak at ~ 119.67 °C and which was disappeared in second run. Thermodynamic analysis of the DSC data has been carried, which provided an excellent basis for the construction of a qualitative energy–temperature diagram (in **Figure 4B.13**)[10]. The difference in melting temperature is insignificant (**Table 4B.1**). Hence, from the heat of transition and heat of fusion rules, polymorphic enantiotropy is attributed between **Forms – I** and **II** and between **Forms – I** and **III**. **Form – I** is thermodynamically a stable polymorph. **Form – II** is assigned as a meta-stable polymorph. In general, enantiotropic transitions are thermodynamically reversible with temperature and pressure but they may

turn out to be irreversible in certain situations[11]. In either case their free energies become equal at the transition temperature T_p^{II-I} and T_p^{III-I}.

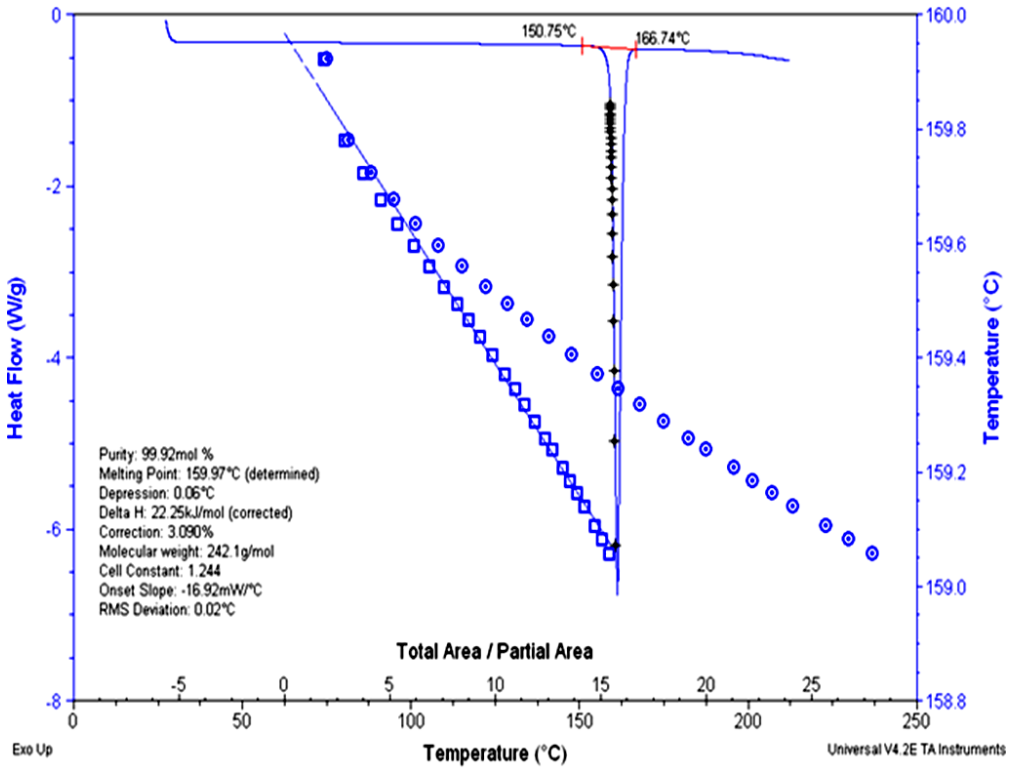

Figure 4B.8: Differential scanning calorimetric thermogram of **Form – I** crystals

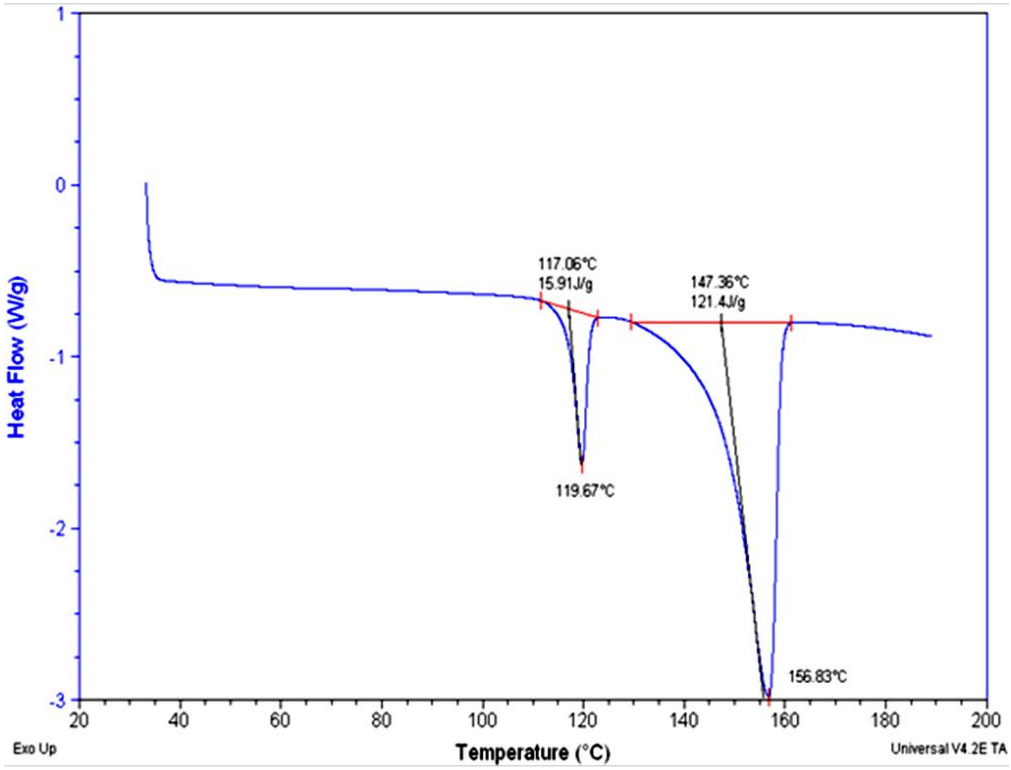

Figure 4B.9: Differential scanning calorimetric thermogram of **Form – II** crystals

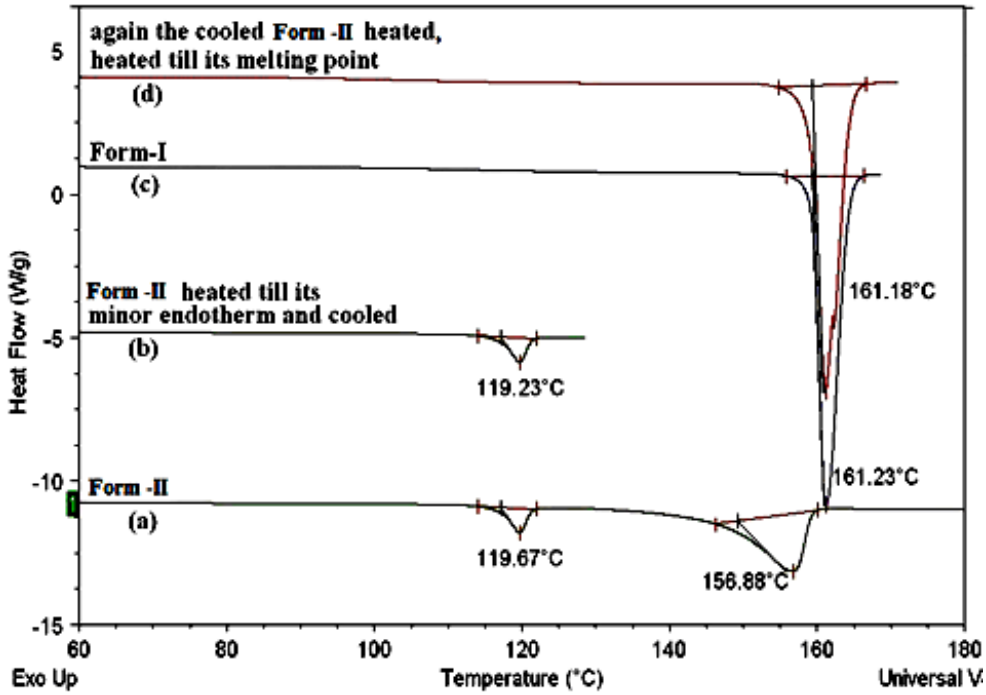

Figure 4B.10: Repitative cycles of **Form – II**. It shows that **Form – I** is a stable polymorph and **Form – II** is a metastable polymorph.

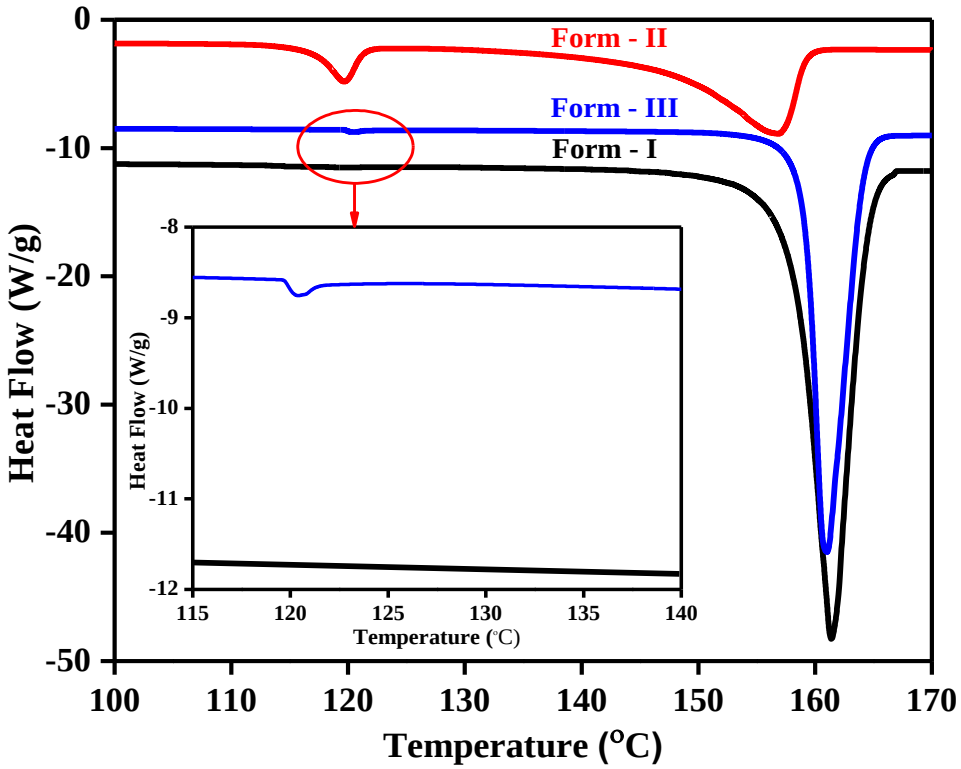

Figure 4B.11: Overlay of DSC thermograms of **Form – I**, **Form – II** and **Form – III**. A minor endotherm of **Form – III** at ~120 ºC (inset view).

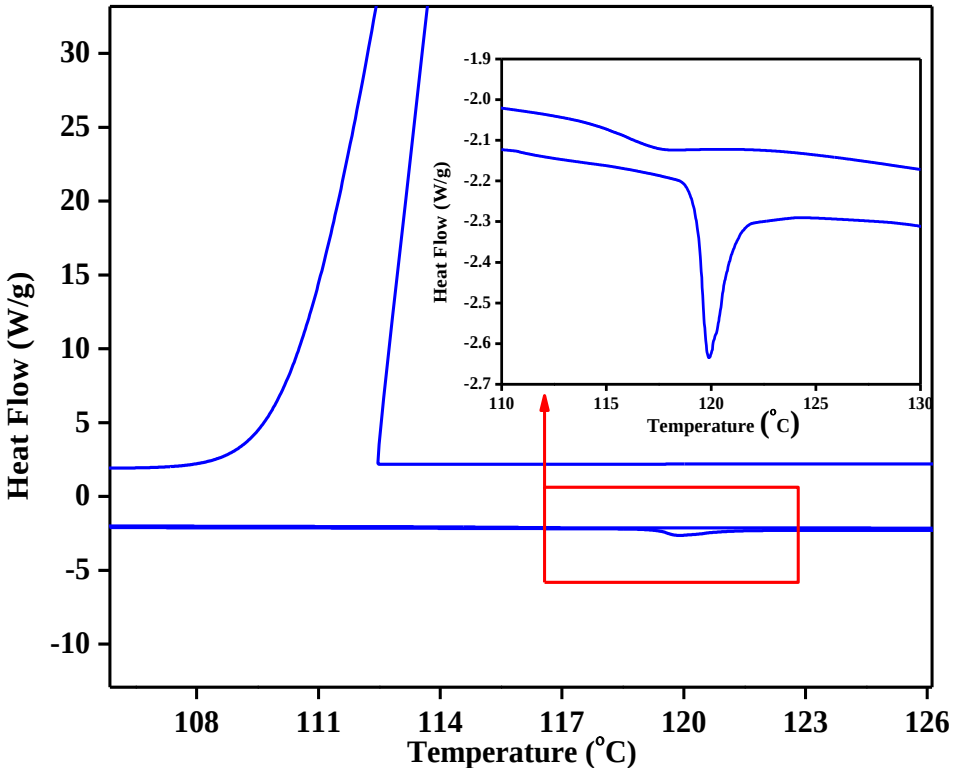

Figure 4B.12: Heat – cool – heat thermogram of **Form – II** (Inset view the endothermo at ~ 119. 67 ºC)

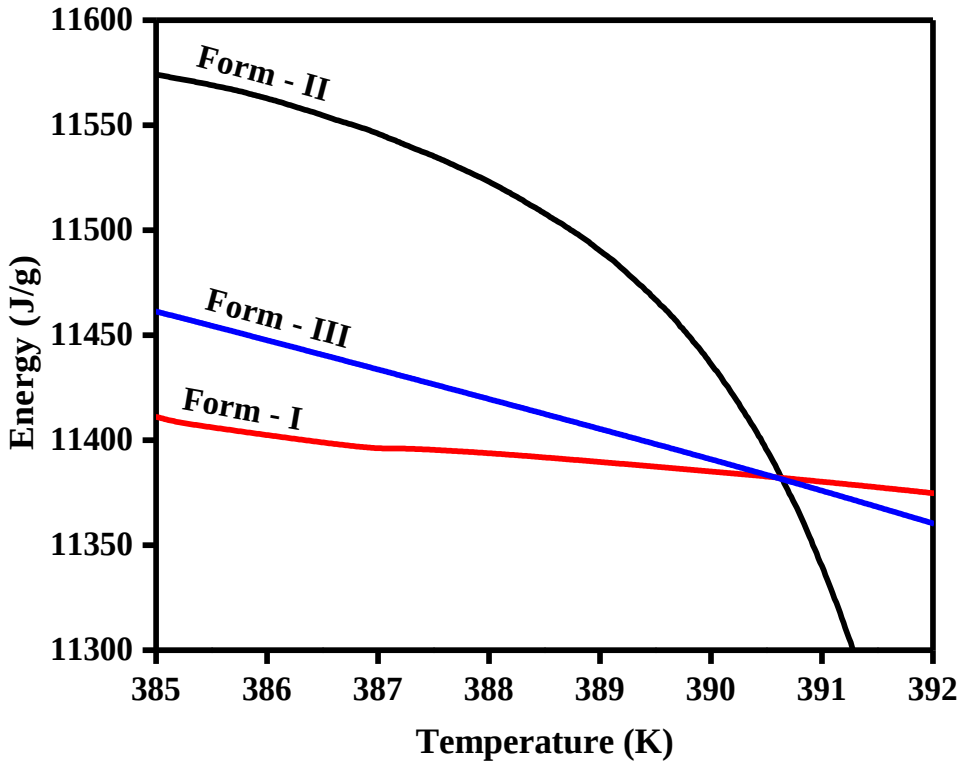

Figure 4B.13: Energy–temperature diagram of an enantiotropic trimorphic system of PNASH.

Table 4B.1: *Thermal Phase Transition properties of polymorphs* ***Forms – I, II*** *and* ***III***

	Form – I	Form – II		Form – III	
		peak 1	peak 2	peak 1	peak 2
Purity (mol%)	98.69	99.79	93.49	-	99.87
Phase Transition (ºC)	-	119.67	-	120.83	-
Melting Point (ºC)	161.44	-	156.83	-	159.04
Depression (ºC)	0.26	0.81	4.01	-	0.04
ΔH (kJ. mol^{-1})	77.96	3.396	25.33	-	51.83
Cell Constant	1.244	1.244	1.244	-	1.244
Onset Slop (mW/ºC)	-16.92	-16.92	-16.92	-	-16.92
RMS Deviation (ºC)	0.01	0.03	0.06	-	0.07

PART C: SINGLE CRYSTAL X-RAY DIFFRACTION STUDIES OF PNASH

4C.1: Powder X-Ray Diffraction Studies

PNASH in **Forms – I** and **II** was screened by powder X-ray diffraction (PXRD) studies in the range of 5º to 50º. The PXRD pattern of PNASH is shown in **Figure 4C.1**. From the figure, it is found that **Forms – I** and **II** are show phase difference. The peak positions (2θ) and inter planar distance (d) values of **Forms – I** and **II** are provided in **Table 4C.1**.

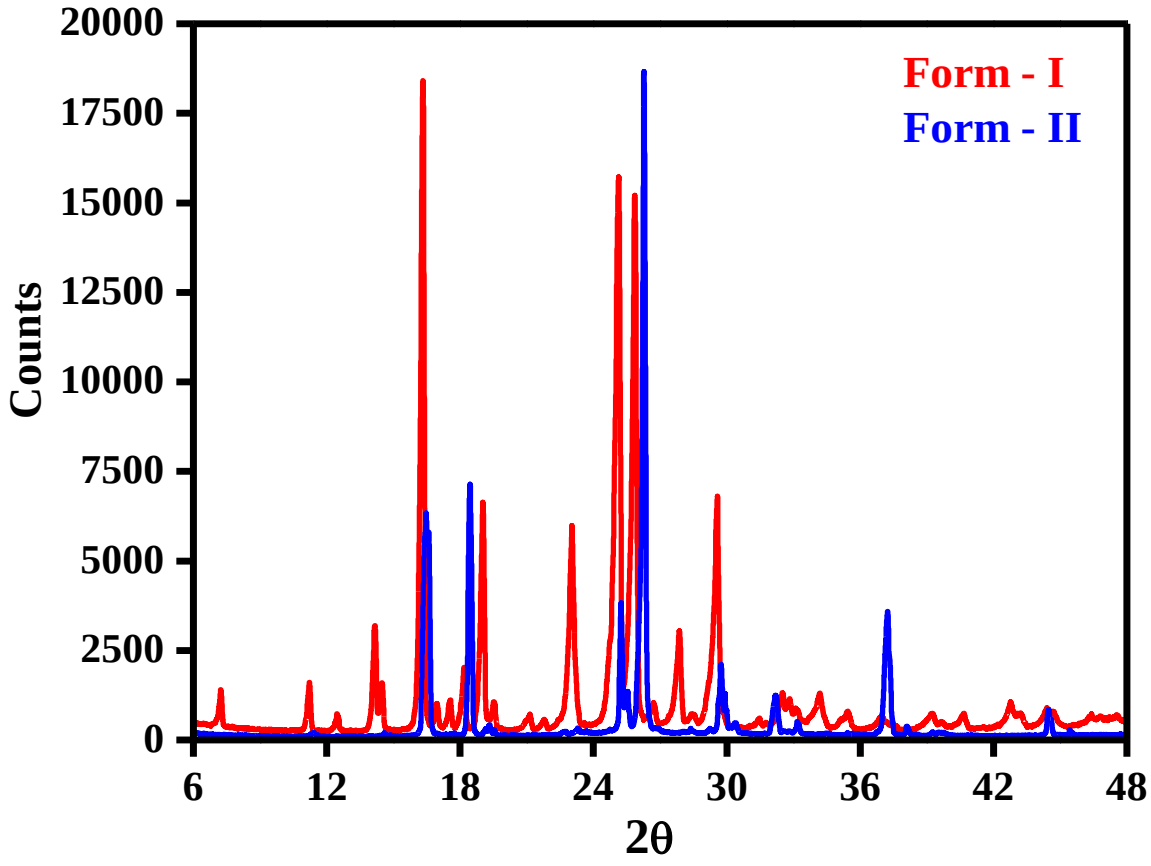

Figure 4C.1: Powder XRD pattern of **Form – I** and **Form – II**

Table 4C.1: *PXRD data of* ***Form – I*** *and* ***Form – II***

Form – I		Form – II	
Peak position (°) (2θ)	**d – Spacing [Å]**	**Peak position (°) (2θ)**	**d - Spacing [Å]**
11.382	7.76795	7.212	12.2481
11.410	7.76795	7.230	12.2481
14.580	6.07062	11.191	7.90017
14.616	6.07062	11.218	7.90017
16.355	5.41557	12.455	7.10124
16.396	5.41557	12.486	7.10124
16.470	5.37778	14.137	6.25971
16.511	5.37778	14.172	6.25971
16.583	5.34127	14.458	6.12139
16.625	5.34127	14.494	6.12139
18.428	4.81054	16.279	5.44058
18.474	4.81054	16.320	5.44058
19.132	4.63533	16.932	5.23234
19.180	4.63534	16.974	5.23234
19.316	4.59152	17.513	5.05980
19.364	4.59152	17.557	5.05980
19.524	4.54302	18.137	4.88721
19.573	4.54302	18.182	4.88721
22.657	3.92138	18.983	4.67129
22.714	3.92138	19.031	4.67129
23.640	3.76067	19.503	4.54798
23.700	3.76067	19.552	4.54798
25.223	3.52796	21.047	4.21764
25.286	3.52796	21.100	4.21764
25.488	3.49192	21.750	4.08289
25.552	3.49192	21.804	4.08289
26.236	3.39396	22.991	3.86512

26.302	3.39396	23.049	3.86512
28.200	3.15740	25.057	3.55105
28.300	3.14980	25.120	3.55105
28.300	3.15740	25.806	3.44963
28.400	3.14980	25.871	3.44963
29.220	3.05382	26.661	3.34088
29.295	3.05382	26.728	3.34088
29.711	3.00445	27.796	3.20698
29.787	3.00445	27.866	3.20698
29.926	2.98340	29.050	3.07145
30.002	2.98340	29.120	3.07145
30.356	2.94207	29.500	3.02548
30.434	2.94207	29.575	3.02548
32.157	2.78126	31.418	2.84502
32.239	2.78126	31.498	2.84502
33.156	2.69976	32.447	2.75712
33.241	2.69976	32.530	2.75711
34.340	2.60956	32.801	2.72819
34.430	2.60956	32.885	2.72819
35.440	2.53085	33.131	2.70177
35.531	2.53085	33.215	2.70177
37.118	2.42020	34.106	2.62669
37.213	2.42020	34.194	2.62669
37.248	2.41206	35.370	2.53565
37.344	2.41206	35.461	2.53565
38.099	2.36012	36.940	2.43146
38.197	2.36012	37.035	2.43146
39.240	2.29405	39.174	2.29775
39.342	2.29405	39.276	2.29775
39.594	2.27437	40.575	2.22160
39.696	2.27437	40.680	2.22160

44.465	2.03582	42.730	2.11440
44.582	2.03582	42.842	2.11440
45.434	1.99467	43.185	2.09320
45.553	1.99467	43.297	2.09320
49.434	1.84221	44.357	2.04056
49.565	1.84221	44.473	2.04056
–	–	44.694	2.02598
–	–	44.811	2.02598
–	–	46.440	1.95383
–	–	46.560	1.95383
–	–	47.430	1.91542
–	–	47.550	1.91542
–	–	48.203	1.88635
–	–	48.330	1.88635
–	–	49.495	1.84010
–	–	49.626	1.84010

4C.2: Single Crystal X-Ray Diffraction Analysis of PNASH

Crystal structure analysis of **Form – I** and **II** of PNASH has been performed by single crystal X-ray diffraction (SXRD). Experimental details are already provided in **Chapter II**. No absorption correction has been performed. A list of essential supramolecular interactions like H-bonding, anisotropic displacement parameters, bond lengths and angles has been given. The lattice parameters were determined from least – squares analysis and the reflection data were integrated using the program SHELXTL[12]. The structures of the **Form – I** and **II** were solved by direct methods using SHELXS-97 and refined by full-matrix least squares on F^2 with anisotropic displacement parameters for non-H atoms, using SHELXL-97[13]. The positions of all aromatic and O—H hydrogen atoms were calculated geometrically. The software employed to preparation of materials to publication was Mercury 2.3 (Build RC4), ORTEP-3 and X-Seed[14]. Crystal data and refinements information has been provided in detail in **Table 4C.2**.

Both **Form – I** and **Form – II** crystallize in the centrosymmetric monoclinic $P2_1/c$ space group with one molecule in the each asymmetric unit (Z' = 1). The unit cell volumes of **Form – I** and **II** are 1130.71 and 1126.79 $Å^3$ respectively. A close inspection of the crystal structures reveals that the molecules of the two forms are conformationally different, thus featuring conformational polymorphism (**Figure 4C.2**). The ORTEP diagrams of both **Forms – I** and **II** are shown in **Figure 4C.3**. Since there were no solvent molecules included in the crystal lattice of **Form – II** crystals, DSC endotherm at ~119.67 ºC indicates the solid-solid phase transition. However, It is also found that **Form – I** and **Form – II** are isostructural with each other. In both the **Forms – I** and **II,** the phenolic O–H group is engaged in an intramolecular O–H···N hydrogen bonding with ylidine N-atom. The nitro and ylidine C–H groups are not essentially coplanar with phenyl groups and the torsion angles in both the forms are not exactly same [(O2–N2–C11–C12: **Form – I** = –177.16º and **Form – II** = 177.04º); (H7–C7–C1–C2: **Form – I =** 175.51 and **Form – II** = –175.95º)] (**Figure 4C.2**). Torsional difference in the $–NO_2$ group causes the formation of anti-parallel helices in **Form – I** and **Form – II**. In **Form – I**, the benzylidine phenyl C–H hydrogens interact with the oxygen atoms of $–NO_2$ group via C–H···O hydrogen bond to form a supramolecular right-handed helix along the crystallographic *b*-axis, whereas in **Form – II**, this helix is propagating along the crystallographic *b*-axis in an anti-parallel fashion (left-handed helix) with the same kind of hydrogen bonding (**Figure 4C.4**). These supramolecular helices extend connected by C–H···O hydrogen bonding to form layered structure in **Form – I** and Form – **II**.

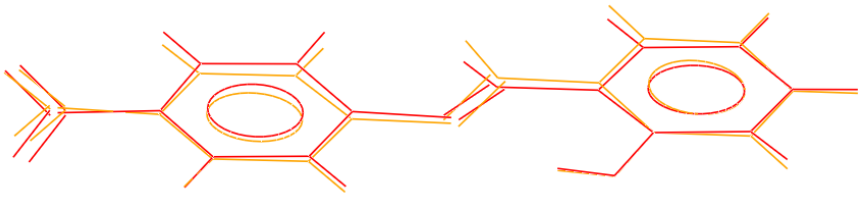

Figure 4C.2: An overlay diagram of **Form – I** (yellow) and **Form – II** (red)**.** The $–NO_2$ and ylidine C–H groups are not in coplanar with phenyl rings.

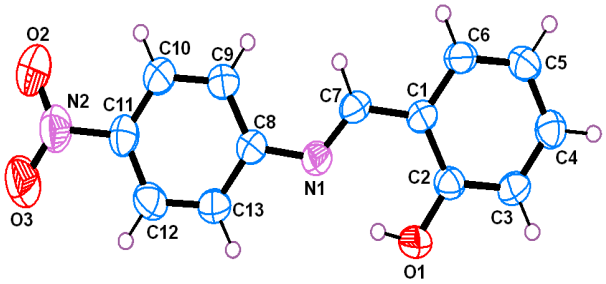

Form – I

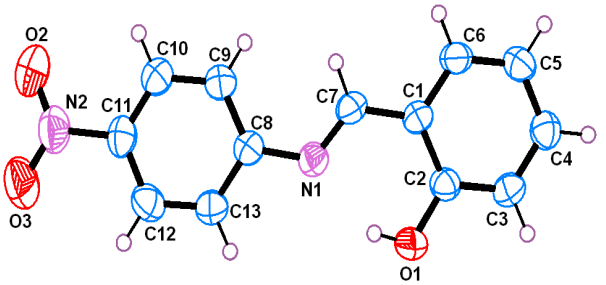

Form – II

Figure 4C.3: ORTEP representation of **Form – I** and **Form – II**, thermal ellipsoids are drawn at 50% probability level

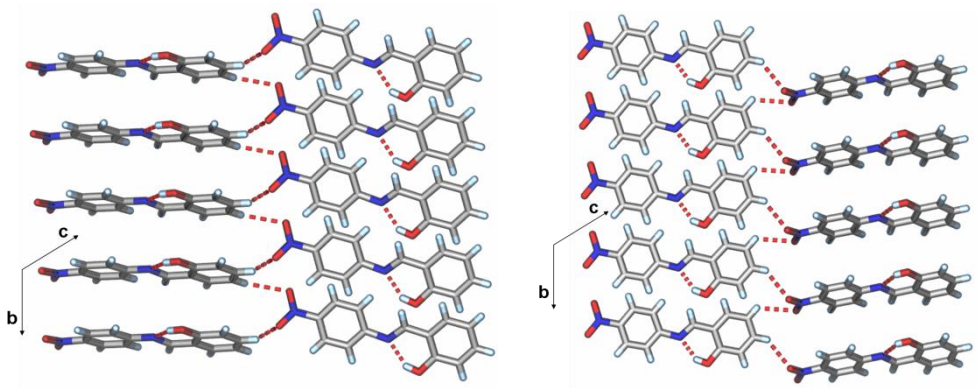

(a) **(b)**

Figure 4C.4: Packing diagrams of **Form – I** and **Form – II**. **Form – I** is in right handed helix and **Form – II** is left hand helix. The two helices are propagating along the crystallographic *b*-axis in oppsite helices.

Table 4C.2: *Crystalographic data of PNASH*

	PNASH – EtOAc (Form – I)	**PNASH – MeCN (Form – II)**
Empirical formula	$C_{13}H_{10}N_2O_3$	$C_{13}H_{10}N_2O_3$
Formula weight	242.23	242.23
System	Monoclinic	Monoclinic
Space group	P21/*c*	P21/*c*
T/K	296	296
a/Å	12.373(2)	12.351(3)
b/Å	5.7839(8)	5.7857(15)
c/Å	15.950(3)	15.917(5)
α/°		
β/°	97.866(4)	97.826(7)
γ/ °		
Z	4	4
V/Å^3	V = 1130.7(3)	1126.8(5)
D_{calc}/ g/cm^3	1.429	1.428
F(000)		
μ/mm^{-1}	0.104	0.104
θ/º		
Index ranges		
N-total	11198	10621
N-independent	2729	2723
N-observed	1439	1483
Parameters	165	165
R_1 ($I > 2\sigma(I)$)	0.0493	0.0508
wR_2 (all data)	0.1227	0.1262
GOF		
CCDC		

PART D: MOLECULAR MODELING STUDIES

Modeling studies have been performed in gas-phase on acid-base conjugate forms and tautomers of PNASH over ChemOffice Ultra platform. Molecular mechanics MM^+ method at RMS gradient 0.01 have been employed for the calculation of possible inter- and intra-molecular H-bonding. The molecular structural parameters such as bond lengths, bond angles, torsional energies, dihedral angles and HOMO – LUMO energies have been calculated. The structure of the energy-minimized free molecule of PNASH in phenolic and enamine tautomeric forms is shown in **Figure 4D.1**. The acid-base conjugates are also shown in **Figure 4D.1**. Almost in all forms the molecule is planar as is evident from the global minimum for zero torsional angle over the bonds C(3)—C(7), N(8)—C(9) in phenolic tautomer and C(9)—N(8) in enamine tautomer shown in **Figure 4D.2**. Double dihedral torsional energy plot of PNASH benzenoid and quinoid forms over C(3)—HC(7)=N(8)— bond are generated and depicted in **Figure 4D.3**. The double dihedral plots of photo-induced forms of PNASH **Form – (a)** and **Form – (b)** are shown in **Figure 4D.4**. The Heats of Formation of PNASH in protonated and deprotonated conjugate forms and photo-induced tautomeric forms are given in **Table 4D.1**. The quantum mechanical HOMO-LUMO orbitals energy calculations have been used to obtain gas-phase electronic transitions. Some of important HOMO-LUMO molecular orbitals are displayed in **Figure 4D.5**. Stereographic images of PNASH are shown in **Figure 4D.6** after global minimization along with the scheme of the atoms. The theoretical and experimental absorption maxima are in great agreement. Neverthlessly, the solvent accessible zonal clouds of the PNASH and $PNAS^-$ are shown in **Figures 4D.7-4D.8**.

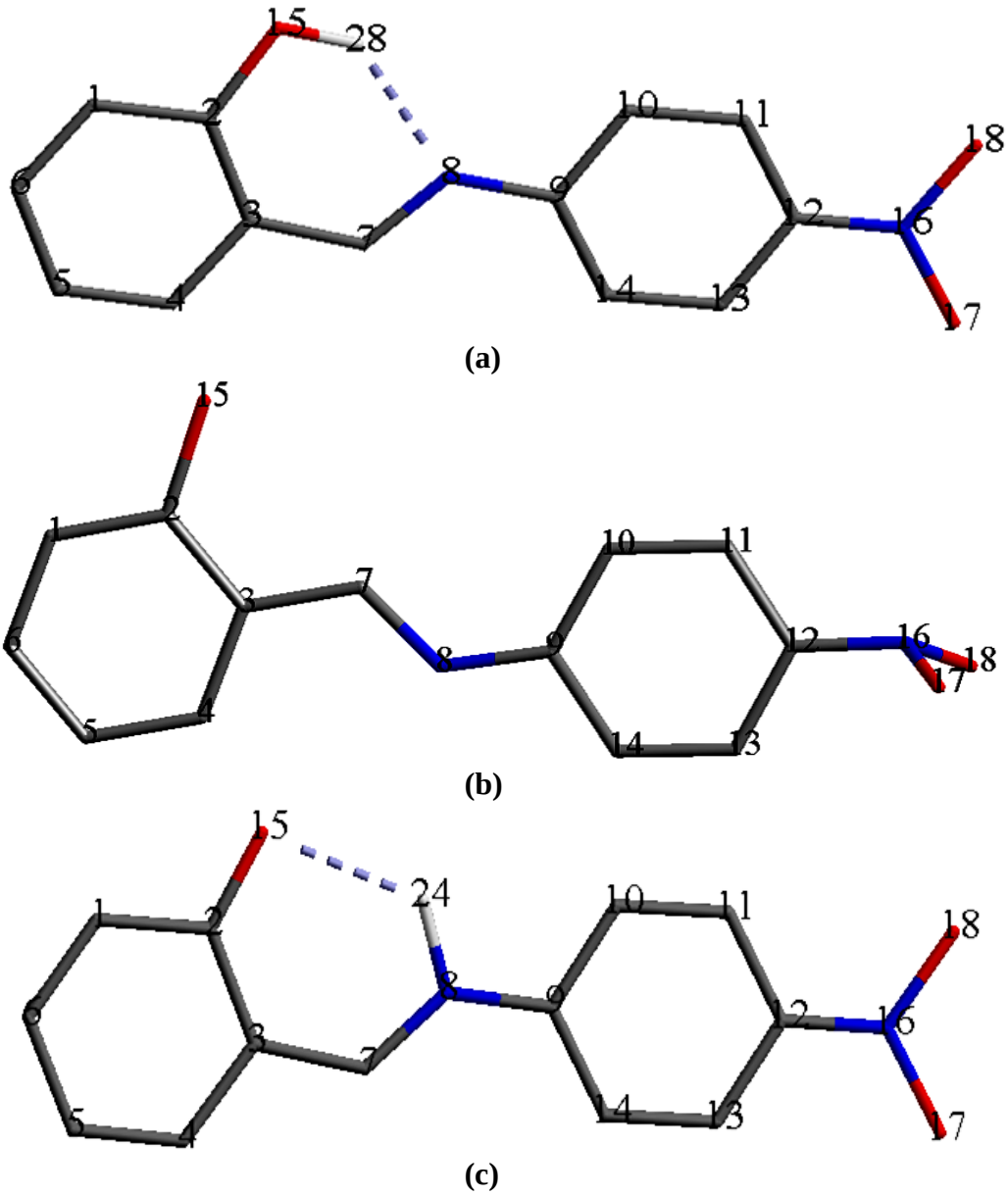

Figure 4D.1: PNASH in (a) Benzenoid form (phenolic), (b) Quinoid form and (b) Enamine tautomeric form.

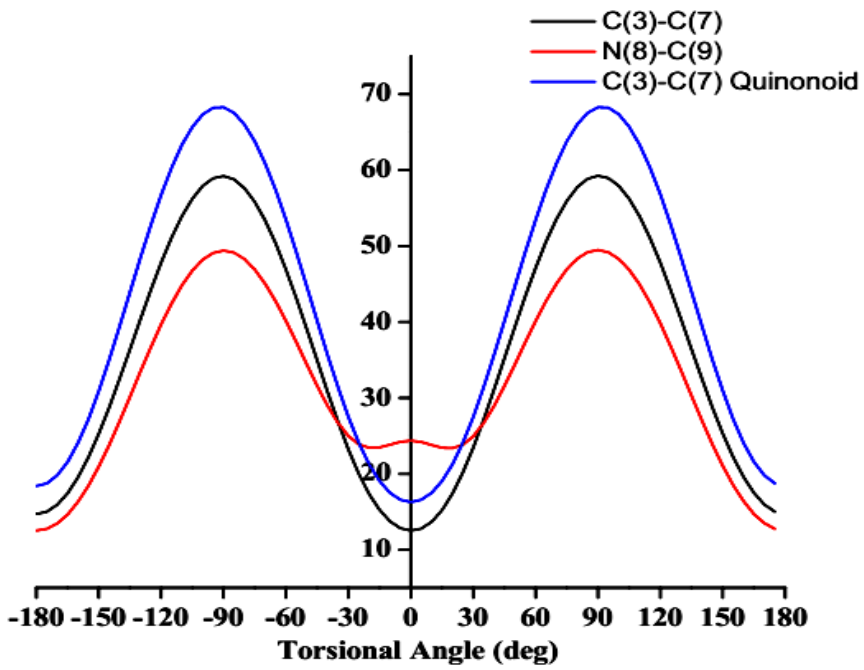

Figure 4D.2: Conformation single dihedral energy plots of PNASH.

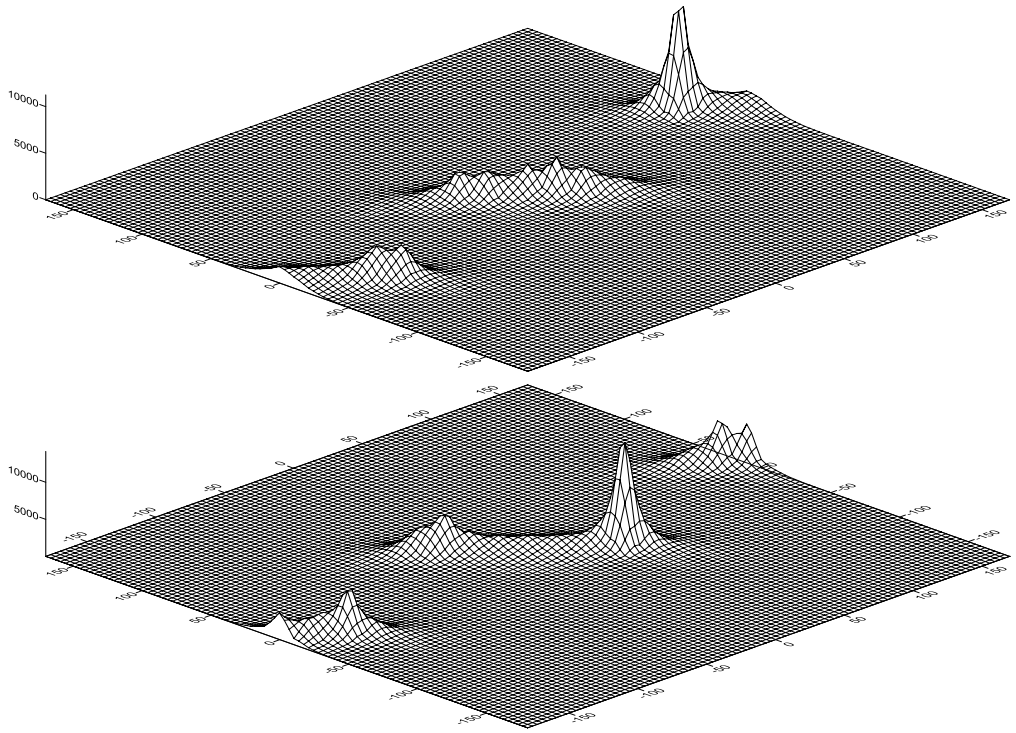

Figure 4D.3: Double dihedral chart of PNASH over C(3)-C(7)-N(8) bonds of benzenoid (upper figure) and quinoid (lower figure) forms (Number sequence of atoms from **Figure 4D.1a**)

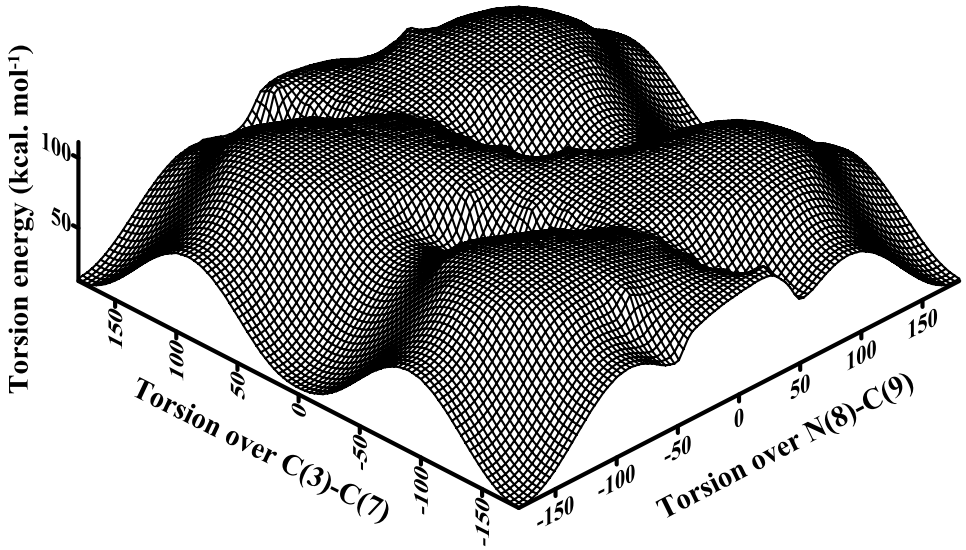

Form – (a)

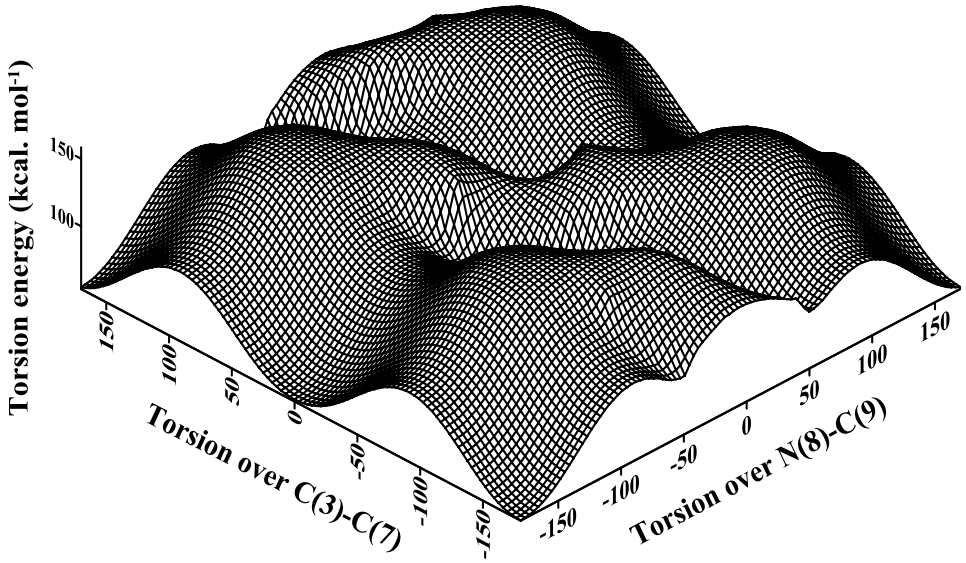

Form – (b)

Figure 4D.4: Double dihedral chart of photo-induced transformation forms of PNASH **Form - (a)** and **Form - (b)** (Horns of the figure chopped to ~155 kcal. mol^{-1}) (Number sequence of atoms from **Figure 4D.1a**)

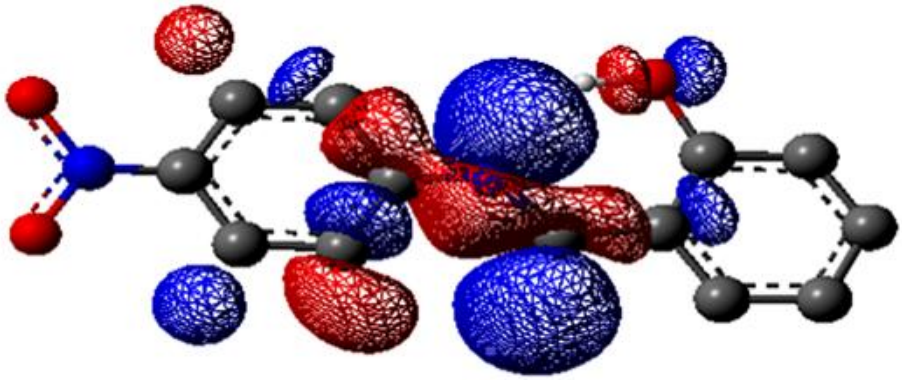

HOMO (-7.767 eV)

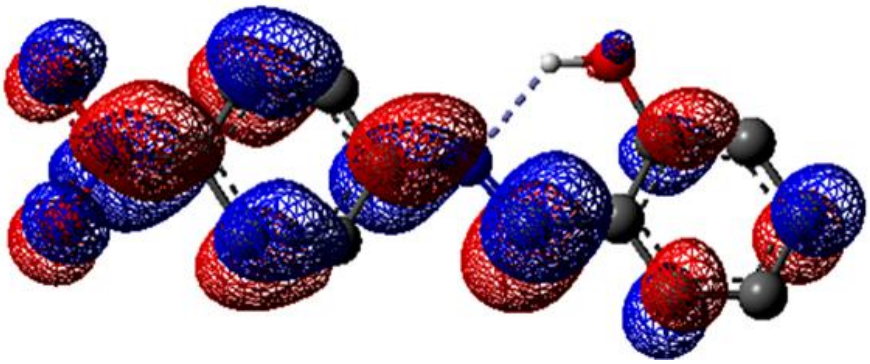

LUMO (-3.900 eV)

Figure 4D.5: HOMO and LUMO molecular orbitals of PNASH in wire mesh format (All the H-atoms are excluded for clarity)

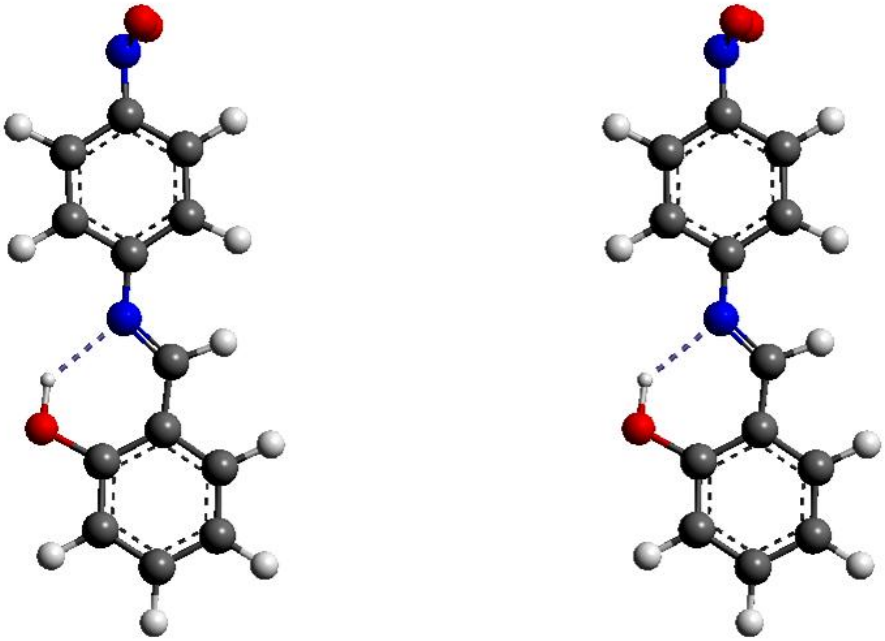

Figure 4D.6: Stereographic view of (a) $PNASH2^+$ (b) PNASH (c) $PNAS^-$ (d) $PNAS^-$ - Quinoid and (e) PNASH-photo induced tautomeric form after global minimization along with the scheme of the atoms

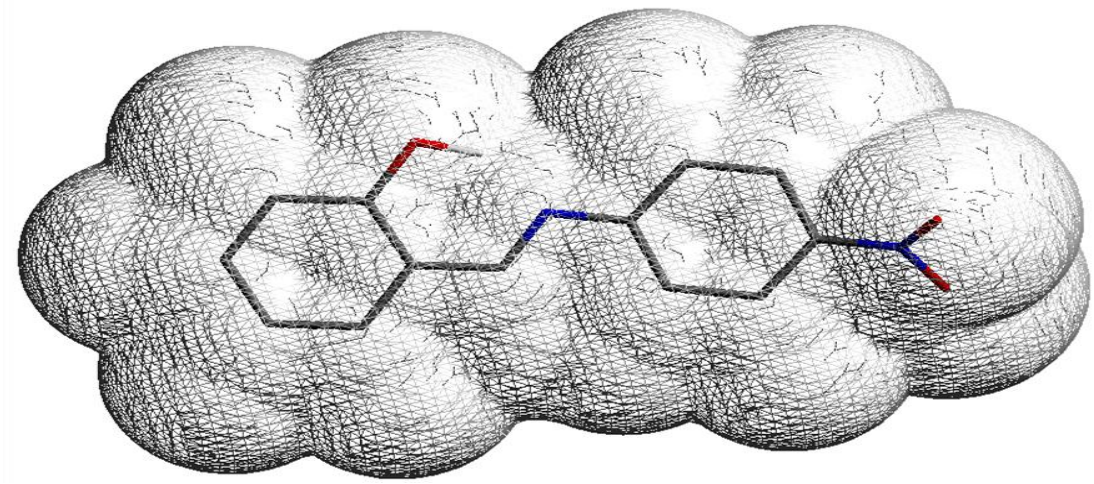

Figure 4D.7: Solvent accessible zonal cloud of PNASH in wire mesh found (Non-polar H bonds are excluded in the figures for clarity)

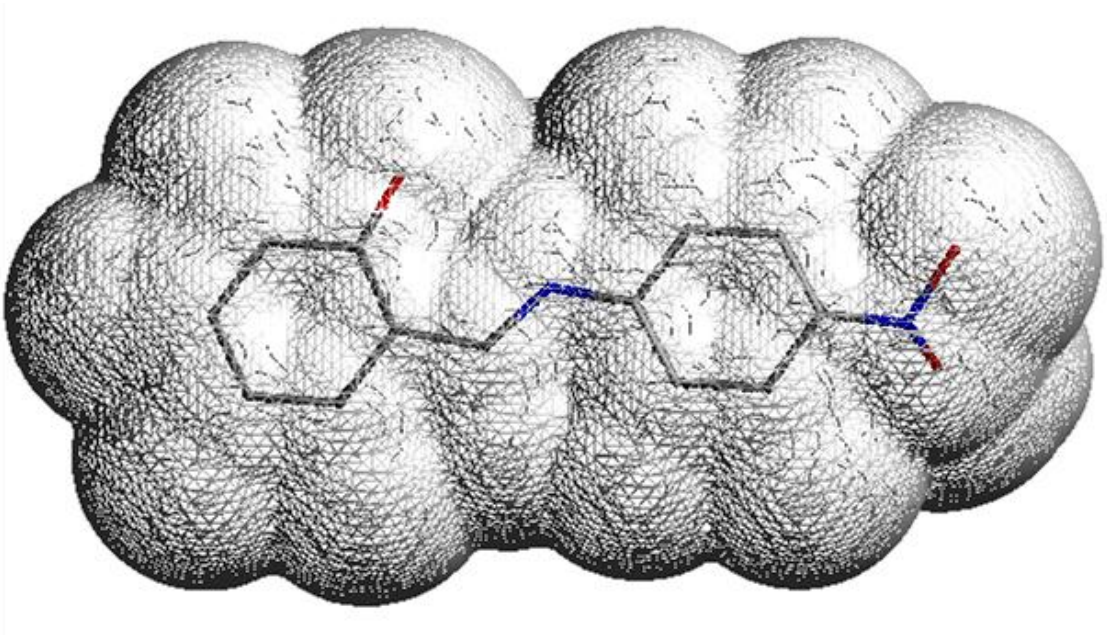

Figure 4D.8: Solvent accessible zonal cloud of $PNAS^-$ in wire mesh found (Non-polar H bonds are excluded in the figures for clarity)

Table 4D.1: *Molecular modeling data of PNASH*

PNASH	$\Delta H°_f$ (kcal. mol^{-1})	HOMO (eV)	LUMO (eV)	Calculated λ_{max} (nm)	Observed λ_{max} (nm)
Benzenoid Form (PNASH)	6.461	-6.835	-3.112	333	368
Quinoid Form (PNAS$^-$)	69.547	-8.342	-4.731	343	372
Photo-Induced: tautomeric Form– (b)	12.102	-7.512	-4.013	354	-

References

1. V. ramamurthy and K. S. Schanz, *Semiconductor Photochemistry and Photophysics*, Marcel Dekker, Inc., New York. Basel, 2003.
2. K. Clays, *J. Nonlinear Opt. Phys. Mater.*, 2003, **12**, 475–494.
3. D. Braga, F. Grepioni, G. R. Desiraju and I. A. Interactions, *Chem. Rev.*, 1998, **98**, 1375–1405.
4. J. B. Lambert, *Introduction to Organic Spectroscopy*, Macmillan, New York, 1987.
5. H. Alemu, P. Wagana and P. F. Tseki, *Analyst*, 2002, **127**, 129–134.
6. R. M. and D. B. S. Nassif, *Chem. Mater. Res.*, 2015, **7**, 63–69.
7. A. J. Bard and L. R. Faulkner, *Electrochemical Methods: Fundamentals and Applications*, John Wiley & Sons, Inc, New York, 2002, vol. 2.
8. P. T. Kissinger and W. R. Heineman, *Laboratory Techniques in Electroanalytical Chemistry*, Marcel Dekker, Inc., New York and Basel, 1984.
9. V. Krishna, *Synthesis and Characterization of Some New Series of Biphenyl Bridged Polynucleating Ligands and Their Bivalent Metal Complexes as Possible Supramolecular Hosts*, 2012.
10. D. Giron, *J. Therm. Anal. Calorim.*, 2001, **64**, 37–60.
11. A. Burger and R. Ramberger, *Mikrochim. Acta*, 1979, **72**, 259–271.
12. *SHELXTL. Program for the Solution and Refinement of Crystal Structures, 242 Bruker AXS: Wisconsin, USA,version 6.*, 2000.
13. G. Sheldrick, G.M. SHELXL-97, Program for Crystal Structure Refinement; University of Göttingen, *The SHELX-97 Manual*, 1997.
14. L. J. Barbour, *X-Seed — A Software Tool for Supramolecular Crystallography*, 2001, vol. 1.

CHAPTER - V

A NOVEL UREA BETTI BASE AND ITS CYCLIZED OXAZINONE DERIVATIVE

In this Chapter, the characterization of urea Betti base (UBBH2) and its DMF solvates (UBBH2.2DMF), along with its oxazinone derivative (OXAZH) are discussed. Spectral (NMR, Mass, IR, UV-visible and Fluorescence), Polarimetric, Halochromic, Thermal, Electrochemical, Single crystal X-ray crystallographic, Biological activities and Molecular Modeling studies have been carried out extensively. The synthesis of Betti base and its oxazinone derivative procedure are described in **Chapter II**. The results are presented in 3 parts and discussed.

In **PART A**, the Spectral, Halochromic, Thermal, Electrochemical studies of urea Betti base (UBBH2) **5.1** and its oxazinone (OXAZH) **5.2** derivative besides optical activities of urea Betti base have been provided and discussed.

In **PART B**, the single crystal X-ray determination studies of UBBH2 and its DMF solvate, UBBH2.2DMF and OXAZH are presented.

In **PART C**, molecular modeling studies of the UBBH2, UBBH2.2DMF and its OXAZH are presented and discussed.

PART A: SPECTRAL, THERMAL AND ELECTROCHEMICAL STUDIES OF UBBH2 AND OXAZH

Structure of the compounds

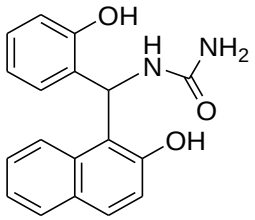

5.1

1-((2-hydroxynaphthalen-1-yl)(2-hydroxyphenyl)methyl)urea

(UBBH2)

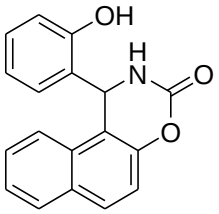

5.2

1-(2-hydroxyphenyl)-1H-naphtho[1,2-e][1,3]oxazin-3(2H)-one

(OXAZH)

5A.1: General Characterization of the UBBH2 and OXAZH

The physical and analytical data of UBBH2, R, S-enantiomers of UBBH2. 2DMF and OXAZH are presented in **Table 5A.1**.

5A.2: Optical Rotation Studies

Optical rotation of UBBH2, R-UBBH2.2DMF, S-UBBH2.2DMF, OXAZH, R-OXAZH and S-OXAZH are measured and presented in **Table 5A.1**. From the data, UBBH2 and OXAZH are not shown any optical rotation. Therefore, the UBBH2 and OXAZH are racemic in nature.

5A.3: Infrared Spectral Studies:

The FTIR spectra of UBBH2, UBBH2.2DMF and OXAZH in KBr disc are recorded in the range of 400-4000 cm^{-1}. The FTIR spectra of R and S enantiomers of UBBH2 are depicted in **Figure 5A.1**. The stretching and bending frequencies of functional groups[1] like –OH of both salicyladehyde and β-naphthol, NH_2, >C=O and >C−N< are given in **Table 5A.2**.

5A.4: ^{1}H NMR and ^{13}C NMR Spectral Studies

^{1}H NMR and ^{13}C NMR spectra of UBBH2 and OXAZH are presented in **Figures 5A.2-5A.4**. The spectral pattern and relative intensities (integrals) of both UBBH2 and OXAZH are compatible with the respective spectra. Important chemical shift values of ^{1}H NMR and ^{13}C NMR of UBBH2 and OXAZH have been provided in **Table 5A.3**.

Table 5A.1: *Physical and analytical data of UBBH2, R, S - UBBH2.2DMF and OXAZH*

Compound	M.P. (ºC)	Molecular Formula	Molecular Weight#	Molar[a] rotation	Elemental Analysis* % C	% H	% N
UBBH2	183	$C_{18}H_{16}N_2O_2$	308(308)	0	74.91 (73.95)	5.15 (5.52)	10.62 (9.58)
R-UBBH2. 2DMF	154	$C_{24}H_{30}N_4O_4$	438 (438)	-256	66.54 (66.73)	6.45 (6.90)	13.15 (12.78)
S-UBBH2. 2DMF	154	$C_{24}H_{30}N_4O_4$	438 (438)	256	66.56 (66.73)	6.41 (6.90)	13.19 (12.78)
OXAZH	262	$C_{18}H_{13}NO_3$	291(291)	0	75.13 (74.22)	4.23 (4.50)	5.17 (4.81)
R-OXAZH	262	$C_{18}H_{13}NO_3$	291(291)	176	75.53 (74.32)	4.03 (4.17)	5.07 (4.99)
S-OXAZH	262	$C_{18}H_{13}NO_3$	291(291)	-176	75.33 (74.29)	4.13 (4.21)	5.27 (5.05)

*, data in parenthesis are calculated ones
#, data in parenthesis are obtained from ESI+/- mass spectra
a, deg $mol^{-1}dm^{-1}$

Table 5A.2: *Infrared spectral data of UBBH2, R, S - UBBH2.2DMF and OXAZH*

S. No.	Compound	IR spectral data (cm^{-1})*				
		$\nu_{O\text{-}H\ sal}$	$\nu_{O\text{-}H\ naph}$	ν_{C-N}	ν_{NH2}	$\nu_{C=O}$
1	UBBH2	3457.96	3373.18	1239.29	3237.01	1643.33
2	R-UBBH2.2DMF	3503.90	3359.18	1255.20	3150.77	1665.70
3	S-UBBH2.2DMF	3503.88	3359.29	1255.70	3151.66	1665.76
4	OXAZH	3519.21	-	1245.43	-	1651.67

*, In KBr pellet, w; weak

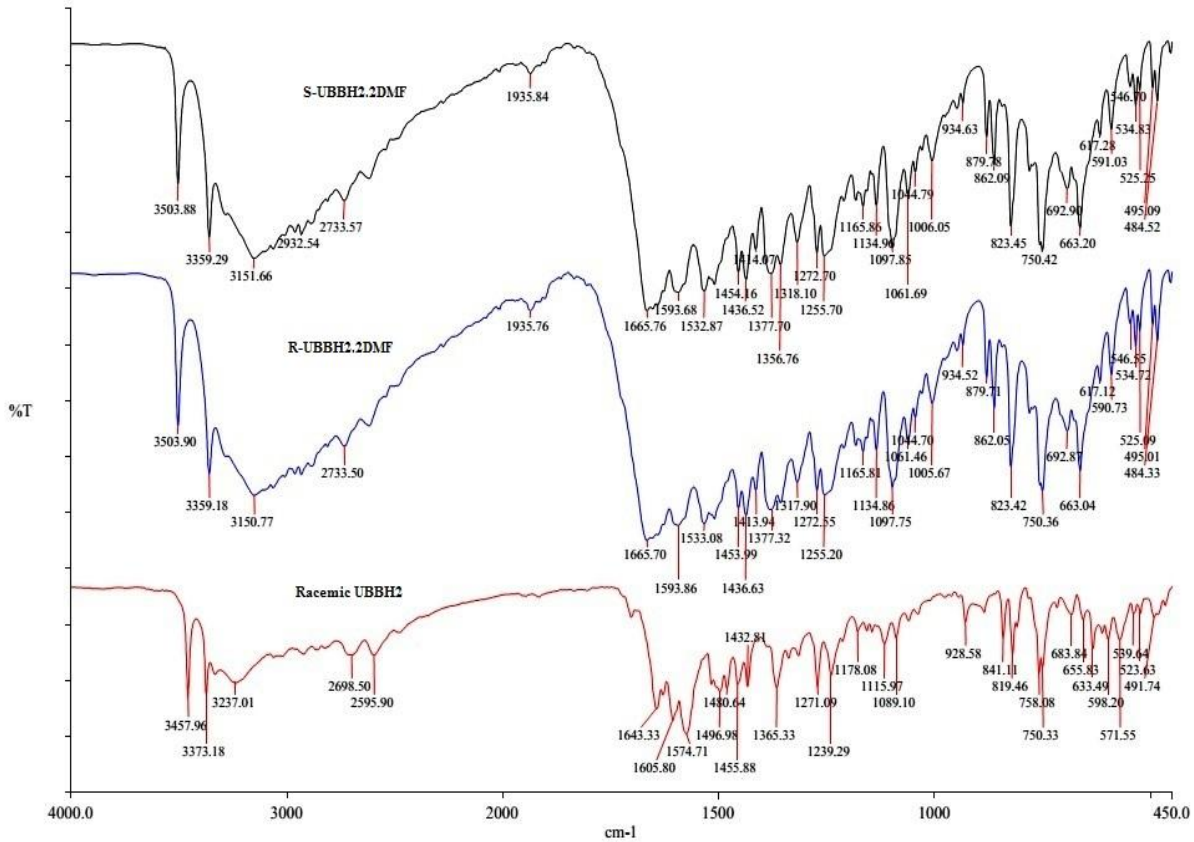

Figure 5A.1: Overlay FTIR spectra of UBBH2, R-UBBH2.2DMF, S-UBBH2.2DMF

Table 5A.3: *^{1}H NMR and ^{13}C NMR spectral data of UBBH2 and OXAZH*

Compound	δ ^{1}H NMR (ppm)	δ ^{13}C NMR (ppm)
UBBH2	10.38 (s, 1H), 10. 08 (s, H), 7.86 (d, J=15 Hz, 2H),7.78–7.61(multiplet, 3H), 7.45–7.11(multiplet, 4H), 7.09–6.91 (multiplet, 2H), 6.84 (d, J=9 Hz, 1H), 6.62 (triplet, J=10 Hz, 1H) and 5.82 (s, 1H)	45.645, 115.791, 118.484, 118.736, 119.210, 122.413, 122.831, 126.173, 127.660, 128.203, 128.341, 128.549, 128.693, 129.474, 132.236 152.952, 154.604, 159.095
OXAZH	6.32 (s,1H), 6.73-6.81 (m, 2H), 7.08 (t,2H), 7.31-7.43 (m, 3H), 7.85-7.93 (m, 3H), 8.51 (s, 1H) and 10.11 (s, 1H)	49.102, 115.014, 116.017, 118.9, 121.921, 122.901, 125.931, 128.138, 128.518 128.920, 130.210, 132.950, 134.512, 134.910, 141.301, 144.801, 150.971, 158.019

s = singlet, d = doublet, m = multiplet ^{1}HNMR (500 MHz, DMSO-D_6)

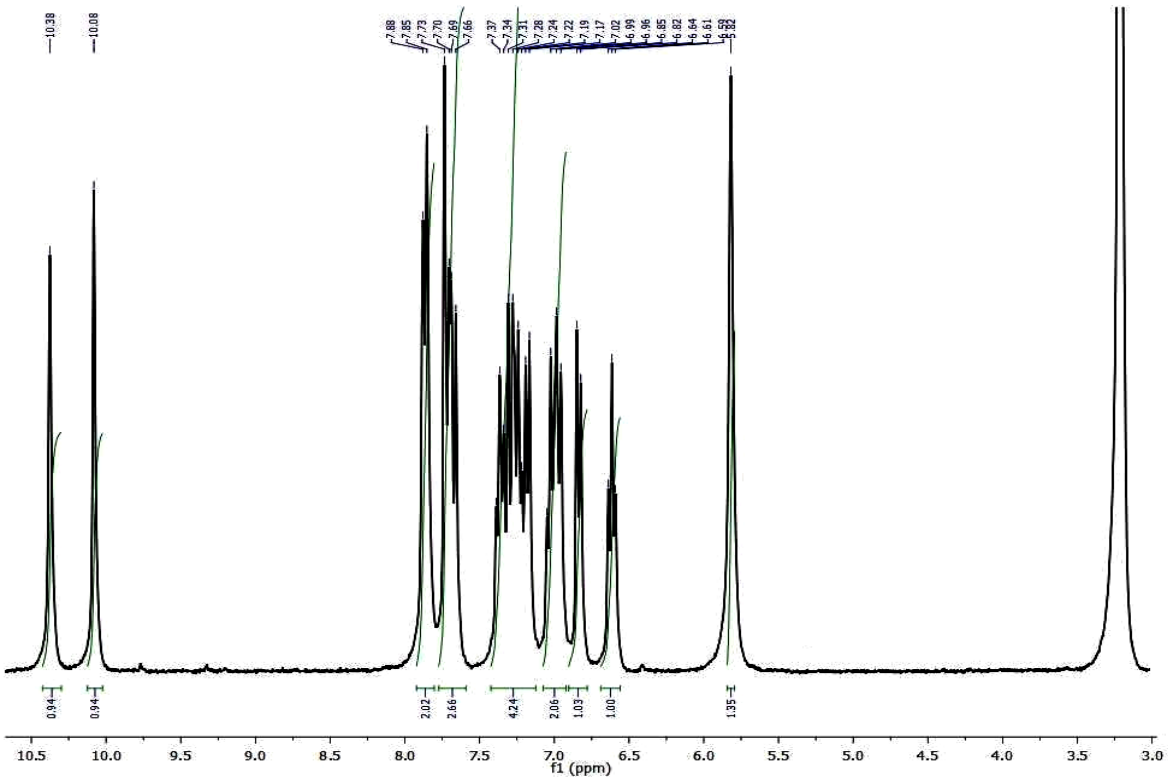

Figure 5A.2: ^{1}H NMR spectrum of UBBH2 in DMSO-D_6

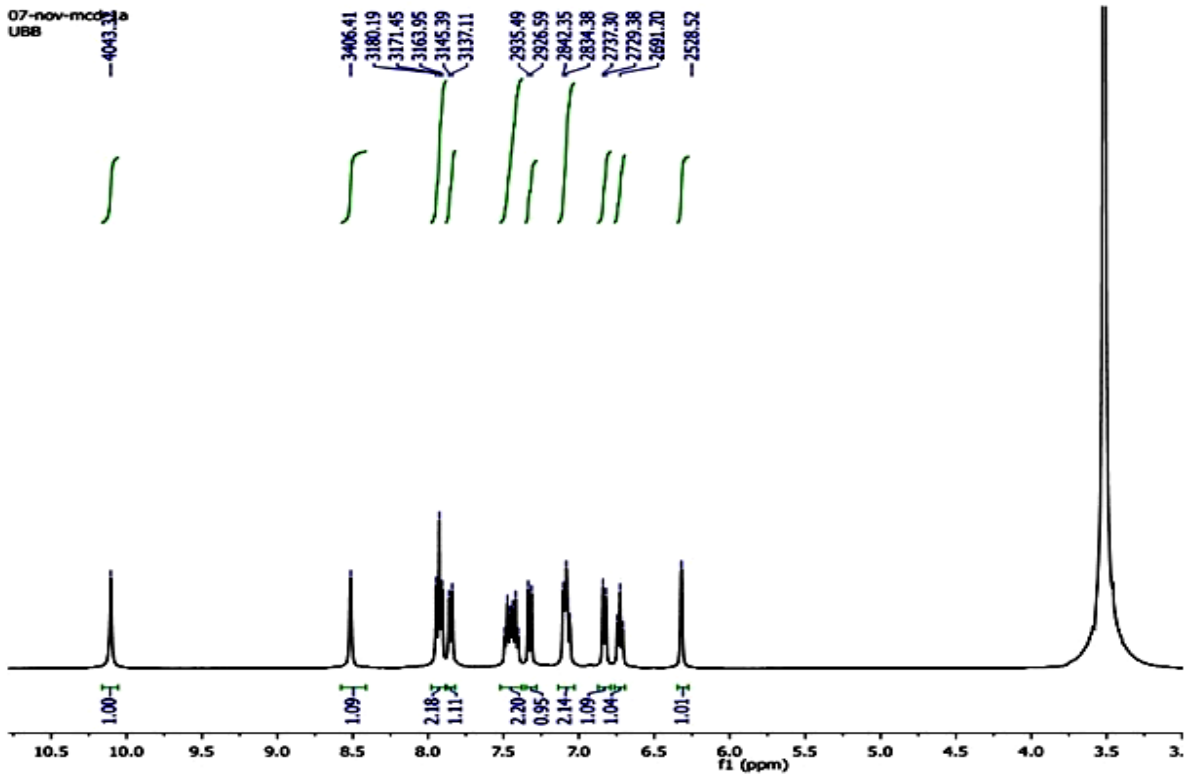

Figure 5A.3: ^{1}H NMR spectrum of OXAZH in DMSO-D_6

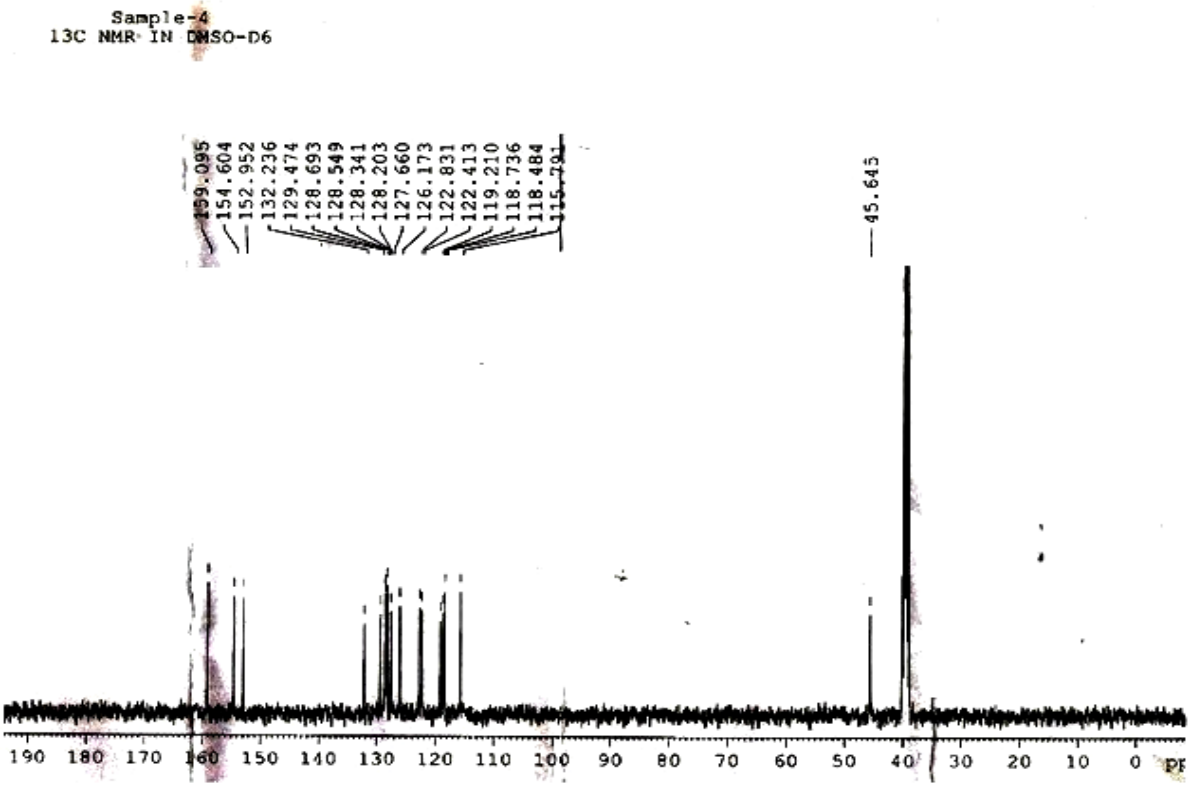

Figure 5A.4: ^{13}C NMR spectrum of UBBH2 in DMSO-D_6

5A.5: Mass Spectral Analysis

The Electrospray ionization mass spectra (MS-ESI$^{+/-}$) of UBBH2 and OXAZH have been investigated. These mass spectra are presented in **Figures 5A.5-5A.6**. The molecular ion peaks were obtained for UBBH2 and OXAZH at 307 [M-1] and 292 [M+1] respectively.

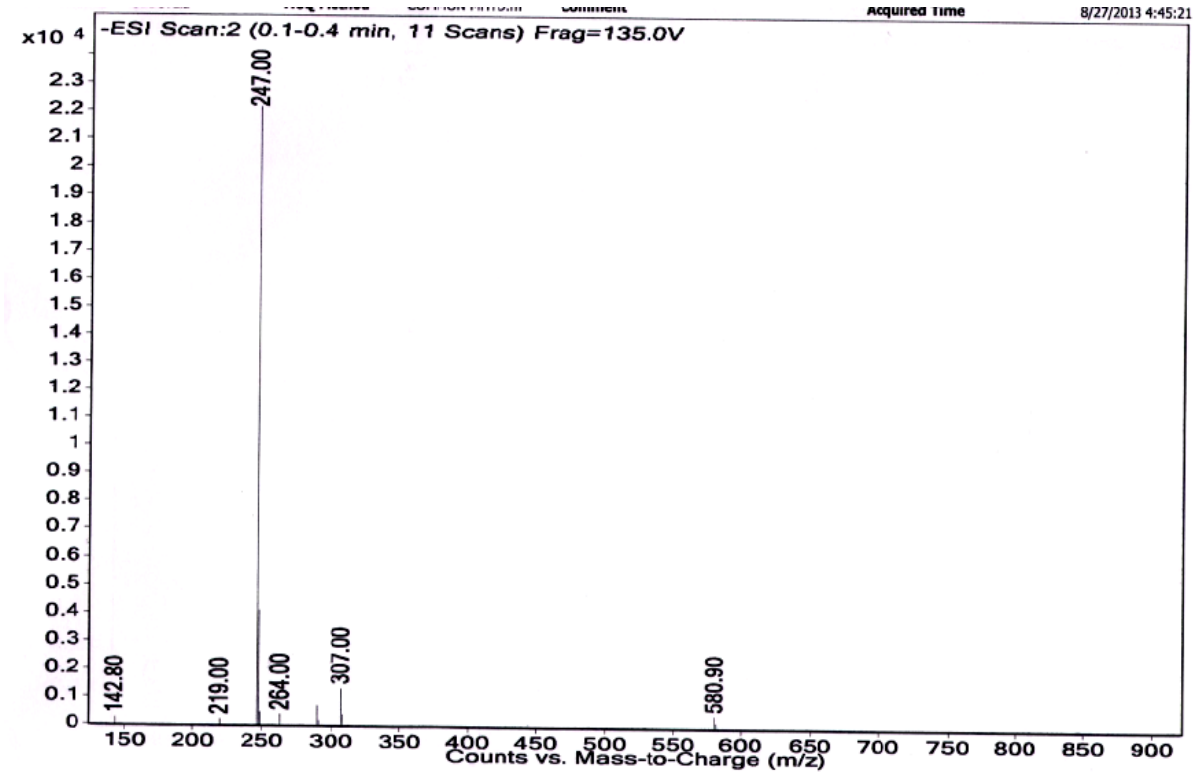

Figure 5A.5: Mass spectrum of UBBH2

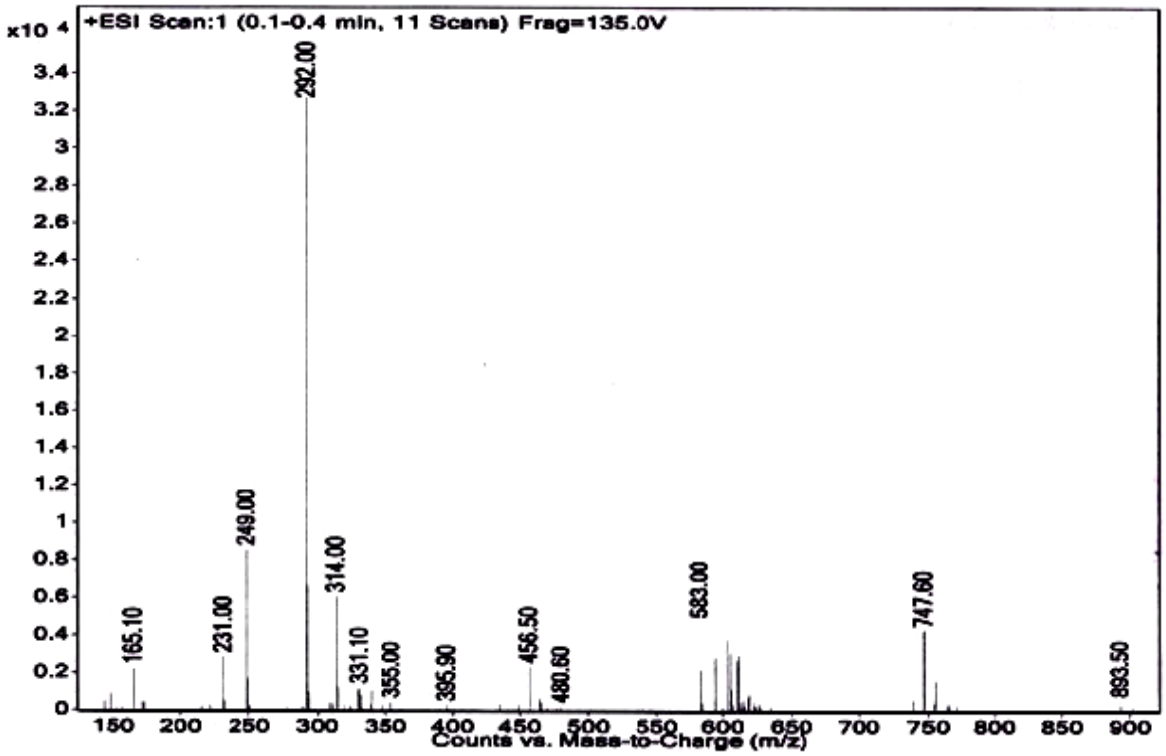

Figure 5A.6: Mass spectrum of OXAZH

5A.6: Electronic Spectral Studies

5A.6.1: *Uv-visible electronic absorption, emission spectral studies and halochromic behavior of UBBH2 and OXAZH*

The electronic spectrum of UBBH2 in DMF solvent is shown in **Figure 5A.7**. The peaks observed at ~ 325 nm and ~ 340 nm are attributed to the $\pi \rightarrow \pi^*$ and $n \rightarrow \pi^*$ transitions respectively. The effect of pH on UBBH2 is shown in **Figure 5A.8**. With an increase of pH from 2.0-12.0. One observes a bathochromic shift in the absorption maximum by ~40 nm. Further, it can be seen from the spectra that there are two isosbestic points one at ~340 nm throughout the pH range and another at ~380 nm in pH range 7.0-12.0. These trends indicate two consecutive, distinct and non-overlapping equilibria each of which possessing only two absorbing species with constant sum of analytical concentrations. The Betti base, UBBH2 has two labile protons in its naphtholic and phenolic groups which would get deprotonated with rise in pH. Since β-naphthol is lower in delocalization energy than that of phenol, it is expected that deprotonation of UBBH2 occurs first at the naphtholic and then at phenolic moieties. The spectral change with pH indicates electronic structural variation upon

deprotonation in the naphthalate and phenolate ions[2–4]. As phenolphthalein colour change from colourless to pink with rise in pH is known to the electronic isomerisation from benzenoid form to quinoid form so is expected the bathochromic shift in λ_{max} of UBBH2 with rise in pH with naphthalate and phenolate ions. The consecutive deprotonation equilibria are presented in **Scheme 1** along with plausible electronic isomerisation that leads to the observed bathochromic shift resulting in two isolated isosbestic points. Since, the isosbestic point at ~340 nm is consistent in the entire pH range and second is in the pH range 7.0-12.0, it is possible to evaluate the deprotonation constants K_{a1} and K_{a2}. A plot of absorbance versus pH is shown in **Figure 5A.9** wherein two sigmoid waves are observed supporting the inference that the UBBH2 is engaged in two consecutive and isolated deprotonation equilibria. Curve fitting of the plot results in the evaluation of K_{a1} and K_{a2} of the consecutive reaction. The associated thermodynamic data are collected in **Table 5A.4**. The repetitive electronic spectra of UBBH2 in pH buffers are presented in **Figure 5A.10**. It is found that the molecule UBBH2 does not undergo any association or dissociation in all pH buffers. The electronic spectrum of OXAZH exhibits two absorption maxima at 260 – 280 nm with no absorption above 300 nm. This facts further supports that the electronic transitions of UBBH2 are with the urea moiety. The cyclization of urea moiety with the naphtholic ring stabilizes the molecule while the π-cloud of the carbonyl group gets merged into the overall aromatic delocalization of the OXAZH molecule along with the lone pair of electrons available on the heterocyclic nitrogen and oxygen atoms (Totally 22 aromatic electrons with n=5 in Huckels 4n+2 rule). The OXAZH is also found to vary with pH with a bathochromic shift of λ_{max} from ~ 260 – 280 nm with an isosbestic point at ~ 270 nm. OXAZH has only phenolic group to be deprotonated. The deprotonation equilibrium, leading to a plausible electronic isomerisation from benzenoid to quinoid of the conjugated phenolate anions, is presented in **Scheme 2**. The pK_a value of OXAZH and associated thermodynamic parameters are evaluated from the curve fitting plot of absorbances at two λ_{max} versus pH. The plot is shown **Figure 5A.11** and the data given in **Table 5A.4**.

$$\mathbf{A_{375}} = \frac{\mathbf{A_{final\ 375}\ K_{a1}.K_{a2}}}{\mathbf{[H^+] + K_{a1}[H^+] + K_{a1}.K_{a2}}} \quad \ldots\ldots\ldots (\mathbf{1})$$

$$\mathbf{A_{260}} = \frac{\mathbf{A_{initial\ 260}\ K_a}}{\mathbf{[H^+] + K_a}} \quad \ldots\ldots\ldots (\mathbf{2})$$

$$A_{279} = \frac{A_{final\ 279}\ K_a}{[H^+] + K_a} \qquad \ldots\ldots\ldots (3)$$

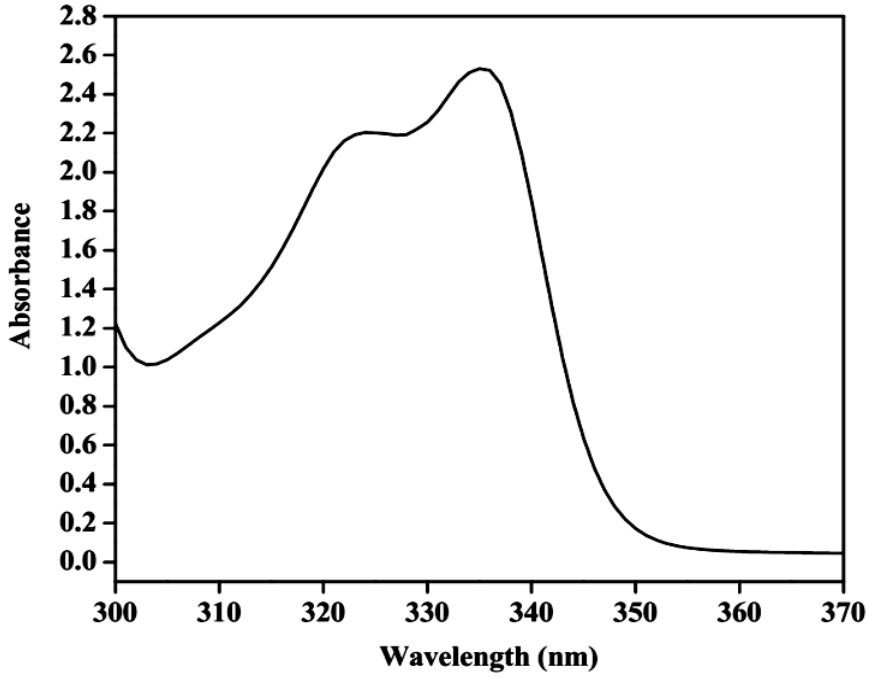

Figure 5A.7: Electronic spectra of UBBH2 (5 x 10^{-5} M) in DMF

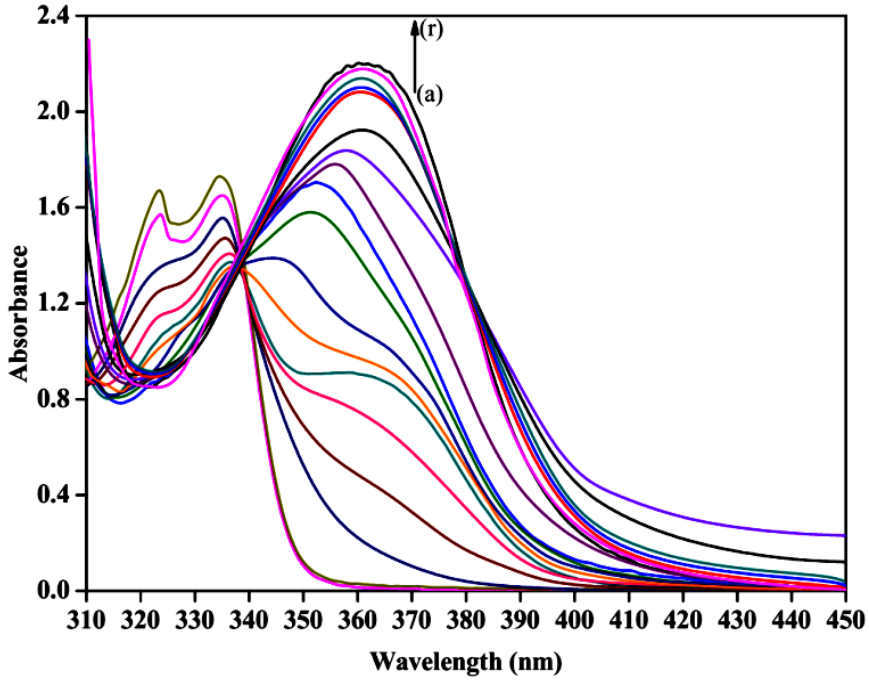

Figure 5A.8: Electronic spectra of UBBH2 (5x10^{-5} M) in 1:9 DMF/Aq. Buffer media of pH (a) 2.01 (b) 3.00 (c) 4.07 (d) 4.58 (e) 5.00 (f) 5.55 (g) 6.01 (h) 6.55 (i) 7.0 (j) 8.02 (k) 8.51 (l) 9.02 (m) 9.56 (n) 10.02 (o) 10.53 (p) 11.07 (q) 11.52 and (r) 12.02

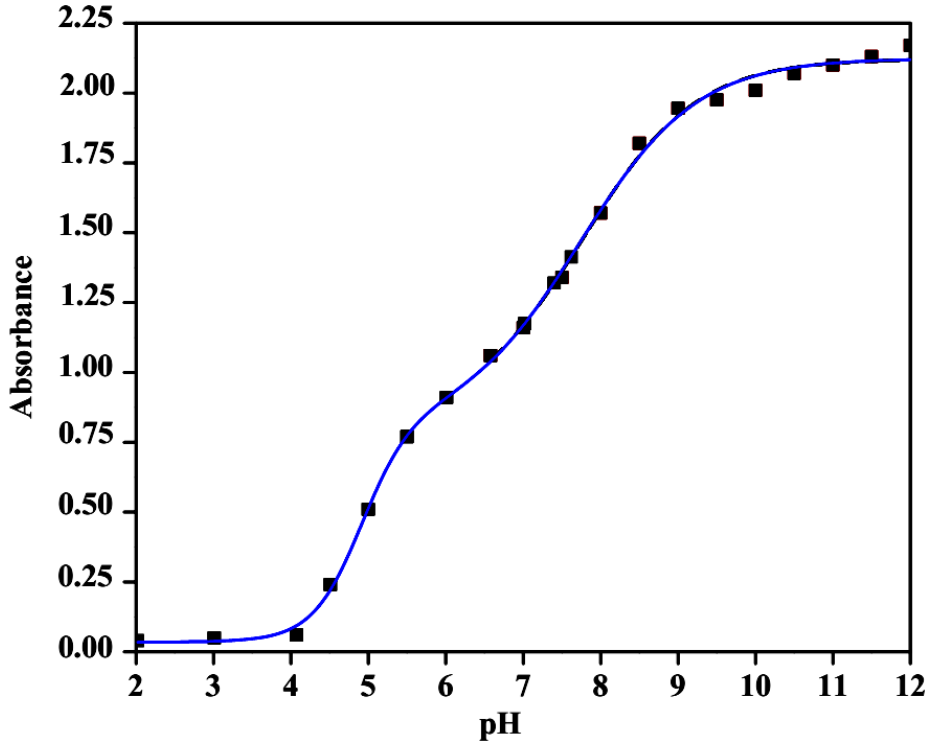

Figure 5A.9: Plot of absorbance versus pH of UBBH2 at 365 nm; experimental points (■); Regression curve-fit line (—) for Eqn. 1 for $K_{a1} = 1.23x10^{-5}$ and $K_{a2} = 1.86x10^{-8}$) with $R^2 = 0.99$

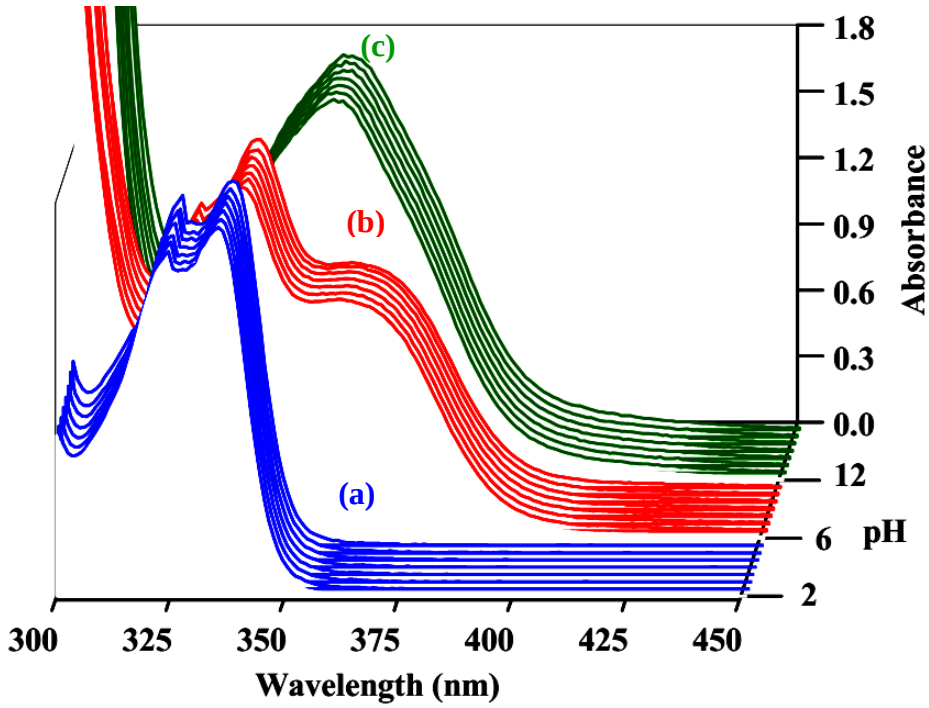

Figure 5A.10: Repetitive electronic spectra of UBBH2 ($5x10^{-5}$ M) at 5 minute intervals in 1:9 DMF/Aq. Buffers of pH (a) 2.00 (blue), (b) 6.00 (red) and (c) 12.00 (green)

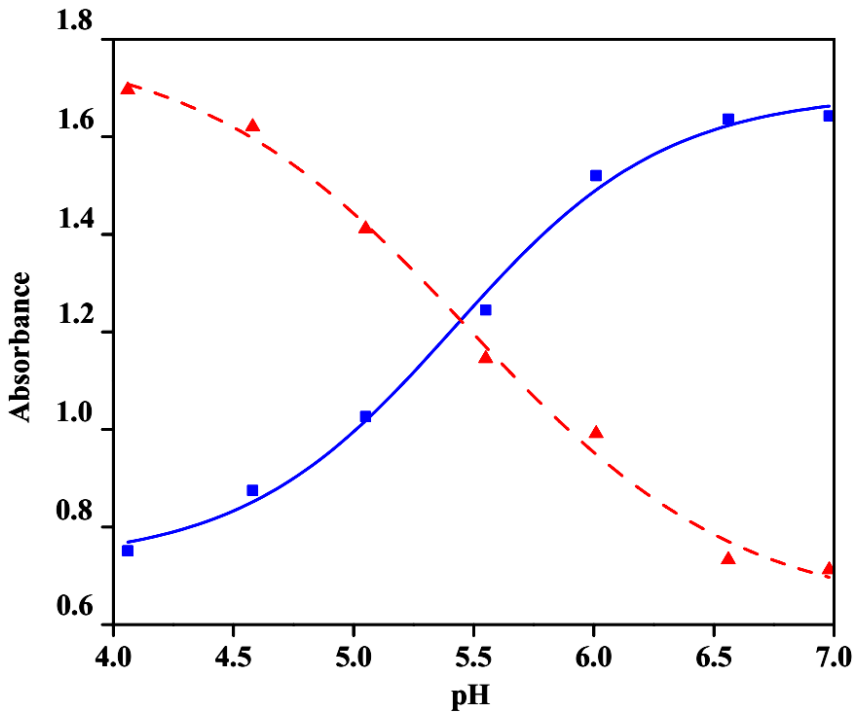

Figure 5A.11: Plot of absorbance versus pH of OXAZH at 260 nm ▲); and 279 nm (■); Regression curve-fit line (----) for Eqn. 2 for K_a = 3.98×10^{-6}) with $R^2 = 0.98$ and (—) for Eqn. 3 for $K_a = 3.97 \times 10^{-6}$ with $R^2 = 0.99$

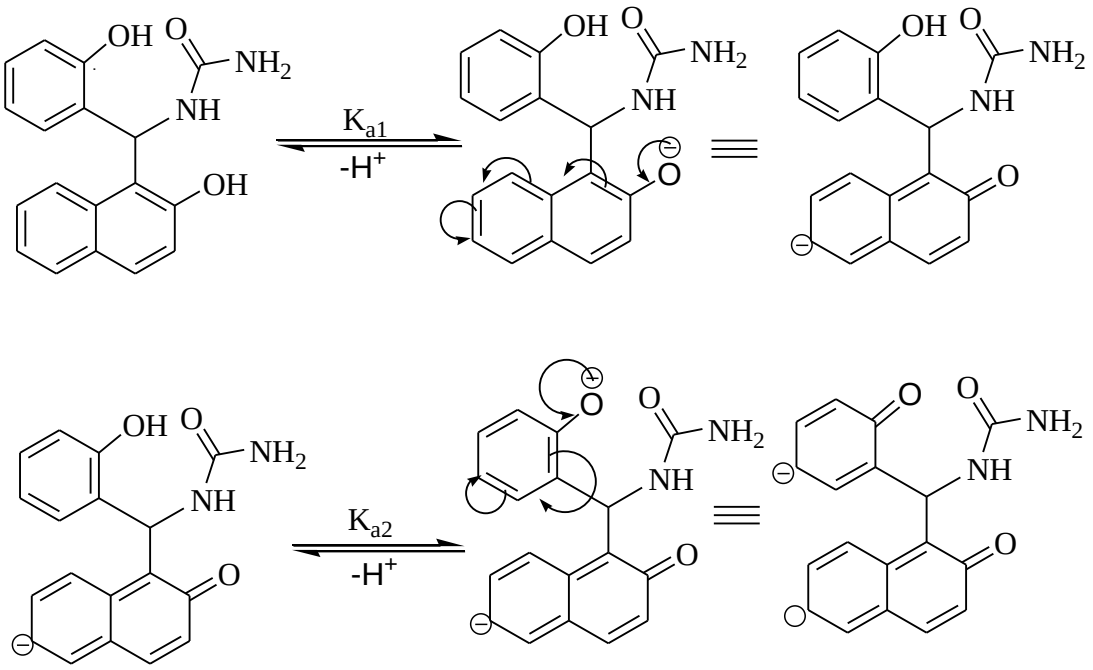

Scheme 1

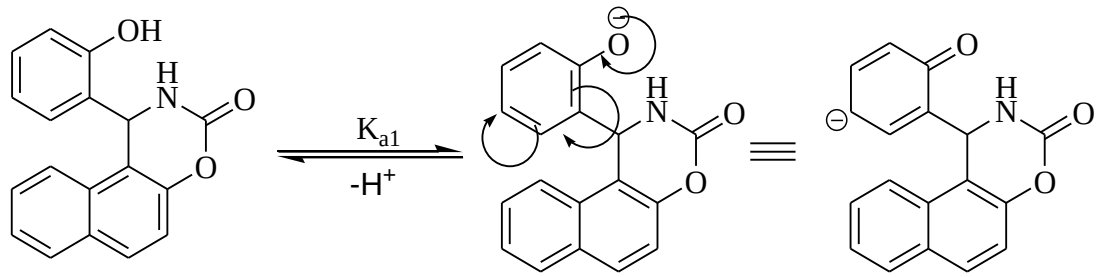

Scheme 2

Table 5A.4: *Acid – base equilibrium thermodynamic data of UBBH2 and OXAZH*

Compound	pK_{a1}	pK_{a2}	K_{a1} (mol. lit^{-1})	K_{a2} (mol. lit^{-1})	ΔG_1^0 (kcal. mol^{-1})	ΔG_2^0 (kcal. mol^{-1})
UBBH2	4.91	7.73	1.23 x 10^{-05}	1.86 x 10^{-08}	6.672	10.504
OXAZH	5.4	-	3.98 x 10^{-06}	-	7.411	-

Here $\Delta G^{\circ} = 2.303RT\ pK_a$

5A.6.2: *Fluorescence emission spectra of UBBH2*

UBBH2 has shown fluorescence emission property in different pH buffers at 365 nm excitation wavelength. The overlay of electronic absorption and fluorescence emission spectra in pH = 12 buffer are depicted in **Figure 5A.12**. The peak at ~450 nm corresponding to the $n \rightarrow \pi^*$ transition of quinoid form of β-naphthol. From the electronic absorption and fluorescence emission spectra of UBBH2 stoke shift values have been calculated in all pH buffers and corresponding data have been tabulated in **Table 5A.5**.

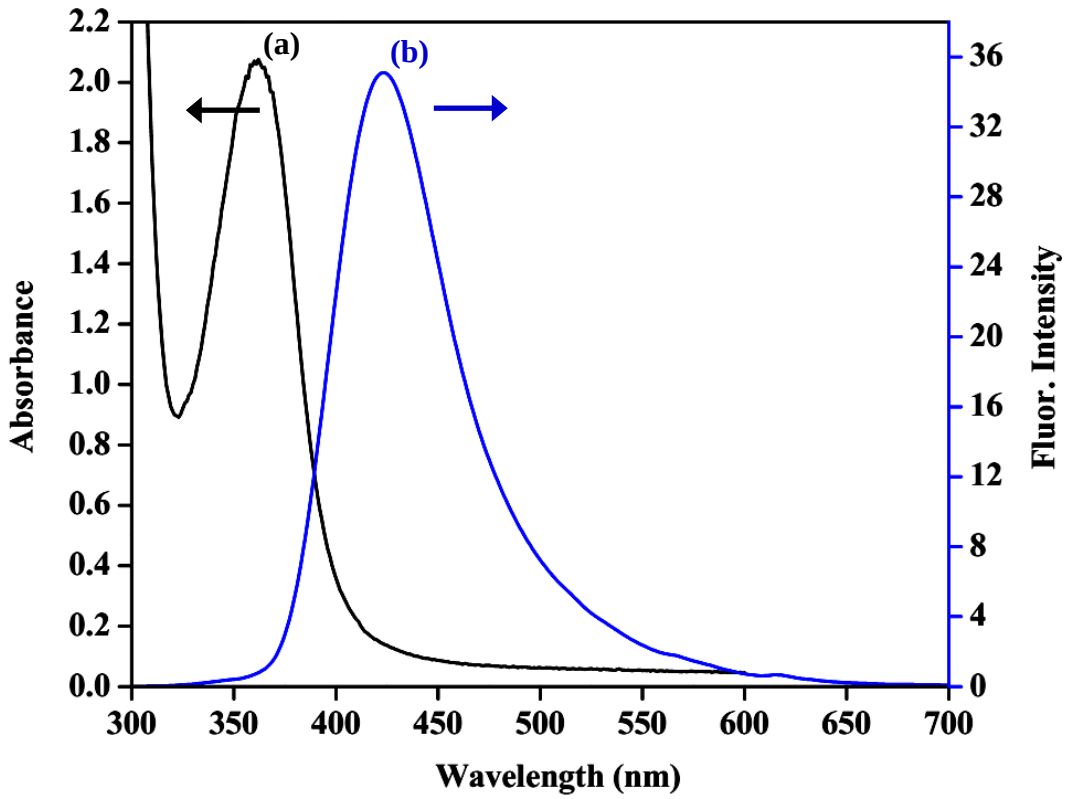

Figure 5A.12: Electronic spectra of UBBH2 (5 x 10^{-5} M) (a) UV-Visble absorption and (b) Fluorescence emission spectra in pH = 12 buffer

Table 5A.5: *Uv – visible electronic absorption and fluorescence emission spectral data of UBBH2 in different pH buffers*

pH	Electronic absorption λ_{max} (nm)	Fluorescence emission $\lambda_{emission}$ (nm)	Stoke Shift (nm)
2	323.54 334.47	417.72 465.17	94.18, 141.63 83.25, 130.70
4	323.54 334.47	358.81, 414.26 465.08	35.27, 90.72, 141.54 24.34, 79.79, 130.61
6	336.43 360.50	416.12 464.37	79.69, 127.94 55.62, 103.87
8	352.06	422.52 467.57	70.46 115.51
10	361.31	418.97, 469.70 484.54	57.66, 108.39 123.23

12	361.04	422.25	61.21

5A.7: Halochromic Effect of UBBH2

UBBH2 has been found to show halochromic behaviour with a spike of dil. NaOH[5]. The resultant solution turns pale yellow from colourlessness. The electronic spectra of UBBH2 in pure DMF solvent and that in alkaline medium are presented in **Figure 5A.13**. The bathochromic shift of the λ_{max} from 335 to 365 nm upon alkali addition is attributed, as mentioned in section 5A.5, to the benzenoid to quinoid conversion of the compound.

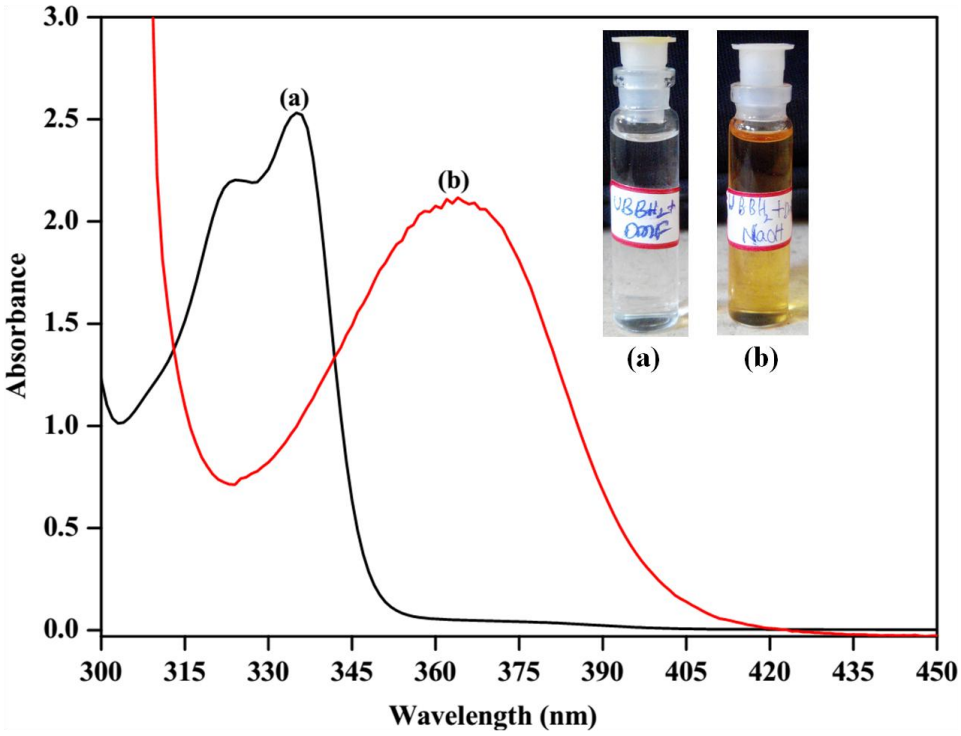

Figure 5A.13: Halochromic electronic shift of UBBH2 (5 x 10^{-5} M); (a) in DMF solvent and (b) with spike of 0.1M NaOH

5A.8: Differential Scanning Calorimetry (DSC)

UBBH2 with its assymmetric carbon centries is expected to exhibit identical spectral, thermal and analytical character. However, the diferential scanning colorigrams of UBBH2 racemic mixture, R-UBBH2.2DMF and S-UBBH2.2DMF did not give identical DSC thermograms. The DSC thermograms of UBBH2 racemic mixture and its R and S DMF solvates are shown in **Figure 5A.14**. The DSC trace of racemic UBBH2 shows an endotherm at 183 ˚C corresponding to its melting event. No thermal events are found below this

temperature. This fact indicates that no solvent molecules intruded into the polycrystalline racemic mixture during the preparation or recrystallization from ethanol. The crystals obtained from DMF (prismatic shaped crystals), i.e., of R-UBBH2.2DMF, however, exhibit two endotherms at ∼137 and ∼155 °C. The event at ∼137 °C is assigned to the expulsion of DMF molecules from the solvate crystals whereas that at ∼155 °C is to the melting process of the desolvated R enantiomeric crystal residue. The lower melting point of the solvate when compared to the melting point of unsolvated racemic mixture is attributed to (i) strained molecular orientations of UBBH2 in solvates (vis a vis the racemic compound), (ii) the depression in freezing point by colligative property and (iii) That unsolvated UBBH2 and solvated UBBH2 (i.e. UBBH2.2DMF) would not have similar inter-molecular distances and interactions. The thermogram of S-UBBH2.2DMF (rectangular shaped crystals) shows two endotherms at ∼144 °C and ∼155 °C. The event at∼144 °C is again assigned to the expulsion of DMF molecules from the solvate crystals whereas that at ∼155 °C is, as usual, to the melting process of the desolvated S enantiomeric crystal residue. That the desolvation point of R-UBBH2.2DMF is lower than that of S-UBBH2.2DMF by ∼7 °C is unexpected. One can relate this anomaly to possible anisotropic packing of UBBH2⋯UBBH2 and UBBH2⋯DMF by supramolecular (intermolecular) interactions. The heat of desolvation is found to be more for S-UBBH2.2DMF (+134.80 kJ mol^{-1}) solvate than that for R-UBBH2.2DMF (+130.4 kJ mol^{-1}) solvate. Hence, the binding energy of DMF molecules in S-UBBH2.2DMF is evaluated as −67.4 kJ mol^{-1} whereas that in R-UBBH2.2DMF as −65.2 kJ mol^{-1}, implying that the DMF molecules are held more firmly in S-UBBH2.2DMF than in R-UBBH2.2DMF. Similarly, OXAZH thermogram has been recorded in same conditions and depicted in **Figure 5A.14**. From the OXAZH thermogram it is understood that the molecule has one endothermic peak at ~262 °C, which is attributed to the melting event of the molecule. The heat of fusion of OXAZH is found to be 158.1 kJ mol^{-1}. The thermal analysis data of UBBH2, R and S-UBBH2.2DMF and OXAZH are given in **Table 5A.6**.

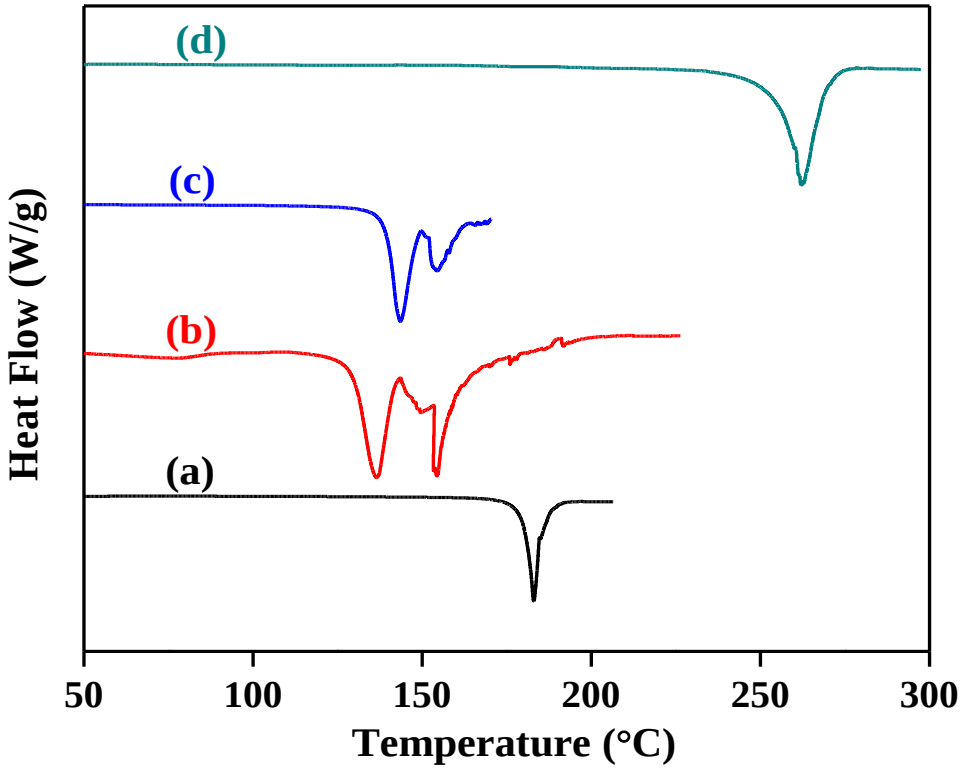

Figure 5A.14: DSC thermograms (a) UBBH2 [M.P = ~183 ˚C] (b) R-UBBH2.2DMF [desolvation,~136 ˚C; M.P = ~154 ˚C] (c) S-UBBH2.2DMF [desolvation,~143 ˚C; M.P = ~154 ˚C] (d) OXAZH [M.P = ~262 ˚C]

Table 5A.6 *DSC data of UBBH2, R-UBBH2.2DMF, S-UBBH2.2DMF and OXAZH*

	UBBH2	R-UBBH2.2DMF	S-UBBH2.2DMF	OXAZH
Purity (mol %)	98.10	98.68	99.89	78.38
Desolvation Point (°C)	-	136.46	143.48	-
Melting Point (°C)	183	154.46	154.65	262.78
Depression (°C)	0.59	0.14	0.01	3.30
Heat of Desolvation (kJ mol^{-1})	-	-65.2	-67.4	-
Heat of Fusion (kJ mol^{-1})	55.96	57.59	77.39	158.1
Cell Constant	1.24	1.24	1.24	1.24
Onset Slop (mW/°C)	-16.92	-16.92	-16.92	-16.92
RMS Deviation (°C)	0.02	0.03	0.01	0.03

5A.9: Electrochemical Studies

5A.9.1: *Aqueous electrochemistry of UBBH2*

The results in **5A.6.1** disclosed that UBBH2 and OXAZH molecules exist in conjugated acid – base forms (**Scheme 1 and 2**). A brief survey of literature indicates that naphthaldimines and salicylaldimines can exist in tautomeric forms[6–8]. Usually, one form is benzenoid and other is quinoid form. Variation in pH alters the relative population of benzenoid and quinoid forms. Change in the molecular structure affects voltammetric behavior of the compound[9–11]. Hence, UBBH2 and OXAZH are expected to show pH – dependent electrochemical features.

The electrochemical behavior of UBBH2 (C_0 = 5 x 10^{-5} M) has been recorded in aqueous and nonaqueous buffers. The static mercury dropping electrode (SMDE) has been employed as working electrode for cathodic sweep whereas glassy carbon electrode (GCE) has been used for anodic sweep for the recording of cyclic voltammograms in the pH range, 2 – 12. These investigations are performed in aqueous and nonaqueous buffer solutions.

The cyclic voltamograms are recorded in the electrochemical potential window of -0.1 V to -1.5 V for the SMDE working electrode whereas for glassy carbon electrode -0.1 V to +1.5 V with respect saturated calomel electrode (Hg/Hg_2Cl_2, KCl(sat)) served as reference electrode and Pt wire as counter electrode for the all the electrochemical runs. A few cyclic voltammograms of UBBH2 are shown in **Figures 5A.15-5A.16**. Each peak in the cyclic voltamograms has the following features:

(a) Cyclic voltammogram of UBBH2 in pH=2 has been recorded and presented in **Figure 5A.15**. It shows a quasi-reversible peak. It is assigned to the reductive de-ureation of UBBH2. Similar kind of trends (**Figure 5A.15**) are observed in pH=4 and in pH=6 buffers.

(b) Cyclic voltammogram of UBBH2 in pH=8 has been recorded and presented in **Figure 5A.15**. It shows two reduction peaks. These peaks are assigned to structural differences in benznoid and quinoid forms and their reductive de-ureation of UBBH2. Similar kind of trends (**Figure 5A.15**) are observed in pH=10 and in pH=12 buffers.

(c) The peak potential is found to be cathodically shifted with increasing analytical concentration, pH and scan rate suggesting the involvement of a following chemical event at low scan rate wherein the chemical event (C) competes with another the electrochemical event (E) that accompanies with a participation of H^+ ion in the electron transfer process.

(d) Cyclic voltammograms of UBBH2 in anodic region has been recorded in pH=2 (**Figure 5A.16**). It shows a irreversible peak. It is ascribed to the oxidation of hydroxyl moieties in UBBH2. Similar kind of trends are observed in pH=4 and in pH=6 buffers.

(e) Cyclic voltammograms of UBBH2 in pH=8 has been recorded and presented in **Figure A.16**. It shows two anodic peaks These peaks are assigned to the consecutive electrochemical oxidation of phenol and naphthol hydroxyl groups in their benznoid and quinoid forme of UBBH2. Similar kind of trends are observed in pH=10 and in pH=12 bufers.

(f) The peak potential is found to be cathodically shifted with increasing analytical concentration, pH and scan rate suggesting the involvement of a following chemical event at low scan rate wherein the chemical event (C) competes with another the electrochemical event (E) that accompanies with a participation of H^+ ion in the electron transfer process.

(g) The current function ($ip/\nu^{1/2}$) is found to be near independent of scan rate at higher range of scan rates indicating the absence of any chemical event following the electrochemical event.

(h) The peak current (i_p) is linear to $\nu^{1/2}$ indicating simple diffusion-controlled electron transfer in cathodic electrochemical process (**Figures 5A.17-5A.28**).

(i) The peak current (i_p) is linear to ν indicating simple adsorption-controlled electron transfer in anodic electrochemical process (**Figures 5A.29-5A.30**).

(j) The peak potentials are linear to pH (**Figure 5A.31**)suggesting a fixed number of H^+ ions participating in the electrochemical reduction.

Based on the above observations, eventually a plausible redox mechanism for both cathodic and anodic electrochemical processes are proposed and shown below.

Cathodic reaction:

pH < pK_{a1}:

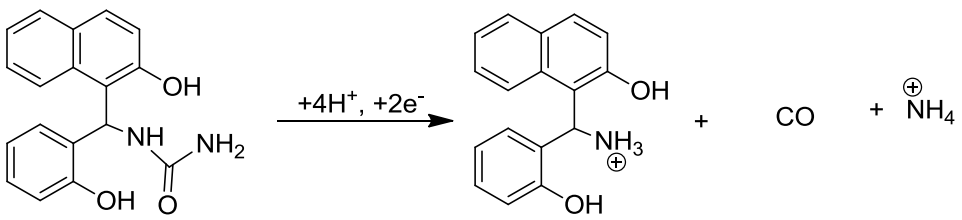

pK_{a1} < pH < pK_{a2}:

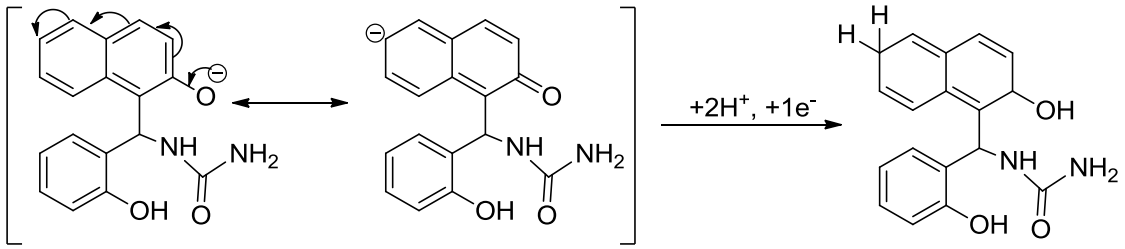

pH > pK_{a2}:

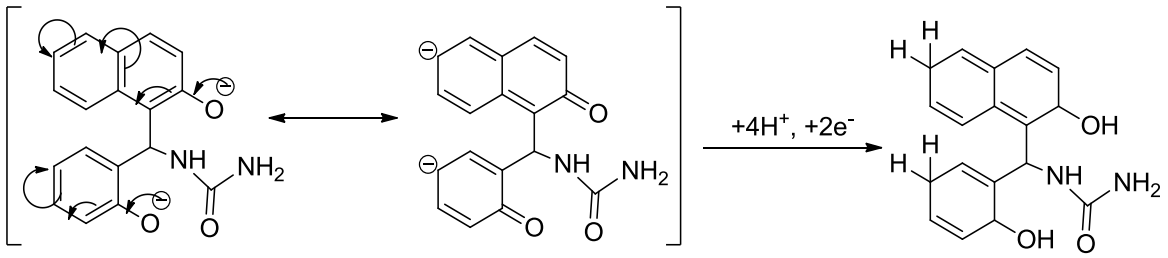

Anodic reaction:

pH < pK_{a1}:

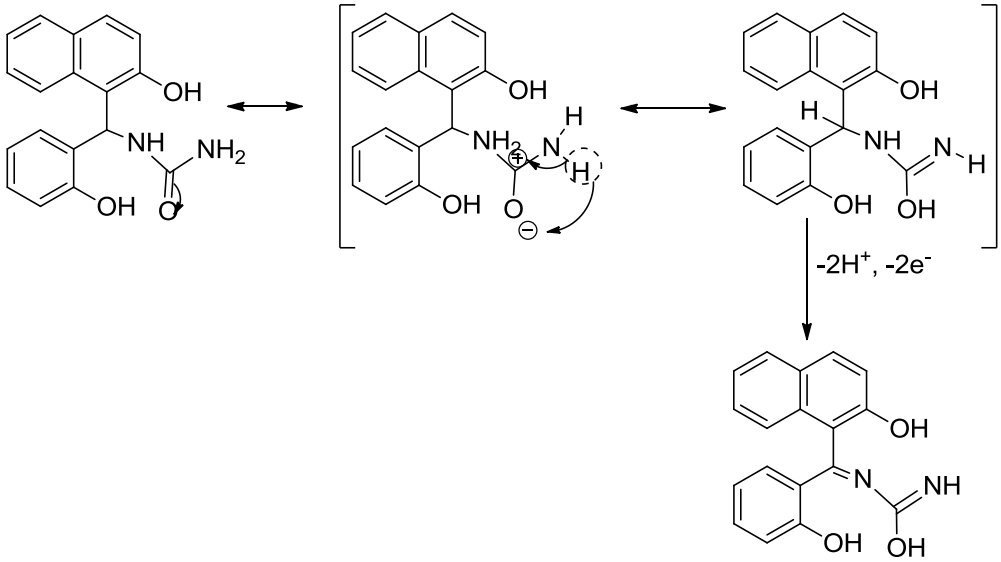

pK_{a1} < pH < pK_{a2}:

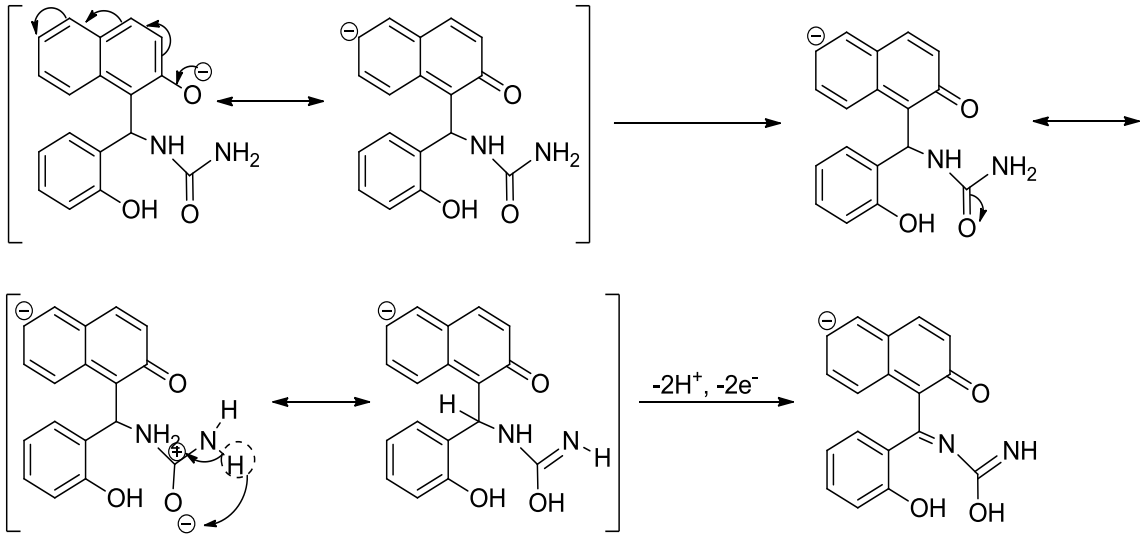

pH > pK_{a2}:

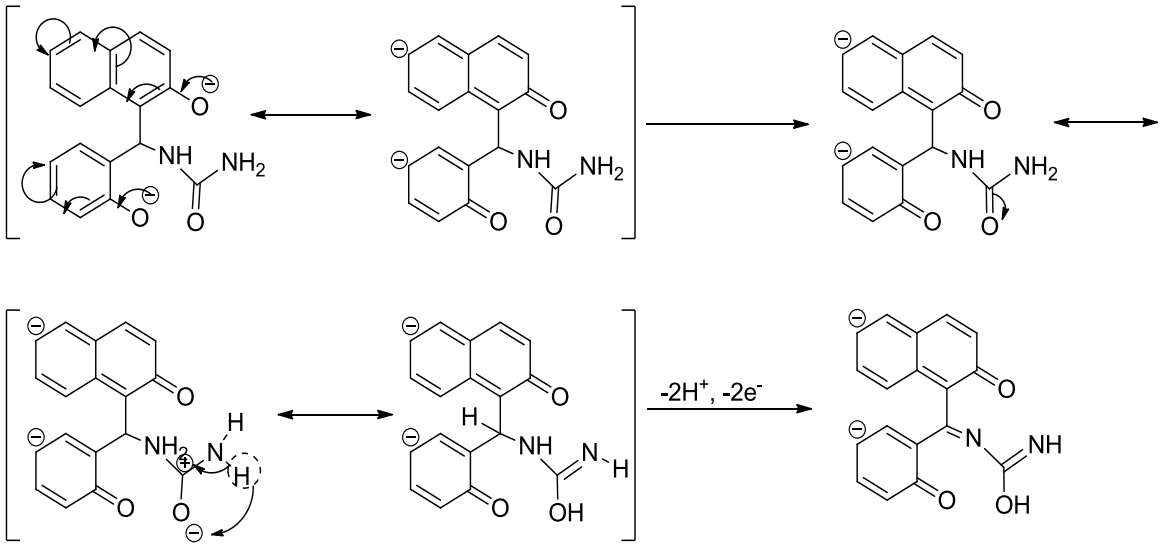

Since the deprotonation of UBBH2 results benzenoid and quinoid structure which are differ in electrochemically two kinds of electrochemically reducible electrophores in equilibrium. The reason for giving two peaks at alkaline pHs is assigned to the presence of the two structurally different species. Hence, one would get two cyclic voltammogram responses. The experimental results are in line with this proposed **Scheme 1** in section **5A.6.1**.

Further, coulometric measurements are undertaken at potential more than 100 mV of the peak potential in all the pH buffers. It suggests that the reduction involves 1 electrons in acidic, basic and neutral pH range. The number of protons participated in the reduction process is found as 1 from the plot of E_p versus pH.

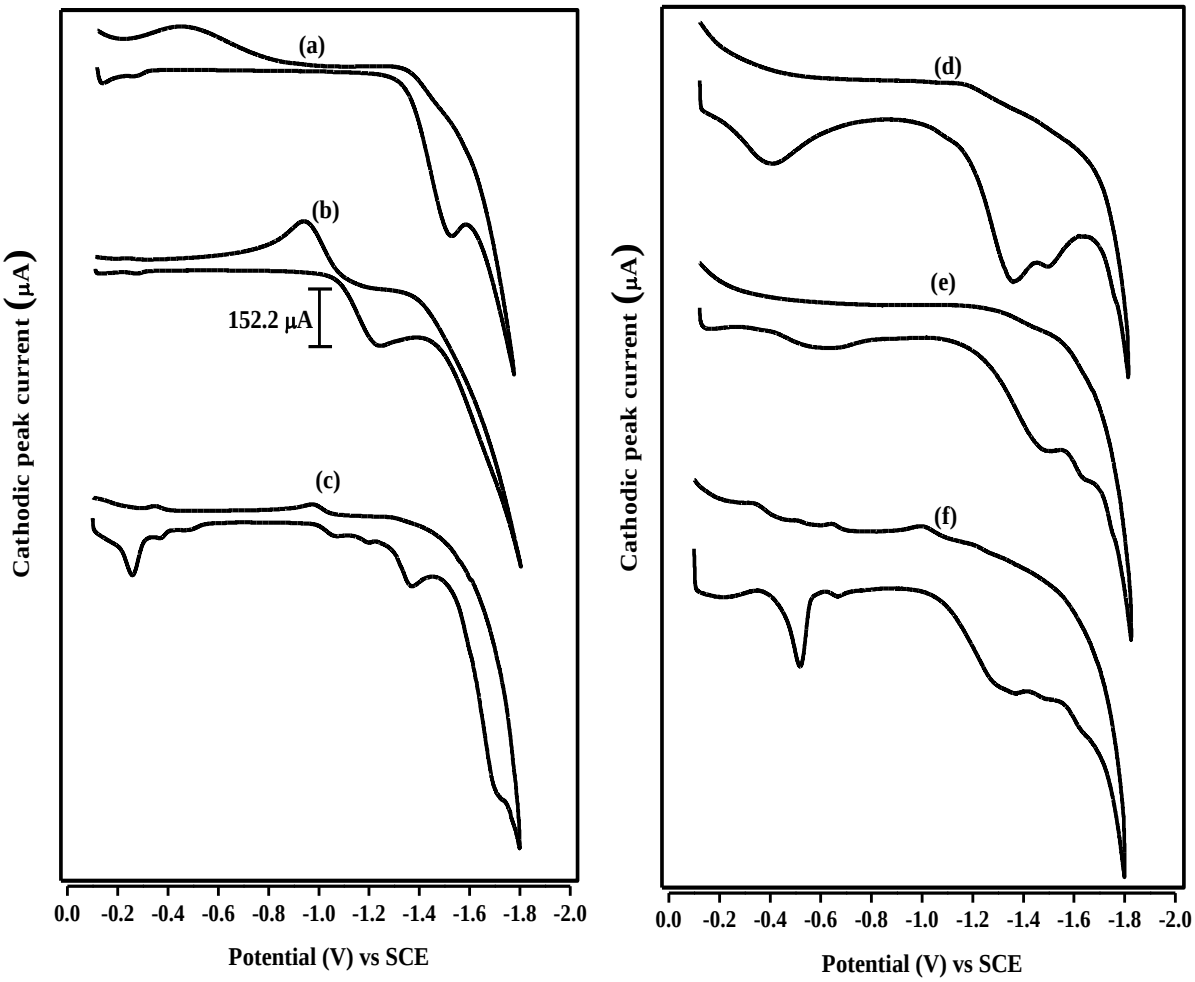

Figure 5A.15: Stacked cyclic voltammograms of UBBH2 (5 x 10^{-5} M) in 1:9 DMF/Aq. buffer media of pH (a) 2.01 (b) 4.07 (c) 6.01 (d) 8.02 (e) 10.02 and (f) 12.02 (Scan rate 100 mVs^{-1}) on SMDE

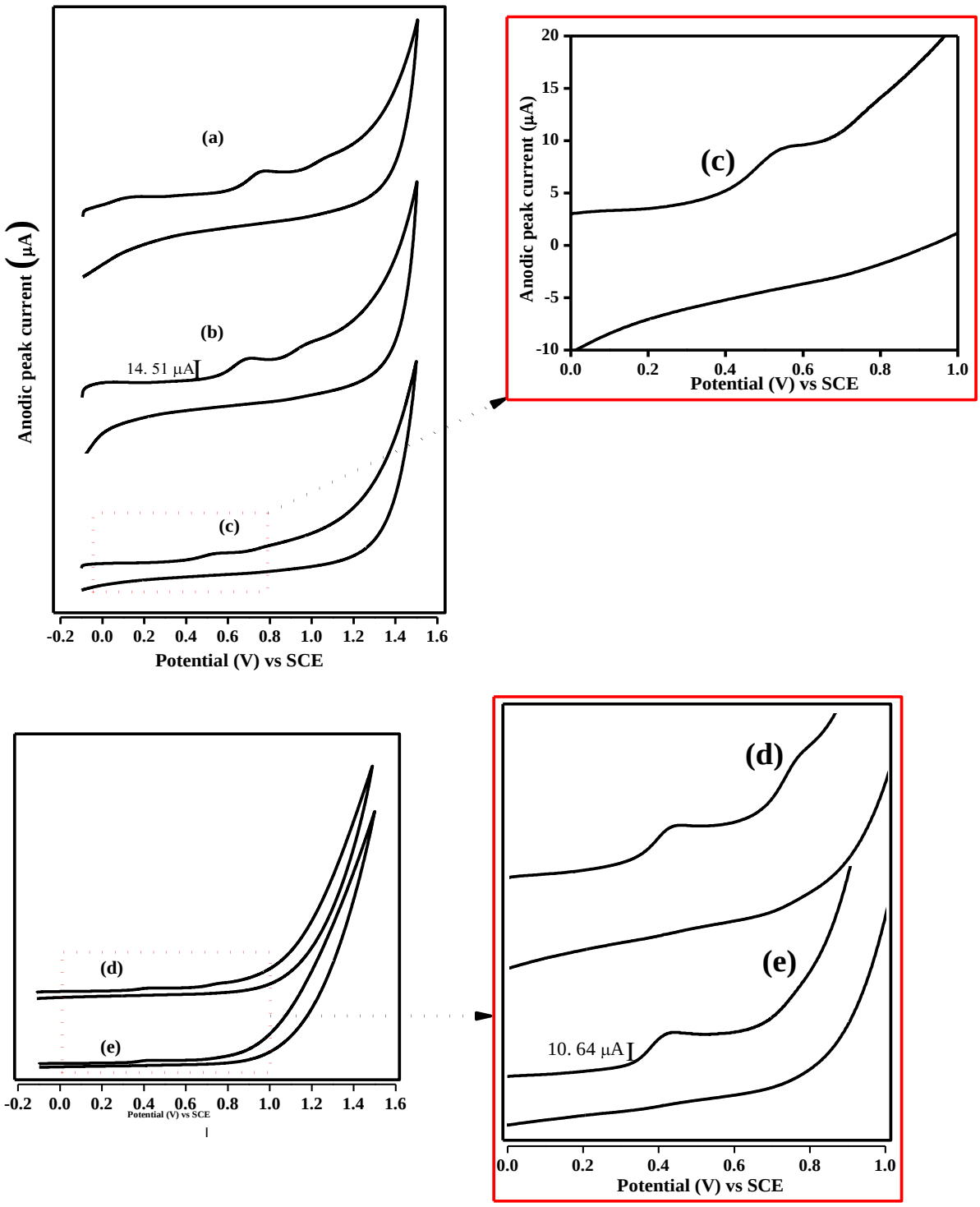

Figure 5A.16: Stacked cyclic voltammograms of UBBH2 ($5x10^{-5}$ M) in 1:9 DMF/Aq. buffer media of pH (a) 2.01 (b) 4.07 (c) 6.01 (inset view) (d) 8.02 (e) 10.02 (inset view) and (f) 12.02 (inset view) (Scan rate 100 mVs^{-1}) on GCE

For an n-electron, an m-proton electrochemical reduction, the cyclic voltammetric peak, E_p is shifted cathodically with pH

$$E_p = E_p^0 - \frac{0.0591m}{n}\, pH$$

Here E^0_p is E_p at $a_{H^+} = 1$. Hence, the plot of E_p versus pH should be straight line with a slope of (0.05916 m)/n from which one can get the value of m with knowledge of n. The value of m evaluated from the two linear segments of **Figure 5A.31** turns out to be 1 in both acid and basic range, relevant data has been given in **Table 5A.7**.

However, the electrochemical data such as peak current i_p, peak potentials E_p diffusion coefficient D_o and heterogeneous electron transfer coefficient, $k°_h$ values of UBBH2 are calculated and given in **Table 5A.7**. The plots of E_p versus log ν at different pH values noticed to be straight line. The slope (S_1) values are proportional to αn_a. Neverthlessly, the values of αn_a is found to be in the range 0.2-0.6 and α values in between 0.34-0.96.

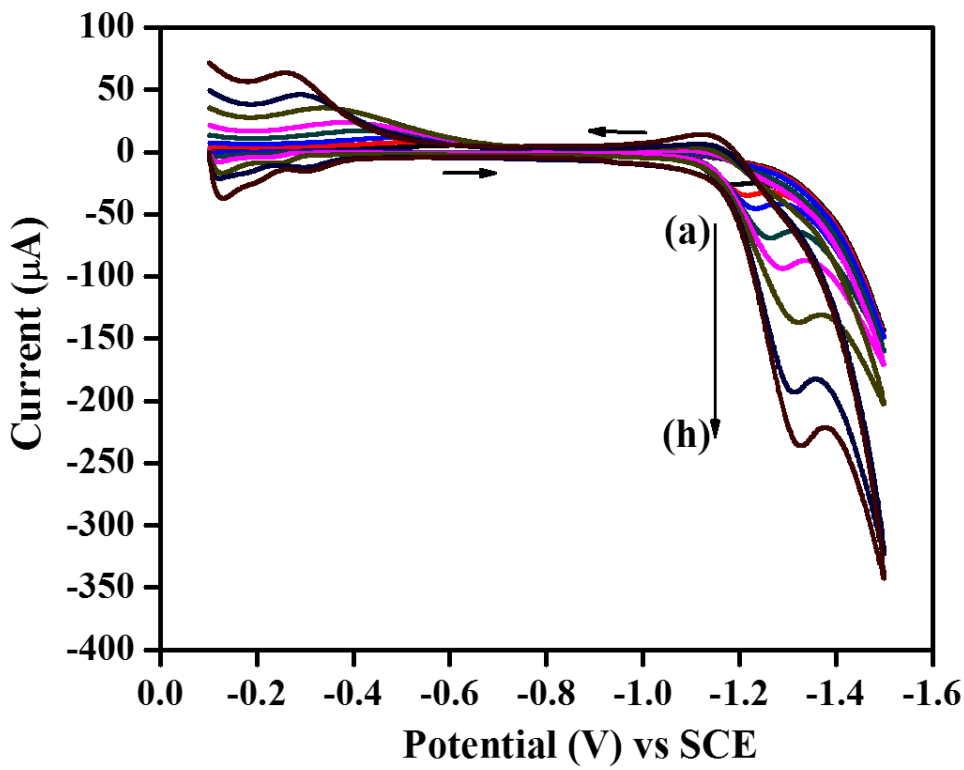

Figure 5A.17: Cyclic voltammograms of UBBH2 (5 x 10^{-5} M) in 1:9 v/v DMF/aq. Buffer media of pH = 2.01, on SMDE at various scan rate (a) 50 mVs^{-1} (b) 100 mVs^{-1} (c) 200 mVs^{-1} (d) 500 mVs^{-1} (e) 1000 mVs^{-1} (f) 2000 mVs^{-1} (g) 3000 mVs^{-1} (h) 5000 mVs^{-1}

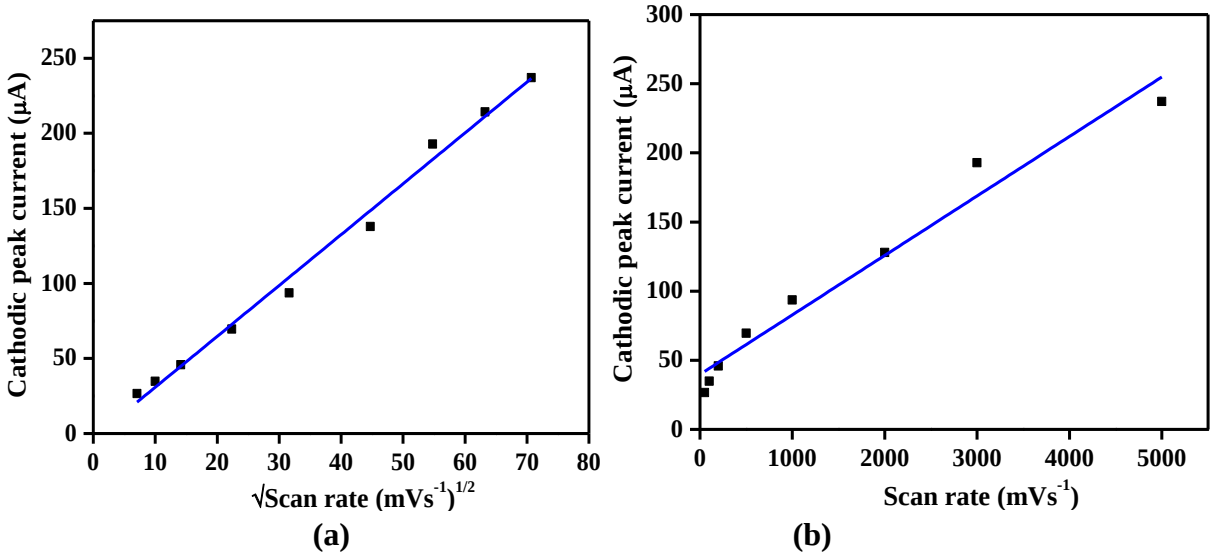

Figure 5A.18: Effect of scan rate on cathodic peak current in 1:9 DMF/aq. Buffer medum of pH = 2.01, on SMDE (a) $\nu^{1/2}$ versus i_{pc} (b) ν versus i_{pc}

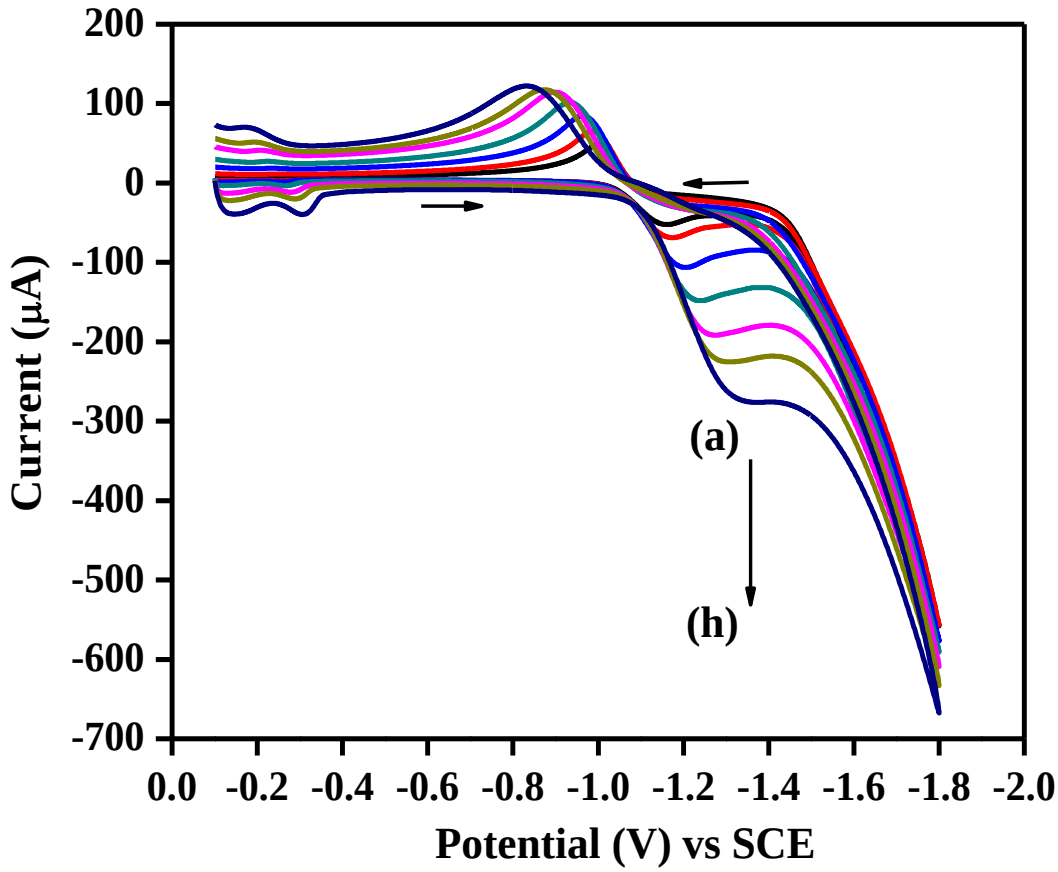

Figure 5A.19: Cyclic voltammograms of UBBH2 (5 x 10^{-5} M) in 1:9 v/v DMF/aq. Buffer media of pH = 4.07, on SMDE at various scan rate (a) 50 mVs^{-1} (b) 100 mVs^{-1} (c) 200 mVs^{-1}(d) 500 mVs^{-1} (e) 1000 mVs^{-1} (f) 2000 mVs^{-1} (g) 3000 mVs^{-1} (h) 5000 mVs^{-1}

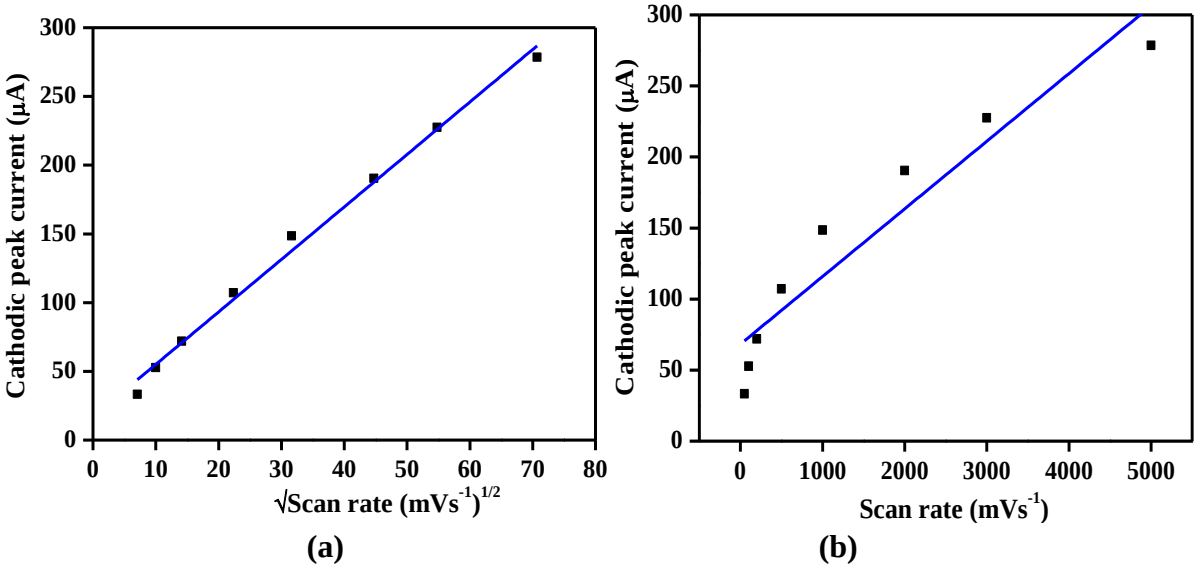

Figure 5A.20: Effect of scan rate on cathodic peak current in 1:9 DMF/aq. Buffer medum of pH = 4.07, on SMDE (a) $\nu^{1/2}$ versus i_{pc} (b) ν versus i_{pc}

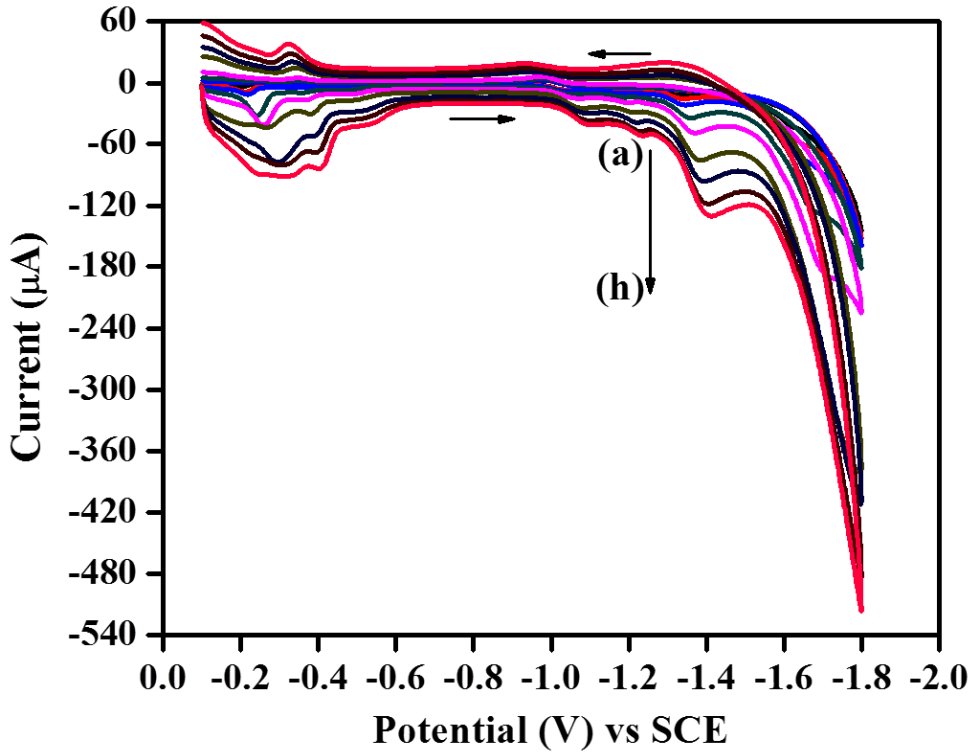

Figure 5A.21: Cyclic voltammograms of UBBH2 (5 x 10^{-5} M) in 1:9 v/v DMF/aq. Buffer media of pH = 6.01, on SMDE at various scan rate (a) 50 mVs^{-1} (b) 100 mVs^{-1} (c) 200 mVs^{-1} (d) 500 mVs^{-1} (e) 1000 mVs^{-1} (f) 2000 mVs^{-1} (g) 3000 mVs^{-1} (h) 5000 mVs^{-1}

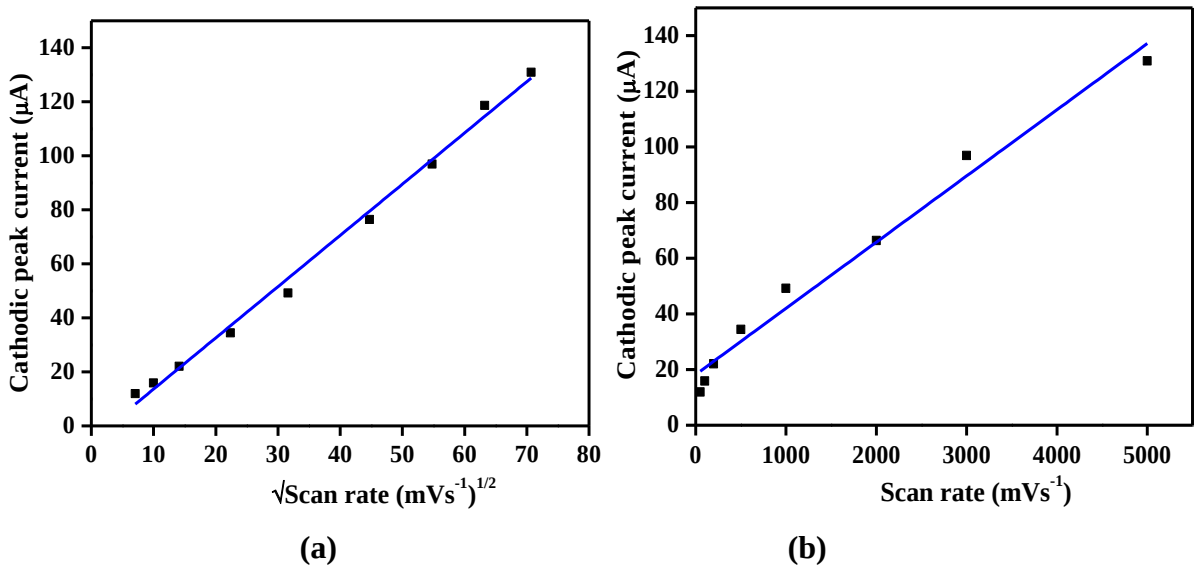

Figure 5A.22: Effect of scan rate on cathodic peak current in 1:9 DMF/aq. Buffer medum of pH = 6.01, on SMDE (a) ν1/2 versus ipc (b) ν versus ipc

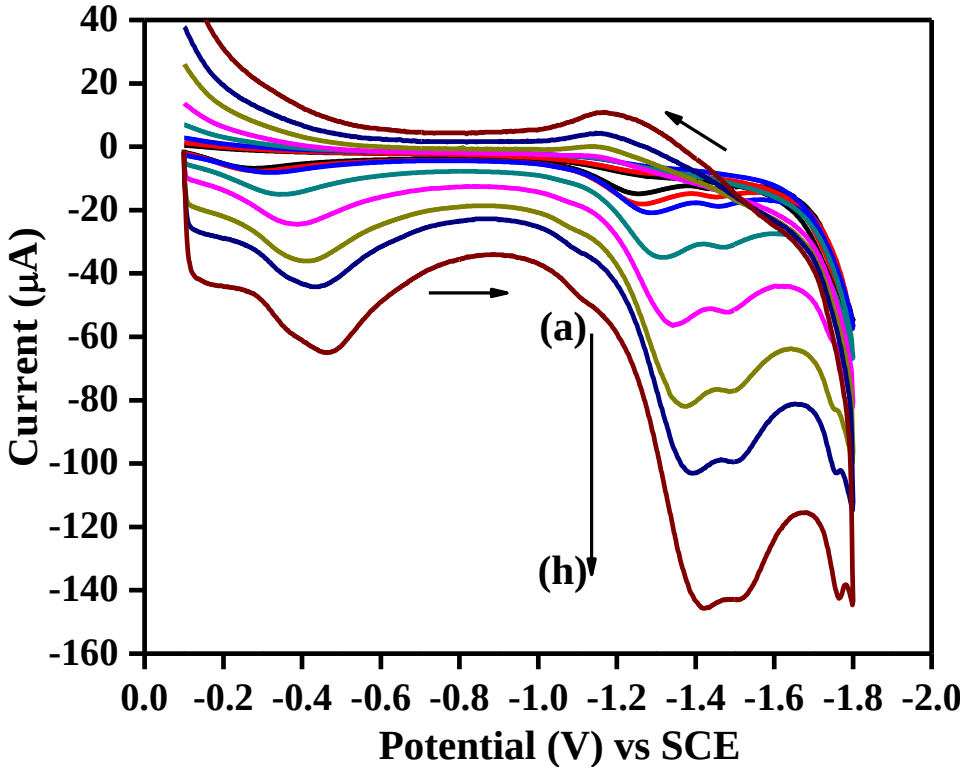

Figure 5A.23: Cyclic voltammograms of UBBH2 (5 x 10^{-5} M) in 1:9 v/v DMF/aq. Buffer media of pH = 8.02, on SMDE at various scan rate (a) 50 mVs^{-1} (b) 100 mVs^{-1} (c) 200 mVs^{-1} (d) 500 mVs^{-1} (e) 1000 mVs^{-1} (f) 2000 mVs^{-1} (g) 3000 mVs^{-1} (h) 5000 mVs^{-1}

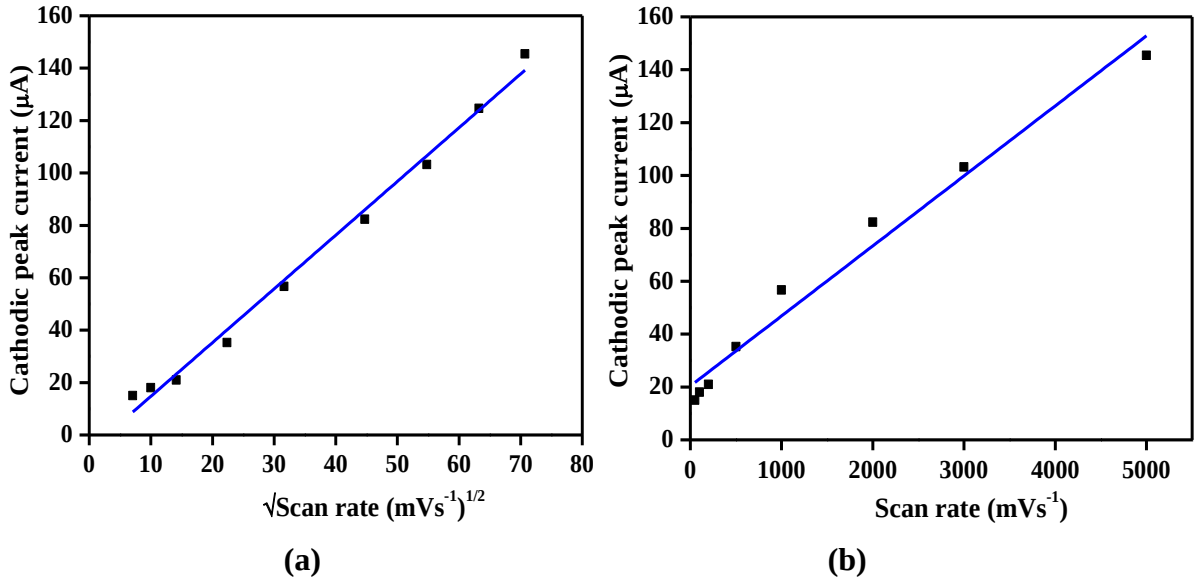

Figure 5A. 24: Effect of scan rate on cathodic peak current in 1:9 DMF/aq. Buffer medium of pH = 8.02, on SMDE (a) $\nu^{1/2}$ versus i_{pc} (b) ν versus i_{pc}

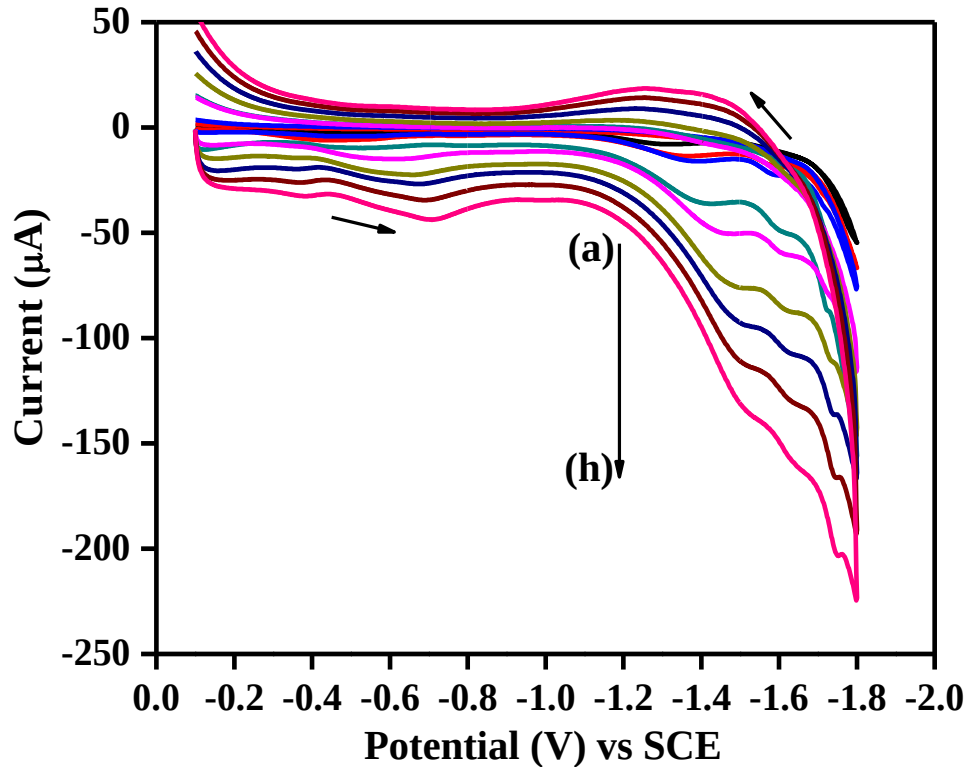

Figure 5A.25: Cyclic voltammograms of UBBH2 (5 x 10^{-5} M) in 1:9 v/v DMF/aq. Buffer media of pH = 10.02, on SMDE at various scan rate (a) 50 mVs^{-1} (b) 100 mVs^{-1} (c) 200 mVs^{-1} (d) 500 mVs^{-1} (e) 1000 mVs^{-1} (f) 2000 mVs^{-1} (g) 3000 mVs^{-1} (h) 5000 mVs^{-1}

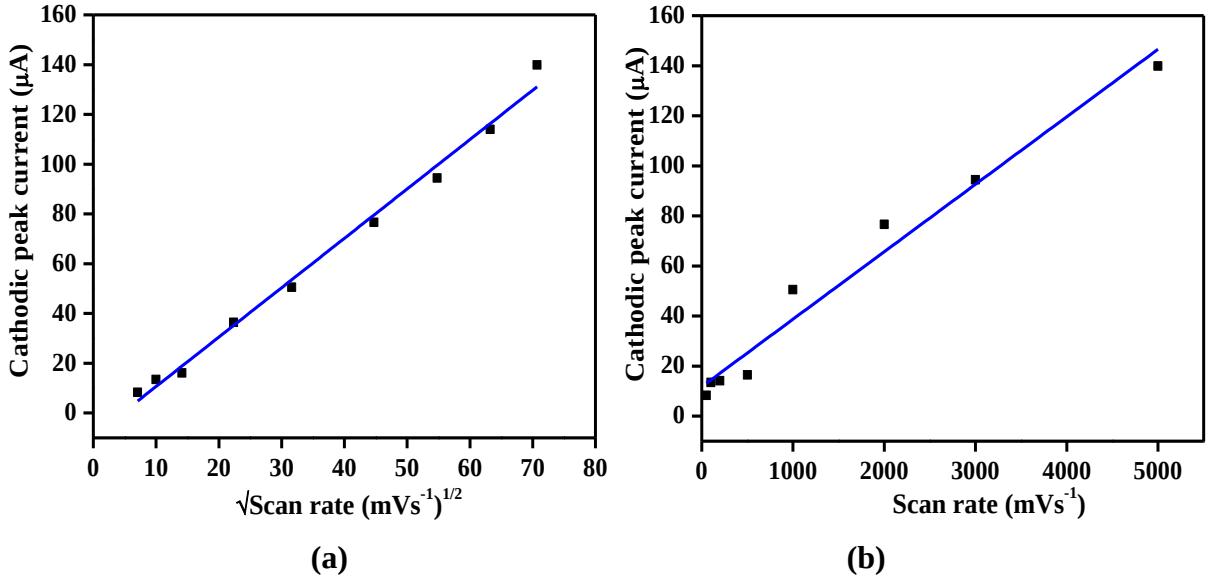

Figure 5A.26: Effect of scan rate on cathodic peak current in 1:9 DMF/aq. Buffer medium of pH = 10.02, on SMDE (a) $\nu^{1/2}$ versus i_{pc} (b) ν versus i_{pc}

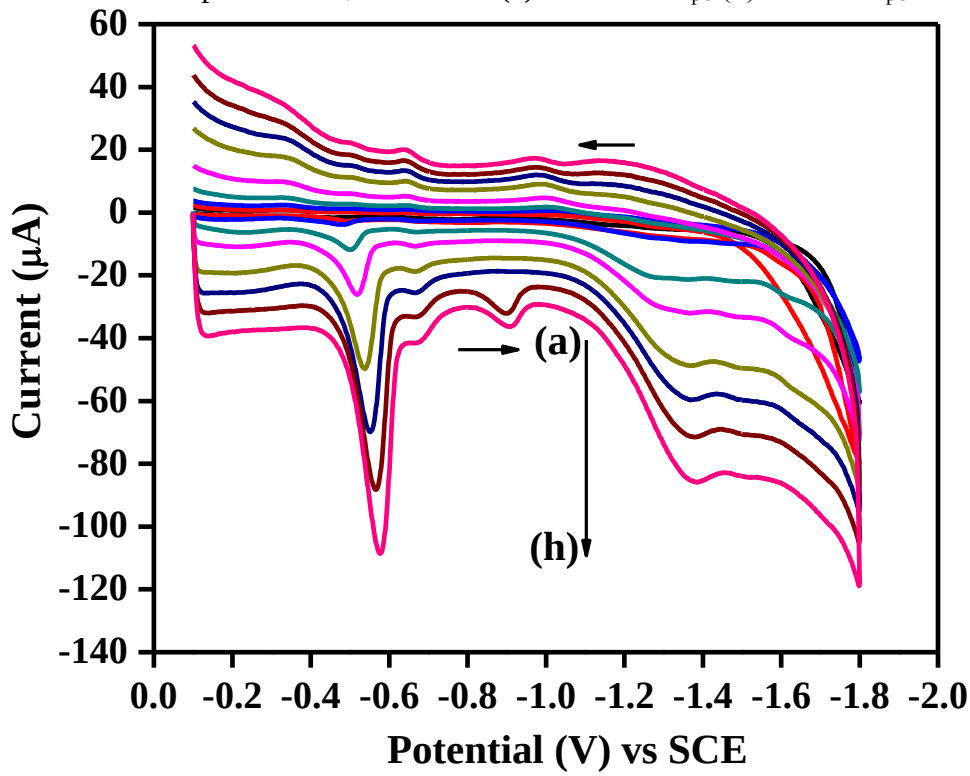

Figure 5A.27: Cyclic voltammograms of UBBH2 (5 x 10^{-5} M) in 1:9 v/v DMF/aq. Buffer media of pH = 12.02, on SMDE at various scan rate (a) 50 mVs^{-1} (b) 100 mVs^{-1} (c) 200 mVs^{-1} (d) 500 mVs^{-1} (e) 1000 mVs^{-1} (f) 2000 mVs^{-1} (g) 3000 mVs^{-1} (h) 5000 mVs^{-1}

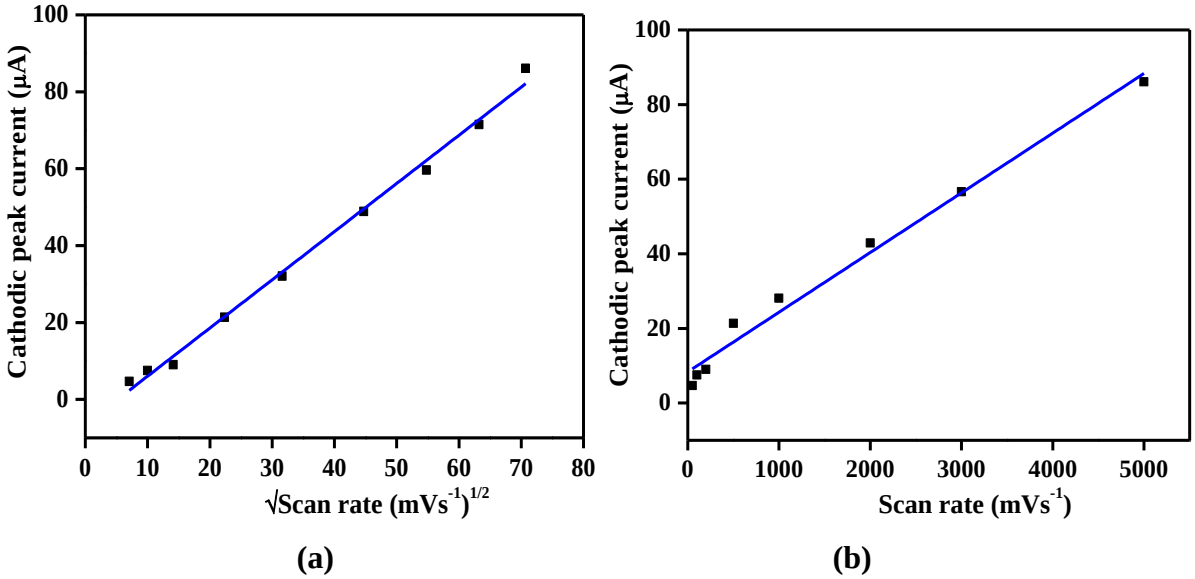

Figure 5A.28: Effect of scan rate on cathodic peak current in 1:9 DMF/aq. Buffer medium of pH = 12.02, on SMDE (a) $\nu^{1/2}$ versus i_{pc} (b) ν versus i_{pc}

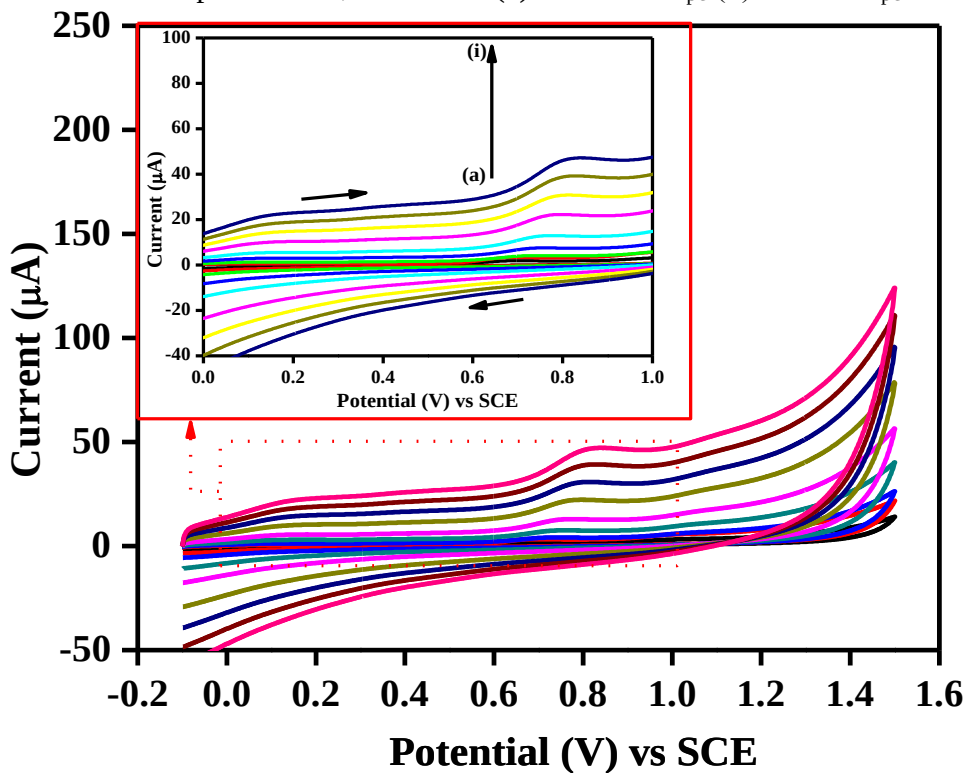

Figure 5A.29: Cyclic voltammograms of UBBH2 (5 x 10^{-5} M) in 1:9 v/v DMF/aq. Buffer media of pH = 4.07, on GCE at various scan rate (a) 50 mVs^{-1} (b) 100 mVs^{-1} (c) 200 mVs^{-1} (d) 500 mVs^{-1} (e) 1000 mVs^{-1} (f) 2000 mVs^{-1} (g) 3000 mVs^{-1} (h) 4000 mVs^{-1} (i) 5000 mVs^{-1}

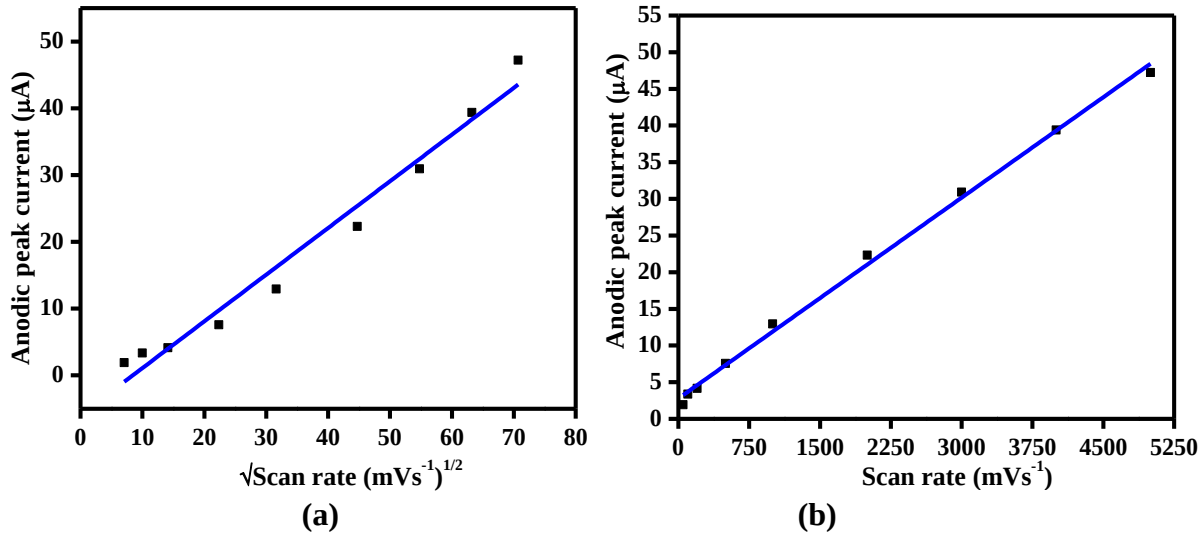

Figure 5A.30: Effect of scan rate on anodic peak current in 1:9 DMF/aq. Buffer medium of pH = 4.07, on GCE (a) $\nu^{1/2}$ versus i_{pa} (b) ν versus i_{pa}

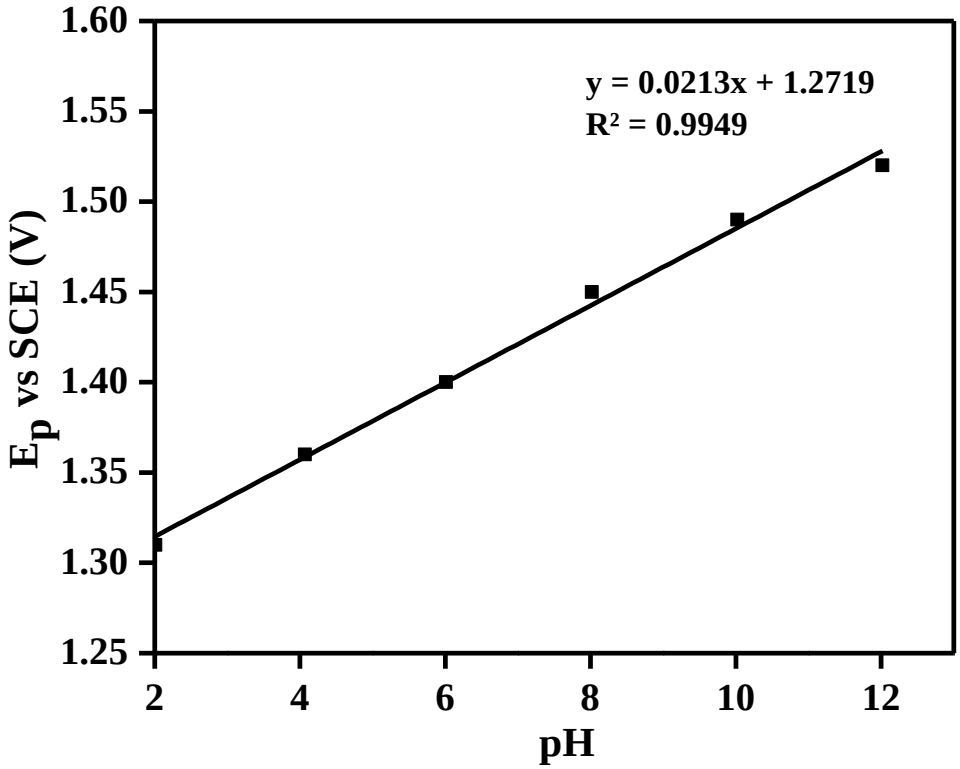

Figure 5A.31: Effect of pH on peak potential of UBBH2 (5×10^{-5} M) (scan rate, 0.5 Vs^{-1}) and drop size of 0.26 mm^2 on SMDE

Table 5A.7 *Voltammetric data of UBBH2*

Compound	pH	$-E_p$ (V)	αn_a	$k°_h \times 10^9$ (cm^2s^{-1})	$D_o \times 10^6$ (cm^2s^{-1})
UBBH2	2.01	1.31	0.35	3.032694	0.683065
	4.07	1.36	0.31	0.882156	1.696545
	6.01	1.4	0.29	0.351958	2.38026
	8.02	1.45	0.26	2.002742	1.524138
	10.02	1.49	0.32	0.546498	2.412531
	12.02	1.52	0.37	2.242525	1.607818

5A.9.2: ***Non-aqueous electrochemistry of UBBH2***

The electron transfer mechanism of UBBH2 in non-aqueous medium have been studied in DMF with 0.1 M tetra ethyl ammonium perchlorate (TEAP) as the supporting electrolyte. A typical cyclic voltammogram obtained in the cathodic region on SMDE is depicted in **Figure 5A. 32**. A reversible electrochemical wave has been discerned. The peak at -1.31 V is assigned to reduction event of UBBH2 whereas the peak at -1.12 V is assigned to the oxidation event of UBBH2. Neverthlessly, plausible reversible mechanism has been proposed as follows.

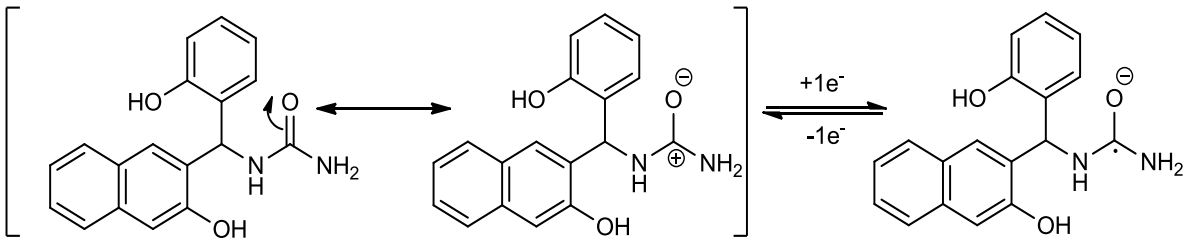

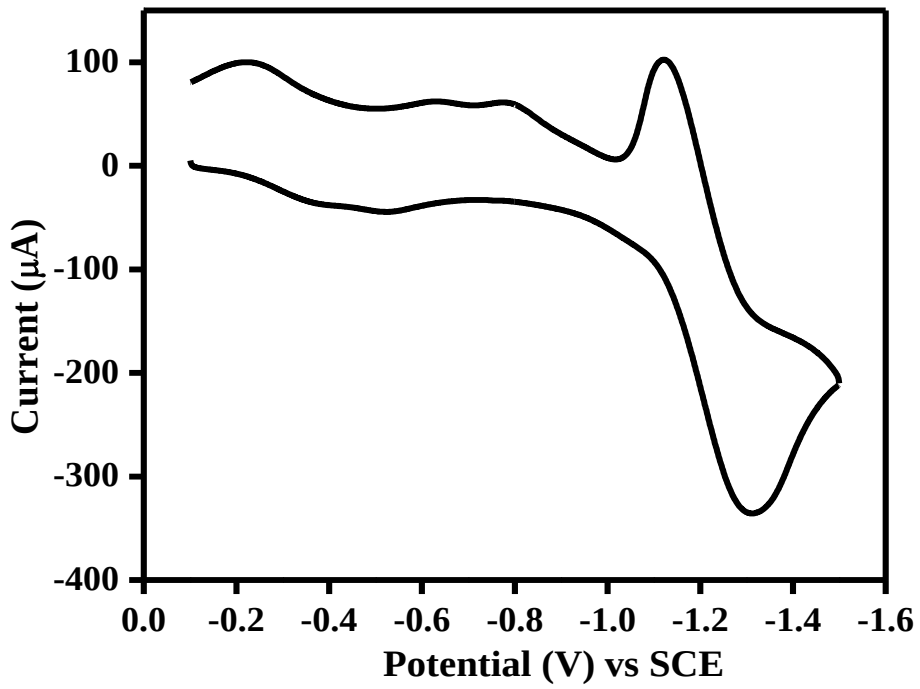

Figure 5A.32: Cyclic voltammogram of UBBH2 (5 x 10^{-5} M) in DMF on 0.26 mm^2 SMDE at scan rate 1 Vs^{-1}, with TEAP (0.1 M)

PART B: SINGLE CRYSTAL X-RAY DIFFRACTION STUDIES OF UBBH2, UBBH2.2DMF AND OXAZH

Molecular structure determination of UBBH2, R, S-enantiomers of DMF solvates of UBBH2 (UBBH2.2DMF), cyclized oxazinone derivates of UBBH2 (OXAZH) have been undertaken by single crystal X-ray diffraction studies. The experimental conditions are already mentioned in **Chapter II**. The shapes of crystals were observed under the LEICA DFC295 polarizing microscope for picking suitable single crystals. The single-crystal X-ray diffraction data of the UBBH2, UBBH2.2DMF solvates and OXAZH crystals were collected on a Bruker Kappa APEX-II CCD DUO X-Ray Diffractometer with an APEX II CCD detector at 296(2) K using graphite-monochromated, Mo K_α radiation (λ=0.71073 Å) as X-ray source. No absorption correction was applied. The lattice parameters were determined from least-squares analysis and the reflection data were integrated using the SHELXTL program[12]. Further, crystal structures have been solved by direct methods using SHELXS-97[13] and refined by full-matrix least-squares refinement on F^2 with anisotropic displacement parameters for non-H atoms using SHELXL-2013[14], constrained and fixed isotropic thermal parameters [$U_{iso}(H) = 1.2U_{eq}(C)$] for aromatic and aliphatic C−H hydrogen atoms following the riding model, localization of Phenolic O−H and N−H hydrogen atoms from the difference fourier map and free refinement of their positions with fixed isotropic thermal parameters [$U_{iso}(H) = 1.2U_{eq}(N)$ or $1.5U_{eq}(O)$ for UBBH2 and $U_{iso}(H) = 1.0U_{eq}(N)$ or $1.1U_{eq}(O)$ for OXAZH]. The software used to prepare material for publication was Mercury 2.3 (Build RC4), ORTEP-3 and X-Seed.

5B.1: Crystal Structure Analysis

5B.1.1: *Crystal structure analysis of UBBH2*

The UBBH2 are crystallized in racemic form. The racemic UBBH2 crystallizes in a centrosymmetric *Pn* space group with each stereoisomer of UBBH2 (**Figure 5B.1**). In each of R and S isomers the same intramolecular hydrogen bondings viz, (naphtholic) O–H⋯O–H (phenolic) and (imido) N–H⋯O–H (naphtholic) exist. The crystal structure analysis reveals that the R and S- stereoisomers of UBBH2 molecules form a one dimensional chain like pattern. For every two R-stereoisomers one S-stereoisomer combine with (terminal amido) N–H⋯O=C (ureaid) and (phenolic) O–H⋯O=C (ureaid) hydrogen bonds and form a cyclic trimer synthon [graph set: $R_3^5(14)$ motif] (**Figure 5B.2**). Similarly, for every two S-stereoisomeric molecules, one R-isomer combines, rendering the whole crystal system racemic. These interactions propagate to form a one dimensional tape like structure along the crystallographic *b*-axis (**Figure 5B.3**). Further the adjacent one dimensional tapes (R-isomers interacting with R-isomers and S-isomer interacting with S-isomers) are stabilized by C–H⋯π (C23–H23⋯C2 and π⋯π [*centroid*$_{(C23\text{-}C24\text{-}C25\text{-}C26\text{-}C28\text{-}C27)}$ ⋯*centroid*$_{(C1\text{-}C2\text{-}C3\text{-}C4\text{-}C9\text{-}C10)}$; 3.872 Å] stacking interactions. The salient crystallographic data and structure refinement parameters of UBBH2 is collected in **Table 5B.1**. The geometrical parameter such as H-bonding, bond length and bond angle have been given in **Tables 5B.2-5B.3**.

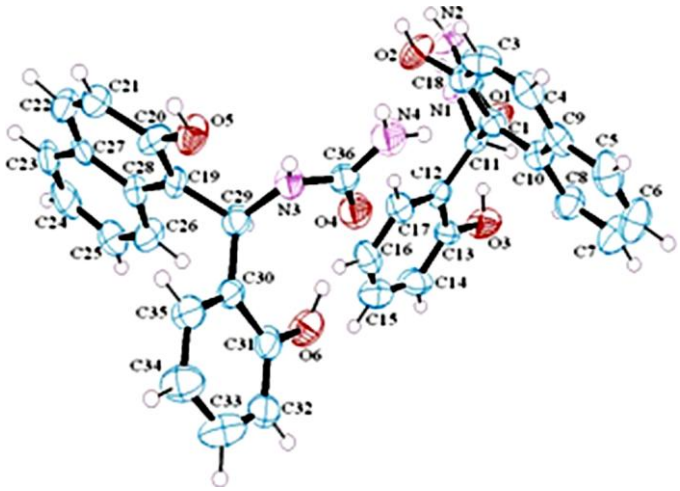

Figure 5B.1: ORTEP representation of R-(right) and S-(left) enantiomers of racemic-UBBH2, thermal ellipsoids are drawn at 50% probability level

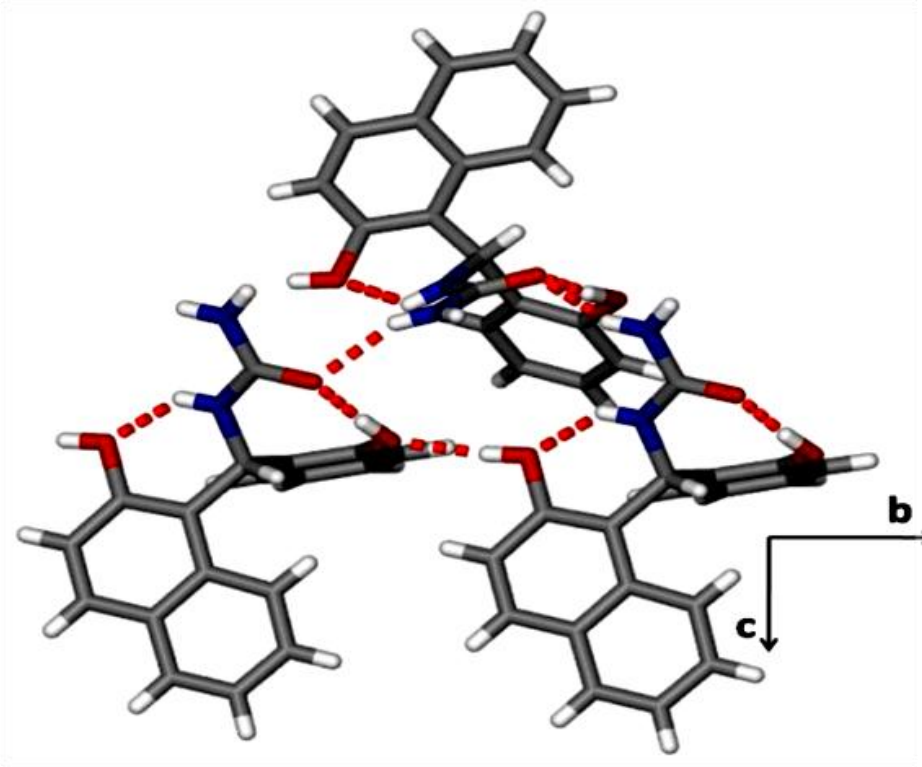

Figure 5B.2: Cyclic trimer synthon formed with two R-stereoisomers and one S stereo-isomers via N–H⋯O and O–H⋯O hydrogen bonds [graph set: $R_3^5(14)$ motif]

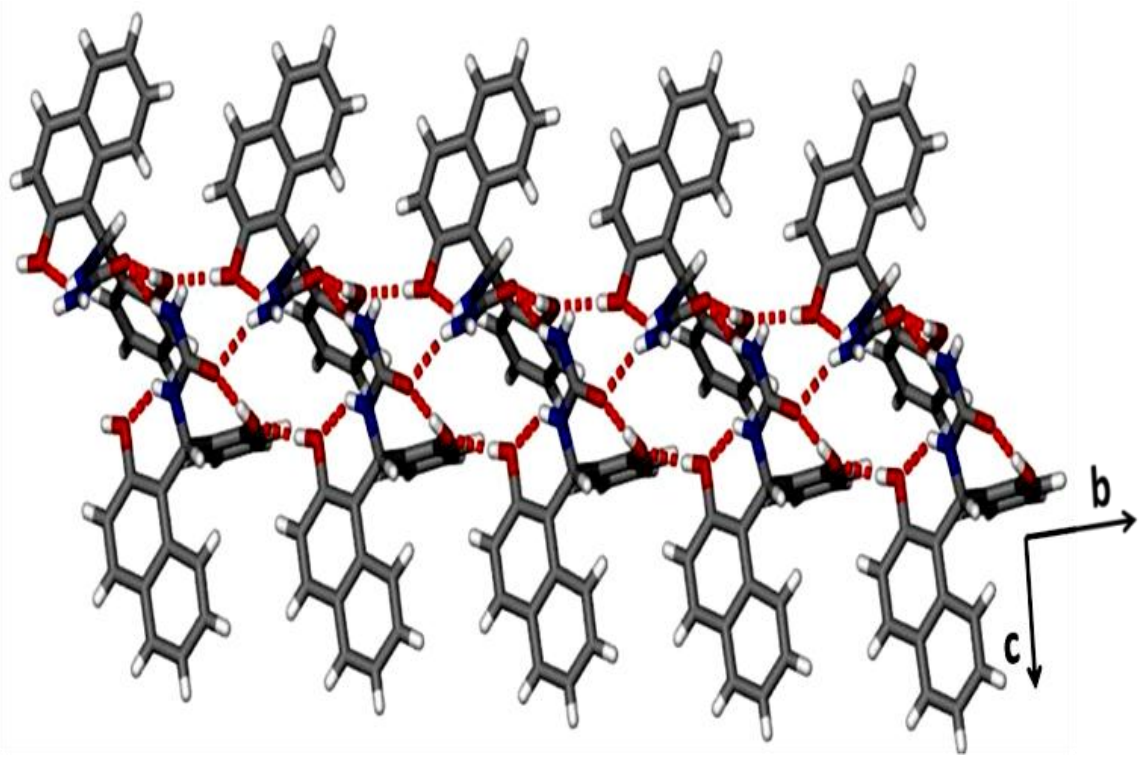

Figure 5B.3: Linear tape like structure of UBBH2 formed aggregation of trimer synthons along the crystallographic b-axis

5B.1.2: *Crystal structure analysis of solvates of UBBH2.2DMF*

The solvate R-UBBH2.2DMF crystallizes in the non-centrosymmetric (chiral) triclinic P_1 space group with one molecule of UBBH2 and two molecules of DMF in the asymmetric unit (**Figure 5B.4**). The UBBH2 molecule in this crystal lattice is exclusively in their R-stereoisomeric absolute configuration. The crystal structure analysis reveals that the UBBH2 and DMF molecules form a one-dimensional triple banded tape-like pattern along the crystallographic a-axis with UBBH2 as the central band and the two DMF molecules forming the lateral bands. The naphthol rings are near-parallel to the crystallographic ab-planes. The –OH group of the phenol is almost coplanar with the benzene ring (torsion angle of H(3)-O(3)-C(13)-C(12) is 178.89° which, in turn, almost, holds the crystallographic b-axis. One of the two molecules of DMF, through its C=O oxygen, interacts with NH-CO-NH hydrogen of the urea moiety to form bifurcated C=O···HN-CO-NH kind (UBBH2···DMF) hydrogen bond. The second DMF molecule, through its C=O oxygen, interacts with the phenolic O–H to form C=O···H–O kind (UBBH2···DMF) hydrogen bond. The β-naphthol O-H group of the UBBH2 interacts with the C=O oxygen of urea moiety of the next UBBH2 molecule to form the 1D tape along the a-axis through O–H···O=C(UBBH2···UBBH2) hydrogen bond (**Figure 5B.5**). The translation related 1D-tapes propagate along the crystallographic c-axis via weak C–H···π interactions. The compound S-UBBH2.2DMF crystallizes in the noncentrosymmetric (chiral) triclinic P_1 space group with one molecule of UBBH2 and two molecules of DMF in the asymmetric unit (**Figure 5B.6**). The UBBH2 molecules in this crystal are exclusively in their S-enantiomeric absolute configuration. The crystal structure analysis reveals that the S-UBBH2.2DMF also forms the similar interactions as in R-UBBH2.2DMF with the C=O···HN-CO-NH kind hydrogen bonds running along the crystallographic a-axis. The Molecular packing array of R-UBBH2.2DMF solvate is shown in **Figure 5B.7** and similar kind of pattern observed in case of S-UBBH2.2DMF solvate. However, an overlay diagram shows differences in the torsion angles of the R and S-enantiomers of the DMF solvated enantiomers of UBBH2.2DMF and UBBH2 (**Figure 5B.8**). Hence, the two crystal structures R-UBBH2.2DMF and S-UBBH2.2DMF are isostructural (**Table 5B.1**). The geometrical parameters such as hydrogen bonds, bond lengths and bond angles are given in **Tables 5B.2-5B.3**.

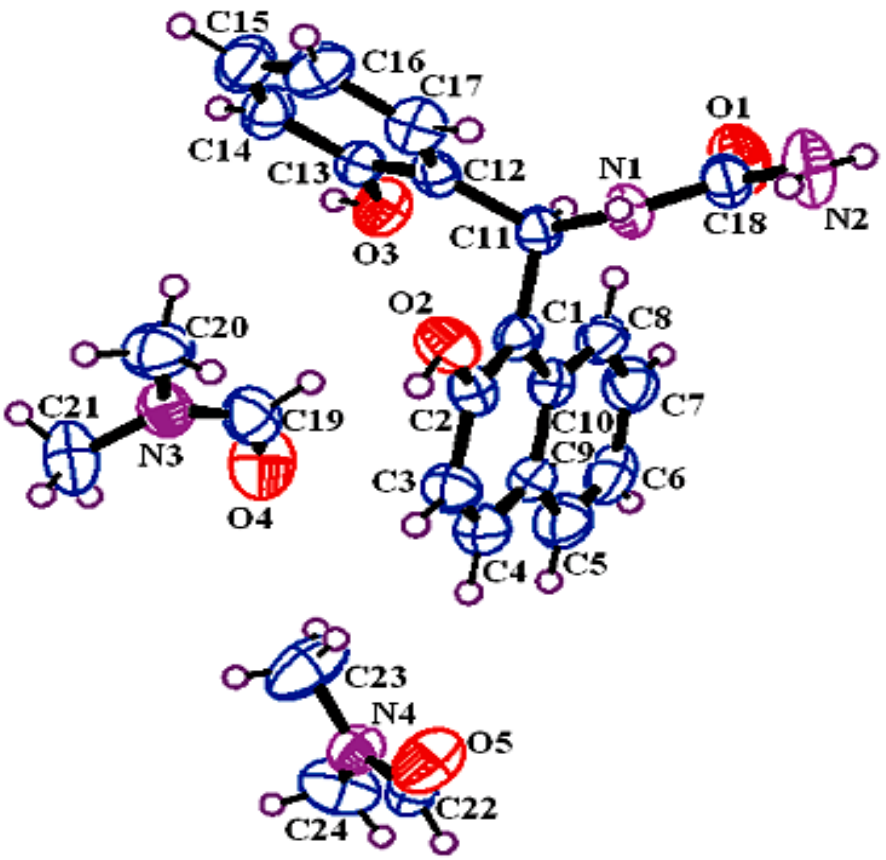

Figure 5B.4: ORTEP representations of R-UBBH2.2DMF, thermal ellipsoids are drawn at 50% probability level

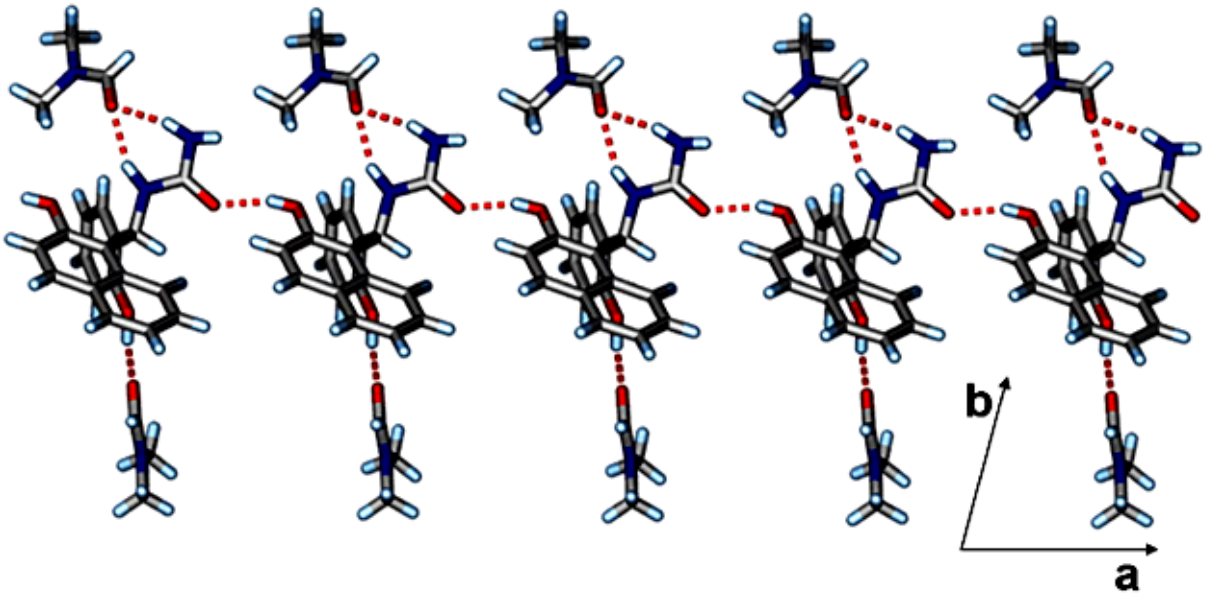

Figure 5B.5: Supramolecular packing in R-UBBH2.2DMF forming one-dimensional triple banded tape like pattern

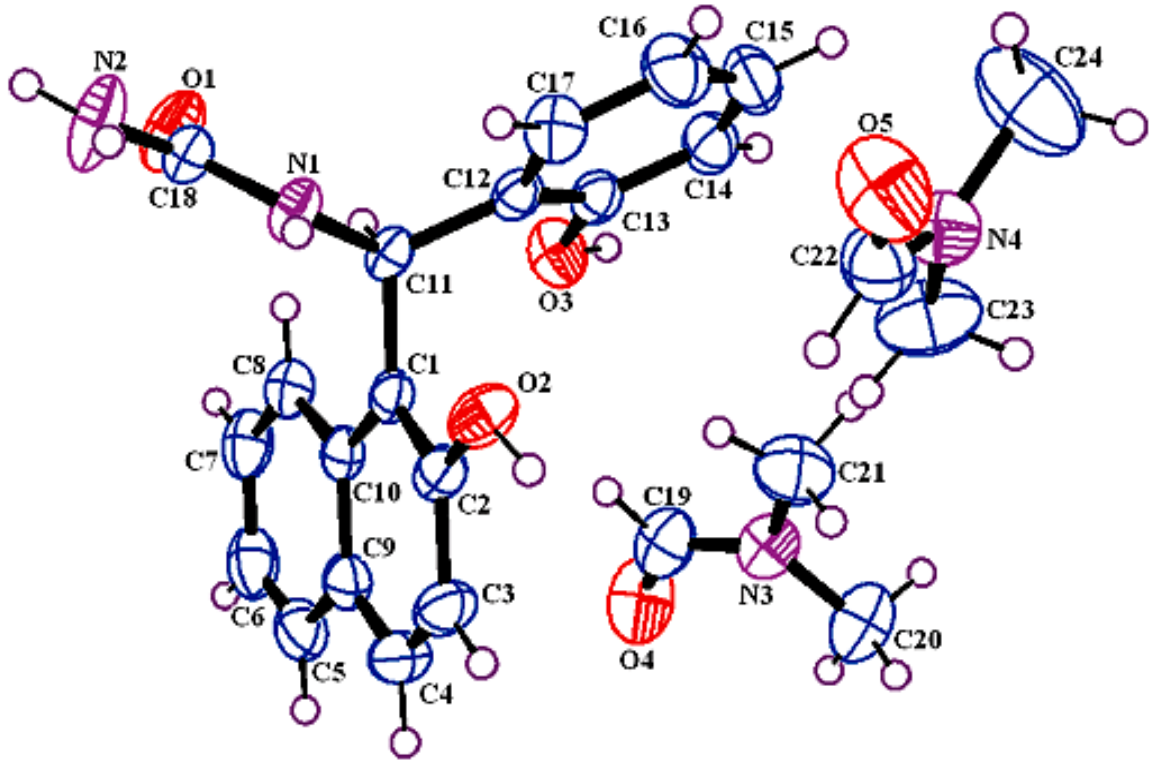

Figure 5B.6: ORTEP representations of S-UBBH2.2DMF, thermal ellipsoids are drawn at 50% probability level

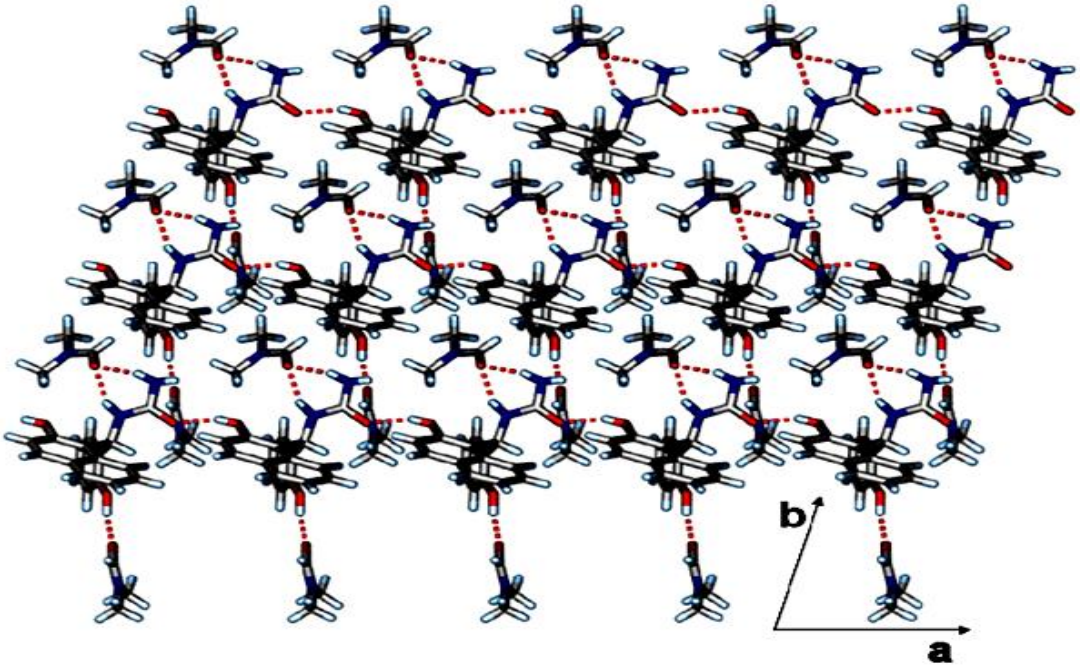

Figure 5B.7: Supramolecular inter-laminar packing in R-UBBH2.2DMF crystal lattice

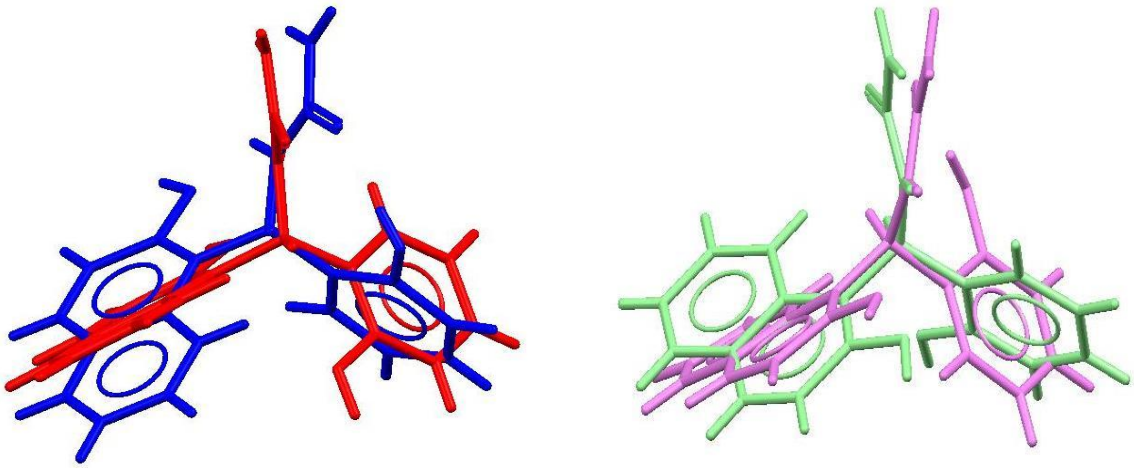

(a) **(b)**

Figure 5B.8: Overlay diagrams of (a) R-UBBH2 (red) on R-UBBH2. 2DMF(blue) and (b) S-UBBH2 (green) on S-UBBH2.2DMF (pink)

5B.1.3: ***Crystal structure analysis of OXAZH***

The racemic OXAZH crystallises in centrosymmetric $P2_1/c$ space group with one R-stereoisomer in asymmetric unit (**Figure 5B.9**). The crystal structure analysis reveals that the two R- and S-isomers form one dimensional tape like structure. R- and S-isomers interact with each other by oxazinone amide homodimer synthon (through N–H···O hydrogen bonds) [graph set: R^2_2 (8) motif] (**Figure 5B.10**). These discrete amide dimer synthons propagate by interconnecting the phenolic O–H and C=O groups of R- and S-isomers via O–H···O hydrogen bonds along the crystallographic *b*-axis (**Figures 5B.11 & 5B.12**). The two parallel one dimensional tapes are interconnected by weak C–H···π interactions (C17–H17···C19; 2.686 Å) and π···π [$centroid_{(C1\text{-}C2\text{-}C3\text{-}C8\text{-}C9\text{-}C10)}$···$centroid_{(C1\text{-}C2\text{-}C3\text{-}C8\text{-}C9\text{-}C10)}$; 3.718 Å] stacking interactions.[14] The salient crystallographic data and structure refinement parameters of OXAZH is collected in **Table 5B.1**. The geometrical parameters such as hydrogen bonds, bond lengths and bond angles are given in **Tables 5B.4-5B.5**.

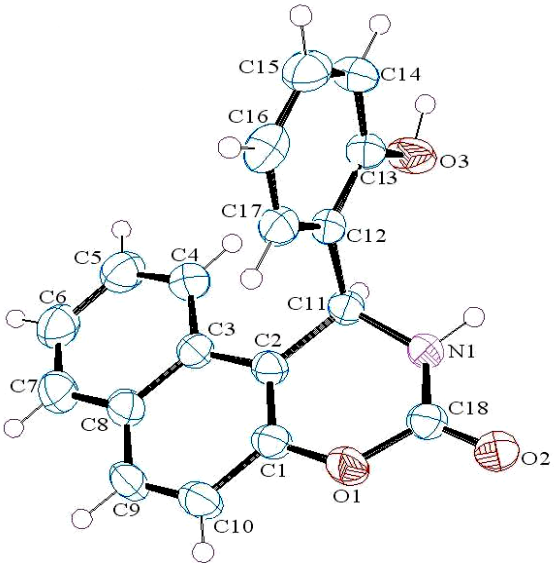

Figure 5B.9: ORTEP representations of R-enantiomer of OXAZH, thermal ellipsoids are drawn at 50% probability level

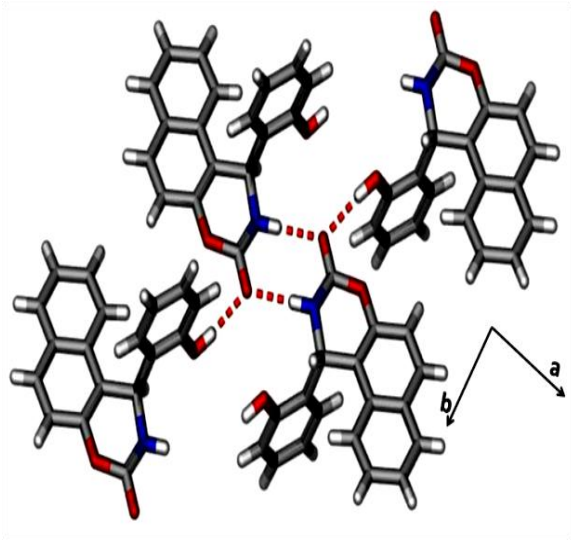

Figure 5B.10: Tetrameric synthon assemblage of R- and S-isomers of OXAZH [graph set: $R^2_2(8)$ motif].

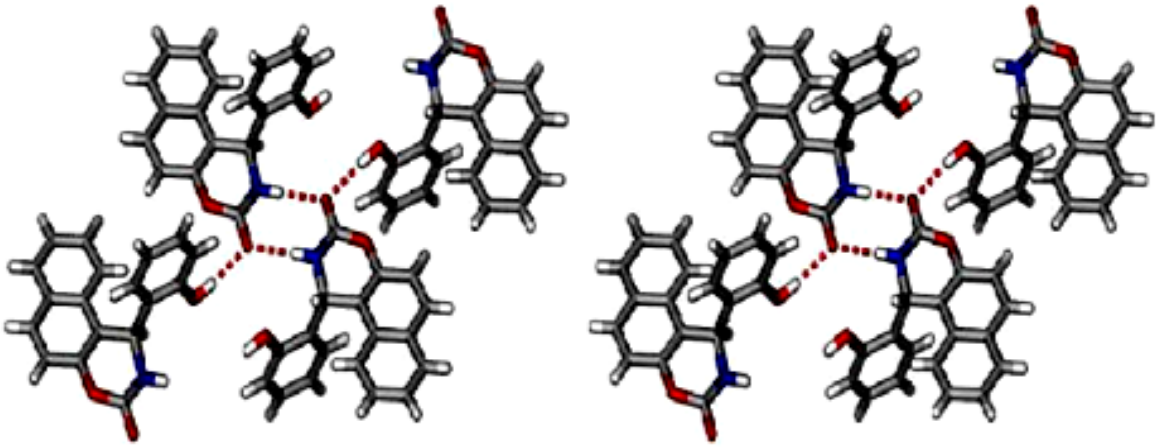

Figure 5B.11: Stereoview of OXAZH tetrameric synthon homodimer (viewed down the *c*-axis).

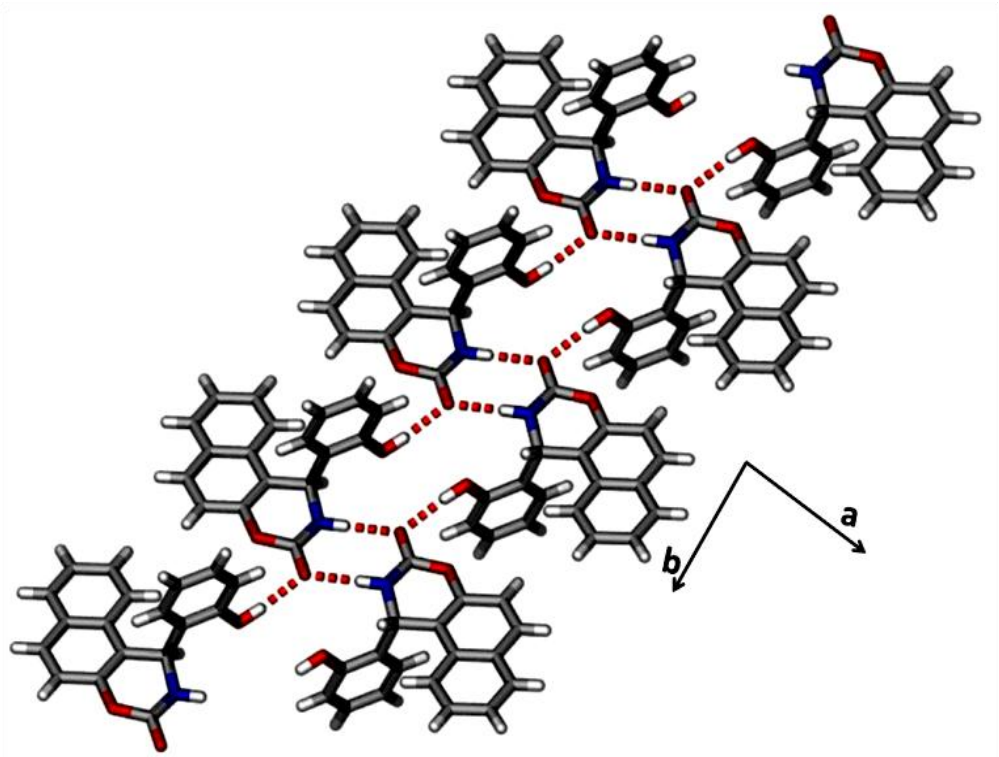

Figure 5B.12: Propagation assemblage of tetrameric synthons via O–H···O hydrogen bonds along the crystallographic *b*-axis.

Table 5B.1: *Salient Crystallographic Data and Structure Refinement Parameters of UBBH2, R- UBBH2.2DMF, S-UBBH2.2DMF and OXAZH*

	UBBH2	**R-UBBH2•2DMF**	**S-UBBH2•2DMF**	**OXAZH**
Empirical formula	$C_{18}H_{16}N_2O_3$	$C_{18}H_{16}N_2O_3$ $2(C_3H_7NO)$	$C_{18}H_{16}N_2O_3$ $2(C_3H_7NO)$	$C_{18}H_{13}NO_3$
Formula weight	308.33	454.52	454.52	291.29
Crystal system	Monoclinic	Triclinic	Triclinic	Monoclinic
Space group	*Pn*	P_1	P_1	$P2_1/c$
T/K	154.40(10)	296(2)	296(2)	293.74(10)
a/Å	8.2105(6)	7.830(4)	7.8277(11)	11.6603(16)
b/Å	8.3066(6)	8.992(5)	8.9915(12)	8.1908(10)
c/Å	22.222(3)	9.388(5)	9.3905(13)	14.3873(17)
α/°	90	81.861(9)	81.853(3)	90
β/°	92.565(9)	66.373(9)	66.399(3)	91.526(13)

γ/ °	90	76.413(9)	76.341(4)	90
Z	4	1	1	4
V/Å^3	1514.1(3)	587.8(5)	587.69(14)	1373.6(3)
D_{calc}/ g/cm^3	1.353	1.482	1.677	1.409
F(000)	648	242.0	313	608
μ/mm^{-1}	0.093	0.091	0.117	0.097
θ/º	2.452 to 27.958	2.33 to 28.00	2.33 to 28.00	1.747 to 28.252
Index ranges	$-10 \leq h \leq 9$ $-8 \leq k \leq 10$ $-28 \leq l \leq 20$	$-10 \leq h \leq 10$ $-11 \leq k \leq 11$ $-12 \leq l \leq 12$	$-10 \leq h \leq 10$ $-10 \leq k \leq 11$ $-12 \leq l \leq 12$	$-15 \leq h \leq 15$ $-8 \leq k \leq 10$ $-18 \leq l \leq 6$
N-total	3418	7489	10659	4652
N-independent	2653	4607	4847	2970
N-observed	2269	1905	4420	2242
Parameters	417	330	305	207
R_1 ($I > 2\sigma(I)$)	0.0631	0.0565	0.0368	0.0729
wR_2 (all data)	0.1603	0.0941	0.1157	0.1780
GOF	1.155	0.943	0.970	1.078
CCDC	1409147	945791	-	1409148

Table 5B.2: *Geometrical parameters of hydrogen bonds in UBBH2, R- UBBH2.2DMF and S-UBBH2.2DMF*

D–H···A[a]	**D···A (Å)**	**H···A (Å)**	**D–H···A (º)**	**Symmetry code**
	UBBH2			
Intra N(1)–H(18)···O(2)	2.665(6)	1.89	131	---
N(2)–H(19B)···O(4)	2.895(9)	1.96	154	-1+x,y,z
O(2)–H(20A)···O(3)	2.709(5)	1.74	169	x,-1+y,z

Intra O(3)–H(20B)···O(1)	2.596(7)	1.64	164	---
Intra O(3)–H(20B) ···N(1)	3.459(6)	2.68	136'	---
Intra N(3)–H(36) ···O(5)	2.707(6)	2.15	113	---
N(4)–H(37B)···O(1)	2.919(8)	1.97	155	1+x,-1+y,z
O(5)–H(38)···O(6)	2.753(5)	1.79	167	x,-1+y,z
Intra O(6)–H(39)···O(4)	2.627(8)	1.65	173	---
Intra O(6)–H(39)···N(3)	3.422(6)	2.71	129'	---
C(3)–H(3)···O(3)	3.360(8)	2.59	128	---
C(21)–H(21)···O(6)	3.481(11)	2.74	125	x,-1+y,z
C(23)–H(23)···N(1)	3.804(10)	2.88	143	1/2+x,-y,-1/2+z
C(24)–H(24)···O(1)	3.509(11)	2.70	132	1/2+x,1-y,-1/2+z
C(24)–H(24)···N(4)	3.689(13)	2.65	160'	-1/2+x,-y,-1/2+z

R-UBBH2.2DMF

N(1)–H(1)···O(4)	2.906(6)	1.99	150	x,1+y,z
O(2)–H(2)···O(1)	2.649(6)	1.75	151	-1+x,y,z
N(2)–H(2B)···O(4)	2.842(10)	1.88	159	x,1+y,z
O(3)–H(3A)···O(5)	2.738(5)	1.78	165	1+x,y,-1+z
C(4)–H(4)···O(5)	3.671(7)	2.62	163	---
Intra C(8)–H(8)···O(1)	3.579(7)	2.77	132	---
C(19)–H(19)···O(3)	3.491(8)	2.66	133	---
C(20)–H(20C)···O(1)	3.760(7)	2.75	156	-1+x,y,z
C(21)–H(21A)···O(2)	3.801(7)	2.79	156	x,-1+y,z
C(21)–H(21C)···O(3)	3.603(9)	2.67	143	-1+x,y,z
C(24)–H(24A)···O(1)	3.746(8)	2.67	175	-1+x,-1+y,1+z

S-UBBH2.2DMF

N(1)–H(1)···O(4)	2.930(2)	2.04	146	x,-1+y,z
O(2)–H(2)···O(1)	2.664(2)	1.69	172	1+x,y,z
N(2)–H(2B)···O(4)	2.853(3)	1.94	149	x,-1+y,z

O(3)–H(3A)···O(5)	2.729(2)	1.75	171	-1+x,1+y,z
C(4)–H(4)···O(5)	3.669(2)	2.62	164	x,1+y,-1+z
Intra C(8)–H(8)···O(1)	3.553(2)	2.73	132	---
C(14)–H(14)···O(5)	3.397(2)	2.65	126	-1+x,1+y,z
C(19)–H(19)···O(3)	3.499(3)	2.68	132	---
C(20)–H(20A)···O(2)	3.805(3)	2.80	155	x,1+y,z
C(20)–H(20B)···O(3)	3.591(3)	2.65	145	1+x,y,z
C(23)–H(23C)···O(1)	3.749(3)	2.67	172	1+x,y,z

Table 5B.3: *Bond lengths (Å) and bond angles (°) for UBBH2, R-UBBH2.2DMF, S-UBBH2.2DMF from XRD data and non-solvated UBBH2 from molecular modeling*

Atoms	**UBBH2 XRD data**	**UBBH2. 2DMF XRD data**		**UBBH2#**
		R	**S**	
C(14)–C(15)	1.38(1)	1.372(7)	1.370(3)	1.420
C(14)–C(13)	1.39(1)	1.374(6)	1.394(2)	1.426
C(14)–H(14)	0.931	0.93	0.93	1.102
C(17)–C(12)	1.378(9)	1.378(6)	1.383(2)	1.429
C(17)–C(16)	1.37(1)	1.386(7)	1.389(3)	1.422
C(17)–H(17)	0.93	0.93	0.93	1.100
N(1)–C(18)	1.328(7)	1.337(6)	1.3392(19)	1.369
N(1)–C(11)	1.461(7)	1.469(5)	1.4571(19)	1.466
N(1)–H(18)	0.785	0.97(10)	0.79(2)	1.018
O(1)–C(18)	1.247(8)	1.253(6)	1.230(2)	1.204
N(2)–C(18)	1.334(8)	1.344(7)	1.345(2)	1.361
N(2)–H(2A)	0.86	0.81(6)	0.86	1.010
N(2)–H(2B)	0.86	0.88(5)	0.86	1.010
C(3)–C(4)	1.34(1)	1.347(7)	1.348(3)	1.418
C(3)–C(2)	1.417(9)	1.411(6)	1.417(2)	1.424
C(3)–H(3)	0.929	0.93	0.93	0.969
O(2)–C(2)	1.385(9)	1.376(5)	1.3574(19)	1.359

O(2)–H(2)	0.821	0.82	0.82	0.970
O(5)–C(22)	—	1.232(6)	1.222(2)	—
C(24)–N(4)	—	1.458(6)	1.438(3)	—
C(24)–H(24A)	—	0.96	0.96	—
C(24)–H(24B)	—	0.96	0.96	—
C(24)–H(24C)	—	0.96	0.96	—
O(4)–C(19)	—	1.237(6)	1.225(2)	—
C(11)–C(12)	1.52(1)	1.532(6)	1.5286(19)	1.521
C(11)–C(1)	1.536(8)	1.533(6)	1.5266(19)	1.519
C(11)–H(11)	0.98	0.98	0.98	1.117
C(1)–C(2)	1.370(8)	1.370(6)	1.3836(19)	1.433
C(1)–C(10)	1.42(1)	1.421(6)	1.430(2)	1.437
C(10)–C(8)	1.425(9)	1.415(6)	1.421(2)	1.431
C(10)–C(9)	1.421(9)	1.423(6)	1.428(2)	1.429
C(9)–C(5)	1.41(1)	1.405(7)	1.413(3)	1.427
C(9)–C(4)	1.403(9)	1.406(7)	1.413(3)	1.422
N(4)–C(22)	—	1.306(6)	1.318(2)	—
N(4)–C(23)	—	1.434(7)	1.455(3)	—
N(3)–C(19)	—	1.305(6)	1.321(2)	—
N(3)–C(21)	—	1.447(6)	1.455(3)	—
N(3)–C(20)	—	1.459(6)	1.452(3)	—
C(15)–C(16)	1.35(1)	1.376(7)	1.375(3)	1.419
C(15)–H(15)	0.93	0.93	0.93	1.101
C(5)–C(6)	1.34(1)	1.357(8)	1.357(3)	1.421
C(5)–H(5)	0.93	0.93	0.93	1.102
C(6)–C(7)	1.38(1)	1.388(8)	1.401(3)	1.421
C(6)–H(6)	0.931	0.93	0.93	1.102
C(16)–H(16)	0.931	0.93	0.93	1.102
C(4)–H(4)	0.93	0.93	0.93	1.102
C(8)–C(7)	1.37(1)	1.363(7)	1.364(2)	1.423
C(8)–H(8)	0.93	0.93	0.93	1.100

C(7)–H(7)	0.93	0.93	0.93	1.102
C(22)–H(22)	—	0.93	0.93	—
C(23)–H(23A)	—	0.96	0.96	—
C(23)–H(23B)	—	0.96	0.96	—
C(23)–H(23C)	—	0.96	0.96	—
C(19)–H(19)	—	0.93	0.93	—
C(21)–H(21A)	—	0.96	0.96	—
C(21)–H(21B)	—	0.96	0.96	—
C(21)–H(21C)	—	0.96	0.96	—
C(20)–H(20A)	—	0.96	0.96	—
C(20)–H(20B)	—	0.96	0.96	—
C(20)–H(20C)	—	0.96	0.96	—
C(13)–O(3)	1.344(9)	1.378(6)	1.363(2)	1.359
C(13)–C(12)	1.409(8)	1.393(6)	1.396(2)	1.434
O(3)–H(3A)	0.806	0.96(5)	0.92(3)	0.968
C(15)–C(14)–C(13)	119.6(8)	120.7(5)	120.35(17)	121.975
C(15)–C(14)–H(14)	120.1	119.7	119.8	118.949
C(13)–C(14)–H(14)	120.3	119.7	119.8	119.076
C(12)–C(17)–C(16)	120.8(7)	121.6(5)	121.17(17)	121.976
C(12)–C(17)–H(17)	119.5	119.2	119.4	121.213
C(16)–C(17)–H(17)	119.6	119.2	119.4	116.805
C(18)–N(1)–C(11)	122.7(5)	121.2(4)	122.06(14)	122.860
C(18)–N(1)–H(1)	121.3	116(6)	116.4(14)	118.824
C(11)–N(1)–H(1)	115.5	123(6)	120.5(14)	118.273
C(18)–N(2)–H(2A)	120.2	103(4)	120	117.451
C(18)–N(2)–H(2B)	119.8	112(3)	120	121.198
H(2A)–N(2)–H(2B)	120	144(5)	120	121.351
C(4)–C(3)–C(2)	120.4(6)	119.8(5)	120.44(15)	121.456
C(4)–C(3)–H(3)	119.7	120.1	119.8	119.254
C(2)–C(3)–H(3)	119.9	120.1	119.8	119.286
C(2)–O(2)–H(2)	109.5	109.5	109.5	110.177

N(4)–C(24)–H(24A)	—	109.5	109.5	—
N(4)–C(24)–H(24B)	—	109.5	109.5	—
H(24A)–C(24)–H(24B)	—	109.5	109.5	—
H(24A)–C(24)–H(24C)	—	109.5	109.5	—
H(24B)–C(24)–H(24C)	—	109.5	109.5	—
N(1)–C(11)–C(12)	114.1(5)	111.8(4)	112.47(12)	113.167
N(1)–C(11)–C(1)	112.6(5)	111.0(3)	110.66(11)	108.875
C(12)–C(11)–C(1)	112.1(5)	113.6(4)	114.00(10)	118.273
N(1)–C(11)–H(11)	105.7	106.7	106.4	106.831
C(12)–C(11)–H(11)	105.7	106.6	106.4	100.544
C(1)–C(11)–H(11)	105.8	106.6	106.4	108.161
C(2)–C(1)–C(10)	118.0(6)	118.4(4)	118.71(12)	119.440
C(2)–C(1)–C(11)	123.3(6)	120.2(4)	119.88(13)	120.315
C(10)–C(1)–C(11)	118.7(6)	121.3(4)	121.36(12)	120.223
C(8)–C(10)–C(1)	123.5(6)	123.7(5)	123.35(13)	122.321
C(8)–C(10)–C(9)	116.4(6)	116.2(4)	117.27(14)	117.305
C(1)–C(10)–C(9)	120.1(6)	120.1(5)	119.37(14)	120.367
C(5)–C(9)–C(4)	121.4(7)	121.3(6)	121.83(15)	119.067
C(5)–C(9)–C(10)	119.5(7)	120.6(5)	119.07(16)	121.132
C(4)–C(9)–C(10)	119.1(6)	118.1(5)	119.10(15)	119.800
O(1)–C(18)–N(1)	122.3(6)	122.3(5)	122.30(15)	122.324
O(1)–C(18)–N(2)	120.1(6)	121.3(6)	121.94(14)	119.283
N(1)–C(18)–N(2)	117.7(6)	116.2(6)	115.74(16)	118.392
C(1)–C(2)–O(2)	118.7(6)	118.7(4)	118.36(12)	121.995
C(1)–C(2)–C(3)	121.7(6)	121.6(5)	121.18(14)	119.216
O(2)–C(2)–C(3)	119.6(6)	119.7(5)	120.43(13)	118.777
C(22)–N(4)–C(23)	—	120.7(5)	121.22(18)	—
C(22)–N(4)–C(24)	—	122.5(5)	121.08(17)	—
C(23)–N(4)–C(24)	—	116.8(5)	117.69(19)	—
C(19)–N(3)–C(21)	—	120.3(5)	121.53(17)	—
C(19)–N(3)–C(20)	—	121.9(5)	120.16(17)	—

C(21)–N(3)–C(20)	—	117.8(5)	118.30(17)	—
C(14)–C(15)–C(16)	121.2(9)	119.2(5)	119.78(16)	118.954
C(14)–C(15)–H(15)	119.4	120.4	120.1	120.533
C(16)–C(15)–H(15)	119.4	120.4	120.1	120.511
C(6)–C(5)–C(9)	121.6(8)	120.6(6)	122.08(17)	120.540
C(6)–C(5)–H(5)	119.2	119.7	119	118.866
C(9)–C(5)–H(5)	119.2	119.7	119	120.594
C(5)–C(6)–C(7)	120.3(9)	119.9(5)	119.02(17)	119.100
C(5)–C(6)–H(6)	119.8	120.1	120.5	120.475
C(7)–C(6)–H(6)	119.9	120.1	120.5	120.412
C(15)–C(16)–C(17)	120.3(8)	120.0(5)	120.18(18)	119.534
C(15)–C(16)–H(16)	119.8	120	119.9	120.091
C(17)–C(16)–H(16)	119.9	120	119.9	120.372
C(3)–C(4)–C(9)	120.7(7)	121.8(5)	121.10(14)	119.617
C(3)–C(4)–H(4)	119.7	119.1	119.5	119.353
C(9)–C(4)–H(4)	119.6	119.1	119.5	121.022
C(7)–C(8)–C(10)	121.8(8)	121.8(5)	121.38(15)	121.755
C(7)–C(8)–H(8)	119.1	119.1	119.3	116.331
C(10)–C(8)–H(8)	119.1	119.1	119.3	121.910
C(8)–C(7)–C(6)	120.4(9)	120.9(6)	121.17(18)	120.070
C(8)–C(7)–H(7)	120	119.6	119.4	120.136
C(6)–C(7)–H(7)	120	119.6	119.4	119.792
O(5)–C(22)–N(4)	—	125.2(5)	125.32(17)	—
O(5)–C(22)–H(22)	—	117.4	117.3	—
N(4)–C(22)–H(22)	—	117.4	117.3	—
N(4)–C(23)–H(23A)	—	109.5	109.5	—
N(4)–C(23)–H(23B)	—	109.5	109.5	—
H(23A)–C(23)–H(23B)	—	109.5	109.5	—
N(4)–C(23)–H(23C)	—	109.5	109.5	—
H(23A)–C(23)–H(23C)	—	109.5	109.5	—
H(23B)–C(23)–H(23C)	—	109.5	109.5	—

O(4)–C(19)–N(3)	—	125.4(5)	125.18(18)	—
O(4)–C(19)–H(19)	—	117.3	117.4	—
N(3)–C(19)–H(19)	—	117.3	117.4	—
N(3)–C(21)–H(21A)	—	109.5	109.5	—
N(3)–C(21)–H(21B)	—	109.5	109.5	—
H(21A)–C(21)–H(21B)	—	109.5	109.5	—
N(3)–C(21)–H(21C)	—	109.5	109.5	—
H(21A)–C(21)–H(21C)	—	109.5	109.5	—
H(21B)–C(21)–H(21C)	—	109.5	109.5	—
N(3)–C(20)–H(20A)	—	109.5	109.5	—
N(3)–C(20)–H(20B)	—	109.5	109.5	—
H(20A)–C(20)–H(20B)	—	109.5	109.5	—
N(3)–C(20)–H(20C)	—	109.5	109.5	—
H(20A)–C(20)–H(20C)	—	109.5	109.5	—
H(20B)–C(20)–H(20C)	—	109.5	109.5	—
C(14)–C(13)–O(3)	118.2(7)	122.3(4)	121.99(15)	118.871
C(14)–C(13)–C(12)	119.1(7)	121.1(5)	120.51(15)	119.170
O(3)–C(13)–C(12)	122.7(6)	116.6(4)	117.49(13)	121.864
C(17)–C(12)–C(13)	119.0(6)	117.4(4)	117.99(13)	118.316
C(17)–C(12)–C(11)	121.7(5)	123.6(4)	123.56(14)	120.906
C(13)–C(12)–C(11)	119.3(5)	118.9(4)	118.36(13)	120.672
C(13)–O(3)–H(3A)	102.3	117(3)	114.9(18)	110.004

#, Molecular modeling data

Table 5B.4: *Geometrical parameters of hydrogen bonds in OXAZH*

D–H···A[a]	**D···A (Å)**	**H···A (Å)**	**D–H···A (º)**	**Symmetry code**
N(1)–H(1)···O(2)	2.961(3)	1.96	169	1-x,-y,2-z
O(3)–H(3)···O(1)	3.202(3)	2.65	116	x,-1+y,z

O(3)–H(3)···O(2)	2.869(3)	1.90	168'	x,-1+y,z
O(3)–H(3)···O(3)	3.431(3)	3.03	106''	1-x,-1-y,2-z
Intra C(11)–H(11)···O(3)	2.786(3)	2.35	102	---
C(14)–H(14)···O(2)	3.448(4)	2.67	128	x,-1+y,z
C(16)–H(16)···O(3)	3.943(4)	2.89	164'	x,-1/2-y,-1/2+z
C(16)–H(16)···N(1)	3.522(4)	2.84	121''	x,-1/2-y,-1/2+z

Table 5B.5: *Bond lengths (Å) and bond angles (°) for XRD data and molecular modeling of OXAZH*

Atoms	**OXAZH XRD data**	**OXAZH#**
O2—C18	1.222(3)	1.2091
O1—C1	1.393(3)	1.3683
O1—C18	1.351(3)	1.3531
O3—C13	1.370(3)	1.3597
O3—H3	0.89(4)	0.9697
N1—C11	1.471(3)	1.4559
N1—C18	1.329(3)	1.3552
N1—H1	0.90(2)	1.0163
C1—C2	1.361(3)	1.3525
C1—C10	1.402(4)	1.3445
C11—H11	0.981	1.1163
C11—C2	1.507(3)	1.5192
C11—C12	1.516(4)	1.5176
C2—C3	1.423(3)	1.3557
C10—H10	0.93	1.1038
C10—C9	1.353(5)	1.3372
C8—C3	1.422(4)	1.3503
C8—C9	1.416(5)	1.3418

C8—C7	1.408(4)	1.3461
C3—C4	1.413(4)	1.3488
C17—H17	0.93	1.1027
C17—C12	1.382(4)	1.3460
C17—C16	1.378(4)	1.3409
C13—C12	1.393(3)	1.3493
C13—C14	1.384(4)	1.3445
C4—H4	0.931	1.0996
C4—C5	1.368(5)	1.3418
C6—H6	0.93	1.1027
C6—C5	1.389(5)	1.3388
C6—C7	1.361(5)	1.3398
C16—H16	0.93	1.1028
C16—C15	1.378(5)	1.3398
C5—H5	0.93	1.1033
C9—H9	0.931	1.1034
C7—H7	0.929	1.1036
C14—H14	0.93	1.1031
C14—C15	1.377(4)	1.3405
C15—H15	0.93	1.1027
C1—O1---C18	120.4(2)	118.9214
C13—O3---H3	106(2)	110.2246
C11—N1---C18	126.5(2)	123.6389
C11—N1---H1	112(2)	119.6343
C18—N1---H1	118(2)	116.6304
O1—C1---C2	122.3(2)	124.7836
O1—C1---C10	114.6(2)	117.1094
C2—C1---C10	123.2(2)	118.1046
N1—C11---H11	108.4	105.1155
N1—C11---C2	108.8(2)	112.1331
N1—C11---C12	109.1(2)	105.9995

H11—C11---C2	108.3	107.4666
H11—C11---C12	108.3	111.6514
C2—C11---C12	113.8(2)	114.1553
C1—C2---C11	119.8(2)	118.6240
C1—C2---C3	118.9(2)	120.2335
C11—C2---C3	121.3(2)	121.1408
O2—C18---O1	117.0(2)	120.9718
O2—C18---N1	124.7(2)	117.5758
O1—C18---N1	118.3(2)	121.4523
C1—C10---H10	120.8	119.0735
C1—C10---C9	118.6(3)	122.1464
H10—C10---C9	120.7	118.7800
C3—C8---C9	119.0(3)	119.4019
C3—C8---C7	119.1(3)	121.1804
C9—C8---C7	121.9(3)	119.4176
C2—C3---C8	118.8(2)	120.3391
C2—C3---C4	123.2(2)	122.7510
C8—C3---C4	118.0(2)	116.9096
H17—C17---C12	119	120.1531
H17—C17---C16	119	118.5429
C12—C17---C16	122.1(2)	121.3040
O3—C13---C12	117.5(2)	121.5678
O3—C13---C14	122.7(2)	119.5092
C12—C13---C14	119.9(2)	118.9182
C11—C12---C17	121.4(2)	119.9635
C11—C12---C13	120.0(2)	120.7252
C17—C12---C13	118.4(2)	119.2806
C3—C4---H4	119.6	122.1923
C3—C4---C5	120.8(3)	122.2423
H4—C4---C5	119.6	115.5642
H6—C6---C5	120.1	120.4027

H6—C6---C7	120.1	120.5879
C5—C6---C7	119.8(3)	119.0088
C17—C16---H16	120.7	120.3368
C17—C16---C15	118.7(3)	119.4848
H16—C16---C15	120.6	120.1773
C4—C5---C6	121.0(3)	119.9363
C4—C5---H5	119.5	120.3087
C6—C5---H5	119.5	119.7547
C10—C9---C8	121.6(3)	119.7659
C10—C9---H9	119.3	118.7307
C8—C9---H9	119.1	121.5030
C8—C7---C6	121.3(3)	120.7195
C8—C7---H7	119.4	121.1391
C6—C7---H7	119.4	118.1413
C13—C14---H14	119.8	119.2614
C13—C14---H15	120.3(3)	121.6040
H14—C14---C15	119.9	119.1344
C16—C15---C14	120.6(3)	119.3965
C16—C15---H15	119.8	120.2472
C14—C15---H15	119.7	120.3535
C3—C4---H4	119.6	118.9214
C3—C4---C5	120.8(3)	110.2246
H4—C4---C5	119.6	123.6389
H6—C6---C5	120.1	119.6343
H6—C6---C7	120.1	116.6304
C5—C6---C7	119.8(3)	124.7836
C17—C16---H16	120.7	117.1094
C17—C16---C15	118.7(3)	118.1046
H16—C16---C15	120.6	105.1155
C4—C5---C6	121.0(3)	112.1331
C4—C5---H5	119.5	105.9995

C6—C5---H5	119.5	107.4666
C10—C9---C8	121.6(3)	111.6514
C10—C9---H9	119.3	114.1553
C8—C9---H9	119.1	118.6240
C8—C7---C6	121.3(3)	120.2335
C8—C7---H7	119.4	121.1408
C6—C7---H7	119.4	120.9718
C13—C14---H14	119.8	117.5758
C13—C14---H15	120.3(3)	121.4523
H14—C14---C15	119.9	119.0735
C16—C15---C14	120.6(3)	122.1464
C16—C15---H15	119.8	118.7800
C14—C15---H15	119.7	119.4019

#, Molecular modeling data

PART C: MOLECULAR MODELING STUDIES OF UBBH2, UBBH2.2DMF AND OXAZH

Molecular modeling studies have been undertaken for addressing the stability aspects of UBBH2, UBBH2.2DMF and OXAZH molecules, for screening the possible conformations and for visualizing the molecules in various formats[15]. To visualize the molecular geometry in different formats such as electron density surfaces for identifing the atoms and bonds positions, electrostatic potential surface mapping for locating the positive and negative potential points in the molecule, solvent accessible zonal clouds in wire mesh format for solvation effect over the molecules, besides to visualize the HOMO-LUMO orbitals for the shapes and symmetries of orbitals (HOMO and LUMO) which are important in predicting the reactivity of a species and the stereochemical and regiochemical outcome of a chemical reaction[16,17]. Some of stereographic global energy minimized structures are obtained through MM2 force field calculation method at RMS gradient 0.01. Further, the double dihedral and conformational analysis have been utilized to obtain the molecular structural parameters such as bond lengths, bond angles, torsion angles along with HOMO-LUMO orbital energies, to verify whether the mechanism proposed for the thermodynamic, spectroscopic and electrochemical behavior of the compound are acceptable.

In present studies, molecular modeling studies have been performed on UBBH2, UBBH2.2DMF and OXAZH by using ChemOffice Ultra (Version 12.0).

The numbering sequence of UBBH2, UBBH2.2DMF and OXAZH molecules are shown in **Figure 5C.1**. Some of important geometrical parameters such as bond lengths, bond angles and torsional angles of molecules are provided in **Table 5C.1-5C.3**. There is an excellent agreement discerned among the corresponding experimental and modeled data. The global minimized structures of these ligands in stereographic projection are shown in **Figure 5C.2-5C.4**.

The torsional energy conformational 3D plots of these ligands are shown in **Figures 5C.5-5C.6**. It is found that the free molecules have the stablest disposition over C(4)-C(8), C(8)-C(10) in UBBH2 (**Figure 5C.1a**) and C(5)-(7), C(7)-C(8) in UBBH2.2DMF (**Figure 5C.1b**). The quantum mechanical HOMO-LUMO orbitals energy calculations have been undertaken for computing the expected gas-phase electronic transitions. Some of important

HOMO-LUMO molecular orbitals are displayed in **Figure 5C.7-5C.9**. Further, HOMO-LUMO energy, formation of heat, heat of desolvation, etc., values are collected in **Table 5C.4** along with the experimental spectral data. The theoretical and experimental absorption maxima are in great agreement. The conformational energy plots of these molecules have been carried out and presented in **Figure 5C.10-5C.12**. Neverthlessly, the solvent accessible zonal clouds of these molecules are shown in **Figure 5C.13-5C.15**.

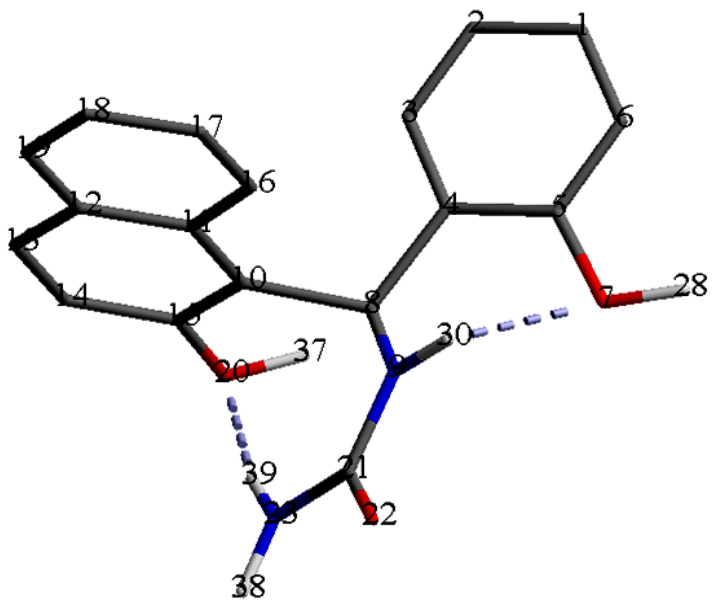

(a)

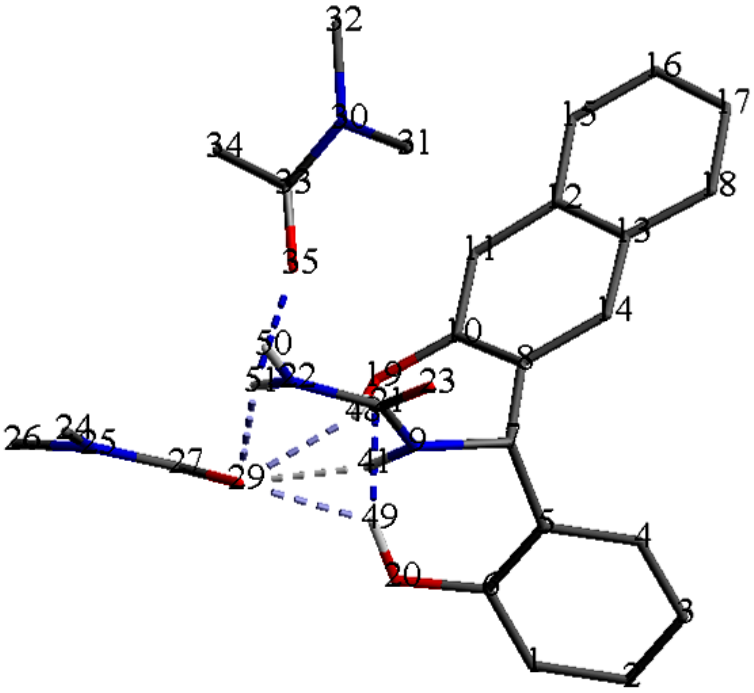

(b)

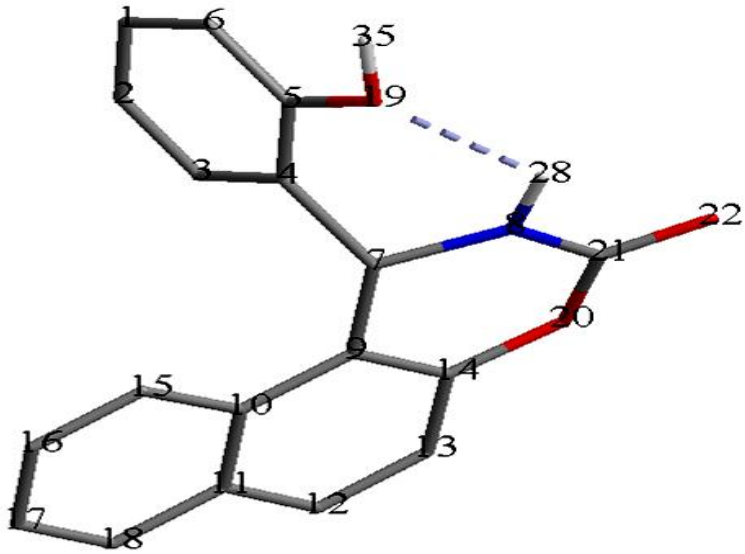

(c)

Figure 5C.1: Stick models of (a) UBBH2 (b) UBBH2.2DMF and (c) OXAZH (Non-polar H-bonds are excluded in the figures for clarity)

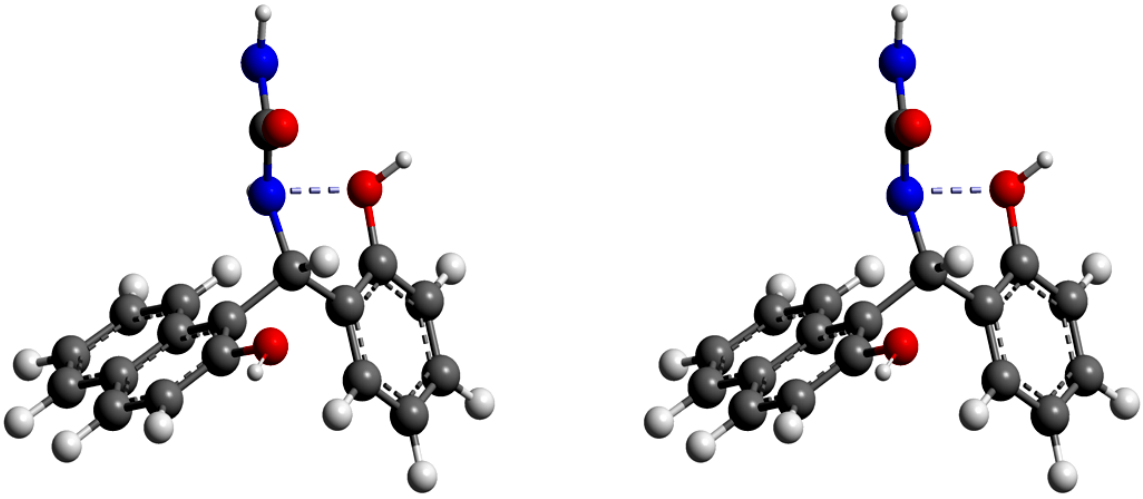

Figure 5C.2: Stereographic view of UBBH2 after global minimization along with the scheme of the atoms

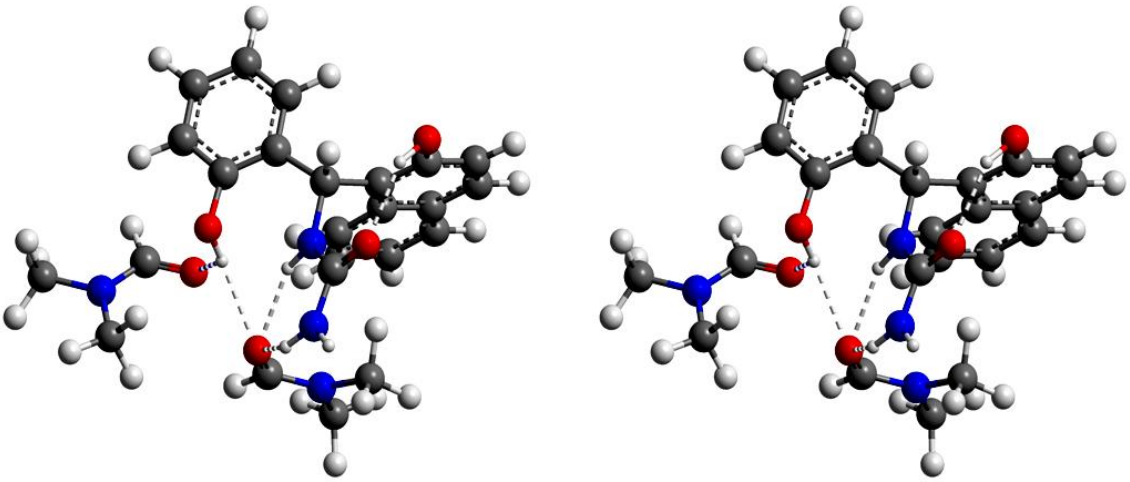

Figure 5C.3: Stereographic view of UBBH2.2DMF after global minimization along with the scheme of the atoms

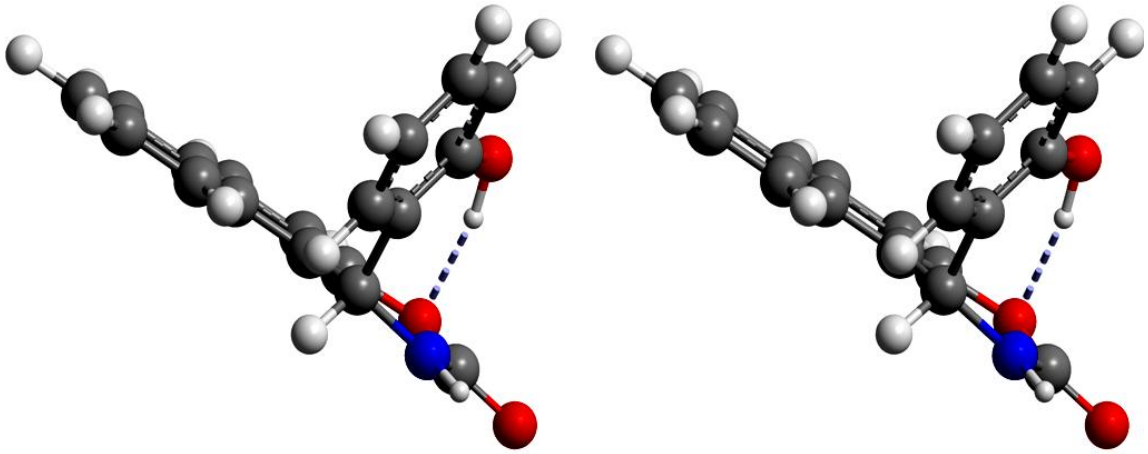

Figure 5C.4: Stereographic view of OXAZH after global minimization along with the scheme of the atoms

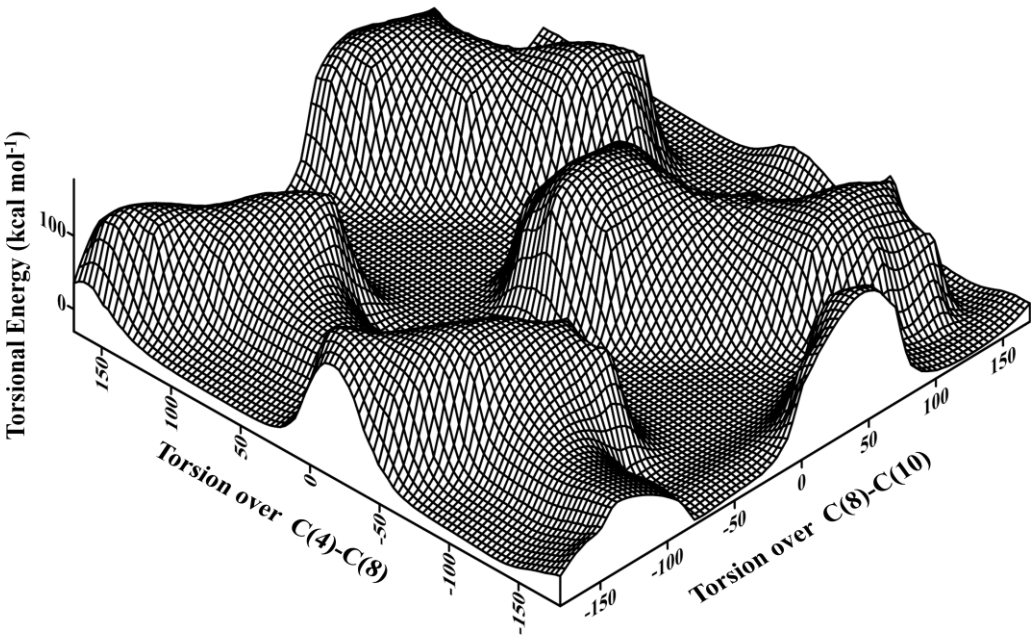

Figure 5C.5: Double dihedral torsional energy plot of UBBH2 over C(4)-C(8) (left) and C(8)-C(10) (right) bonds from -180 to +180 (Number sequence of atoms from **Figure 5C.1a**)

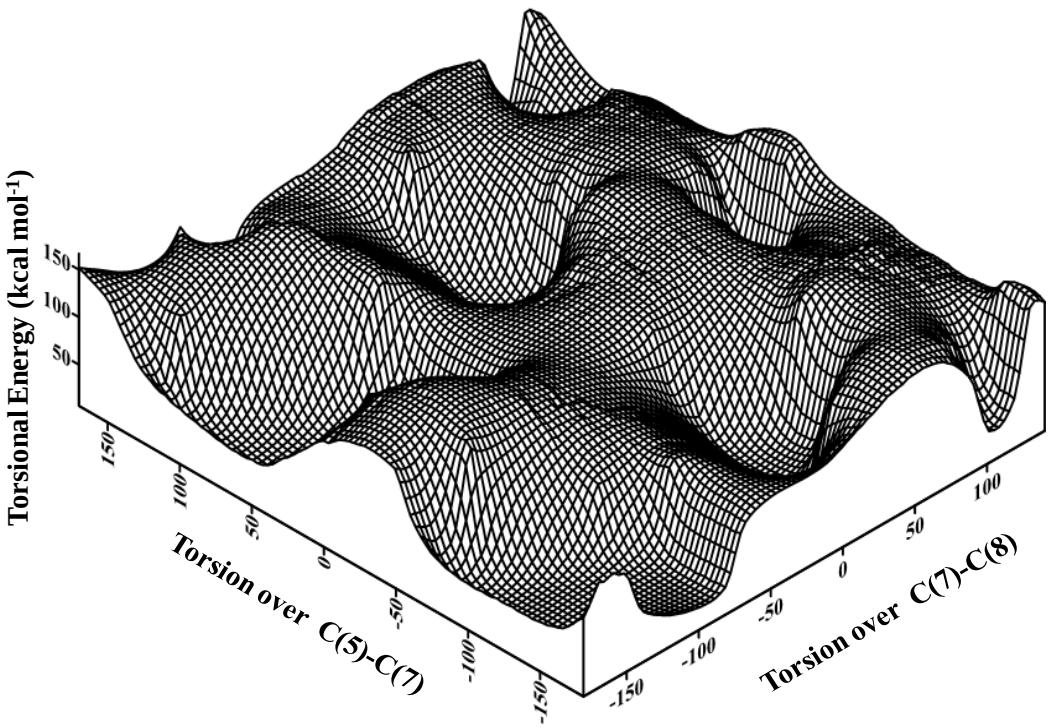

Figure 5C.6: Double dihedral torsional energy plot of UBBH2.2DMF over C(5)-C(7) (left) and C(7)-C(8) (right) bonds from -180 to +180 (Number sequence of atoms from **Figure 5C.1b**)

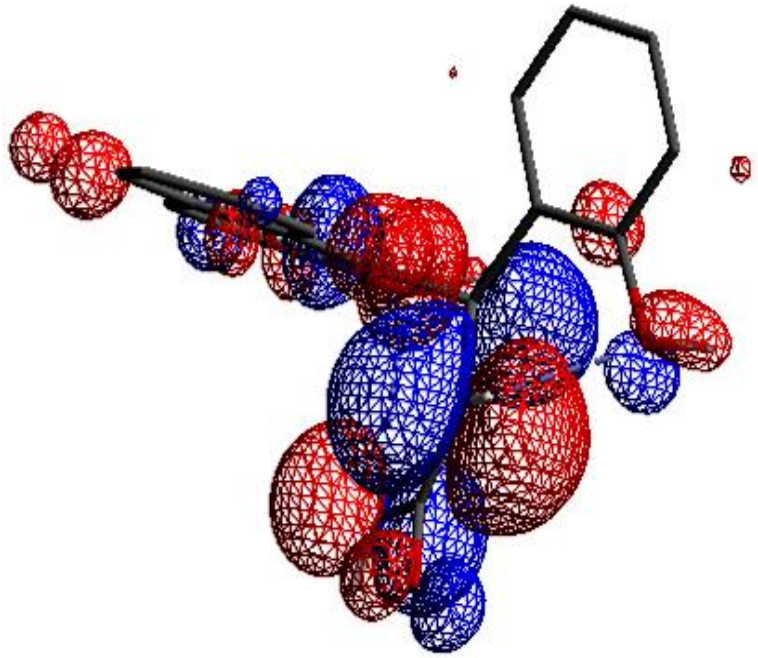

HOMO (-10.470 eV)

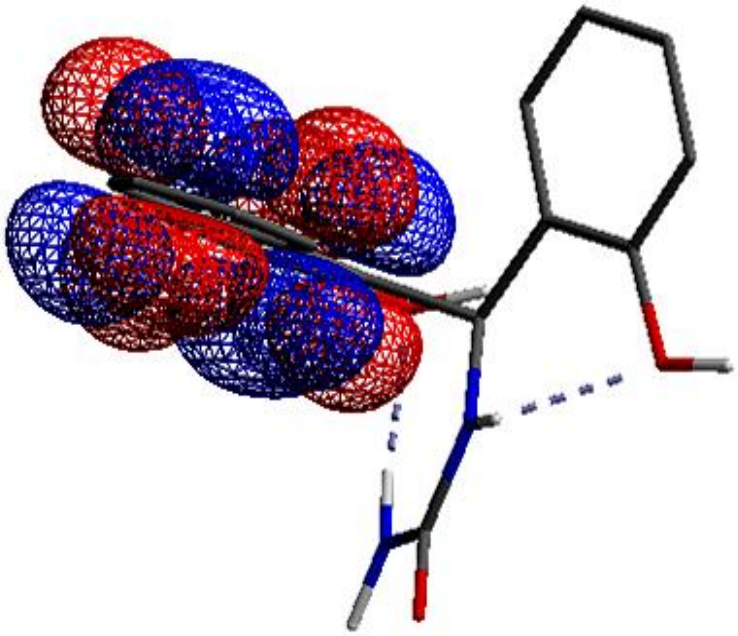

LUMO (-2.946 eV)

Figure 5C.7: HOMO and LUMO molecular orbitals of UBBH2 in wire mesh format (Non-polar H-atoms are excluded for clarity)

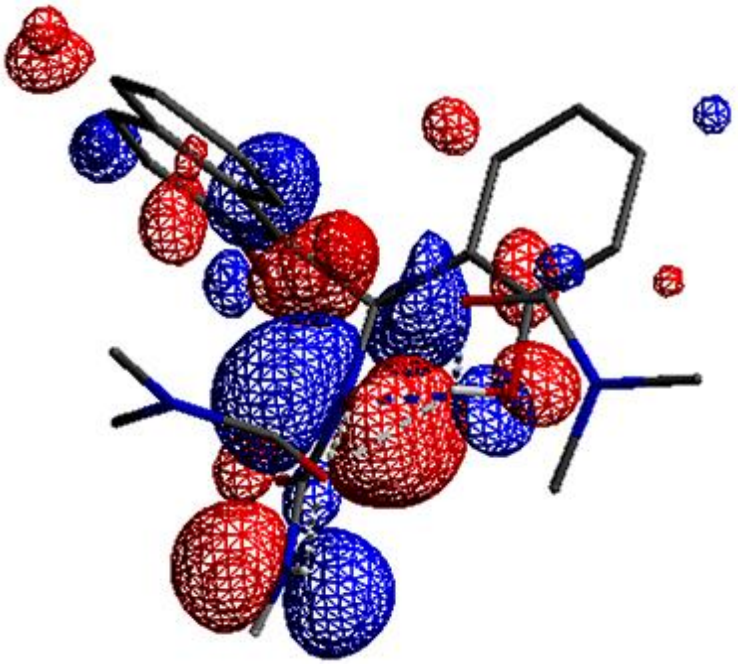

HOMO (-9.913 eV)

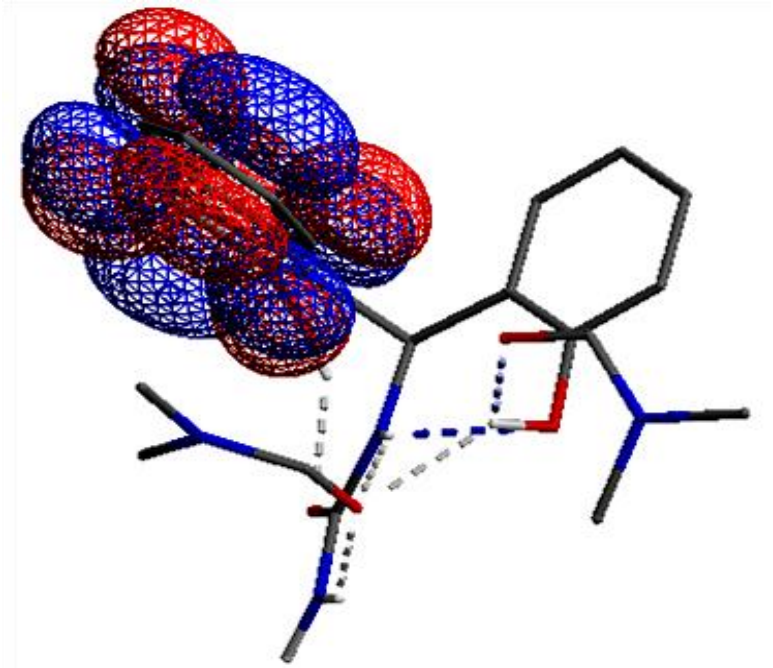

LUMO (-2.927 eV)

Figure 5C.8: HOMO and LUMO molecular orbitals of UBBH2.2DMF in wire mesh format (Non-polar H-atoms are excluded for clarity)

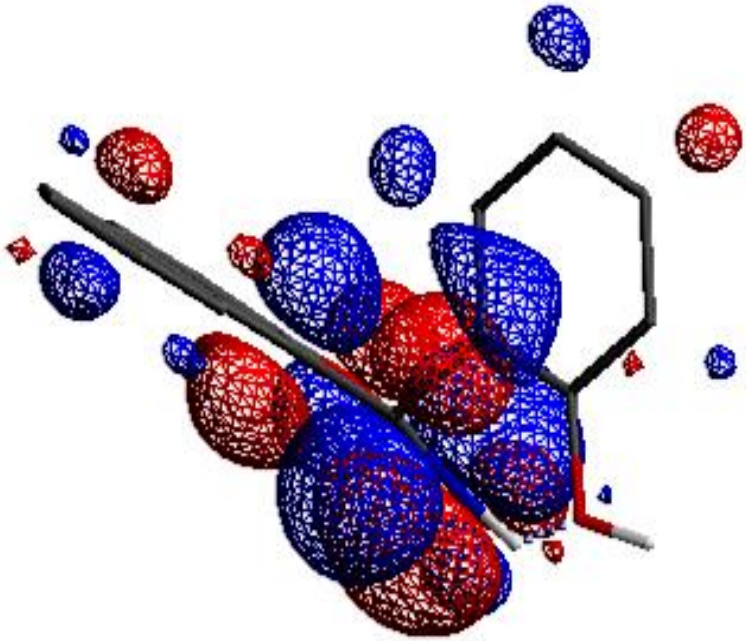

HOMO (-10.069 eV)

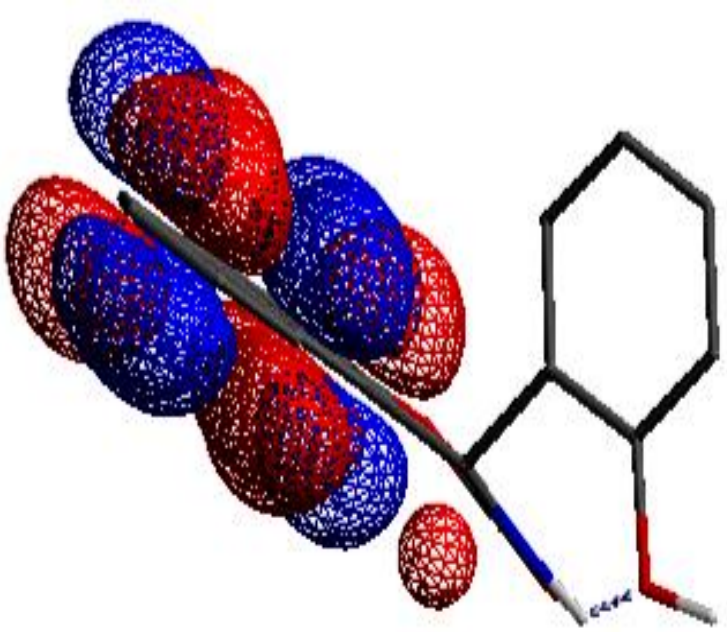

LUMO (-4.090 eV)

Figure 5C.9: HOMO and LUMO molecular orbitals of OXAZH in wire mesh format (Non-polar H-atoms are excluded for clarity)

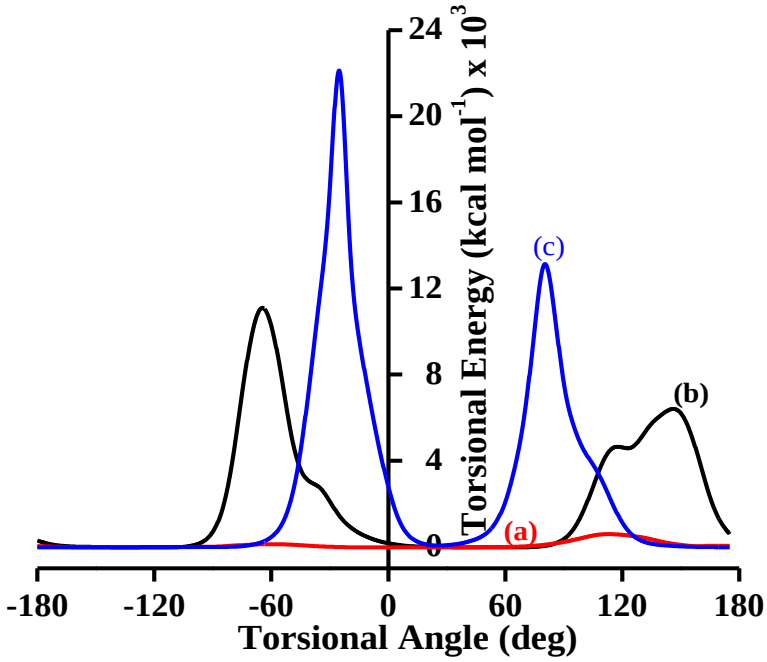

Figure 5C.10: Conformation single dihedral energy plot of UBBH2 over (a) C(10)-C(8) (b) C(4)-C(8) and (c) C(8)-N(9) (Number sequence of atoms from **Figure 5C.1a**)

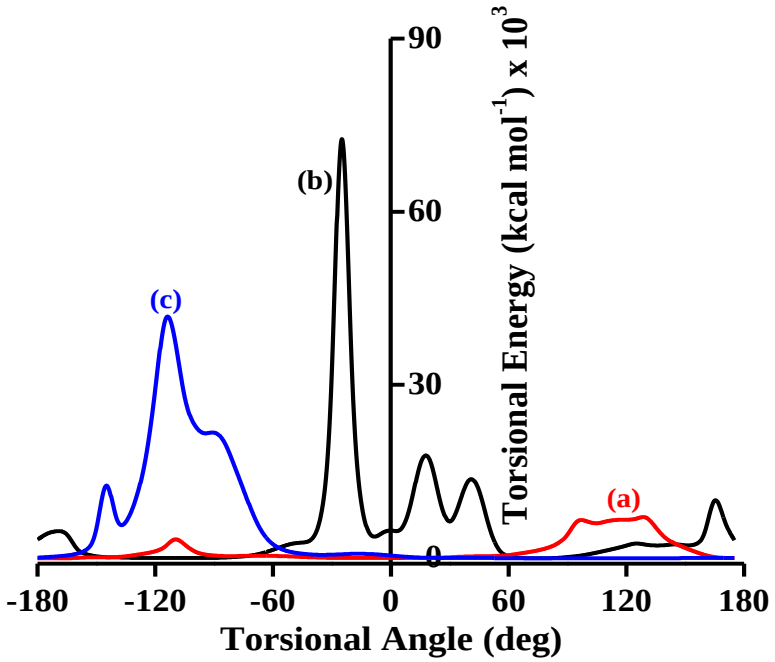

Figure 5C.11: Conformation single dihedral energy plot of UBBH2.2DMF over (a) C(5)-C(7) (b) C(7)-C(8) and (c) C(7)-N(9) (Number sequence of atoms from **Figure 5C.1b**)

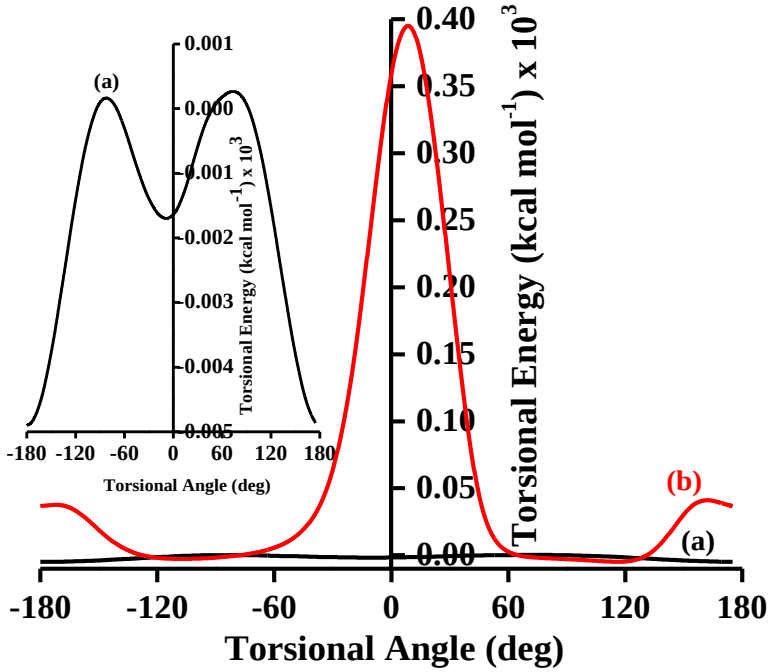

Figure 5C.12: Conformation single dihedral energy plot of OXAZH over (a) C(5)-O(19) and (b) C(4)-C(7) (Number sequence of atoms from **Figure 5C.1c**)

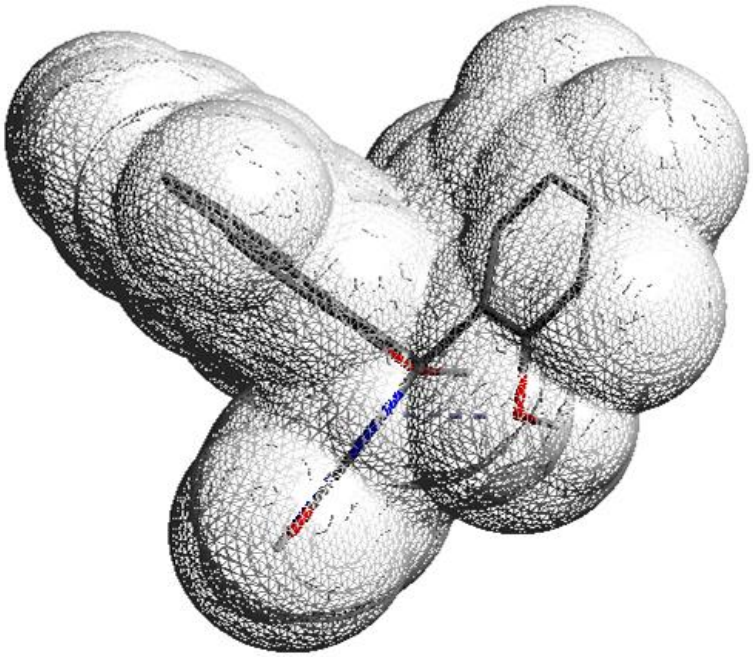

Figure 5C.13: Solvent accessible zonal cloud of UBBH2 in wire mesh found (Non-polar H-bonds are excluded in the figures for clarity)

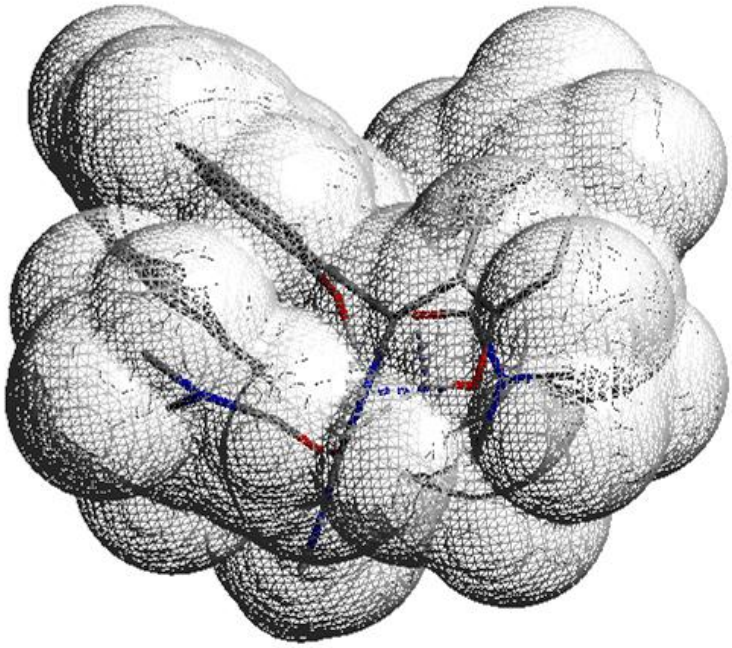

Figure 5C.14: Solvent accessible zonal cloud of UBBH2.2DMF in wire mesh found (Non-polar H- bonds are excluded in the figures for clarity)

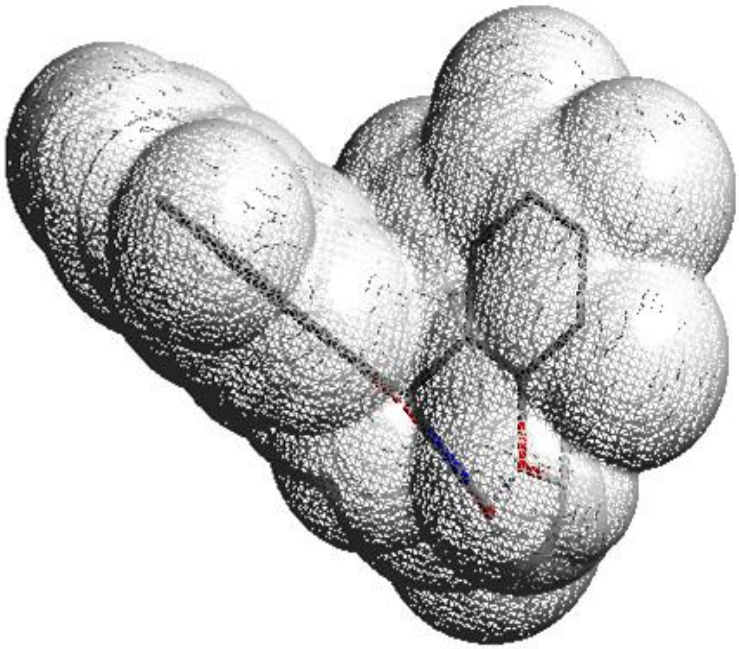

Figure 5C.15: Solvent accessible zonal cloud of OXAZH in wire mesh found (Non-polar H-bonds are excluded in the figures for clarity)

Table 3C.1: *Some of the important geometric parameters of UBBH2*

Bond	Bond length (Å)	Bond	Bond angle (deg)	Bond	Dihedral angle (deg)
N(23)-H(39)	1.0121	H(39)-N(23)-H(38)	121.253	C(8)-C(10)-C(11)-C(12)	178.311
N(23)-H(38)	1.0094	H(39)-N(23)-C(21)	120.950	O(20)-C(15)-C(10)-C(8)	2.504
O(20)-H(37)	0.9698	H(38)-N(23)-C(21)	117.783	C(14)-C(15)-C(10)-C(8)	178.803
N(9)-H(30)	1.0174	N(23)-C(21)-O(22)	119.572	C(8)-C(4)-C(5)-O(7)	0.120
O(7)-H(28)	0.9704	N(23)-C(21)-N(9)	120.598	C(3)-C(4)-C(5)-O(7)	177.783
C(21)-N(23)	1.362	O(22)-C(21)-N(9)	119.827	N(9)-C(21)-N(23)-H(39)	0.962
C(21)-O(22)	1.1995	H(37)-O(20)-C(15)	109.775	O(22)-C(21)-N(23)-H(38)	0.121
N(9)-C(21)	1.3644	C(10)-C(15)-O(20)	121.903	O(22)-C(21)-N(23)-H(39)	178.569
C(15)-O(20)	1.3613	C(14)-C(15)-O(20)	118.861	C(8)-N(9)-C(21)-N(23)	0.432
C(8)-C(10)	1.5253	H(30)-N(9)-C(21)	117.630	H(30)-N(9)-C(21)-O(22)	0.984
C(8)-N(9)	1.4645	H(30)-N(9)-C(8)	118.915	H(30)-N(9)-C(21)-N(23)	178.546
C(4)-C(8)	1.5209	C(21)-N(9)-C(8)	123.446	C(14)-C(15)-O(20)-H(37)	152.171
C(5)-O(7)	1.3604	C(10)-C(8)-N(9)	107.893	C(10)-C(15)-O(20)-H(37)	26.526
		C(10)-C(8)-C(4)	114.524	C(4)-C(8)-C(10)-C(15)	116.523

		N(9)-C(8)-C(4)	111.424	C(4)-C(8)-C(10)-C(11)	65.439
		H(28)-O(7)-C(5)	109.985	N(9)-C(8)-C(10)-C(15)	118.781
				N(9)-C(8)-C(10)-C(11)	59.256
				C(4)-C(8)-N(9)-C(21)	171.354
				C(4)-C(8)-N(9)-H(30)	9.678
				C(10)-C(8)-N(9)-C(21)	62.114
				C(10)-C(8)-N(9)-H(30)	116.852
				C(3)-C(4)-C(8)-N(9)	147.463
				C(3)-C(4)-C(8)-C(10)	24.656
				C(5)-C(4)-C(8)-N(9)	34.657
				C(5)-C(4)-C(8)-C(10)	157.463
				C(4)-C(5)-O(7)-H(28)	176.086
				C(6)-C(5)-O(7)-H(28)	3.147

Table 3C.2: *Some of the important geometric parameters of UBBH2.2DMF*

Bond	**Bond length (Å)**	**Bond**	**Bond angle (deg)**	**Bond**	**Dihedral angle (deg)**
N(22)-H(51)	1.0121	N(30)-C(33)-O(35)	122.766	C(7)-C(8)-C(10)-O(19)	1.167
N(22)-H(50)	1.0123	C(34)-C(33)-O(35)	120.943	C(7)-C(5)-C(6)-O(20)	0.028
O(20)-H(49)	0.9725	N(25)-C(27)-O(29)	122.093	C(32)-N(30)-C(33)-O(35)	178.260
O(19)-H(48)	0.9722	C(21)-N(22)-H(50)	118.507	C(32)-N(30)-C(33)-C(34)	1.751
N(9)-H(41)	1.0229	C(21)-N(22)-H(51)	118.726	C(31)-N(30)-C(33)-O(35)	2.732
C(33)-O(35)	1.2085	H(50)-N(22)-H(51)	121.672	C(31)-N(30)-C(33)-C(34)	177.255
C(27)-O(29)	1.2083	N(9)-C(21)-N(22)	116.704	C(26)-N(25)-C(27)-O(29)	169.077
C(21)-O(23)	1.2086	N(9)-C(21)-O(23)	123.547	C(24)-N(25)-C(27)-O(29)	8.452
C(6)-O(20)	1.3557	N(22)-C(21)-O(23)	119.610	O(23)-C(21)-N(22)-H(51)	167.481
C(10)-O(19)	1.3559	C(6)-O(20)-H(49)	113.023	O(23)-C(21)-N(22)-H(50)	0.771
C(7)-N(9)	1.4601	C(10)-O(19)-H(48)	113.202	N(9)-C(21)-N(22)-H(51)	8.400
C(7)-C(8)	1.4972	O(19)-C(10)-C(11)	118.462	N(9)-C(21)-N(22)-H(50)	176.654
C(5)-C(7)	1.4975	O(19)-C(10)-C(8)	123.770	H(41)-N(9)-C(21)-O(23)	173.403
C(27)-N(9)	3.9682	C(7)-N(9)-C(21)	123.638	H(41)-N(9)-C(21)-N(22)	10.892
C(27)-H(55)	3.3198	C(7)-N(9)-H(41)	116.020	C(7)-N(9)-C(21)-O(23)	22.489

C(24)-O(29)	2.8014	C(21)-N(9)-H(41)	118.545	C(7)-N(9)-C(21)-N(22)	153.215
H(39)-H(43)	2.2901	N(9)-C(7)-C(5)	114.309	C(5)-C(6)-O(20)-H(49)	10.196
N(22)-C(32)	5.5781	N(9)-C(7)-C(8)	109.106	C(1)-C(6)-O(20)-H(49)	168.502
		C(5)-C(7)-C(8)	107.904	C(8)-C(10)-O(19)-H(48)	22.834
				C(11)-C(10)-O(19)-H(48)	151.744
				C(8)-C(7)-N(9)-H(41)	71.213
				C(8)-C(7)-N(9)-C(21)	93.259
				C(5)-C(7)-N(9)-H(41)	49.681
				C(5)-C(7)-N(9)-C(21)	145.844
				C(5)-C(7)-C(8)-C(10)	86.383
				C(5)-C(7)-C(8)-C(14)	91.656
				N(9)-C(7)-C(8)-C(10)	38.348
				N(9)-C(7)-C(8)-C(14)	143.611
				C(4)-C(5)-C(7)-C(8)	83.078
				C(4)-C(5)-C(7)-N(9)	155.362
				C(6)-C(5)-C(7)-C(8)	94.926
				C(6)-C(5)-C(7)-N(9)	26.632

Table 3C.3: *Some of the important geometric parameters of OXAZH*

Bond	**Bond length (Å)**	**Bond**	**Bond angle (deg)**	**Bond**	**Dihedral angle (deg)**
O(19)-H(35)	0.9691	O(20)-C(21)-N(8)	121.640	C(21)-N(8)-C(7)-C(4)	123.112
N(8)-C(7)	1.4554	O(20)-C(21)-O(22)	120.840	C(21)-N(8)-C(7)-C(9)	1.851
O(20)-C(14)	1.3687	N(8)-C(21)-O(22)	117.410	H(28)-N(8)-C(7)-C(4)	47.117
C(21)-O(20)	1.3535	C(14)-O(20)-C(21)	118.830	H(28)-N(8)-C(7)-C(9)	172.081
N(8)-C(21)	1.3559	H(35)-O(19)-C(5)	111.401	C(10)-C(9)-C(7)-N(8)	173.675
C(21)-O(22)	1.2092	H(28)-N(8)-C(7)	119.188	C(14)-C(9)-C(7)-C(4)	114.447
C(5)-O(19)	1.3611	H(28)-N(8)-C(21)	115.851	C(14)-C(9)-C(7)-N(8)	5.363
O(20)-H(35)	2.2753	C(7)-N(8)-C(21)	124.292	C(21)-O(20)-C(14)-C(13)	173.190
O(19)-H(28)	1.7465	N(8)-C(7)-C(9)	111.889	C(21)-O(20)-C(14)-C(9)	7.146
		N(8)-C(7)-C(4)	105.418	O(22)-C(21)-O(20)-C(14)	172.856
		C(9)-C(7)-C(4)	114.423	N(8)-C(21)-O(20)-C(14)	10.952

C(7)-N(8)-C(21)-O(22)	177.190
C(7)-N(8)-C(21)-O(20)	6.493
H(28)-N(8)-C(21)-O(22)	12.285
H(28)-N(8)-C(21)-O(20)	164.031
C(6)-C(5)-O(19)-H(35)	8.903
C(3)-C(4)-C(7)-C(9)	21.633
C(3)-C(4)-C(7)-N(8)	145.000
C(5)-C(4)-C(7)-C(9)	161.130
C(5)-C(4)-C(7)-N(8)	37.763

Table 5C.4: *HOMO-LUMO energies of the ligands*

S.No.	Species	$\Delta H°_f^{\#}$ (kcal. mol^{-1})	HOMO (eV)	LUMO (eV)	Calculated λ_{max} (nm)	Observed λ_{max} (nm)
1	UBBH2	13.381	-6.973	-3.731	302	334
2	R-UBBH2 .2DMF	13.776 (20.217)	-6.851	-3.590	311	345
3	OXAZH	37.824	-8.012	-4.771	235	260

#, The value in parenthesis is calculated heat of desolvation

References

1. J. B. Lambert, *Introduction to Organic Spectroscopy*, Macmillan, New York, 1987.
2. L. Antonov, V. Deneva, S. Simeonov, V. Kurteva, D. Nedeltcheva and J. Wirz, *Angew. Chemie Int. Ed.*, 2009, **48**, 7875–7878.
3. I. Sheikhshoaie and W. Fabian, *Curr. Org. Chem.*, 2009, **13**, 149–171.

4. P. Neyroz, L. Franzoni, A. Spisni, L. Masotti and L. Brand, *Chem. Phys. Lipids*, 1992, **61**, 255–63.

5. V. T. Kasumov, F. Ucun, I. Kartal and F. Köksal, *Spectrosc. Lett.*, 1999, **32**, 485–495.

6. A. Blagus, D. Cincic, T. Friscic, B. Kaitner and V. Stilinovic, *Maced. J. Chem. Chem. Eng.*, 2010, **29**, 117–138.

7. B. Kaitner, E. Mestrovic and G. Pavlovic, *J. Chem. Cryst.*, 1998, **28**, 77–82.

8. S. Bilge, Z. Kiliç, Z. Hayvali, T. Hökelek and S. Safran, *J. Chem. Sci.*, 2009, **121**, 989–1001.

9. L. M. Ignjatović, J. M. Dimitrić Marković, D. A. Marković and J. M. Baranac, *J. Serbian Chem. Soc.*, 2002, **67**, 53–60.

10. A. Simić, D. Manojlović, D. Šegan and M. Todorović, *Molecules*, 2007, **12**, 2327–2340.

11. N. Parveen, A. Shah, S. Z. Khan, S. U. Khan, U. A. Rana, F. Fathi, A. H. Shah, M. N. Ashiq, A. Rauf, R. Qureshi, Z. -u. Rehman and H.-B. Kraatz, *J. Electrochem. Soc.*, 2014, **162**, H32–H39.

12. SHELXTL. Program for the Solution and Refinement of Crystal Structures, *(version 6.14); Bruker AXS Wisconsin USA, 2000*.

13. G. Sheldrick, G.M. SHELXL-97, Program for Crystal Structure Refinement; University of Göttingen, *The SHELX-97 Manual*, 1997.

14. C. B. Hübschle, G. M. Sheldrick and B. Dittrich, *J. Appl. Crystallogr.*, 2011, **44**, 1281–1284.

15. Molecular Modeling Programs, *http://biowiki.ucdavis.edu/@api/deki/pages/1323/pdf/Molecular%2bModeling%2bPrograms%253A.pdf?origin=mt-web&deep=false&showtoc=false*, .

16. T. Gardner, *Molecular Modeling in Undergraduate Chemical Education*, 2005.

17. W. J. Hehre and A. J. Shusterman, *Molecular Modeling in Undergraduate Chemistry Education*, Wavefunction, Inc., 2000.

CHAPTER - VI

BIOLOGICAL ACTIVITY

In this Chapter, the biological activities of o-TOLI-Pyral and its metal complexes Co(II), Ni(II), Cu(II) and Zn(II) besides racemic-UBBH2, R-UBBH2.2DMF, S-UBBH2.2DMF, racemic-OXAZH, R-OXAZH and S-OXAZH are presented. Biological activities of these compounds were screened for antibacterial (Gram-positive bacteria - *Bacillus subtilis*, *Staphylococcus aureus* and Gram-negative bacteria - *Escherichia coli*, *Klebsiella pneumoniae* strains) and antifungal activities (*Aspergillus niger* and *Fusarium oxysporum* strains) by zone of inhibition method[1–4]. Zone of inhibition of these compounds were compared against a standard drug, *Streptomycin*[2,5] and *Griseofulvin*[6] for antibacterial and antifungal activities (**Figure 6.1**) respectively.

6.1: Minimum Inhibitory Concentration (MIC)

Compounds showing promising antibacterial/antifungal activities were selected to determine minimum inhibitory concentration by dilution method[3,7]. The minimum inhibitory concentrations were determined by assaying at 3000 μg mL^{-1}, 1500 μg mL^{-1} and 500 μg mL^{-1} concentrations of selected compounds by comparison with the standard antibacterial and antifungal antibiotics of at the same concentrations.

6.2: Antibacterial and Antifungal Activities of o-TOLI-Pyral and Its Metal Complexes

The microbial results of Schiff base and its Co(II), Ni(II) Cu(II) and Zn(II) complexes are systematized in **Table 6.1**. The antibacterial activity of the Schiff base exhibited a considerable enhancement on coordination with the metal ions against selected bacterial strains (*S. aureus*, *B. subtilis*, *E. coli* and *K. pneumonia*)[8–10]. A typical zone of inhibition images of o-TOLI-Pyral over gram positive and gram negative bacterial cells are shown in **Figure 6.2** and which is further presented as histogram in **Figure 6.3**. From the histogram, it is found that $[Zn_2(\text{o-TOLI-Pyral})_2]Cl_4$ exhibits potential antibacterial and antifungal activities. o-TOLI-Pyral activity is altered great extent upon coordination of metal ion in all the complexes Co(II), Ni(II), Cu(II) and Zn(II).

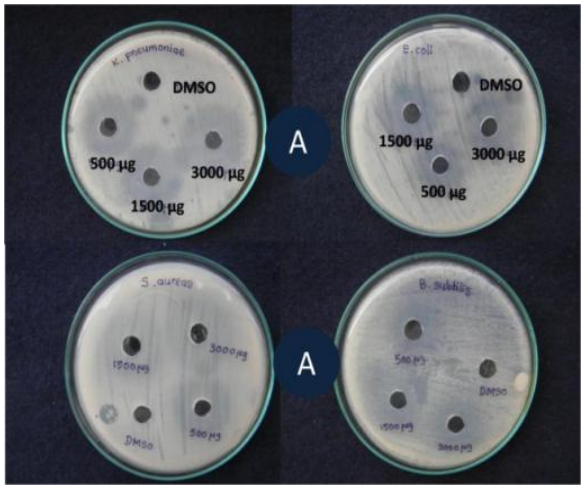

Figure 6.1: Zone of inhibition of streptomycine over Gram-positive and Gram-negative strains

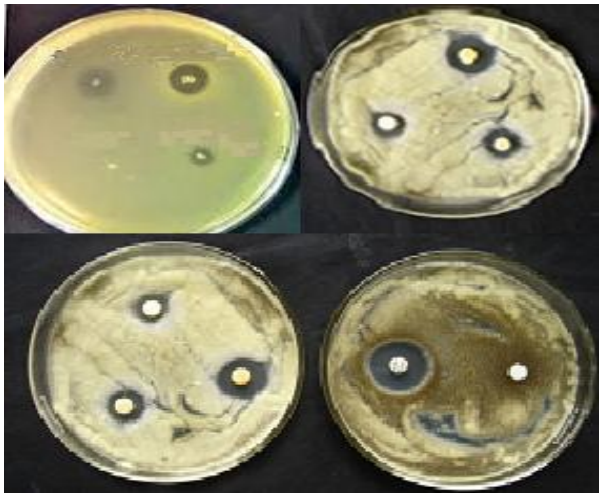

Figure 6.2: Zone of inhibition of o-TOLI-Pyral over Gram-positive and Gram-negative strains

Table 6.1: *Antibacterial and antifungal results of Schiff base and its Co(II), Ni(II) Cu(II) and Zn(II) complexes*

Compound	Concentration (in µg mL^{-1})	Inhibition zones (in mm)					
		Gram-positive bacteria		Gram-negative Bacteria		Fungal strains	
		B. subtilis	*S. aureus*	*E. coli*	*K. pneumonia*	*A. niger*	*F. oxysporum*
o-TOLI-Pyral	500	2	1	3	2	2	3
	1500	4	2	4	3	3	4
	3000	6	4	6	5	4	6
$[Co_2(o\text{-}TOLI\text{-}Pyral)_2]Cl_4$	500	1	2	2	2	3	1
	1500	2	4	4	3	4	2
	3000	4	6	8	9	5	3
$[Ni_2(o\text{-}TOLI\text{-}Pyral)_2]Cl_4$	500	1	1	2	1	3	2
	1500	2	2	3	2	4	4
	3000	3	4	5	4	6	5
$[Cu_2(o\text{-}TOLI\text{-}Pyral)_2]Cl_4$	500	2	2	3	3	2	3
	1500	4	4	5	5	3	4
	3000	6	6	7	7	5	6
$[Zn_2(o\text{-}TOLI\text{-}Pyral)_2]Cl_4$	500	4	2	2	2	2	2
	1500	6	4	3	5	4	3
	3000	7	5	4	6	6	4
Standard (streptomycin)	500	8	9	9	10	-	-
	1500	9	10	10	11	-	-
	3000	9	13	11	12	-	-
Griseofulvin	500	-	-	-	-	10	11
	1500	-	-	-	-	12	10
	3000	-	-	-	-	12	13

Key for interpretation: less than 1 mm – inactive; 2 mm – weakly active; 3 mm – moderately active; above 4 mm – highly active

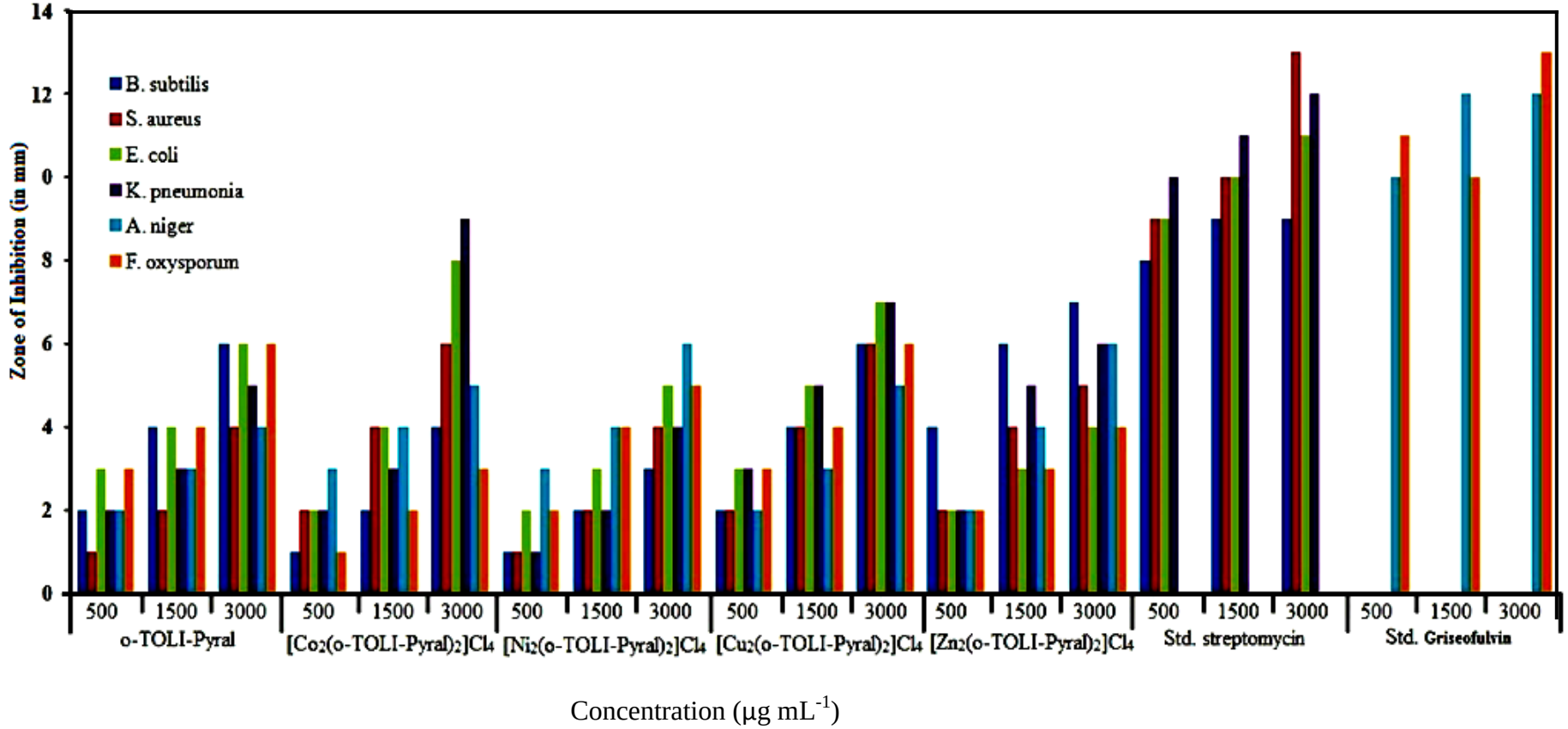

Figure 6.3: Histogramphic representation of the antibacterial and antifungal activities of o-TOLI-Pyral, $[Co_2(o\text{-TOLI-Pyral})_2]Cl_4$, $[Ni_2(o\text{-TOLI-Pyral})_2]Cl_4$, $[Cu_2(o\text{-TOLI-Pyral})_2]Cl_4$ and $[Zn_2(o\text{-TOLI-Pyral})_2]Cl_4$ against standard drug streptomycin for antibacterial and standard drug griseofulvin for antifungal activities

6.3: Antibacterial and Antifungal Activities of UBBH2, R-UBBH2.2DMF, S-UBBH2.2DMF, OXAZH, R-OXAZH and S-OXAZH

The antibacterial activities of the UBBH2, R-UBBH2.2DMF, S-UBBH2.2DMF, OXAZH, R-OXAZH and S-OXAZH compounds are carried out by agar well diffusion method[3,7]. Antibacterial activity of these compounds are tested over Gram positive (*Bacillus subtilis* and *Staphylococcus aureus)* and Gram negative (*Escherichia coli* and *Klebsiella pneumonia)* strains All the compounds have a significant inhibitory action against Gram-positive and Gram- negative bacteria. The inhibitory effect of all the compounds increased with the increasing concentration of the compound. The racemic-OXAZH is separated into R and S enantiomers and observed the activity. Interestingly the R-isomer of OXAZH shows inhibitory effect on all the four bacterial strains while, S-isomer of OXAZH shows a meager activity which is insignificant on three bacterial strains (*B. subtilis*, *E. coli* and *K. pneumonia*) except Gram positive bacterium *S. aureus*. Among Gram-positive bacteria *S. aureus* is more susceptible than *B. subtilis*, while in Gram-negative bacteria *K. pneumoniae* is more susceptible. The microbial activity of these compounds are shown in **Figures 6.4-6.10**. From antibacterial activity of these compounds, it is noticed that no compound shows greater zone of inhibition than the standard antibiotic *streptomycin* which is shown as histogram in **Figure 6.11**. However, racemic-UBBH2 have shown maximum activity at 3000 µg mL^{-1} well against Gram-positive bacterium *S. aureus*. The corresponding data are given in **Table 6.2**. From the antifungal activity studies, it is noticed that the compounds do not shown significant activity over these fungal organisms.

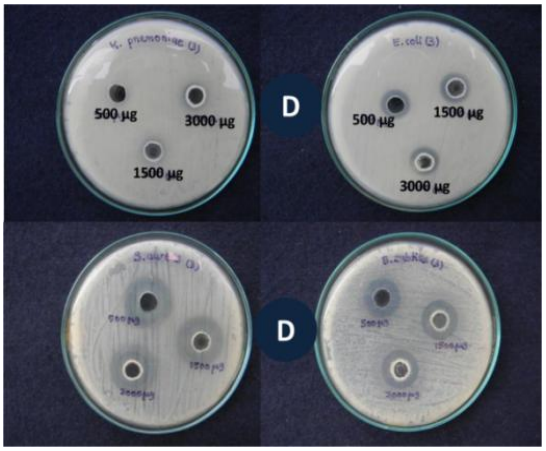

Figure 6.4: Zone of inhibition of racemic UBBH2 over Gram positive and Gram negative strains

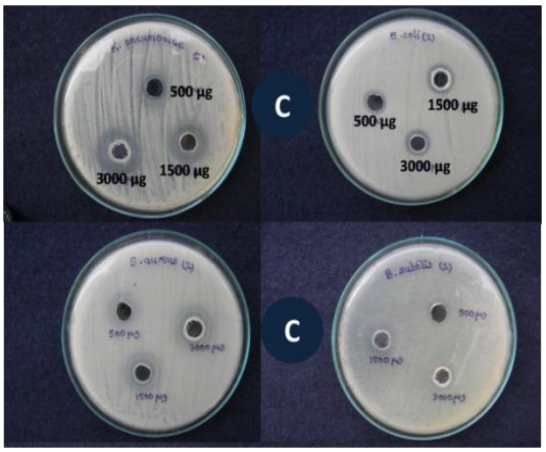

Figure 6.5: Zone of inhibition of racemic R-UBBH2.2DMF over Gram positive and Gram negative strains

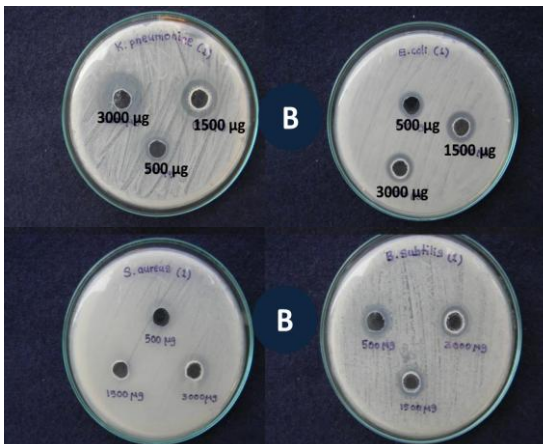

Figure 6.6: Zone of inhibition of racemic S-UBBH2.2DMF over Gram positive and Gram negative strains

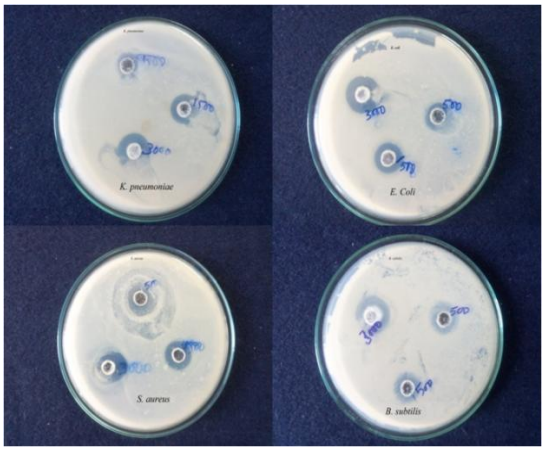

Figure 6.7: Zone of inhibition of racemic-OXAZH over Gram positive and Gram negative strains

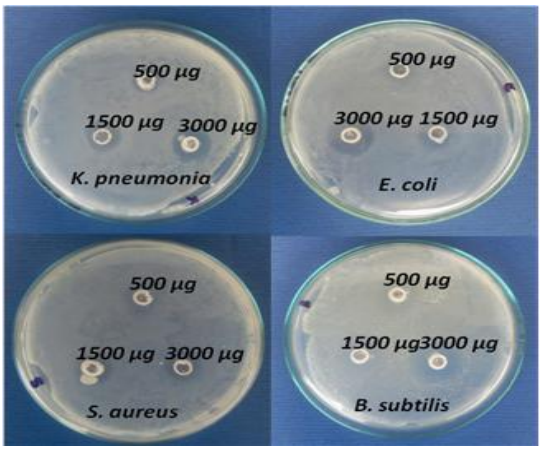

Figure 6.8: Zone of inhibition of R-OXAZH over Gram positive and Gram negative strains

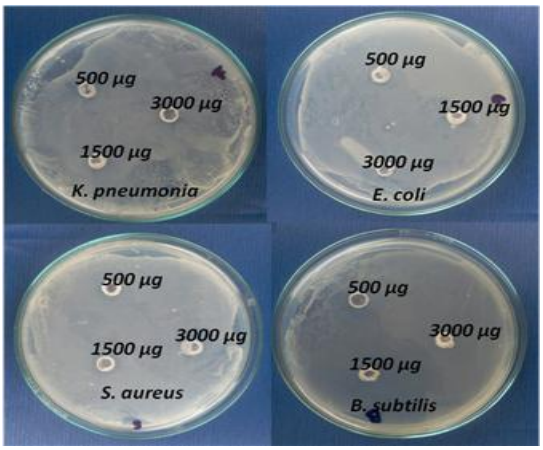

Figure 6.9: Zone of inhibition of S-OXAZH over Gram positive and Gram negative strains

Table 6.2: *Antibacterial results of racemic-UBBH2, R-UBBH2.2DMF, S-UBBH2.2DMF and OXAZH*

Compound	Concentration (in µg mL^{-1})	Inhibition zones (in mm)			
		Gram-positive bacteria		Gram-negative Bacteria	
		B. subtilis	*S. aureus*	*E. coli*	*K. pneumonia*
R-UBBH2•2DMF	500	1	4	2	2
	1500	3	5	3	5
	3000	1	6	3	8
S-UBBH2•2DMF	500	2	3	2	2
	1500	3	3	3	3
	3000	3	3	3	9
racemic-UBBH2	500	5	8	4	1
	1500	5	8	4	2
	3000	5	9	4	2
OXAZH	500	5	5	6	4
	1500	7	6	8	5
	3000	8	8	9	6
Standard (streptomycin)	500	8	9	9	10
	1500	9	10	10	11
	3000	9	13	11	12

Key for interpretation: less than 1 mm – inactive; 2 mm – weakly active; 3 mm – moderately active; above 4 mm – highly active

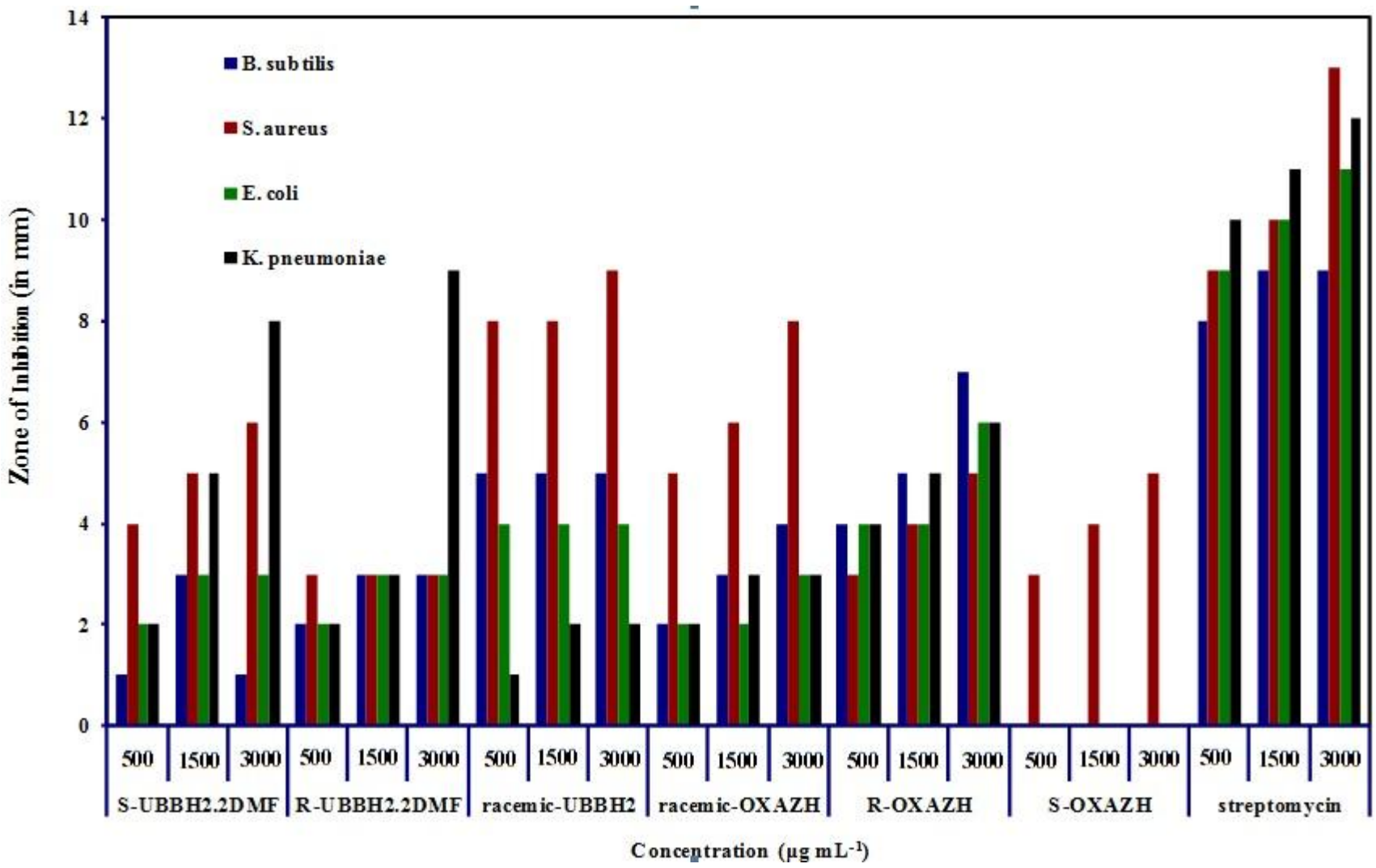

Figure 6.10: Histogramphic representation of the antibacterial activities of (S)-UBBH2.2DMF, (R)-UBBH2.2DMF, racemic-UBBH2, racemic-OXAZH, (R)-OXAZH and (S)-OXAZH against standard drug streptomycin

CHAPTER VI

References

1. R. Perumal Samy and S. Ignacimuthu, *J. Ethnopharmacol.*, 2000, **69**, 63–71.
2. O. O. Igbinosa, E. O. Igbinosa and O. A Aiyegoro, *African J. Pharm. Pharmacol.*, 2009, **3**, 58–62.
3. C. Valgas, S. M. De Souza, E. F. A Smânia and S. J. Artur, *Brazilian J. Microbiol.*, 2007, **38**, 369–380.
4. N. Bhalodia and V. Shukla, *J. Adv. Pharm. Technol. Res.*, 2011, **2**, 104.
5. E. A. Hayouni, M. Abedrabba, M. Bouix and M. Hamdi, *Food Chem.*, 2007, **105**, 1126–1134.
6. P. W. Brian, P. J. Curtis, H. G. Hemming and G. L. F. Norris, *Trans. Br. Mycol. Soc.*, 1957, **40**, 365–IN3.
7. A. Abdul jameel and M. Syed ali padusha, *Asian J. Chemsirty*, 2010, **22**, 3422–3428.
8. Z. H. Abd El-Wahab and M. R. El-Sarrag, *Spectrochim. Acta - Part A Mol. Biomol. Spectrosc.*, 2004, **60**, 271–277.
9. A. K. Abu Al-Nasr and R. M. Ramadan, *Spectrochim. Acta - Part A Mol. Biomol. Spectrosc.*, 2013, **105**, 14–19.
10. A. Golcu, M. Tumer, H. Demirelli and R. A. Wheatley, *Inorganica Chim. Acta*, 2005, **358**, 1785–1797.

With a view to generate multi-functional organic compounds with azomethine as a common functionality that are expected to possess mechanochromic, thermochromic, photochromic, halochromic, polymorphic, etc., properties. Four different class compounds were prepared along with some of their metal complexes. Detailed spectral, electrochemical, crystallographic, pharmacological and molecular modeling studies were carried out. The results of the investigation are compiled in the form of a thesis, entitled, "*Spectral, Electrochemical, Single Crystal XRD and Molecular Modeling Studies of Azomethine and Dihydroazomethine Compounds of Supramolecular Significance*" in six chapters.

Chapter I deals with the introduction to the kind of studies carried out as a back drop.

In **Chapter II** presents the details of the synthesis, sampling along with the features of the instruments.

In **Chapter III**, the nitrogenous biphenyl bridged-2-carboxaldimines ligands and their metal complexes synthesized and characterized by modern instrumental methods such as electronic absorption and fluorescence emission spectroscopic, electrochemical, thermometric, magnetochemical and computational methods were presented. Kinetics of hydrolysis of these ligands were studied by spectroscopically and voltammetrically. The stoichiometric ratio of metal to ligand were determined by Job's mono-variation method. Molar conductivities of these ionic complexes were measured. The metal content in the complexes were further analysized by ICPOES. Cyclic voltammetric studies were conducted

In **Chapter IV**, the studies of a non-linear Schiff base PNASH are presented. From the studies it is found that the molecule exhibits polymorphic, mechanochromic, thermochromic and photochromic (photo-switching) behavior. Crystallization of PNASH in EtOAc and MeCN yields two different morphological crystals which were further characterized by single crystal x-ray diffraction, PXRD and DSC techniques. It is found that there are two different polymorphs. Single crystal x-ray diffraction study revealed that PNASH is crystallized in right-handed and left handed helical $P2_1/_c$ space group and it is due to the difference in H-bonding dihedral angles. Further cyclic voltametric analysis were done over PNASH in different pH buffers and non-aqueous media. From the cyclic voltammograms of PNASH it is found that the molecule

undergoes structural changes in both acidic and basic pH buffers. It is due to the electrochemical reduction azomethine moiety. Molecular modeling studies were carried out over acid-base conjugates and photo-induced tautomeric forms. It is observed that the experimental results are good in agreement with the modeling data.

In **Chapter V**, the electronic absorption and fluorescence emission, electrochemical, thermal, magnetochemical and molecular modeling studies carried out of a novel urea Betti base were presented. From the electronic absorption and emission studies, it is found that the molecules UBBH2 and OXAZH exhibit acid-base equilibria. Acid-base equilibria in both UBBH2 and OXAZH are due to presence of labile protons in their molecular skeleton. The UBBH2 undergoes consecutive acid-base equilibrium besides exhibiting halochromism. UBBH2 and OXAZH compounds were crystallized in different organic solvents. From the crystal structure analysis it is understood that UBBH2 is crystallized as DMF enantiomeric solvates in the presence of DMF molecules with P_1 space group whereas in the absence of DMF it is crystallized in racemic form with *Pn* space group and OXAZH is crystallized in $P2_1/_c$ space group without solvent molecule in their unit cells. Differential scanning calorimetric studies were carried out for solvates, non-solvates and OXAZH. From the thermograms, it is observed that in solvates two endo-thermometric events are noticed. The first endo-thermometric event is corresponding to the desolvation and the second endo-thermometric event is corresponding to the melting. In case of non-solvate UBBH2 and OXAZH one endo-thermometric event was observed for each. It is due to the melting event. Heat of desolvation and heat of fusion were calculated for solvated UBBH2 whereas heat of fusion was calculated for non-solvated UBBH2 and OXAZH at each endo-thermometric event separately. However, molecular modeling studies were carried out for the solvated, non-solvated and OXAZH. From the molecular modeling studies it is found that modeling data is in good agreement with experimental data.

In **Chapter VI**, the bactericidal and fungicidal activities of some the compounds were screened against the gram-positive bacteria (*B. Subtilis* and *S. Aureus*) and Gram-negative bacteria (*E. Coli* and *K. Pneumoniae*) strains and antifungal (*Aspergillus niger* and *Fusarium oxysporum*) strains by zone of inhibition method. From the results it is found that $[Zn_2(o\text{-TOLI-Pyral})_2]Cl_4$ is exhibiting potential antibacterial and antifungal activities. o-TOLI-Pyral activity is altered great extent upon coordination with metal ion in all the complexes Co(II), Ni(II), Cu(II)

and Zn(II). Similarly, bactericidal and fungicidal activities of racemic-UBBH2, R&S enantiomeric solvates of UBBH2, racemic-OXAZH and R&S enantiomers of OXAZH were screened. It is found that racemic-UBBH2 is shown potential bactericidal activity. None of these compounds shows more activity than standard drugs, *Streptomycin* and *Griseofulvin*. Interestingly, the R-isomer of OXAZH shows inhibitory effect on all the four bacterial strains whereas S-isomer of OXAZH shows a meager activity which is insignificant on three bacterial strains (B. Subtilis, E. Coli and K. Pneumonia) except gram positive bacterium S. Aureus.

Publications

1. Synthesis and Crystal Structure Analysis of 1-((2-hydroxynaphthalen-1-yl)(2- hydroxy phenyl)methyl)urea • 2DMF Solvate

   G. Srinivasa Rao, Srinivas Basavoju and Ramachandraiah A
   (Mol. Cryst. Liq. Cryst., Vol. 603: pp. 1–15, 2014)

2. Study on Polymer Coated Etched Optical Fiber for pH Sensing

   P.V.N. Kishore, M. Sai Shanar, P. Vengal Rao, K. Yugender Goud and **G. Srinivasa Rao**

   12th International Conference on Fiber Optics and Photonics – 2014, IIT Kanpur in association with American Optical Society (OSA), T3A.11

3. Photo - Induced Transformation and Buffer Effect Studies of A Non-linear Molecule for Electrochromic Device Applications

   G Srinivasa Rao, Ashutosh Kumar Yadav and A. Ramachandraiah
   (INCEEE-2015, ISBN: 978-81-928314-1-1)

4. Crystal Structure Analysis, Spectral, Halochromic Studies of Urea Betti Base and Its Oxazinone Derivative

   Gudipati Srinivasa Rao, Srinivas Basavoju and A. Ramachandraiah
   (Journal of Molecular Structure under review*)*

Conference papers

1. Spectral, Electrochemical and Molecular Modeling Studies of A Non-linear Schiff Base in Aqueous Buffer Media.

   Gudipati Srinivasa Rao, Ashutosh Kumar Yadav and A. Ramachandraiah

   Andhra Pradesh Akademi of Science Golden Jubilee Science Congress (APAS GJSC 2014), Organized by Andhra Pradesh Akademi o Science in association with CSIR-CCCMB and IICT, Hyderabad, 13th -15th , November, 2015.

2. Spectral and Molecular Modeling Studies of Some Binuclear Copper (II) and VO(IV) Complexes of a New Series of Schiff Bases of 3-Formyl Chromone and 4,4'-Diaminobiphenyls

   Ashutosh Kumar Yadav, **Gudipati Srinivasa Rao** and A. Ramachandraiah

   Andhra Pradesh Akademi of Science Golden Jubilee Science Congress (APAS GJSC 2014), Organized by Andhra Pradesh Akademi o Science in association with CSIR-CCCMB and IICT, Hyderabad, 13th -15th , November, **2015**.

3. Spectral, Electrochemical, and Molecular Modeling Studies of A Urea Betti Base in Aqueous and Non-Aqueous Media

   G. Srinivasa Rao, Ashutosh Kumar Yadav and A. Ramachandraiah
   International conference on Electrochemical Science and Technology (ICONEST-2014), Organized by the Electrochemical Society of India, at IISc – Bangaluru, 7th – 9th August **2014**.

4. Spectral and Electrochemical studies of the kinetics hydrolysis of biphenyl bridged pyridine-2-imine Schiff bases and their metal complexes

   G. Srinivasa Rao, Ashutosh Kumar Yadav and A. Ramachandraiah

   International conference on "Recent Advances in Analytical Science (RAAS)" Organized by Department of Chemistry, IIT-BHU & Indian Society of Analytical Scientists ISAS (Varanasi Chapter), at IITBHU- Varanasi, 27th – 29th march **2014**.

5. Fast Scan Spectrophotometry and Spectroelectrochemicalvoltammetry as tools to monitor fast kinetics and transient reaction intermediates

   Ashutosh Kumar Yadav, **G. Srinivasa Rao** and A. Ramachandraiah

   International conference on "Recent Advances in Analytical Science (RAAS)" Organized by Department of Chemistry, IIT-BHU & Indian Society of Analytical Scientists ISAS (Varanasi Chapter), at IITBhu- Varanasi, 27th – 29th march **2014**.

6. Spectral, Electrochemical and Molecular Modelling Studies of (N4E, N4'E)-3,3'-dimethyl-N4,N4'-bis (pyridin-2-ylmethylene)biphenyl-4,4'- diamine

   Gudipati Srinivasa Rao and Allikayala Ramachandraiah

   An International conference on "Emerging Trends in Chemical Sciences (ICETCS)" Organized by Central University of Gujarat , held on 14th -15th March, **2013**.

7. Spectral and Electrochemical Investigation of Some Aromatic Azo Dyes in Different pH Buffers

   Srinivasa Rao G, Krishna V and Ramachandraiah A

   2nd International Conference on "*Trends in Chemical Sciences Going Beyond Frontiers*" , at Indian Council of Chemist, Malaysia , held on 10th-12th June, **2012**.

8. Electrochemical Behavior of a Double Diphenylether-Bridged Binuclear Copper (II) Schiff Base Complexes in Non-Aqueous Media

   Krishna V, **Srinivasa Rao G** and Ramachandraiah A

   2nd International Conference on "*Trends in Chemical Sciences Going Beyond Frontiers*" , at Indian Council of Chemist, Malaysia , held on 10th-12th June, **2012**.

9. Spectral, Electrochemical and Molecular Modeling Studies of 6-Hydroxy, 5-((E)(4'((E)-(2-hydroxy-4, 6-dioxocyclohex-1-enyl) diazenyl)-3, 3'-dimethoxy biphenyl-4yl)diazenyl)pyrimidine-2, 4(1H, 3H)-Dione

   Srinivasa Rao G, Krishna V and Ramachandraiah A

   National Conference On "*Interface between Chemical Sciences and Technologies*", at National Institute of Technology, Warangal, held on 29th-30th December, **2011**.

BIO-DATA

Gudipati Srinivasa Rao

Contact Address
S/O. G. Muthilingam
Vallapuram (Vill & Post)
Nadigudem (Mandal)
Nalgonda (District) – 508 234
Telangana, India.
E-mail:
srinugudipati4u@mail.com
srinugudipati4u@nitw.ac.in
Mobile: +91-9963976237

Objective: Desire to join in a progressive organization that gives me scope to apply my knowledge and technical skills, and to be a part of the team that dynamically works towards growth of the organization.

Academic Qualifications:

July 2010 – Present : **Research Scholar (PhD Student)**

Under the supervision of **Prof. A. Ramachandraiah**, Department of Chemistry, National Institute of Technology Warangal, Telangana, India

Research Topic: " Spectral, Electrochemical, Single Crystal XRD and Molecular Modeling Studies of Azomethine and Dihydroazomethine Compounds of Supramolecular Significance"

July 2007 – June 2009 : **Master of Science in Chemistry (Analytical Chemistry)**
National Institute of Technology Warangal, Telangana, India
Grade Point Average: **7.97** (First Class with Distinction)

June 2003 – May 2006 : **Bachelor of Science (Mathematics, Physics and Chemistry)**
Osmania University, Hyderabad, Telangana, India
Percentage of Marks: **71.6%** (First Class with Distinction)

June 2001 – May 2003 : **Intermediate (Mathematics, Physics and Chemistry)**
Board of Intermediate Education, Andhra Pradesh, India
Percentage of Marks: **76.7 %** (First Class with Distinction)

June 2000 – April 2001 : **Secondary School Certificate (High School)**
Board of Secondary Education, Andhra Pradesh, India
Percentage of Marks: **70.3 %** (First Division)

Professional Summary:

- **Senior Research Fellow** at National Institute of Technology, Warangal, Telangana, India, from July 2012 to till date.
- **Industrial training experience** from April 2009 to June 2009 at **NATCO** Research Centre, Hyderabad during M. Sc. Program as a part of External Project.

Personal Details:

- Name : Gudipati Srinivasa Rao
- Father's Name : Muthilingam
- Date of Birth : 31-10-1984
- Gender : Male
- Marital Status : Married
- Nationality : Indian
- Languages Known : Telugu, English and Hindi

Achievements:

- Qualified Andhra Pradesh State Eligibility Test (**APSET**) 2012 for Assistant Professor/Lectureship in the subject of **Chemical Sciences**.
- Qualified Graduate Aptitude Test in Engineering (**GATE**) 2010.
- Secured 37th rank in National Institute of Technology Warangal Entrance Test **(NITWET)** 2007 for M. Sc. Admissions.
- Elected as Research Scholar's representative and student council member in the academic year 2011-2012 in NIT-Warangal.

Technical Skills:

- Expertise in utilizing the software - Microsoft Office, Surfer, Origin etc., Molecular Modeling Systems - ChemDraw Ultra 12.0, HyperChem Release - 8.0.9 and Sybyl.
- Expertise in MENDELEY Desktop.

Expertise in Instrumental Techniques:

- Electrochemical Impedance Analyzer, Zahner-Elektrik (IM6e), GmbH, Germany
- Electrochemical Workstation, Sinsil CHI 619D
- UV-Visible Spectrophotometers, Analytik Jena Specord 205 and Shimadzu 1601
- UV-Visible-NIR Agilent cary 5000
- Thermoscientific UV-Visible spectrophotometer Evolution 600 Instrument
- Analytika F96pro Fluorescence Spectrophotometer
- FTIR Spectrophotometer, PerkinElmer 100s
- NETZSCH STA 2500 Regulus
- Differential Scanning Calorimeter, Q10 TA instruments, USA
- Jeol FA-100, X-band ESR spectrometer
- Agilent ICPOES 720 series
- BioLogic MOS-500 CD and ORD spectrophotometer.
- PANalytical's X'Pert³ Powder X-ray diffractometer
- Other small instruments relevant for materials characterization and analysis

Research Interests:

- Electrochemical Sensors
- Electrochromic, Photochromic, Mechanochromic and other chromic material
- Optochemical Sensors, Spectroelectrochemistry
- Perovskite solar cells

Memberships:

- Society for Advancement of Electrochemical Science and Technology (SAEST)

Other Capabilities:

- Capable of carrying out both collaborative and independent research
- Motivated strong ethics and providing efficient service
- Very good interpersonal and communication skills along with management skills
- Good experience in writing technical papers, presentations and reports
- Worked with many post-graduate students for their projects